Nanophotonique pour la détection exaltée de molécules fluorescentes

Jérôme Wenger

Jérôme Wenger. Nanophotonique pour la détection exaltée de molécules fluorescentes. Optique [physics.optics]. Aix-Marseille Université, 2012. tel-00840843

HAL Id: tel-00840843
https://theses.hal.science/tel-00840843

Submitted on 3 Jul 2013

Dossier de Travaux

Présenté par

Jérôme Wenger

Pour l'obtention d'une

Habilitation à Diriger des Recherches

Nanophotonique pour la détection exaltée de molécules fluorescentes

Discipline : Physique et Sciences de la Matière

Soutenance publique le 05 juin 2012

Devant la Commission d'Examen

Prof. Marie Houssin	**Rapporteur**
Dr. Sandrine Lévêque-Fort	**Rapporteur**
Prof. Jérôme Plain	**Rapporteur**
Dr. Alexandre Bouhelier	**Examinateur**
Prof. Hugues Giovannini	**Examinateur**
Dr. Andreï Kabashin	**Examinateur**
Dr. Hervé Rigneault	**Membre invité**

Table des Matières

Introduction

Combiner la Spectroscopie de Fluorescence avec des Structures Photoniques

La spectroscopie de fluorescence est devenue une technique incontournable pour l'analyse biochimique grâce à sa forte efficacité optique et à la vaste librairie de sondes moléculaires disponibles. L'essence même de la fluorescence repose sur les phénomènes d'absorption et d'émission de photons par des molécules. Améliorer le rendement d'émission (ou brillance) de chaque émetteur augmente de fait l'efficacité et la sensibilité des différentes méthodes de spectroscopie reposant sur le contraste de fluorescence. Un telle amélioration de brillance peut se faire essentiellement au travers de deux voies : (i) par voie chimique, en améliorant la section efficace d'absorption et le rendement quantique des molécules, et (ii) par voie physique, en contrôlant l'environnement électromagnétique des émetteurs, pour renforcer localement l'intensité optique d'excitation, augmenter le taux d'émission et collecter plus efficacement le signal de fluorescence. C'est cette voie physique qui fait l'objet principal de mes recherches. Pour fixer un ordre de grandeur typique, rappelons qu'une molécule fluorescente émet un nombre de photons relativement faible, au mieux de l'ordre de 10^7 photons par seconde, ce qui équivaut à une puissance moyenne d'environ 4 picowatts répartie dans toutes les directions de l'espace. Avec un signal aussi faible, il est essentiel de maîtriser l'interaction entre la molécule et le champ lumineux, et de mettre en œuvre des techniques innovantes pour la détection exaltée de l'émission.

Un second défi majeur pour l'analyse de fluorescence porte sur la capacité à suivre des réactions de molécules individuelles dans des solutions fortement concentrées. Un grand nombre de réactions biochimiques (les réactions enzymatiques en particulier) ne se déclenchent que si la distance inter-molécules est suffisamment faible, ou autrement dit, que si la concentration est suffisamment élevée. Typiquement, il faut considérer des concentrations de l'ordre de quelques dizaines de micromoles par litre. Or, la microscopie classique est limitée par les lois de la diffraction pour des volumes d'analyse de l'ordre de la fraction de micromètre cube, ce qui se traduit par des concentrations de l'ordre de la dizaine de nanomoles par litre pour isoler une molécule dans le volume d'analyse. Il est ainsi nécessaire de gagner près de trois ordres de grandeurs sur le volume d'analyse pour atteindre des régimes pertinents au sens des concentrations biochimiques. Cela impose de dépasser les limites de la diffraction, et donc de repenser complètement l'usage et le design des microscopes optiques.

L'état des techniques de spectroscopies actuelles est similaire à celui des premiers ordinateurs au début des années 1950 : des appareils encombrants avec des performances à la pointe de la technique disponible, mais impossibles à extraire du laboratoire. Une question actuelle est de savoir si l'incorporation de nanosciences photoniques permettra le développement de nouvelles méthodes d'analyses moléculaires.

Le paramètre essentiel pour améliorer la sensibilité des montages de fluorescence repose sur la brillance intrinsèque de chaque émetteur. Pour maximiser le signal détecté par molécule, les systèmes actuels reposent sur des montages de microscopes équipés d'objectifs à forte ouverture numérique et de photodiodes à avalanche de forte sensibilité. Pour isoler le signal utile du bruit, on emploie généralement un microscope confocal, où un faisceau laser d'excitation est fortement focalisé par un objectif de forte ouverture numérique et où un trou de filtrage spatial – conjugué optiquement au point de focalisation laser – permet de rejeter le bruit de fond. Pour obtenir le meilleur rapport signal sur bruit, il est nécessaire d'utiliser une forte ouverture numérique de focalisation afin de maximiser l'intensité d'excitation et la fluorescence collectée, tout en minimisant la contribution du bruit de fond (proportionnel au volume d'analyse).

D'un point de vue fondamental, la microscopie confocale se heurte au phénomène de diffraction, qui limite le diamètre minimal d'un faisceau focalisé à environ la longueur d'onde optique. D'un point de vue technique, cette approche est de plus limitée par le coût et la complexité des objectifs ayant une ouverture supérieure à 1,45. Le plus petit volume défini par la microscopie confocale est alors de 0,1 fL (soit 0,1 μm^3). Pour obtenir des volumes d'analyse plus réduits et une contribution plus faible du bruit, le recours à des techniques de nanophotonique s'impose. Par ailleurs, l'ouverture limitée de l'optique pour collecter la fluorescence fixe une limite au signal maximum détectable par molécule. L'efficacité typique de la collection de fluorescence est de 5 %, ce qui amène à un signal moyen par molécule de 500 000 photons détectés par seconde. Des structures nanophotoniques permettent de dépasser ce seuil.

Pour analyser le signal de fluorescence, il existe de nombreuses méthodes pour obtenir le maximum d'informations d'un échantillon. Cela vient bien au-delà de la simple mesure de l'intensité moyenne de la fluorescence émise telle que décrite plus haut. En particulier, la spectroscopie de corrélation de fluorescence (ou FCS pour fluorescence correlation spectroscopy) est une technique puissante et polyvalente pour l'analyse biochimique. Cette technique est développée depuis le milieu des années 1970, et repose sur l'analyse directe des évolutions temporelles du signal de fluorescence. Cette analyse s'effectue en calculant la corrélation temporelle de l'intensité de fluorescence. La figure 1 illustre le principe général de fonctionnement de la FCS. L'intensité de fluorescence provenant d'un volume d'analyse limité est mesurée au cours du temps. Du fait par exemple de la diffusion de molécules dans et hors de ce volume, l'intensité de fluorescence détectée fluctue naturellement au cours du temps. L'analyse FCS porte sur le calcul de la fonction mathématique de corrélation temporelle de l'intensité de fluorescence détectée. Aux temps courts, cette fonction de corrélation permet d'avoir accès aux paramètres photophysiques des émetteurs ainsi qu'au nombre moyen de molécules détectées. Aux temps longs, elle renseigne sur le temps de séjour moyen (temps de diffusion) des molécules et sur leur mode de diffusion au travers du volume d'analyse. Pour les lecteurs plus familiers de l'analyse dynamique de diffusion laser DLS (dynamic light scattering), on peut dire que la FCS est l'analogue de la DLS pour la fluorescence. Elle permet généralement un meilleur rapport signal à bruit, et peut atteindre la résolution d'une molécule individuelle. La capacité de suivre des réactions chimiques à l'échelle d'une molécule individuelle ouvre des perspectives prometteuses pour l'analyse biochimique. En effet, isoler une molécule unique permet de révéler des informations supplémentaires cachées dans des moyennes d'ensemble opérées sur des milliers de molécules. Parmi ces informations, on peut ainsi isoler des mutations rares, accéder aux variétés des dynamiques temporelles, ou révéler des états transitoires

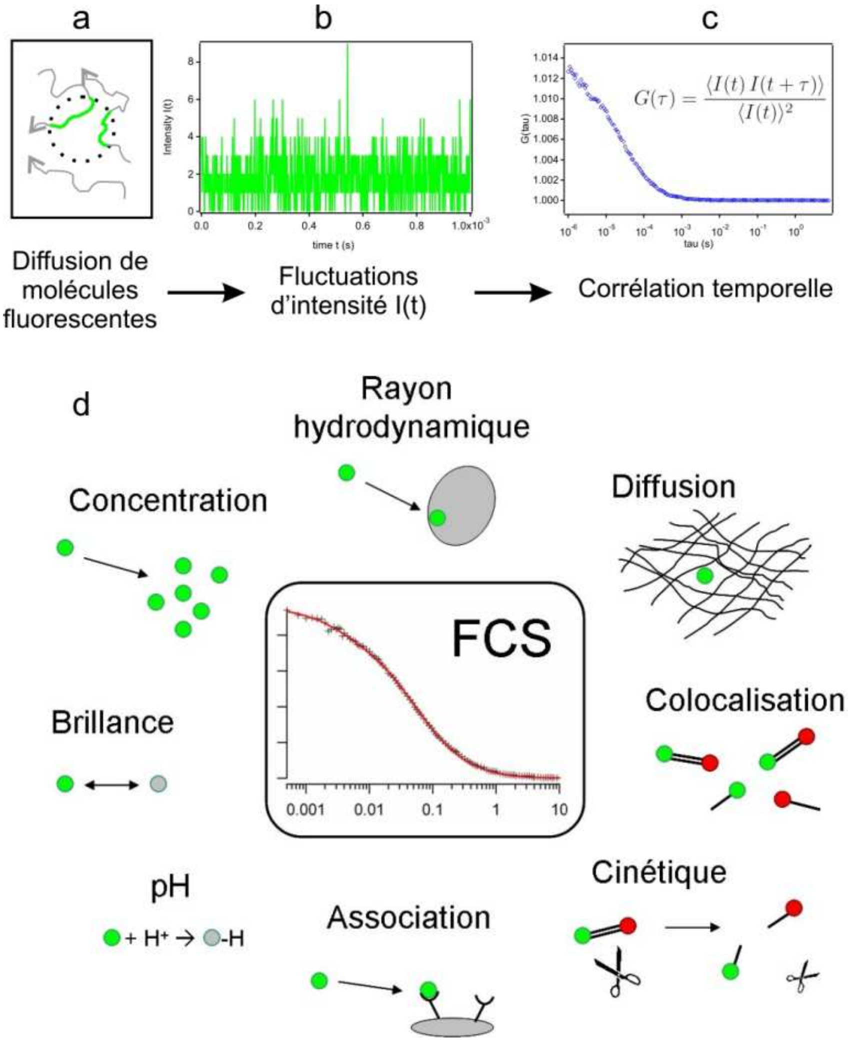

Fig. 1 Schéma de principe de la spectroscopie par corrélation de fluorescence. Les mouvements de diffusion spatiale (Brownienne ou non) de molécules fluorescentes (a) induisent des fluctuations temporelles dans l'intensité de fluorescence détectée (b). La FCS analyse ces fluctuations en calculant la fonction mathématique de corrélation temporelle de l'intensité de fluorescence (c). L'encart (d) indique les principaux domaines d'application de la corrélation de fluorescence.

La capacité de réaliser des nanostructures dont les formes sont contrôlées avec une résolution de quelques nanomètres ouvre des perspectives prometteuses pour la nanophotonique et la biophotonique. Des avancées récentes permettent de confiner et d'exalter le champ lumineux, et donnent accès à un contrôle de l'environnement électromagnétique d'une molécule individuelle. Ces nouvelles possibilités apportent des améliorations essentielles dans la détection de fluorescence, et ouvrent des perspectives d'applications innovantes en biochimie analytique à l'échelle d'une molécule individuelle. La figure 2 résume les principales techniques disponibles actuellement, et compare leurs performances pour deux facteurs de mérite : le volume d'analyse et le gain de fluorescence par émetteur. Plus de détails et de références bibliographiques sont données dans l'article paru dans International Journal of Molecular Sciences inclus ci-après.

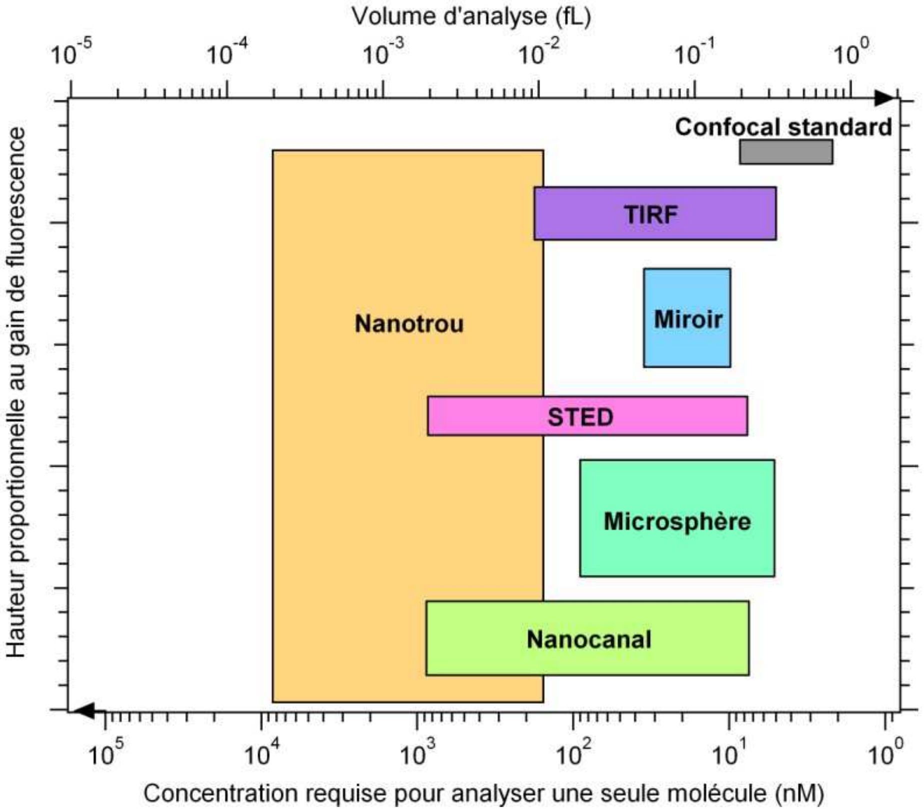

Fig. 2 Représentation graphique des volumes d'analyse obtenus avec les différentes structures photoniques discutées ici. La hauteur relative des rectangles représente pour chaque technique le gain moyen sur le signal de fluorescence par émetteur.

La suite de ce dossier de travaux présente mes principales contibutions à l'amélioration de la technique FCS avec des micro et nanostructures photoniques. Les trois premier chapitres présentent les trois structures que j'ai principalement étudiées au cours de la période 2005-2011 : les nano-ouvertures métalliques, les nano-ouvertures avec corrugations et les microsphères diélectriques. Le quatrième et dernier chapitre présente quelques applications en biophotonique.

Int. J. Mol. Sci. **2010**, *11*, 206-221; doi:10.3390/ijms11010206

OPEN ACCESS

International Journal of
Molecular Sciences
ISSN 1422-0067
www.mdpi.com/journal/ijms

Review

Photonic Methods to Enhance Fluorescence Correlation Spectroscopy and Single Molecule Fluorescence Detection

Jérome Wenger * and Hervé Rigneault

Institut Fresnel, Aix-Marseille Université, CNRS, Ecole Centrale Marseille, Domaine Universitaire de Saint-Jérôme, 13397 Marseille cedex 20, France

* Author to whom correspondence should be addressed; E-Mail: jerome.wenger@fresnel.fr;
Tel.: +33-491-288-494.

Received: 24 November 2009; in revised form: 4 January 2010 / Accepted: 8 January 2010 / Published: 13 January 2010

Abstract: Recent advances in nanophotonics open the way for promising applications towards efficient single molecule fluorescence analysis. In this review, we discuss how photonic methods bring innovative solutions for two essential questions: how to detect a single molecule in a highly concentrated solution, and how to enhance the faint optical signal emitted per molecule? The focus is set primarily on the widely used technique of fluorescence correlation spectroscopy (FCS), yet the discussion can be extended to other single molecule detection methods.

Keywords: single molecule; fluorescence correlation spectroscopy FCS; nanophotonics; biophotonics

---

1. Introduction

The capacity to detect and analyze optical signals emitted from single molecules is a key issue in nanosciences, especially for biological applications. Data from a single molecule may reveal information hidden by ensemble measurements, such as variances in kinetic rates, memory effects, or transient states [1]. Observing a single or few dye molecules enables the study of dynamics and characteristics of the sample without actually disturbing their equilibrium. Therefore, efficiently detecting a single molecule has become a major goal with applications in chemical, biochemical and biophysical analysis.

Among the large number of methods that have been developed to investigate single molecules [2], fluorescence spectroscopy plays the largest role today. Fluorescence bears a high intrinsic optical efficiency, and provides information about the molecular environment and structure in many different ways: brightness, lifetime, anisotropy or spectrum.

To analyse the fluorescence signal from a single molecule, fluorescence correlation spectroscopy (FCS) is a powerful and versatile method [3, 4]. FCS is based on the statistical analysis of the temporal fluctuations affecting the fluorescence intensity. It can in principle provide information about any molecular process that induces a change in the fluorescence intensity. For instance, fluctuations occur when molecules diffuse in and out of an observation volume, or when reaction kinetics or conformational changes induce a change in the fluorescence brightness. Applications include determining translational and rotational diffusion, molecular concentrations, chemical kinetics, and binding reactions [5].

A critical issue in FCS as in any single molecule experiment is to discriminate the (weak) relevant signal from the noise, which requires simultaneously high fluorescence count rates per molecule and low background. Therefore, FCS is commonly implemented on a confocal microscope with a high-end immersion objective, providing high resolution and large numerical aperture (see Figure 1). Despite its extreme sensitivity, this approach remains limited by the phenomenon of optical diffraction.

Figure 1. State-of-the-art for single molecule detection in solution based on a confocal microscope and fluorescence correlation analysis. The inset shows the size of the typical analysis volume.

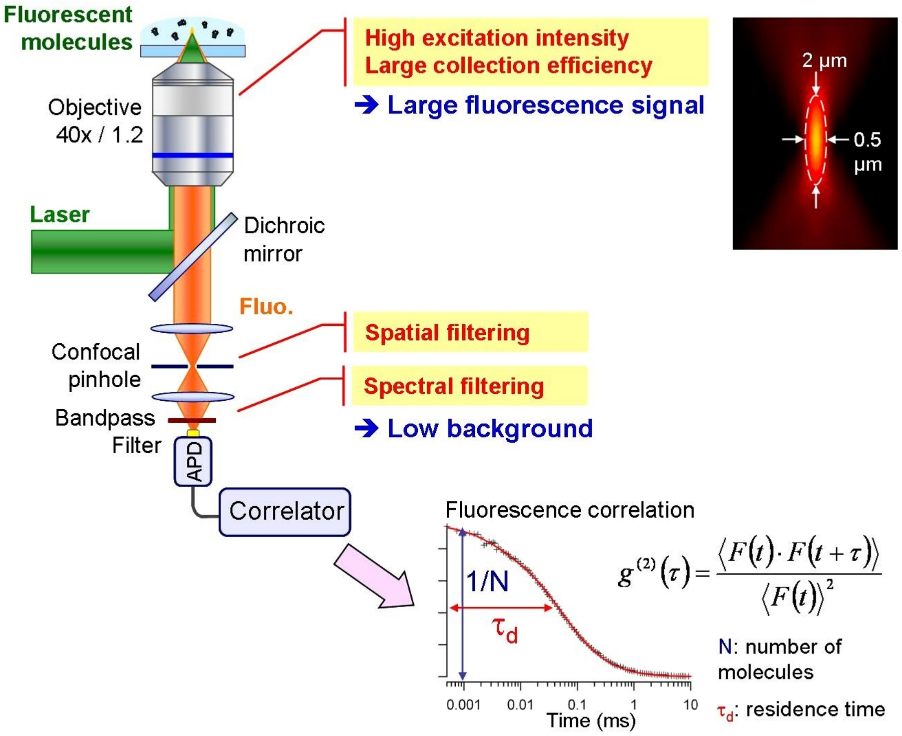

Optical diffraction limits confocal microscopy in two ways. First, it restricts the analysis volume to rather large values of typically 0.5 femtoliter ($= 0.5\ \mu m^3$). This amounts to a useful concentration in the nanomolar range in order to isolate only a few molecules, which comes in contradiction to the concentrations in the micro to the millimolar range typically found in living cells. Second, optical diffraction restricts confocal microscopy to relatively low detection rates per molecule. This limits the choice of fluorescence markers to relatively bright species, and imposes long integration times.

Recent advances in nanophotonics and fluorescence microscopy offer new solutions to overcome the limits imposed by diffraction [6–8]. Drawing a parallel with computer engineering (Figure 2), nanosciences enable major breakthroughs in designing novel photonic tools for single molecule analysis. The observation volume can be reduced by several orders of magnitude below the diffraction-limited confocal volume, while the detected fluorescence rate per molecule can be enhanced more than ten times. The photonic environment can affect the fluorescence emission in three ways: (i) by locally enhancing the excitation intensity, (ii) by increasing the emitter's radiative rate and quantum efficiency, and (iii) by modifying its radiation pattern, towards a higher emission directionality to the detectors. A major goal is to tailor the electromagnetic environment surrounding the molecules, so as to simultaneously enhance the collected fluorescence and decrease the detection volume to reduce background noise and enlarge the practicable domain of concentrations for single-molecule analysis.

Figure 2. As in computer engineering, nanosciences enable major breakthroughs in designing novel microscope tools and devices (computers pictures courtesy of Wikipedia.org).

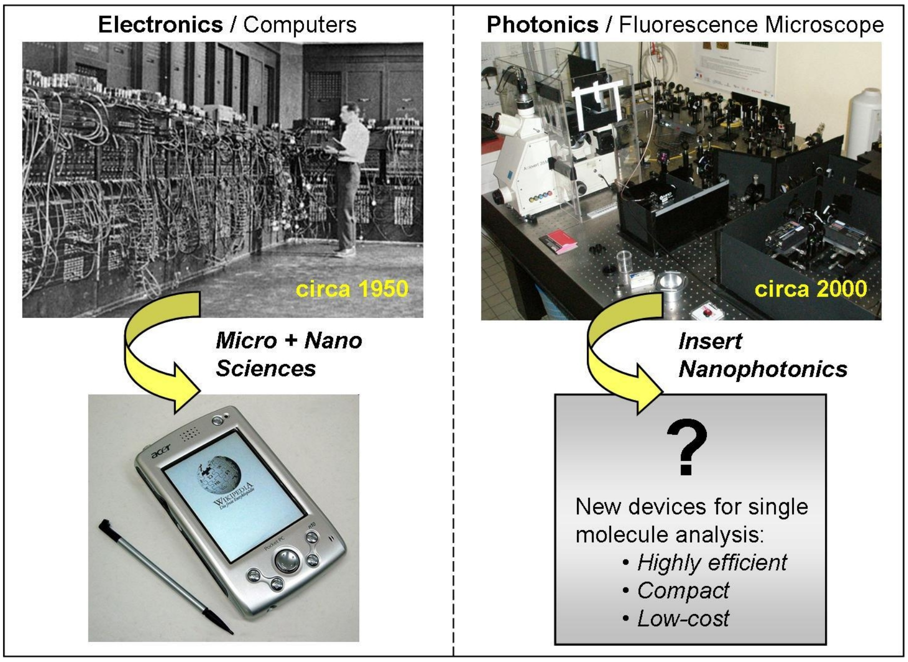

In this contribution, we focus on two fundamental questions that bear highly practical applications: how to detect one single molecule in a highly concentrated solution, and how to enhance the faint optical signal emitted per molecule? Both key parameters of volume reduction and fluorescence rate enhancement will be discussed. The focus is set primarily on the widely used technique of fluorescence correlation spectroscopy (FCS), yet the discussion can be extended to other single molecule detection methods. We divide the different strategies into two main areas. The first one takes advantages of shaping the laser excitation beam in an unconventional manner (Section 2), while the second introduces photonic structures to overcome the diffraction limit (Section 3).

2. Improved Single Molecule Fluorescence Detection by Structuring the Laser Excitation Beam

To improve single molecule fluorescence detection, several optical methods have been suggested and tested in light microscopy. The methods regrouped in this section share the fact that they primarily focus on modifying the laser excitation beam to further confine light on the nanoscale and improve the spatial resolution. Figure 3 describes the different methods of this section, the line at the bottom of each picture summarizes the main physical concept used.

Figure 3. Designs for improved single molecule fluorescence detection by structuring the laser excitation beam; see text for details.

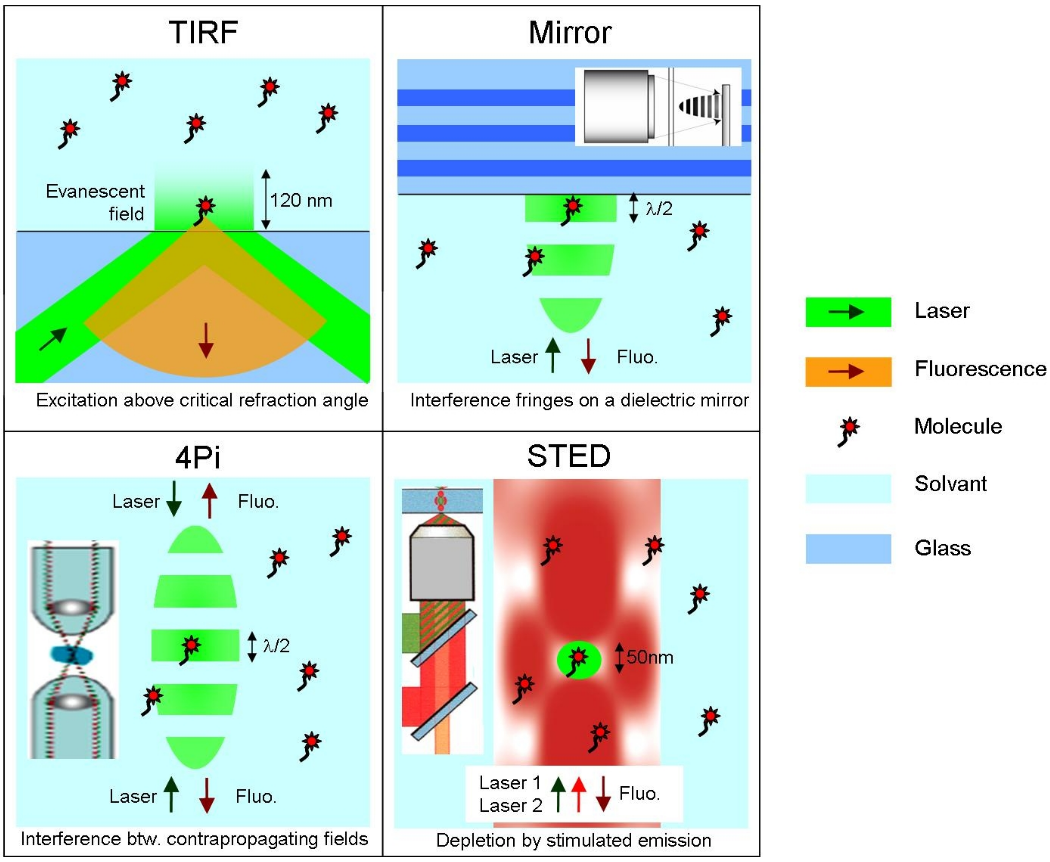

2.1. Total Internal Reflection Fluorescence Microscopy: TIRF

This system takes advantage of a total internal reflection fluorescence (TIRF) microscopy setup. Fluorescent molecules diffusing above the upper interface of the TIRF prism or objective are excited by an evanescent wave generated by total internal reflection at the solid/liquid interface [9]. The shallow evanescent field in the liquid elegantly defines an analysis volume that is strongly reduced along the longitudinal direction. Its longitudinal extend typically amounts to $\sim \lambda/6$, which offers a reduction of 10 compared to conventional confocal microscopes. An important feature for this technique is that still a confocal pinhole conjugated to the object plane has to be used in order to reduce the lateral dimensions of the fluorescence analysis volume [10]. TIRF-FCS offers an excellent axial confinement, yet it does not provide lateral confinement of the excitation profile and a pinhole in the image plane is needed to reduce the lateral extension of the detection profile. Therefore, out-of-focus photobleaching can be a major issue in TIRF-FCS, leading to a depletion of fluorophores and limiting the accuracy of FCS measurements.

Originally introduced in 1981 [9], this technique can now be combined with commercially available microscope objectives for TIRF imaging [10]. This tool can be used as efficiently for analyzing molecules diffusion in solution or in a lipid membrane [11], and is also compatible with multi-dye fluorescence detection [13].

Lastly, it can be combined with a thin metal layer for specific excitation of surface plasmon modes, which offers further background noise reduction and longitudinal confinement [12].

2.2. Fluorescence Detection on a Mirror

Single molecule detection in solution is tightly bound to the implementation of confocal microscopy, as depicted on Figure 1. An elegant way to reduce the confocal analysis volume and enhance the fluorescence rate emitted per molecule takes advantage of a dielectric mirror set at the focal point of the excitation beam (see Figure 3). The mirror affects both the laser excitation intensity and pattern, and the collection of the emitted fluorescence. The coherent excitation beam, which is reflected, produces an interference pattern along the optical axis with an interfringe spacing of $\lambda/2n$, where λ is the excitation wavelength and n is the medium refractive index.

Two important effects occur when the confocal detection volume is located on the mirrors surface [14, 15]. First,interference fringes in the excitation beam give rise to a new characteristic time in the fluorescence correlation function. This new time is found to be independent of the transverse excitation fields beam waist and permits accurate measurement of diffusion coefficients without any a priori knowledge of the confocal volume geometry. Second, the count rate per emitter is significantly enhanced owing to control of spontaneous emission and enhancement of the excitation field, with a gain up to four times.

This technique has been applied to accurately measure the diffusion coefficient of the enhanced green fluorescent protein (EGFP) in the cytoplasm of living *Escherichia coli* [16].

2.3. 4Pi Microscopy

New light microscopy concepts have been developed to improve the spatial resolution up to about 20 nm [17]. Among them, 4Pi microscopy takes advantage of two opposite microscope objectives with high numerical apertures [18]. Its principle is illustrated in Figure 3. Coherent light from a laser is split into two beams, which are focused at the same point onto a sample by two opposite objectives. Constructive interference of the two beams enhances the focusing of the light, and the illuminated region is narrower along the optical axis than in the case of the common confocal microscope. In 4Pi microscopy, various types of illumination and detection are utilized: type A corresponds to the illumination via two objectives with constructive interference and detection through one of the objectives in a confocal mode (commercially available); in type C, both illumination and detection are performed using two objectives, with constructive interference in both cases.

Increasing the number of objectives to two (or more) decreases the detection volume and increases the fluorescence collection efficiency. The 4Pi microscope features a point spread function with a central peak of 100 nm width in the axial direction and 220 nm width in the focal plane. In addition, the point spread function has smaller secondary maxima spaced on the optical axis at a distance of about half a wavelength from the main maximum. The essential point is that about 90% of the fluorescence signal stems from the main peak. Thus, the observation volume is virtually coincident with that of the main maximum of the point spread function.

A major problem in the adaptation of 4Pi microscopy to FCS is to account for the complicated point spread function of the microscope. A theoretical and computational framework has therefore been developed for data analysis, and validated by measurements on model systems [19].

2.4. Stimulated Emission Depletion Microscopy: STED

A different approach to overcome the diffraction barrier is to use stimulated emission depletion (STED) of the fluorescent molecular state (Figure 3) [17]. STED is a far-field method bearing sub-diffraction analysis volumes suitable for FCS. In STED, a regular diffraction-limited focal spot (green) is used to excite the fluorescence, while a second laser beam (red) stimulates the excited molecules down to their ground state. The laser beam for stimulated emission is custom-tailored to feature a zero-intensity minimum at the center but high intensity in the focal periphery. This configuration ensures that fluorescence occurs only in the very center of the focal spots and is strongly suppressed in the spots periphery. An additional attractive feature of STED is that it allows to adjust the detection volume by increasing the power of the stimulating beam.

The first implementation of a STED experiment with FCS was published by Kastrup *et al.* [20]. In a series of FCS measurements on a dilute solution of a red-fluorescing oxazine dye, the STED irradiance was successively increased yielding a 25-fold reduction of the axial diffusion time, equivalent to a 5-fold reduction of the focal volume. However, much stronger analysis volume reduction can be expected with that method.

In a second contribution, STED-FCS was used to investigate the cell membrane architecture at the nanoscale [21]. Single diffusing lipid molecules were detected in nanosized areas in the plasma membrane of living cells. Tuning of the probed area 70-fold below the diffraction barrier reveals that sphingolipids and glycosylphosphatidylinositol-anchored proteins are transiently trapped in cholesterol-mediated molecular complexes dwelling within 20 nm diameter areas. This tunable noninvasive optical recording combined to nanoscale imaging is a powerful new approach to study the dynamics of molecules in living cells.

3. Improved Single Molecule Fluorescence Detection by Using Photonic Structures

Optical methods of this section introduce photonic structures from millimeter to nanometer size to improve the detection of the fluorescence signal. The first two techniques (paraboloid collector and solid immersion lens) make the transition with the methods discussed in Section 2 and introduce many key concepts of nanophotonics. The last four techniques go really into the nanoworld of photonics. In addition to Figure 3, Figure 4 describes the photonic methods of this section for enhanced detection.

Figure 4. Designs for improved single molecule fluorescence detection by using photonic structures; see text for details.

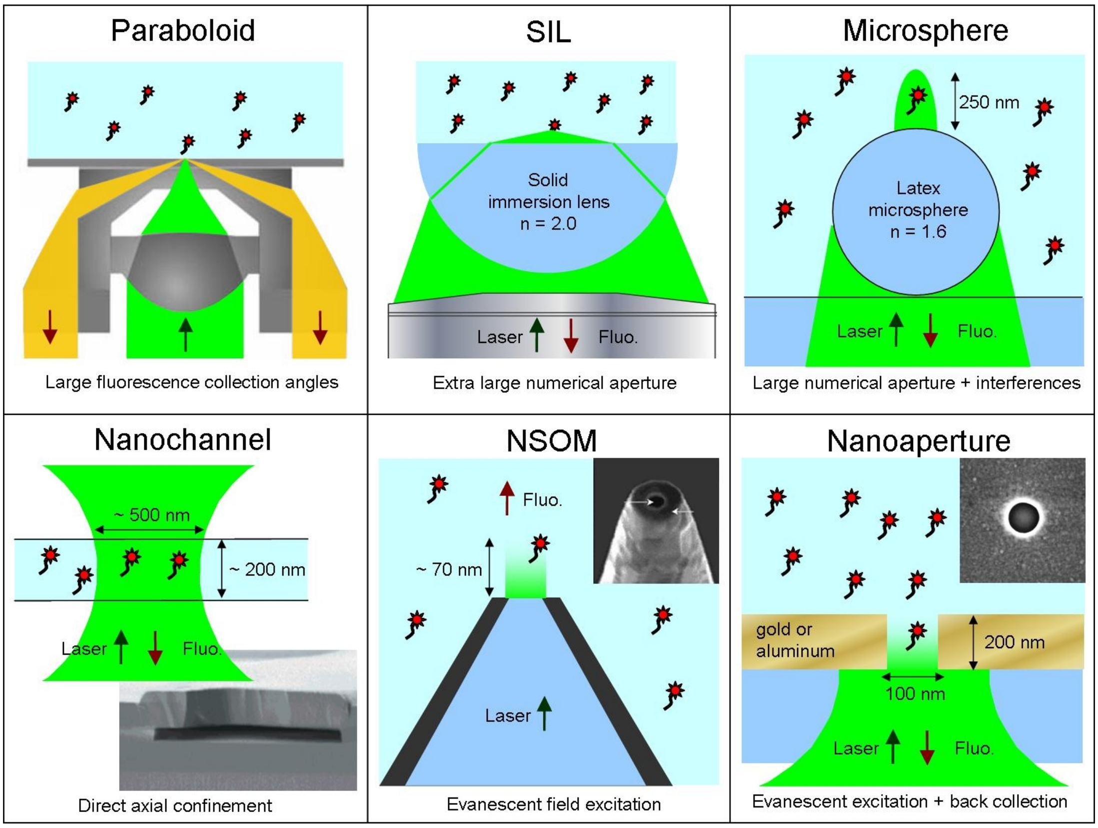

3.1. *Paraboloid Collector*

This main core of this technique is to replace the microscope objective by a paraboloid glass segment acting as a mirror for collecting the fluorescence (Figure 4). A special feature of the system is its ability to sample not only fluorescence that is emitted below the angle of total internal reflection (known as the critical angle) but also particularly the light above the critical angle. This is especially advantageous for collecting the fluorescence of surface-bound molecules. This specific optical system leads to a fluorescence collection efficiency to more than 65% of the total of emitted light, whereas high numerical aperture microscope objectives are able to collect 44% at best. Moreover, the detection volume can be restricted ten times below the standard confocal volume [22, 23]. This allows for a strong discrimination of bulk-generated against surface-generated fluorescence, which may be of great value when surface-binding processes are monitored.

The potential of a paraboloid collector (also referred to as supercritical angle objective) for FCS has been discussed in [24], demonstrating a clear advantage of paraboloid-FCS for diffusion measurements in lipid membranes. This method circumvents the need to illuminate at large angles as with TIRF and achieves an excellent axial confinement in combination with a small lateral excitation spot of a customized confocal microscope.

3.2. Solid Immersion Lens: SIL

For FCS, confinement of the excitation field and high fluorescence collection efficiency are key parameters. Both are directly proportional to the numerical aperture (NA) of the microscope objective system. Immersing the analysis volume with a liquid of a high refractive index, e.g., oil, increases the effective NA. Another way to increase the NA can be achieved by utilizing a solid immersion lens or SIL (Figure 4). A SIL is generally a hemisphere made in a material of high refractive index that is set at the focus of a microscope objective to further increase the overall NA of the whole system [25].

To perform FCS at high molecular concentrations with an ultra-high NA, an option is to combine a 0.6 NA air objective to a solid immersion lens (SIL) with refractive index close to 2 [26]. Experiments performed on a commercial FCS apparatus (Zeiss ConfoCorr 1) shown 50% higher collection efficiency and better field confinement for the SIL system in comparison to the conventional confocal set-up. Performances can be increased further by aberration compensation and pre-shaping the incident wavefront to obtain near diffraction-limited performance [27].

3.3. Microspheres

Dielectric microspheres can be a viable alternative for enhanced fluorescence detection in solution, offering a simple and low-cost method [28]. When a latex microsphere is illuminated with a tightly-focused Gaussian beam, it over-focuses light in a region with subwavelength dimensions in both the transverse and longitudinal directions, creating high local intensities. This effect stems from interferences between the field scattered by the sphere and the high angular components of the incident Gaussian beam passing aside the sphere [29].

Latex microspheres have been exploited to enhance the detection of single fluorescent molecules in FCS, yielding a simultaneous decrease of the confocal observation volume by an order of magnitude and an enhancement of the fluorescence brightness by a factor of five [28]. This phenomenon was explained as the microsphere increases the excitation intensity sensed by the molecule up to a factor of 2.2, while at the same time it allows for a gain in collection efficiency up to 60% by redirecting the light emitted at large incidences towards the optical axis [30]. Commercially available latex microspheres therefore appear as an attractive and cost-effective route to enhance the confocal microscopes for FCS without requiring expensive nanofabrication facilities.

Latex microspheres can also be combined with a simple low NA lens to form a high performance disposable optical system. This offers a simple and low-cost alternative to the expensive microscope objectives used in FCS [31]. Moreover, microspheres can be combined to an optical fiber for remote FCS analysis in an endoscopic apparatus [32]. The technique is sensitive enough to detect single fluorescent molecules. This offers new opportunities for reducing the bulky microscope setup and extending FCS to remote or in vivo applications.

3.4. Nanofluidic Channels

Novel nanofabrication techniques enable the realization of structures to confine the sampling volume in the fluorescent solution on sizes much smaller than the diffraction limit. Mechanically restricting the observation volume directly improves the efficiency of FCS toward micromolar concentration ranges [33]. It also simultaneously improves slightly the fluorescence rate per molecule by detecting only the molecules that sense the strongest excitation intensity at the center of the laser spot.

Foquet and coworkers have used nanofabricated channels with dimensions smaller or equal to the width and depth of a diffraction-limited detection volume in confocal microscopy for FCS studies [34, 35]. An effective detection volume of few tens of attoliters was achieved (see Figure 4). The nanochannels had typical dimensions of a few hundred nanometers in their cross-section. Such nanometer sized channels offer natural platforms for optofluidic sensing devices to achieve high-throughput analysis systems at the single molecule level. Furthermore, FCS can be applied successfully to measure velocities and directionalities in different capillaries for hydrodynamic and electrophoretic flows [36].

Lastly, nanochannels open new opportunities for full implementation of FCS on a chip [37]. Full planar integration can be achieved by lithographic definition of sub-picoliter excitation volumes using intersecting solid and liquid-core optical waveguides. Silicon micro and nanophotonics are thus to replace free-space microscopes, and offer even higher performances. This permits implementation of numerous diagnostic applications on compact planar optofluidic devices.

3.5. Near-Field Scanning Optical Microscope: NSOM

Near-field scanning optical microscopy (NSOM) is based on a subwavelength-sized light source that is raster-scanned across a surface at a distance of a few nanometers to image the sample. Near-field optical methods have been widely developed to provide spatial resolutions of 10?30 nm [38]. Compared to the other systems described in this section, NSOM bears the essential ability to image the sample.

NSOM microscopes are typically implemented using tapered optical single-mode fibers that are coated with a thin layer of aluminum. At the apex of the tip, an aperture of nanometer size is opened by focused ion beam milling (Figure 4). The region illuminated at the apex of the tip is constrained both in the lateral and longitudinal directions (for an aperture diameter typically below half the wavelength, the laser field evanescently decays inside the aperture, with a longitudinal extend of about 100 nm).

FCS measurements using NSOM probes have been reported in [39]. An order of magnitude reduction in the area compared to confocal FCS has been achieved, while the use of probes with smaller apertures is expected to provide an additional order of magnitude reduction. It was also reported that bare chemically etched, tapered fiber tips could be implemented for NSOM-FCS [40].

Very recently, NSOM-FCS was applied to study proteins diffusion passing through individual nuclear pore complexes of the nuclear envelope [41]. FCS characterizes the translocation as driven by Brownian motion and determines the related kinetic constants.

3.6. Nanometric Apertures

A simple and elegant way of generating a reduced analysis volume for FCS implements a single nanometric aperture milled in an opaque metallic film. As illustrated on Figure 4, the nanoaperture acts as a pinhole filter located directly into the object plane. When the aperture diameter is sufficiently reduced below the cut-off diameter of the fundamental excitation mode that may propagate through the aperture, the light inside the aperture is confined to a rapidly decaying evanescent mode, with a decay length of a few tens of nanometers (such devices have thus been named zero-mode waveguides). This concepts bears strong relations with NSOM probes, yet in a much more robust and easy to use configuration. Since both excitation and fluorescence collection are performed from the glass substrate side, very high detection efficiencies can be reached.

An impressive amount of literature has been published about the use of nanoapertures for FCS, since the pioneering demonstration of Levene and coworkers in 2003 [42]. With aperture diameters down to 30 nm, detection volumes of a few tens of zeptoliters (1 zL = 10^{21} L) have been generated, which are about four orders of magnitude smaller than diffraction-limited confocal volumes. DNA polymerase activity can be monitored at the single molecule level at dye concentrations of a few tens of micromolar. Implementation of nanoapertures currently provides the best performances for FCS at high concentrations [43, 44]. The applications can be extended to dual-color cross-correlation FCCS analysis [45], and to monitor flow mixing [46].

A second major effect brought by the sub-wavelength aperture is that it can significantly enhance the detected fluorescence rate per emitter. Using single rhodamine 6G molecules in isolated 150 nm diameter apertures milled in an aluminum film, a 6.5 fold enhancement of the fluorescence rate per molecule was reported as compared to free solution [47, 48]. Further enhancement up to 25-fold can be obtained by tuning the plasmon properties of the nanoapertures [49–51]. This provides a dramatic increase in signal-to-noise ratio (SNR) for FCS even at single molecule resolution. An experimental gain in SNR of about 1 order of magnitude, corresponds to a 100-fold reduction of the experiment duration, evidencing the feasibility of FCS analysis with fast integration times of about 1 s [52]. This opens the way to monitoring of a variety of biochemical reactions at reduced time scales.

Biophotonic applications of nanoapertures are reviewed for instance in [53]. The illuminated area well below the diffraction limit has proven of essential interest for FCS studies in lipid bilayers [54, 55] as well as in live cell membranes [56–58]. Nanoapertures combined to FCS offer the advantages of both high spatial and temporal resolution together with a direct statistical analysis.

Lastly, a very promising application of nanometric apertures concerns real-time single-molecule DNA sequencing [59]. Performing high-throughput, high-accuracy DNA sequencing at low costs has become a major issue, largely attracted by the growing potential of quantitative genomics. Each nanoaperture forms a nano-observation chamber for watching the activity of a single DNA polymerase enzyme performing DNA sequencing by synthesis.

4. Conclusions

At least ten different strategies have been demonstrated to enhance single molecule detection techniques beyond the limits set by optical diffraction. Table 1 summarizes their respective properties for reducing the analysis volume and enhancing the detected fluorescence rate per molecule. This enables fast comparison between the techniques and standard confocal microscopy. Table 1 also provides our arbitrary vision of the respective complexity required while setting up these novel strategies. Lastly, Figure 5 illustrates the practical ranges of concentrations offered by each method for single molecule detection.

Table 1. Summary of the two main characteristics for single molecule detection systems: volume reduction and fluorescence signal enhancement factors as compared to state-of-the-art confocal microscope.

Type	Volume reduction	Fluo. enhancement	Complexity
Confocal	x1	x1	*
TIRF	x10	x2	*
Mirror	x6	x4	*
4Pi	x6	x4	***
STED	x100	?	***
Paraboloid	x10	x2	*
SIL	x3	x1.5	**
Microsphere	x10	x5	*
Nanofluidics	x100	x3	**
NSOM	x100	?	***
Nanoapertures	x1000	x25	**

Figure 5. Range for analysis volumes and corresponding concentrations to ensure one single molecule in the analysis volume for the different schemes discussed here.

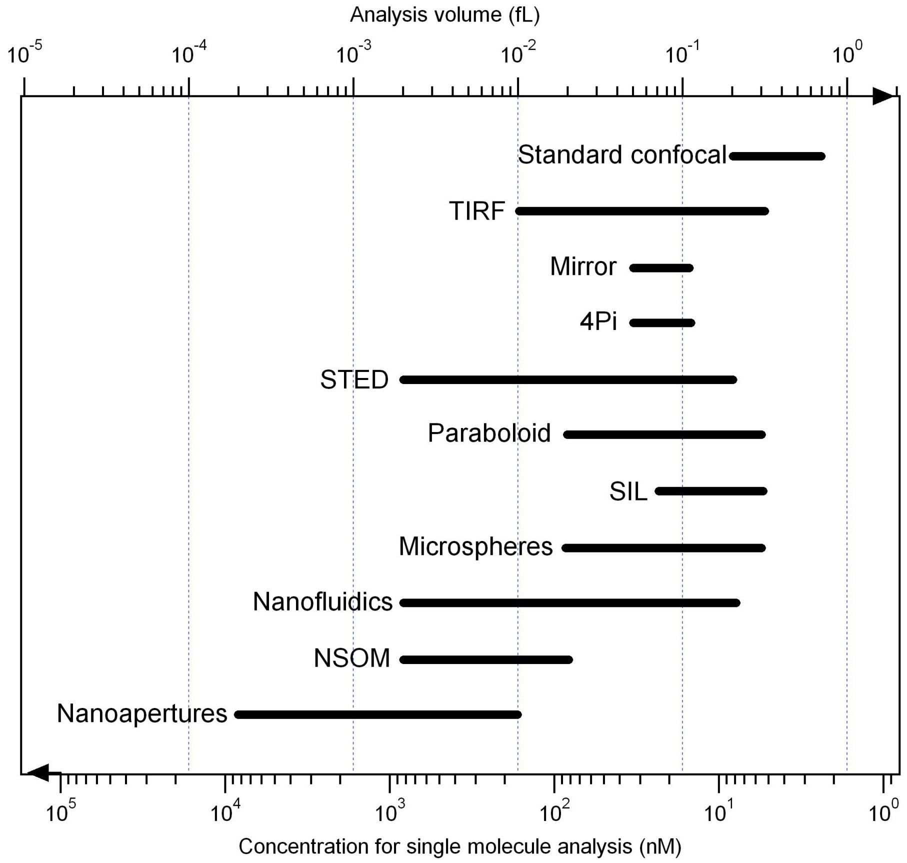

Based on the end-user application requirements, we believe that many photonic strategies exist to enhance single molecule fluorescence detection. For those needing simple and robust integration with commercially available systems, TIRF microscope objectives, paraboloid objectives and polystyrene microspheres offer relevant improvements. For maximum integration into optofluidic systems, nanochannels possibly equipped with microspheres or nanoapertures are the natural choice. Lastly, for maximum performance, nanoapertures offer the best gains, both in volume reduction and fluorescence rate enhancement.

Acknowledgements

The authors acknowledge stimulating discussions with S. Blair, N. Bonod, T. W. Ebbesen, D. Gérard, E. Popov and H. Aouani. This work has been funded by the French Agence Nationale de la Recherche under contract ANR-07-NANO-006-03 “ANTARES”.

References

1. Zander, C.; Enderlein, J.; Keller, R.A. *Single-Molecule Detection in Solution—Methods and Applications*; VCH-Wiley: Berlin, German, 2002.
2. Craighead, H.G. Future lab-on-a-chip technologies for interrogating individual molecules. *Nature* **2006**, *442*, 387–393.
3. Maiti, S.; Haupts, U.; Webb, W.W. Fluorescence correlation spectroscopy: diagnostics for sparse molecules. *Proc. Nat. Acad. Sci. USA* **1997**, *94*, 11753–11757.
4. Webb, W.W. Fluorescence correlation spectroscopy: Inception, biophysical experimentations, and prospectus. *Appl. Opt.* **2001**, *40*, 3969–3983.
5. Briddon, S.J.; Hill, S.J. Pharmacology under the microscope: The use of fluorescence correlation spectroscopy to determine the properties of ligandreceptor complexes. *Trends Pharmacol. Sci.* **2007**, *28*, 637–645.
6. Huser, T. Nano-Biophotonics: New tools for chemical nano-analytics. *Curr. Opin. Chem. Biol.* **2008**, *12*, 497-504.
7. Blom, H.; Kastrup, L.; Eggeling, C. Fluorescence fluctuation spectroscopy in reduced detection Volumes. *Curr. Pharm. Biotechnol.* **2006**, *7*, 51–66.
8. Mannion, J.T.; Craighead, H.G. Nanofluidic structures for single biomolecule fluorescent detection. *Biopolymers* **2006**, *85*, 131–143.
9. Thompson, N.L.; Burghardt, T.P.; Axelrod, D. Measuring surface dynamics of biomolecules by total internal–Reflection fluorescence with photobleaching recovery or correlation spectroscopy. *Biophys. J.* **1981**, *33*, 435–454.
10. Hassler, K.; Leutenegger, M.; Rigler, P.; Rao, R.; Rigler, R.; Gösch, M.; Lasser, T. Total internal reflection fluorescence correlation spectroscopy (TIR-FCS) with low background and high count-rate per molecule. *Opt. Express* **2005**, *13*, 7415–7423.
11. Starr, T.E.; Thompson, N.L. Total internal reflection with fluorescence correlation spectroscopy: Combined surface reaction and solution diffusion. *Biophys. J.* **2001**, *80*, 1575–1584.

12. Borejdo, J.; Calander, N.; Gryczynski, Z.; Gryczynski, I. Fluorescence correlation spectroscopy in surface plasmon coupled emission microscope. *Opt. Express* **2006**, *14*, 7878–7888.
13. Leutenegger, M.; Blom, H.; Widengren, J.; Eggeling, C.; Gösch, M.; Leitgeb, R.A.; Lasser, T. Dual-color total internal reflection fluorescence cross-correlation spectroscopy. *J. Biomed. Optics* **2006**, *11*, 040502, doi:10.1117/1.2221714.
14. Lenne, P.F.; Etienne, E.; Rigneault, H. Subwavelength patterns and high detection efficiency in fluorescence correlation spectroscopy using photonic structures. *Appl. Phys. Lett.* **2002**, *80*, 4106–4108.
15. Rigneault, H.; Lenne, P.F. Fluorescence correlation spectroscopy on a mirror. *J. Opt. Soc. Am. B* **2003**, *20*, 2203–2214.
16. Etienne, E.; Lenne, P.F.; Sturgis, J.N.; Rigneault, H. Confined diffusion in tubular structures analyzed by fluorescence correlation spectroscopy on a mirror. *Appl. Opt.* **2006**, *45*, 4497–4507.
17. Hell, S.W. Toward fluorescence nanoscopy. *Nat. Biotechnol.* **2003**, *21*, 1347–1355.
18. Hell, S.W.; Stelzer, E.H.K. Fundamental improvement of resolution with a 4Pi-confocal fluorescence microscope using twophoton excitation. *Opt. Commun.* **1992**, *93*, 277–282.
19. Arkhipov, A.; Hüve, J.; Kahms, M.; Peters, R.; Schulten, K. Continuous fluorescence microphotolysis and correlation spectroscopy using 4Pi microscopy. *Biophys. J.* **2007**, *93*, 4006–4017.
20. Kastrup, L.; Blom, H.; Eggeling, C.; Hell, S.W. Fluorescence fluctuation spectroscopy in subdiffraction focal volumes. *Phys. Rev. Lett.* **2005**, *94*, 178104:1–178104:4.
21. Eggeling, C.; Ringemann, C.; Medda, R.; Schwarzmann, G.; Sandhoff, K.; Polyakova, S.; Belov, V.N.; Hein, B.; von Middendorff, C.; Schönle, A.; Hell, S.W. Direct observation of the nanoscale dynamics of membrane lipids in a living cell. *Nature* **2008**, *457*, 1159–1162.
22. Enderlein, J.; Ruckstuhl, T.; Seeger S. Highly efficient optical detection of surface-generated fluorescence. *Appl. Opt.* **1999**, *38*, 724–732.
23. Ruckstuhl, T.; Enderlein, J.; Jung, S.; Seeger, S. Forbidden light detection from single molecules. *Anal. Chem.* **2000**, *72*, 2117–2123.
24. Ries, J.; Ruckstuhl, T.; Verdes, D.; Schwille, P. Supercritical angle fluorescence correlation spectroscopy. *Biophys. J.* **2008**, *94*, 221–229.
25. Koyama, K.; Yoshita, M.; Baba, M.; Suemoto, T.; Akiyama, H. High collection efficiency in fluorescence microscopy with a Solid Immersion Lens. *Appl. Phys. Lett.* **1999**, *75*, 1667–1669.
26. Serov, A.; Rao, R.; Gösch, M.; Anhut, T.; Martin, D.; Brunner, R.; Rigler, R.; Lasser, T. High light field confinement for fluorescent correlation spectroscopy using a solid immersion lens. *Biosens. Bioelectron.* **2004**, *20*, 431–435.
27. Rao, R.; Mitic, J.; Serov, A.; Leitgeb, R.A. ; Lasser, T. Field confinement with aberration correction for solid immersion lens based fluorescence correlation spectroscopy. *Opt. Commun.* **2007**, *271*, 462–469.
28. Gérard, D.; Wenger, J.; Devilez, A.; Gachet, D.; Stout, B.; Bonod, N.; Popov, E.; Rigneault, H. Strong electromagnetic confinement near dielectric microspheres to enhance single-molecule fluorescence. *Opt. Express* **2008**, *16*, 15297–15303.

29. Devilez, A.; Bonod, N.; Stout, B.; Gérard, D.; Wenger, J.; Rigneault, H.; Popov, E. Three-dimensional subwavelength confinement of photonic nanojets. *Opt. Express* **2009**, *17*, 2089–2094.
30. Gérard, D.; Devilez, A.; Aouani, H.; Stout, B.; Bonod, N.; Wenger, J.; Popov, E.; Rigneault, H. Efficient excitation and collection of single molecule fluorescence close to a dielectric microsphere. *J. Opt. Soc. Am. B* **2009**, *26*, 1473–1478.
31. Wenger, J.; Gérard, D.; Aouani, H.; Rigneault, H.; Disposable microscope objective lenses for fluorescence correlation spectroscopy using latex microspheres. *Anal. Chem.* **2008**, *80*, 6800–6804.
32. Aouani, H.; Deiss, F.; Wenger, J.; Ferrand, P.; Sojic, N.; Rigneault, H. Optical-fiber-microsphere for remote fluorescence correlation spectroscopy. *Opt. Express* **2009**, *17*, 18912–18919.
33. Brinkmeier, M.; Dijrre, K.; Riebeseel, K.; Rigler, R. Confocal spectroscopy in microstructures. *Biophys. Chem.* **1997**, *66*, 229–239.
34. Foquet, M.; Korlach, J.; Zipfel, W.R.; Webb, W.W.; Craighead, H.G. DNA fragment sizing by single molecule detection in submicrometer-sized closed fluidic channels. *Anal. Chem.* **2002**, *74*, 1415–1422.
35. Foquet, M.; Korlach, J; Zipfel, W.R.; Webb, W.W.; Craighead, H.G. Focal volume confinement by submicrometer-sized fluidic channels. *Anal. Chem.* **2004**, *76*, 1618–1626.
36. Lenne, P.F.; Colombo, D.; Giovannini, H.; Rigneault, H. Flow profiles and directionality in microcapillaries measured by fluorescence correlation spectroscopy. *Single Mol.* **2002**, *3*, 194–200.
37. Yin, D.; Lunt, E.J.; Barman, A.; Hawkins, A.R.; Schmidt, H. Microphotonic control of single molecule fluorescence correlation spectroscopy using planar optofluidics. *Opt. Express* **2007**, *15*, 7290–7295.
38. Lewis, A.; Taha, H.; Strinkovski, A.; Menevitch, A.; Katchatouriants, A.; Dekhter, R.; Amman, E. Near-field optics: From subwavelength illumination to nanometric shadowing. *Nat. Biotechnol.* **2003**, *21*, 1378–1386.
39. Vobornik, D.; Banks, D.S.; Lu, Z.; Fradin, C.; Taylor, R.; Johnston, L.J. Fluorescence correlation spectroscopy with sub-diffraction-limited resolution using near-field optical probes. *Appl. Phys. Lett.* **2008**, *93*, 163904:1-163904:3.
40. Lu, G.; Lei, F.H.; Angiboust, J.F.; Manfait, M. Confined detection volume of fluorescence correlation spectroscopy by bare fiber probes. *Eur. Biophys. J.* **2009**, doi:10.1007/s00249-009-0508-z.
41. Herrmann, M.; Neuberth, N.; Wissler, J.; Pérez, J.; Gradl, D.; Naber, A. Near-field optical study of protein transport kinetics at a single nuclear pore. *Nano Lett.* **2009**, *9*, 3330–3336.
42. Levene, M.J.; Korlach, J.; Turner, S.W.; Foquet, M.; Craighead, H.G.; Webb, W.W. Zero-mode waveguides for single-molecule analysis at high concentrations. *Science* **2003**, *299*, 682–686.
43. Samiee, K.T.; Foquet, M.; Guo, L.; Cox, E.C.; Craighead, H.G. Lambda repressor oligomerization kinetics at high concentrations using fluorescence correlation spectroscopy in zero-mode waveguides. *Biophys. J.* **2005**, *88*, 2145–2153.
44. Leutenegger, M.; Gösch, M.; Perentes, A.; Hoffmann, P.; Martin, O.J.F.; Lasser, T. Confining the sampling volume for Fluorescence Correlation Spectroscopy using a sub-wavelength sized aperture. *Opt. Express* **2006**, *14*, 956–969.

45. Wenger, J.; Gérard, D.; Lenne, P.F.; Rigneault, H.; Dintinger, J.; Ebbesen, T.W.; Boned, A.; Conchonaud, F.; Marguet, D. Dual-color fluorescence cross-correlation spectroscopy in a single nanoaperture: Towards rapid multicomponent screening at high concentrations. *Opt. Express* **2006**, *14*, 12206–12216.
46. Liao, D.; Galajda, P.; Riehn, R.; Ilic, R.; Puchalla, J.L.; Yu, H.G.; Craighead, H.G.; Austin, R.H. Single molecule correlation spectroscopy in continuous flow mixers with zero-mode waveguides. *Opt. Express* **2008**, *16*, 10077–10090.
47. Rigneault, H.; Capoulade, J.; Dintinger, J.; Wenger, J.; Bonod, N.; Popov, E.; Ebbesen, T.W.; Lenne, P.F. Enhancement of single-molecule fluorescence detection in subwavelength apertures. *Phys. Rev. Lett.* **2005**, *95*, 117401:1–117401:4.
48. Wenger, J.; Lenne, P.F.; Popov, E.; Rigneault, H.; Dintinger, J.; Ebbesen, T.W. Single molecule fluorescence in rectangular nano-apertures. *Opt. Express* **2005**, *13*, 7035–7044.
49. Wenger, J.; Gérard, D.; Bonod, N.; Popov, E.; Rigneault, H.; Dintinger, J.; Mahboub, O.; Ebbesen, T.W. Emission and excitation contributions to enhanced single molecule fluorescence by gold nanometric apertures. *Opt. Express* **2008**, *16*, 3008–3020.
50. Gérard, D.; Wenger, J.; Bonod, N.; Popov, E.; Rigneault, H.; Mahdavi, F.; Blair, S.; Dintinger, J.; Ebbesen, T.W. Nanoaperture-enhanced fluorescence: Towards higher detection rates with plasmonic metals. *Phys. Rev. B* **2008**, *77*, 045413, doi:10.1103/PhysRevB.77.045413.
51. Aouani, H.; Wenger, J.; Gérard, D.; Rigneault, H.; Devaux, E.; Ebbesen, T.W.; Mahdavi, F.; Xu, T.; Blair, S. Crucial role of the adhesion layer on the plasmonic fluorescence enhancement. *ACS Nano* **2009**, *3*, 2043–2048.
52. Wenger, J.; Gérard, D.; Aouani, H.; Rigneault, H.; Lowder, B.; Blair, S.; Devaux, E.; Ebbesen, T.W. Nanoaperture-enhanced signal-to-noise ratio in fluorescence correlation spectroscopy. *Anal. Chem.* **2009**, *81*, 834–839.
53. Lenne, P.F.; Rigneault, H.; Marguet, D.; Wenger, J. Fluorescence fluctuations analysis in nanoapertures: Physical concepts and biological applications. *Histochem. Cell Biol.* **2008**, *130*, 795–805.
54. Samiee, K.T.; Moran-Mirabal, J.M.; Cheung, Y.K.; Craighead, H.G. Zero mode waveguides for single-molecule spectroscopy on lipid membranes. *Biophys. J.* **2006**, *90*, 3288–3299.
55. Wenger, J.; Rigneault, H.; Dintinger, J.; Marguet, D.; Lenne, P.F. Single-fluorophore diffusion in a lipid membrane over a subwavelength aperture. *J. Biol. Phys.* **2006**, *32*, SN1–SN4.
56. Edel, J.B.; Wu, M.; Baird, B.; Craighead, H.G. High spatial resolution observation of single molecule dynamics in living cell membranes. *Biophys. J.* **2005**, *88*, L43–L45.
57. Wenger, J.; Conchonaud, F.; Dintinger, J.; Wawrezinieck, L.; Ebbesen, T.W.; Rigneault, H.; Marguet, D.; Lenne, P.F.; Diffusion analysis within single nanometric apertures reveals the ultrafine cell membrane organization. *Biophys. J.* **2007**, *92*, 913–919.
58. Moran-Mirabal, J.M.; Torres, A.J.; Samiee, K.T.; Baird, B.; Craighead, H.G. Cell investigation of nanostructures: Zero-mode waveguides for plasma membrane studies with single molecule resolution. *Nanotechnology* **2007**, *18*, 195101:1–195101:10.

59. Eid, J.; Fehr, A.; Gray, J.; Luong, K.; Lyle, J.; Otto, G.; Peluso, P.; Rank, D.; Baybayan, P.; Bettman, B.; Bibillo, A.; Bjornson, K.; Chaudhuri, B,; Christians, F.; Cicero, R.; Clark, S.; Dalal, R.; deWinter, A.; Dixon, J.; Foquet, M.; Gaertner, A.; Hardenbol, P.; Heiner, C.; Hester, K.; Holden, D.; Kearns, G.; Kong, X.; Kuse, R.; Lacroix, Y.; Lin, S.; Lundquist, P.; Ma, C.; Marks, P.; Maxham, M.; Murphy, D.; Park, I.; Pham, T.; Phillips, M.; Roy, J.; Sebra, R.; Shen, G.; Sorenson, J.; Tomaney, A.; Travers, K.; Trulson, M.; Vieceli, J.; Wegener, J.; Wu, D.; Yang, A.; Zaccarin, D.; Zhao, P.; Zhong, F.; Korlach, J.; Turner, S.;. Real-time DNA sequencing from single polymerase molecules. *Science* **2009**, *323*, 133–138.

Chapitre 1

Nano-Ouvertures Métalliques

Percer des trous de quelques nanomètres dans un film métallique est une manière conceptuellement simple de réaliser des nouveaux composants photoniques. Malgré son apparente simplicité, ce composant nano-optique continue à inspirer de nouvelles études et applications.

Bien que la diffraction par une ouverture circulaire ait été étudiée depuis des siècles, un défi persistant concerne la compréhension précise des phénomènes physiques intervenant lorsque le diamètre de l'ouverture est en-dessous de la demi-longueur d'onde. Les études sur les ouvertures nanométriques dans un métal portent essentiellement sur leurs propriétés de transmission optique en champ lointain. Je poursuis une autre approche : étudier ces structures avec des molécules luminescentes pour sonder localement le champ lumineux à l'échelle nanométrique. Dans ce but, l'émission de fluorescence est un outil idéal du fait de sa forte efficacité optique intrinsèque (forte section efficace d'absorption, haut rendement quantique). De plus, de nombreux outils d'analyse du signal de fluorescence sont disponibles (FCS, FLIM, FRET, FRAP…) ce qui ouvre de nombreuses voies d'investigations complémentaires.

Mes travaux de recherche analysent principalement les évolutions temporelles du signal de fluorescence de molécules individuelles qui diffusent dans les ouvertures nanométriques considérées (figure 1.1). Ces ouvertures sont percées dans un film métallique avec un faisceau d'ion focalisé (en collaboration étroite avec l'équipe de Thomas Ebbesen, université de Strasbourg). En appliquant la technique de spectroscopie par corrélation de fluorescence (FCS), le nombre moyen de molécules observées peut être déterminé très précisément. Ceci permet de quantifier ensuite sans équivoque le taux d'émission de photons par émetteur, et fournit un outil original et essentiel pour caractériser les gains apportés par les antennes plasmoniques.

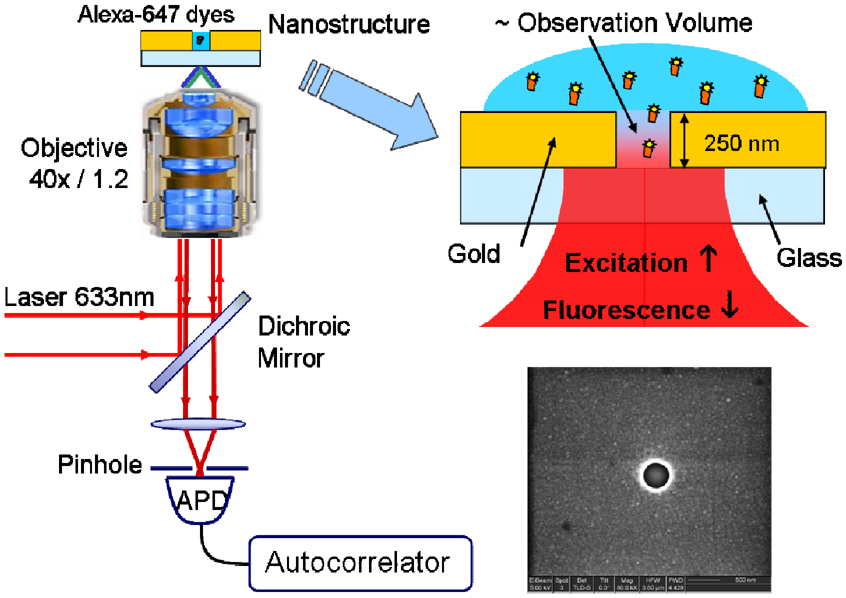

Fig. 1.1. Principe de l'expérience de suivi dynamique de la diffusion de molécules fluorescentes dans une nanoouverture.

Les premières démonstrations ont été réalisées au cours de la période 2004-2006, principalement sur des ouvertures nanométriques dans un film d'aluminium. Nous avons ainsi démontré une exaltation significative de la fluorescence de molécules individuelles d'un facteur égal à 6x pour une ouverture de 150 nm de diamètre [1].

Une partie importante des travaux de recherche sur la période 2007-2010 concerne la compréhension détaillée du phénomène d'exaltation de fluorescence et sa caractérisation fine. Pour cela, une procédure originale a été développée. Elle permet de quantifier clairement de renforcement de taux de comptage de fluorescence par molécule, ce qui fournit directement le facteur d'exaltation moyen au voisinage de la nanostructure. De plus, en faisant varier la puissance d'excitation et en mesurant le temps de vie moyen de fluorescence, la procédure permet de quantifier la contribution des gains à l'excitation et à l'émission dans le gain total en fluorescence. Cette procédure a été initiée dans la référence [2], mais a été pleinement développée dans la publication [3] qui combine mesures de corrélations temporelles de fluorescence (FCS) avec mesures de temps de vie (FLIM) simultanément sur le même dispositif (article Optics Express ci-après). La figure 1.2 présente les principaux gains observés dans le cas de nano-ouvertures dans un film d'or.

---

[1] H. Rigneault, et al, Enhancement of single molecule fluorescence detection in subwavelength apertures, Phys. Rev. Lett. 95, 117401 (2005).

[2] Wenger J., et al, Radiative and Nonradiative Photokinetics Alteration Inside a Single Metallic Nanometric Aperture, J. Phys. Chem. C 111, 11469-11474 (2007).

[3] J. Wenger, et al, Emission and excitation contributions to enhanced single molecule fluorescence by gold nanometric apertures, Opt. Express 16, 3008-3020 (2008).

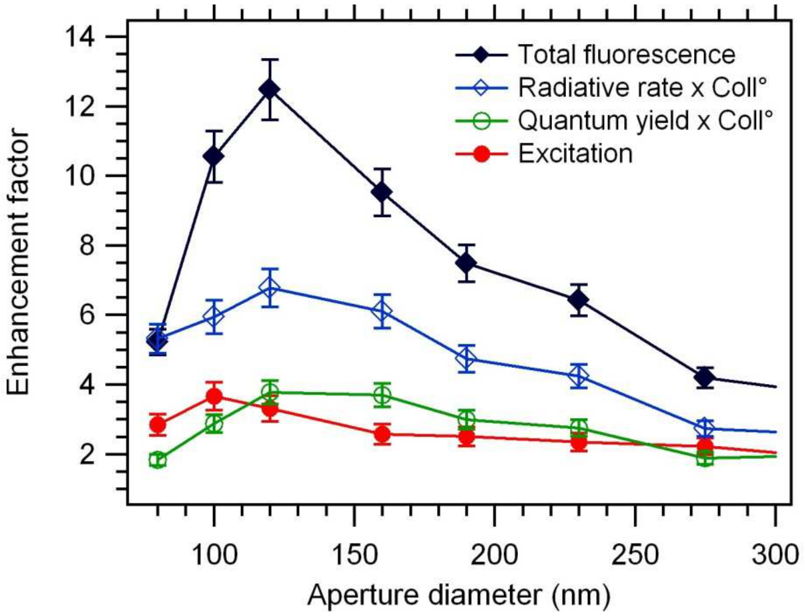

Fig. 1.2. Exaltation de la fluorescence par une nano-ouverture dans un film métallique opaque et contributions électromagnétiques à ce phénomène en fonction du diamètre de l'ouverture.

Cette méthode est généralisable à de nombreuses configurations différentes en nanophotonique, et est actuellement transposée pour l'étude d'autres structures plasmoniques. La compréhension détaillée du phénomène d'exaltation de fluorescence paraît nécessaire pour le développement de nano-antennes efficaces, ainsi que pour l'étude de l'interaction lumière-matière dans un environnement complexe.

Pour la première fois, ces études expérimentales démontrent l'importance de la densité locale d'états photoniques : un renforcement optimum est trouvé pour un minimum de vitesse de groupe du mode fondamental dans la nano-ouverture [4] (article Phys Rev B ci-après) L'influence des modes de plasmons de surface a également été quantifiée en comparant expérimentalement des ouvertures percées dans des films d'or et d'aluminium [4,5] (figure 1.3).

---

[4] D. Gérard, et al, Nanoaperture-enhanced fluorescence: Towards higher detection rates with plasmonic metals, Phys. Rev. B 77, 045413 (2008).

[5] J. Wenger, et al, Enhanced fluorescence from metal nanoapertures: physical characterizations and biophotonic applications, Proc. of SPIE, Vol. 7577, pp.75770J (2010)

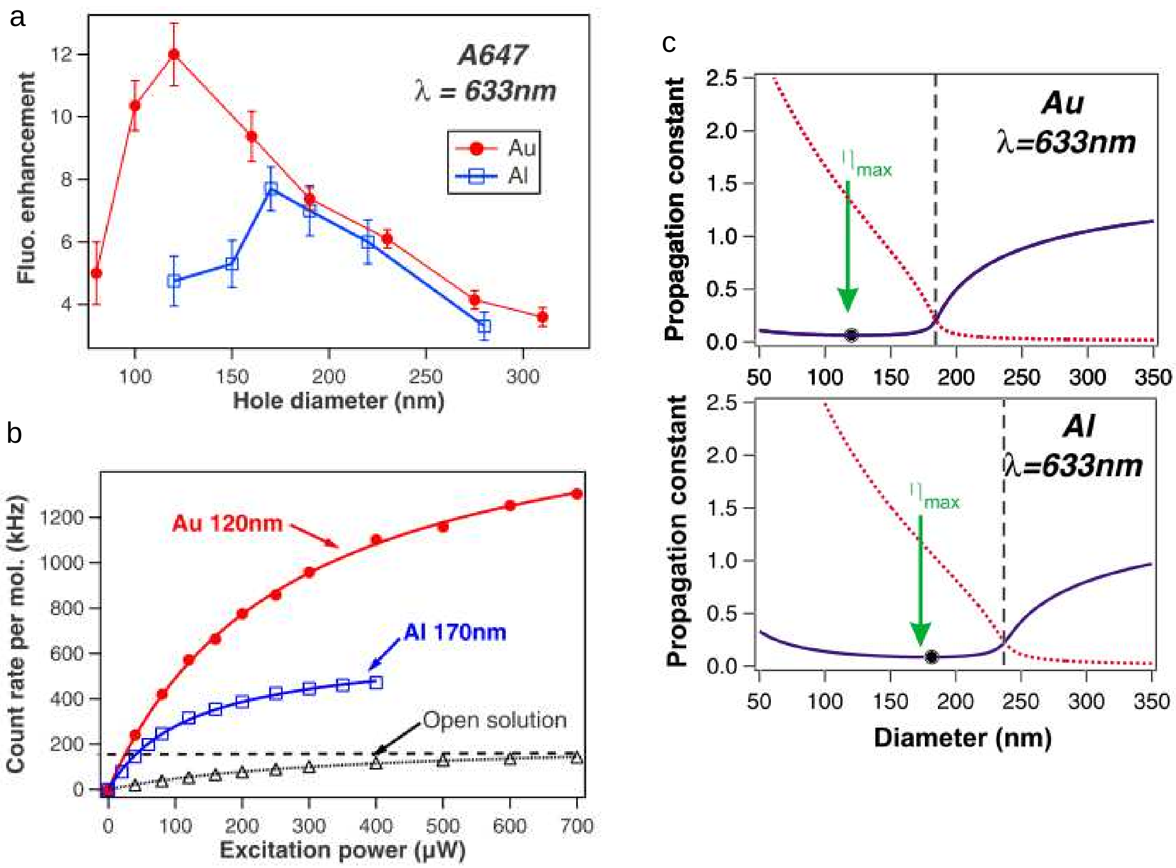

Fig. 1.3. (a) Facteurs d'exaltation de fluorescence comparée pour des molécules Alexa Fluor 647 dans des ouvertures percées dans un film d'or ou d'aluminium. L'influence du métal apparaît clairement aux faibles diamètres. (b) Taux de comptage par molécule en fonction de la puissance d'excitation pour des ouvertures optimisées. (c) Constante de propagation dans une ouverture métallique en fonction du diamètre du guide. Le poin noir indique la position du minimum de vitesse de groupe (maximum de densité photonique), la flèche indique la position du maximum de gaini de fluorescence observé, et la ligne verticale donne le diamètre de coupure attendue (transition propagatif → évanescent).

En parallèle de ces mesures expérimentales, une étude théorique a été réalisée sur l'influence de la permittivité du métal sur la directionnalité de l'onde diffractée par une nano-ouverture [6]. De manière surprenante, la directivité d'une ouverture simple est démontrée dépendre principalement de la valeur absolue de la permittivité du film, mais n'est pas reliée à la présence de plasmons de surface, ni à la présence d'un métal.

---

[6] E. Popov, et al, Single-scattering theory of light diffraction by a circular subwavelength aperture in a finitely conducting screen, J. Opt. Soc. Am. A 24, 339-358 (2007)

Une inconnue importante en plasmonique concerne l'influence exacte de la couche d'adhésion nanométrique communément utilisée pour adhérer fermement un film d'or à un substrat de verre. Nous présentons la première preuve expérimentale directe de l'influence de cette couche d'accroche sur l'exaltation électromagnétique [7] (figure 1.4). Cette étude profite directement des avancées en caractérisation de fluorescence développées au cours des années 2007-2008.

Nous montrons que la nature de la couche d'accroche possède une influence essentielle sur le renforcement local d'intensité électromagnétique. Toute perte d'absorption dans la couche d'accroche (pourtant d'épaisseur inférieure à 10 nm) induit une forte réduction de l'exaltation locale. L'amortissement de la résonance plasmonique est important car la source de pertes est directement en contact avec la zone de plus forte accumulation local de charges électriques. Cette étude sur la couche d'accroche a récemment été étendue au cas de la diffusion Raman exaltée en surface [8], où elle possède une influence encore plus marquée (figure 1.4B).

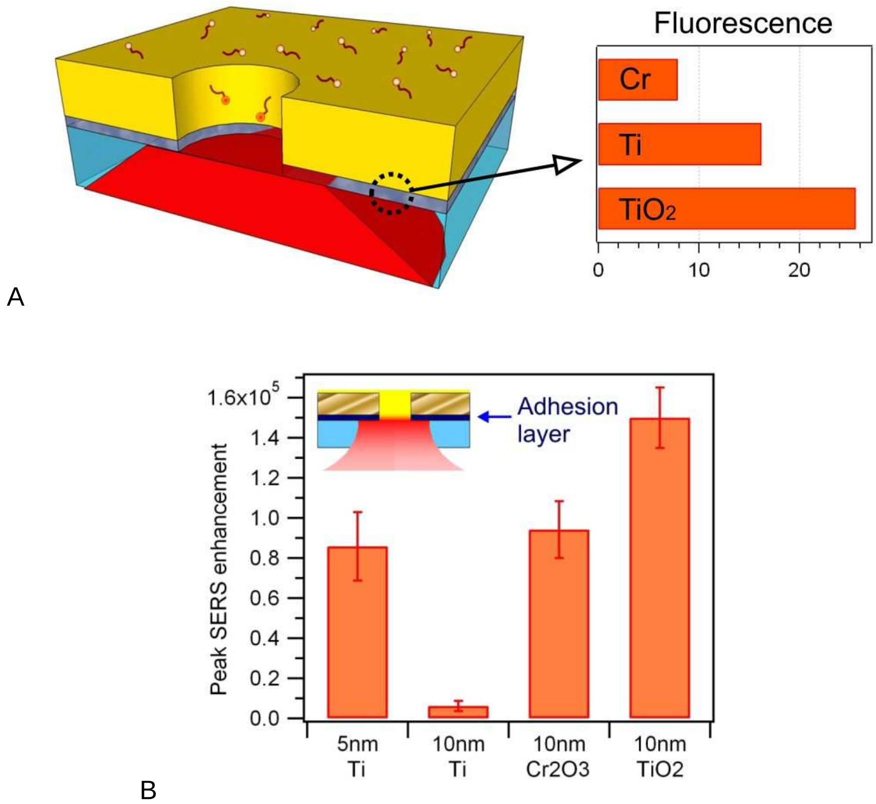

Fig. 1.4. Influence de la couche d'accroche or-verre sur le gain en fluorescence par molécule (A) et sur le renforcement maximum de diffusion Raman SERS (B). Ces résultats sont largement généralisables aux autres designs de nanoantennes plasmoniques.

---

[7] H. Aouani, et al, Crucial Role of the Adhesion Layer on the Plasmonic Fluorescence Enhancement, ACS Nano 3, 2043-2048 (2009).

[8] N. Djaker, et al, Surface Enhanced Raman Scattering on a Single Nanometric Aperture, J. Phys. Chem. C 114, 16250-16256 (2010)

Il est donc indispensable de prendre la nature de la couche d'accroche en considération lors de la conception de nano-antennes plasmoniques pour la détection exaltée de molécules. Nous avons également obtenue un design optimisé donnant le plus fort gain (x25) sur l'émission de fluorescence de molécules individuelles (dans le cas de molécules fluorescentes communément employées en biophotonique).

L'émission optique de molécules a également été employée pour caractériser le renforcement maximal d'intensité électromagnétique en bord de nano-ouverture (suivant la direction de la polarisation linéaire incidente, à l'endroit où le renforcement est maximum). Afin de s'affranchir des pertes liées au transfert non-radiatif dans le métal qui affectent le signal de fluorescence, nous avons développé un montage spécifique de spectroscopie confocal de diffusion Raman [8]. Cette spectroscopie Raman a permis la première mesure optique du renforcement électromagnétique en bord d'ouverture, ainsi qu'une comparaison directe avec des simulations numériques par méthode FDTD (figure 1.5).

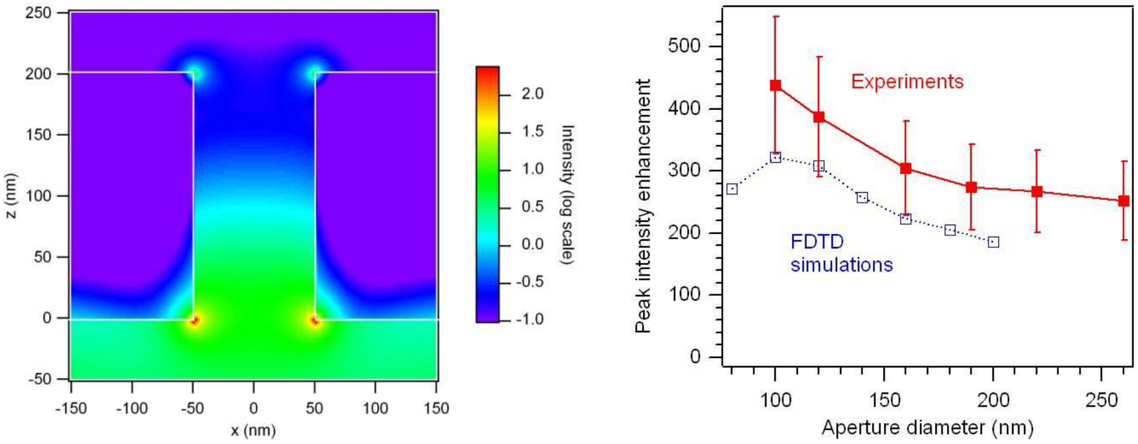

Fig. 1.5. Simulation numérique FDTD dans le cas d'une ouverture de diamètre 100 nm dans un film d'or de 200 nm d'épaisseur. Le milieu environnant est homogène d'indice 1,5, la longueur d'onde est de 633 nm dans le vide. La figure de droite compare les renforcements maximums d'intensité électromagnétique.

Ces différentes études ont montré toute la difficulté expérimentale que soulève la caractérisation fine des renforcements électromagnétiques au voisinage de nanoantennes plasmoniques. La technique de spectroscopie par corrélation de fluorescence FCS est une méthode originale pour quantifier les différents facteurs contribuant à l'exaltation optique (gains en excitation, émission, rendement quantique, efficacité de collection). Cependant, la mise en œuvre de la FCS peut s'avérer délicate, certains artefacts de mesures sont possibles suivant la photochimie des molécules sondes. De plus, le traitement de l'information requiert de nombreuses étapes, ce qui induit une propagation des incertitudes de mesure.

Afin de s'affranchir de l'utilisation de la FCS, nous avons proposé une nouvelle méthode pour quantifier directement le renforcement en intensité d'excitation au voisinage d'une nano-antenne optique, indépendamment des renforcements en émission [9]. Pour cela, on étudie la photodynamique de boîtes quantiques semiconductrices. Contrairement aux molécules organiques, les boîtes quantiques présentent des états multi-excitoniques. Par une mesure de temps de vie de photoluminescence, on mesure les ratios entre les amplitudes des déclins mono et bi-excitoniques X et BX. Le point essentiel est que le ratio BX/X ne dépend pas du taux d'émission radiative, et est linéairement proportionnel à l'intensité d'excitation [9] (figure 1.6). Cette étude propose une méthode simple et quasi-directe pour quantifier le renforcement d'intensité à l'excitation seulement, ce qui constituait jusqu'alors un défi important de la nano-optique et une étape essentielle pour caractériser et améliorer le design de nanoantennes.

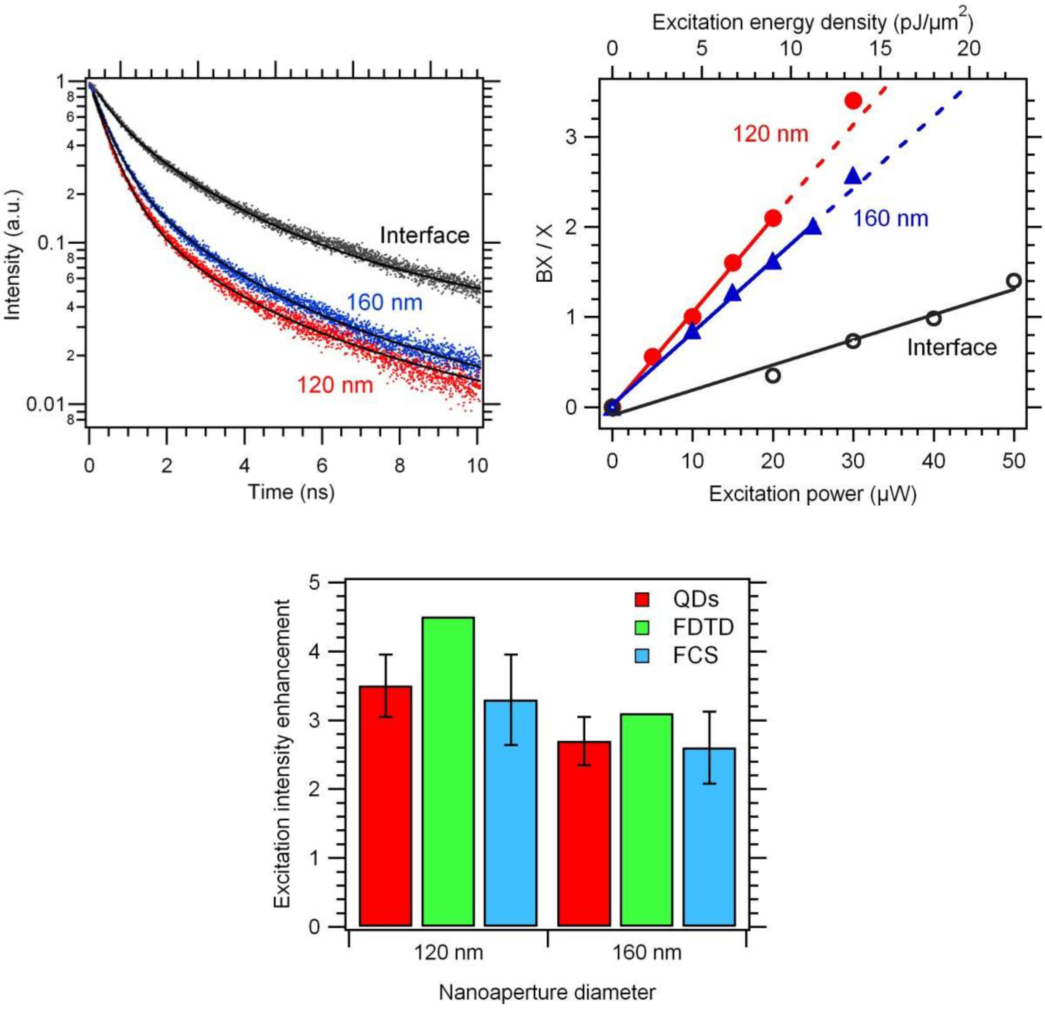

Fig. 1.6. Mesure de déclins de photoluminescence pour quantifier le rapport des amplitudes bi-exciton BX / exciton X. Ce ratio dépend linéairement de l'intensité pompe, son renforcement quantifie directement le gain en excitation dans le cas de nano-ouvertures dans un film d'or.

---

[9] H. Aouani, et al, Colloidal Quantum Dots as Probes of Excitation Field Enhancement in Photonic Antennas, ACS Nano 4, 4571-4578 (2010)

Enfin, au cours de l'année 2010, l'étude sur le couplage lumière-matière dans une nanoouverture métallique a été étendu à d'autres formes d'émission optique que la fluorescence ou la luminescence. Les gains en exaltation pour la diffusion Raman exaltée en bord de nano-ouverture ont été quantifiés pour la première fois [8], ce qui constitue une étape importante à la fois pour la compréhension des phénomènes physiques dans ce type de structure et pour le développement de substrats reproductibles et robustes pour la spectroscopie Raman exaltée de surface SERS.

Ensuite, nous avons étudié la capacité d'une nano-ouverture à exalter la génération de second harmonique à l'interface diélectrique-métal [10]. Cette expérience d'optique non-linéaire est la première à montrer clairement le renforcement de génération de second harmonique dans le cas d'une structuration circulaire du film d'or. Une étude polarimétrique a été menée sur des ouvertures de formes circulaires et triangulaires, montrant que les formes triangulaires sont plus efficaces (comme attendu de part leur absence de centrosymétrie pour une polarisation linéaire incidente).

---

[10] P. Schön, et al, Enhanced second harmonic generation from individual metallic nanoapertures, Opt. Lett. 35, 4063-4065 (2010).

Emission and excitation contributions to enhanced single molecule fluorescence by gold nanometric apertures

Jérôme Wenger,[1*] **Davy Gérard,**[1] **José Dintinger,**[2]
Oussama Mahboub,[2] **Nicolas Bonod,**[1] **Evgeny Popov,**[1]
Thomas W. Ebbesen,[2] **and Hervé Rigneault**[1]

[1] *Institut Fresnel, Aix-Marseille Université, CNRS, Campus de St Jérôme,*
13397 Marseille, France
[2] *Institut de Science et Ingénierie Supramoléculaires, Université Louis Pasteur, CNRS,*
8 allée G. Monge, 67000 Strasbourg, France
[*] *Corresponding author: jerome.wenger@fresnel.fr*

www.fresnel.fr/mosaic

Abstract: We detail the role of single nanometric apertures milled in a gold film to enhance the fluorescence emission of Alexa Fluor 647 molecules. Combining fluorescence correlation spectroscopy and lifetime measurements, we determine the respective contributions of excitation and emission in the observed enhanced fluorescence. We characterize a broad range of nanoaperture diameters from 80 to 310 nm, and highlight the link between the fluorescence enhancement and the local photonic density of states. These results are of great interest to increase the effectiveness of fluorescence-based single molecule detection and to understand the interaction between a quantum emitter and a nanometric metal structure.

OCIS codes: (050.1220) Apertures; (240.6680) Surface plasmons; (170.6280) Spectroscopy, fluorescence and luminescence; (160.4236) Nanomaterials

---

References and links

1. W. L. Barnes, "Fluorescence near interfaces: the role of photonic mode density," J. Mod. Opt. **45**, 661-699 (1998).
2. J. R. Lakowicz, "Radiative decay engineering 5: metal-enhanced fluorescence and plasmon emission," Anal. Biochem. **337**, 171-194 (2005).
3. E. Fort and S. Grésillon, "Surface enhanced fluorescence," J. Phys. D: Appl. Phys. **41**, 013001 (2008).
4. P. Anger, P. Bharadwaj and L. Novotny, "Enhancement and Quenching of Single-Molecule Fluorescence," Phys. Rev. Lett. **96**, 113002 (2006).
5. S. Kühn, U. Håkanson, L. Rogobete and V. Sandoghdar, "Enhancement of Single-Molecule Fluorescence using a Gold Nanoparticle as an Optical Nanoantenna," Phys. Rev. Lett. **97**, 017402 (2006).
6. J. Zhang, Y. Fu, M. H. Chowdhury, and J. R. Lakowicz, "Metal-Enhanced Single-Molecule Fluorescence on Silver Particle Monomer and Dimer: Coupling Effect between Metal Particles," Nano Lett. **7**, 2101-2107 (2007).
7. S. Gerber, F. Reil, U. Hohenester, T. Schlagenhaufen, J. R. Krenn, and A. Leitner, "Tailoring light emission properties of fluorophores by coupling to resonance-tuned metallic nanostructures," Phys. Rev. B **75**, 073404 (2007).
8. Y. Zhang, K. Aslan, M. J. R. Previte, and C. D. Geddes, "Metal-enhanced fluorescence: Surface plasmons can radiate a fluorophore's structured emission," Appl. Phys. Lett. **90**, 053107 (2007).
9. F. Tam, G. P. Goodrich, B. R. Johnson, and N. J. Halas, "Plasmonic Enhancement of Molecular Fluorescence," Nano Lett. **7**, 496-501 (2007).
10. J. Enderlein and T. Ruckstuhl, "The efficiency of surface-plasmon coupled emission for sensitive fluorescence detection," Opt. Express **13**, 8855-8865 (2005).

#92310 - $15.00 USD Received 31 Jan 2008; revised 15 Feb 2008; accepted 15 Feb 2008; published 20 Feb 2008

11. J. N. Farahani, D. W. Pohl, H.-J. Eisler, and B. Hecht, “Single Quantum Dot Coupled to a Scanning Optical Antenna: A Tunable Superemitter,” Phys. Rev. Lett. **95**, 017402 (2005).
12. O. L. Muskens, V. Giannini, J. A. Sanchez-Gil, and J. Gomez Rivas, “Strong Enhancement of the Radiative Decay Rate of Emitters by Single Plasmonic Nanoantennas,” Nano Lett. **7**, 2871-2875 (2007).
13. J. S. Biteen, D. Pacifici, N. S. Lewis and H. A. Atwater, “Enhanced Radiative Emission Rate and Quantum Efficiency in Coupled Silicon Nanocrystal-Nanostructured Gold Emitters,” Nano Lett. **5**, 1768-1773 (2005).
14. G. L. Liu, J. Kim, and L. P. Lee, “Fluorescence enhancement of quantum dots enclosed in Au nanopockets with subwavelength aperture,” Appl. Phys. Lett. **89**, 241118 (2006).
15. Y.-J. Hung, I. I. Smolyaninov, C. C. Davis and H.-C. Wu, “Fluorescence enhancement by surface gratings,” Opt. Express **14**, 10825-10830 (2006).
16. G. Sun, J. B. Khurgin and R. A. Soref, “Practicable enhancement of spontaneous emission using surface plasmons,” Appl. Phys. Lett. **90**, 111107 (2007).
17. Y. Liu and S. Blair, “Fluorescence enhancement from an array of subwavelength metal apertures,” Opt. Lett. **28**, 507-509 (2003).
18. A. G. Brolo, S. C. Kwok, M. D. Cooper, M. G. Moffitt, C.-W. Wang, R. Gordon, J. Riordon, and K. L. Kavanagh, “Surface Plasmon-Quantum Dot Coupling from Arrays of Nanoholes,” J. Phys. Chem. B **110**, 8307-8313 (2006).
19. J. H. Kim and P. J. Moyer, “Laser-induced fluorescence within subwavelength metallic arrays of nanoholes indicating minimal dependence on hole periodicity,” Appl. Phys. Lett. **90**, 131111 (2007).
20. U. C. Fischer, “Submicrometer aperture in a thin metal film as a probe of its microenvironment through enhanced light scattering and fluorescence,” J. Opt. Soc. Am. B **3**, 1239-1244 (1986).
21. H. Rigneault, J. Capoulade, J. Dintinger, J. Wenger, N. Bonod, E. Popov, T. W. Ebbesen and P.-F. Lenne, “Enhancement of Single-Molecule Fluorescence Detection in Subwavelength Apertures,” Phys. Rev. Lett. **95**, 117401 (2005).
22. J. Wenger, B. Cluzel, J. Dintinger, N. Bonod, A.- L. Fehrembach, E. Popov, P.-F. Lenne, T. W. Ebbesen, and H. Rigneault, “Radiative and Nonradiative Photokinetics Alteration Inside a Single Metallic Nanometric Aperture,” J. Phys. Chem. C **111**, 11469-11474 (2007).
23. D. Gérard, J. Wenger, N. Bonod, E. Popov, H. Rigneault, F. Mahdavi, S. Blair, J. Dintinger, and T. W. Ebbesen, “Nanoaperture-enhanced fluorescence: Towards higher detection rates with plasmonic metals,” Phys. Rev. B **77**, 045413 (2008).
24. H. G. Craighead, “Future lab-on-a-chip technologies for interrogating individual molecules,” Nature (London) **442**, 387-393 (2006).
25. J. T. Mannion, and H. G. Craighead, “Nanofluidic Structures for Single Biomolecule Fluorescent Detection,” Biopolymers **85**, 131-143 (2006).
26. C. Genet and T. W. Ebbesen, “Light in tiny holes,” Nature (London) **445**, 39-46 (2007).
27. M. J. Levene, J. Korlach, S. W. Turner, M. Foquet, H. G. Craighead, and W. W. Webb, “Zero-Mode Waveguides for Single-Molecule Analysis at High Concentrations,” Science **299**, 682-686 (2003).
28. K. T. Samiee, M. Foquet, L. Guo, E. C. Cox, H. G. Craighead, “Lambda repressor oligomerization kinetics at high concentrations using fluorescence correlation spectroscopy in zero-mode waveguides,” Biophys. J. **88**, 2145-2153 (2005).
29. M. Leutenegger, M. Gösch, A. Perentes, P. Hoffmann, O. J. F. Martin, T. Lasser, “Confining the sampling volume for Fluorescence Correlation Spectroscopy using a sub-wavelength sized aperture,” Opt. Express **14**, 956-969 (2006).
30. J. Wenger, F. Conchonaud, J. Dintinger, L. Wawrezinieck, T. W. Ebbesen, H. Rigneault, D. Marguet, P. F. Lenne, “Diffusion Analysis within Single Nanometric Apertures Reveals the Ultrafine Cell Membrane Organization,” Biophys. J. **92**, 913-919 (2007).
31. J. Wenger, D. Gérard, P.-F. Lenne, H. Rigneault, J. Dintinger, T. W. Ebbesen, A. Boned, F. Conchonaud, D. Marguet, “Dual-color fluorescence cross-correlation spectroscopy in a single nanoaperture : towards rapid multicomponent screening at high concentrations,” Opt. Express **14**, 12206-12216 (2006).
32. J. Widengren, R. Rigler, and U. Mets, “Triplet-state monitoring by fluorescence correlation spectroscopy,” J. Fluoresc. **4**, 255-258 (1994).
33. J. Widengren, U. Mets, and R. Rigler, “Fluorescence correlation spectroscopy of triplet states in solution: a theoretical and experimental study,” J. Phys. Chem. **99**, 13368-13379 (1995).
34. V. Buschmann, K. D. Weston, and M. Sauer, “Spectroscopic Study and Evaluation of Red-Absorbing Fluorescent Dyes,” Bioconjugate Chem. **14**, 195-204 (2003).
35. J. Widengren and P. Schwille, “Characterization of Photoinduced Isomerization and Back-Isomerization of the Cyanine Dye Cy5 by Fluorescence Correlation Spectroscopy,” J. Phys. Chem. A **104**, 6416-6428 (2000).
36. C. Zander, J. Enderlein and R. A. Keller (Eds.), *Single-Molecule Detection in Solution - Methods and Applications*, (VCH-Wiley, Berlin/New York, 2002).
37. F. Mahdavi, Y. Liu, and S. Blair, “Modeling Fluorescence Enhancement from Metallic Nanocavities,” Plasmonics **2**, 129-142 (2007).
38. E. Popov, M. Nevière, J. Wenger, P.-F. Lenne, H. Rigneault, P. Chaumet, N. Bonod, J. Dintinger, T. W. Ebbesen, “Field enhancement in single subwavelength apertures,” J. Opt. Soc. Am. A **23**, 2342-2348 (2006).

#92310 - $15.00 USD Received 31 Jan 2008; revised 15 Feb 2008; accepted 15 Feb 2008; published 20 Feb 2008

1. Introduction

The fluorescence emission of a single molecule can be enhanced by properly tailoring its photonic environment, leading to new opportunities for single molecule detection. The environment can affect the fluorescence emission in three ways: (i) by locally enhancing the excitation intensity, (ii) by increasing the emitter's radiative rate and quantum efficiency, and (iii) by modifying its radiation pattern, towards a higher emission directionality to the detectors. Determining the influence of these processes is a crucial issue to characterize nanodevices for enhanced fluorescence, which has been a topic of great interest for the last decade [1, 2, 3].

In the growing field of nanostructure-enhanced fluorescence, much attention is currently devoted to metal structures, where surface plasmons can play an additional role [2, 3]. For instance, recent studies involve metallic nanoparticles [4, 5, 6, 7, 8], core-shell particles [9], thin films [10], nanoantennas [11, 12], nanoporous gold [13], nanopockets [14], metallic gratings [15, 16], nanoaperture arrays [17, 18, 19], and single nanoapertures [20, 21]. For all these geometries, determining the specific influence of a nanostructure on the fluorescence emission remains a challenging task, as the detected signal results from a product of excitation and emission processes. Excitation depends on the interaction between the driving field and the nanostructure, while at moderate optical powers, the emission efficiency is set by the balance of radiative and non-radiative decays and the modification of the radiation pattern.

In this paper, we discuss the fluorescence alteration induced by a single nanometric aperture milled in a gold film with diameters ranging from 80 to 310 nm. Fluorescence correlation spectroscopy (FCS) is combined with fluorescence lifetime measurements on the same setup to characterize the photokinetic rates of Alexa Fluor 647 molecules inside the nanoapertures. Compared to previous studies [21, 22, 23], we now quantitatively detail the contributions of excitation and emission enhancements in the reported fluorescence gain for a broad range of aperture diameters, and relate these effects to the alteration of the local density of states [1].

In spite of their conceptual simplicity, nanoapertures bear appealing properties to increase the effectiveness of fluorescence-based single-molecule detection [24, 25, 26]. Thanks to these devices, a large range of biologic processes can be efficiently monitored with single molecule resolution at micromolar concentrations [27, 28, 29]. The use of nanoaperture for biophotonics applications can also be extended to the investigation of live cell membranes [30] and dual-labels cross-correlation studies [31]. Therefore, understanding the fluorescence alteration in a nanoaperture is of practical importance for high-efficiency single-molecule analysis.

The paper is outlined as follows. In Section 2, we describe the procedure used to characterize the different photokinetic rates. Section 3 presents the experimental methods used throughout the paper. Results on the fluorescence detection rates and lifetimes are presented in Section 4 for aperture diameters ranging from 80 to 310 nm. In Section 5, we combine the experimental results to detail the fluorescence photokinetics alteration and assess the respective role of excitation and emission enhancements in the fluorescence process. Finally, we summarize our conclusions in Section 6.

2. Fluorescence characterization procedure

To introduce our characterization procedure in a few words, we implement FCS to reliably quantify the detected number of molecules and the fluorescence count rate per molecule *CRM*, which is recorded as the excitation power I_e is raised. Global analysis of the *CRM* vs. I_e curve, combined to lifetime measurements using time correlated single photon counting (TCSPC) alongside the FCS setup, gives the relative contribution of emission and excitation gains in the overall fluorescence enhancement, in a similar trend as in references [32, 33]. We point out that this characterization procedure combining FCS and TCSPC can be straightforwardly extended to other types of plasmonic nanostructures.

#92310 - $15.00 USD Received 31 Jan 2008; revised 15 Feb 2008; accepted 15 Feb 2008; published 20 Feb 2008

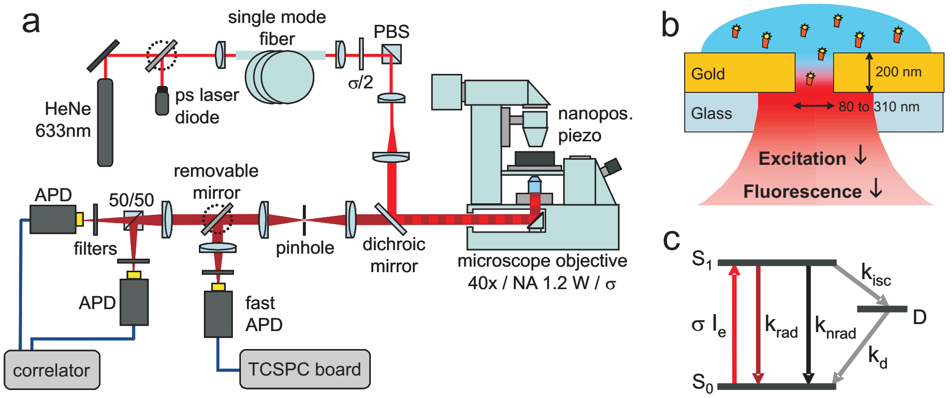

Fig. 1. (a) Schematic view of the experimental setup combining FCS and TCSPC. (b) Nanoaperture configuration. (c) Notations used to describe the molecular transition rates.

We introduce the fluorescence enhancement η_F in a nanoaperture as the ratio of the detected fluorescence rate per molecule in the aperture CRM_{aper} and in open solution CRM_{sol} at a fixed excitation power, that is $\eta_F = CRM_{aper}/CRM_{sol}$. To understand the physical origin of the increase in the fluorescence brightness already reported in [23], we begin by expressing the fluorescence rate per molecule CRM. Throughout this paper, we treat Alexa Fluor 647 as a three energy levels system, as illustrated in Fig. 1(c). S_0 denotes the ground state, S_1 the excited singlet state and D is a dark (non-fluorescent) state that accounts for both triplet state and non-fluorescing isomerized form. Although the molecular structure of Alexa Fluor 647 has not been made available yet, the FCS curves and fluorescence lifetimes clearly indicate that it has a carbocyanine structure, with a quantum yield in water solution of about 30% [34]. To the aim of the study reported here, and as far as the fluorescence brightness is concerned, this model will be sufficient. A more detailed description of the photokinetics of cyanine 5 dyes can be found in [35].

The photokinetic rates are noted as follows, and are summarized in appendix A : σI_e stands for the excitation rate, where σ denotes the excitation cross-section and I_e the excitation intensity. k_{rad} and k_{nrad} are the rate constants for radiative emission and non-radiative deexcitation from S_1 to the ground state. k_{isc} and k_d are the rate constants for inter-system crossing to the dark state and relaxation to the ground state respectively. The total deexcitation rate from the excited singlet state S_1 is noted as $k_{tot} = 1/\tau_{tot}$, where τ_{tot} is the excited state lifetime.

Under steady-state conditions, the fluorescence rate per molecule CRM is given by [36]

$$CRM = \kappa\phi \frac{\sigma I_e}{1 + I_e/I_s} \tag{1}$$

where κ is the light collection efficiency, $\phi = k_{rad}/k_{tot}$ the quantum yield and $I_s = \frac{k_{tot}}{\sigma} \frac{1}{1+k_{isc}/k_d}$ is the saturation intensity.

To ease the understanding of our measurements, we introduce the emission rate $k_{em} = \kappa k_{rad}$, which denotes the effectively detected radiation rate by our instrument. Both radiative rate and collection efficiency are accounted into a single factor k_{em}. Eq. (1) then rewrites

$$CRM = \frac{k_{em}}{k_{tot}} \frac{\sigma I_e}{1 + I_e/I_s} \tag{2}$$

In the low excitation regime $I_e \ll I_s$, Eq. (2) reduces to

$$CRM_{low} = \frac{k_{em}}{k_{tot}} \sigma I_e \qquad (I_e \ll I_s) \tag{3}$$

which indicates that the fluorescence rate per molecule is proportional to the excitation intensity and to the ratio of the detected emission rate to the overall decay rate. The fluorescence enhancement η_F can therefore be expressed as

$$\eta_{F,low} = \frac{CRM_{aper}}{CRM_{sol}} = \frac{\eta_{k_{em}}}{\eta_{k_{tot}}} \eta_{I_e} \qquad (I_e \ll I_s) \tag{4}$$

where $\eta_{k_{em}} = k_{em-aper}/k_{em-sol}$, $\eta_{k_{tot}} = k_{tot-aper}/k_{tot-sol}$ and $\eta_{I_e} = \sigma I_{e-aper}/\sigma I_{e-sol}$ are the enhancements in the collected emission rate, total decay rate and excitation rate.

In the saturation regime $I_e \gg I_s$, Eq. (2) reduces to

$$CRM_{sat} = \frac{k_{em}}{k_{tot}} \sigma I_s = \frac{k_{em}}{1 + k_{isc}/k_d} \qquad (I_e \gg I_s) \tag{5}$$

which indicates that the fluorescence rate per molecule at saturation is determined by the collected emission rate and the ratio k_{isc}/k_d. It is important to note that k_{isc}/k_d is proportional to the relative population of the dark state D once saturation is reached [32, 33]. We verified experimentally that the dark state fraction at fluorescence saturation was similar for all the nanoaperture diameters, as for the open solution. We therefore make the reasonable assumption that *at fluorescence saturation* the ratio k_{isc}/k_d is a constant set by the Alexa Fluor 647 properties, and that it is independent of the photonic environment. While computing the ratios of the fluorescence rates at saturation $\eta_{F,sat}$, the term $\frac{1}{1+k_{isc}/k_d}$ in Eq. (5) thus disappears, and one ends up with the simple expression

$$\eta_{F,sat} = \eta_{k_{em}} \qquad (I_e \gg I_s) \tag{6}$$

To characterize the fluorescence photokinetics enhancement induced by a single nanoaperture we will thus perform the following procedure :

- The fluorescence rates per molecule CRM are measured by FCS for increasing excitation powers in open solution and in single nanoapertures.
- The data points for CRM versus I_e are fitted according to Eq. (2). The ratio to the open solution gives η_F versus I_e. From the numerical fits, we infer the fluorescence enhancement at the limit below saturation $\eta_{F,low}$ and at saturation $\eta_{F,sat}$.
- According to Eq. (6), the value of $\eta_{F,sat}$ at saturation equals the emission rate enhancement $\eta_{k_{em}}$.
- The fluorescence decay rate k_{tot} is characterized by pulsed time-correlated measurements. The ratio of the results in the nanoaperture to the open solution gives $\eta_{k_{tot}}$.
- According to Eq. (4), the excitation rate enhancement is obtained as $\eta_{I_e} = \eta_{F,low}\, \eta_{k_{tot}} / \eta_{k_{em}}$.

As we will show below, this procedure turns out to be very efficient in discriminating the contributions of excitation and emission to the overall fluorescence process. The limit of this method is that all the presented results account for spatial averaging over all the possible molecular orientations and positions inside the analyzed volume. There is no sensitivity to individual

Received 31 Jan 2008; revised 15 Feb 2008; accepted 15 Feb 2008; published 20 Feb 2008

molecular trajectories or dipole orientations, but one ends up directly with global figures to characterize the (spatially averaged) emitted fluorescence. Besides, it is very difficult to reveal the physics underneath the emission rate $k_{em} = \kappa k_{rad}$ enhancement. Distinguishing between the contributions of the radiative rate k_{rad} and the collection efficiency κ remains a challenge, mainly because of the intrinsic difficulty to reliably measure a collection efficiency [22, 23]. Last, the fluorescence enhancement factors are spectrally averaged within the fluorescence bandpass detection window.

3. Materials and methods

Our experimental set-up is based on an inverted microscope with a NA= 1.2 water-immersion objective, allowing single aperture studies (Fig. 1). It combines on the same setup FCS and time-correlated lifetime measurements facilities, used to determine the complete photokinetics alteration in a nanoaperture following the procedure derived in section 2. We emphasize that for all experiments, a droplet of solution containing Alexa-Fluor 647 molecules is deposited on top of the aperture sample. The droplet acts as a reservoir of molecules, that are constantly diffusing inside the aperture, which strongly limits photobleaching effects.

3.1. Nanoapertures

Opaque gold films (thickness 200 nm) were coated on conventional microscope coverslips (thickness 150 μm) by thermal evaporation. A 15 nm thick chromium layer ensures adhesion between the gold film and the glass substrate. Circular apertures with diameters ranging from 80 nm to 310 nm were then directly milled by focused ion beam (FEI Strata DB235).

3.2. FCS measurements and analysis

For FCS measurements, the excitation is set to a CW HeNe laser operating at 633 nm. After a 50 μm confocal pinhole conjugated to the sample plane, the detection is performed by two avalanche photodiodes (Perkin-Elmer SPCM-AQR-13) with 670 ± 20 nm fluorescence bandpass filters. The fluorescence intensity fluctuations are analyzed by cross-correlating the signal of each photodiode with a ALV6000 hardware correlator. Each individual FCS measurement was obtained by averaging 5 runs of 10 s duration.

As an illustration, Fig. 2 presents typical correlograms $g^{(2)}(\tau)$ recorded in a 120 nm nanoaperture for three different excitation powers. The analysis of this FCS data relies on a numerical fit based on a three dimensional Brownian diffusion model [23, 36]:

$$g^{(2)}(\tau) = 1 + \frac{1}{N}\left(1 - \frac{\langle B\rangle}{\langle F\rangle}\right)^2 \left[1 + n_T \exp\left(-\frac{\tau}{\tau_{b_T}}\right)\right] \frac{1}{(1+\tau/\tau_d)\sqrt{1+s^2\,\tau/\tau_d}} \tag{7}$$

where N is the total number of molecules, $\langle F\rangle$ the total signal, $\langle B\rangle$ the background noise, n_T the amplitude of the dark state population, τ_{b_T} the dark state blinking time, τ_d the mean diffusion time and s the ratio of transversal to axial dimensions of the analysis volume. Numerical fit of the FCS data following Eq. (7) provides the average number of molecules N which is used to compute the fluorescence count rate per molecule CRM.

The background noise $\langle B\rangle$ originates mainly from the back-reflected laser light and from gold autofluorescence. At 40 μW excitation powers, it typically amounts to $\langle B\rangle = 3$ kHz, which is almost negligible as compared to the count rates per molecule in the nanoapertures in the range 50-150 kHz (Fig. 3). In the configuration of Fig. 1, the aperture subwavelength diameter and the 200 nm gold thickness provide strong electromagnetic confinement at the aperture bottom. Therefore, fluorescence contribution from the pool of molecules above the nanoaperture was shown to be negligible [21].

#92310 - $15.00 USD Received 31 Jan 2008; revised 15 Feb 2008; accepted 15 Feb 2008; published 20 Feb 2008

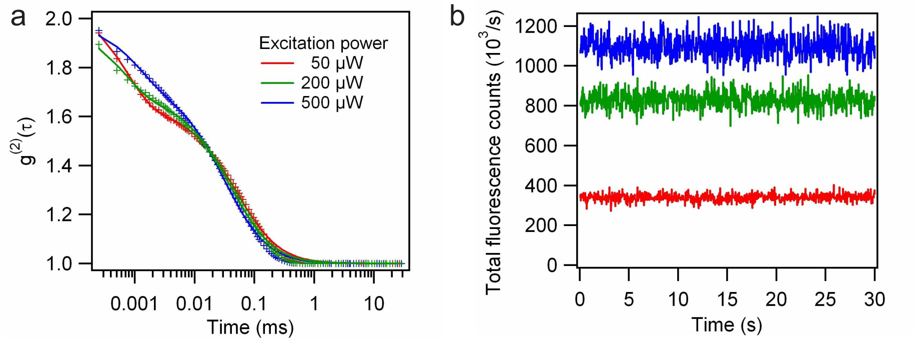

Fig. 2. (a) Typical fluorescence autocorrelations in a 120 nm aperture (crosses, raw data) and numerical fits according to Eq. (7) (lines). (b) Snapshot of the raw fluorescence signal corresponding to (a).

3.3. TCSPC measurements and fluorescence lifetime analysis

For TCSPC lifetime measurements, the excitation is turned to a picosecond laser diode operating at 636 nm (PicoQuant LDH-P-635 with PicoQuant driver SEPIA-II-SLM828). A single-mode optical fiber (Thorlabs P3-630A-FC-5) ensures a perfect spatial overlap between the pulsed laser diode and the CW HeNe laser. This guarantees the same excitation spot for FCS and TCSPC and almost same wavelength, contrary to previous experiments [21, 22]. For our measurements, the laser diode repetition rate was set to 80 MHz and the averaged excitation power measured at the microscope entrance port was 80 μW. Single photon detection is performed by a fast avalanche photodiode (Micro Photon Devices by PicoQuant MPD-5CTC, with timing jitter about 50 ps and active area 50 μm) with 670 ± 20 nm fluorescence bandpass filter. The photodiode output is coupled to a fast TCSPC module (PicoQuant PicoHarp 300, resolution per channel 4 ps). Overall, the temporal resolution of our setup is 120 ps FWHM. Switching from FCS to TCSPC is easily done by a set of two removable mirrors (Fig. 1(a)).

To measure the fluorescence decay rate, we use the following procedure that takes into account the limited resolution of our setup. Careful analysis of the instrument response function (IRF) (shown later on Fig. 5(a)) reveals a double exponential decay : $IRF(t) \propto A_1 \exp(-k_1 t) + A_2 \exp(-k_2 t)$ with $A_1 = 0.516$, $A_2 = 0.484$, $k_1 = 5.7\ 10^9$ s^{-1} and $k_2 = 20.7\ 10^9$ s^{-1}. The output signal $O(t)$ of the TCSPC card corresponds to the convolution of the system IRF with the averaged fluorescence decay, which is assumed to be mono-exponential. Convolving a mono-exponential fluorescence decay with a double exponential IRF results in a triple exponential :

$$O(t) \propto (A_1 + A_2) \exp(-k_{tot} t) - A_1 \exp(-k_1 t) - A_2 \exp(-k_2 t) \qquad (8)$$

where k_{tot} is the molecular total deexcitation rate, and A_1, A_2, k_1 and k_2 are fixed parameters set by the IRF analysis. While analyzing the experimental decay curves, k_{tot} is thus kept as the only free varying parameter. This procedure yields a fluorescence lifetime of 1.0 ns for Alexa Fluor 647 in open water solution, which corresponds well to the data in the literature [34].

4. Experimental results

To get a global picture of the fluorescence photokinetics alterations in a single nanoaperture, we carried extensive FCS experiments for aperture diameters ranging from 80 up to 310 nm. The excitation power was increased from 25 to 500 μW (the upper limit was set to avoid damaging the sample and photobleaching the dyes). Each correlation function was analyzed to compute

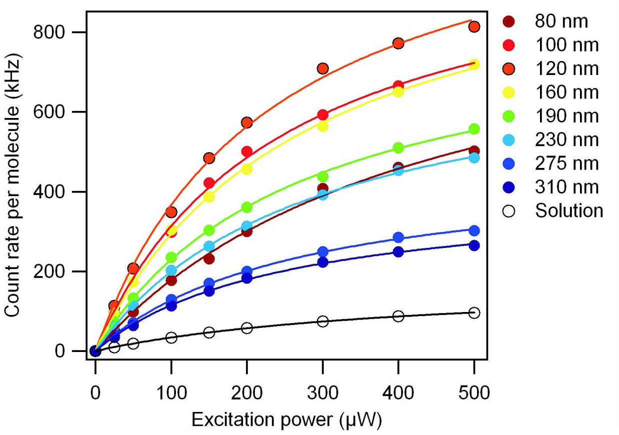

Fig. 3. Fluorescence rates per molecule *CRM* versus excitation power in open solution and in single nanoapertures. Circles are experimental data, lines are numerical fits using Eq. (2).

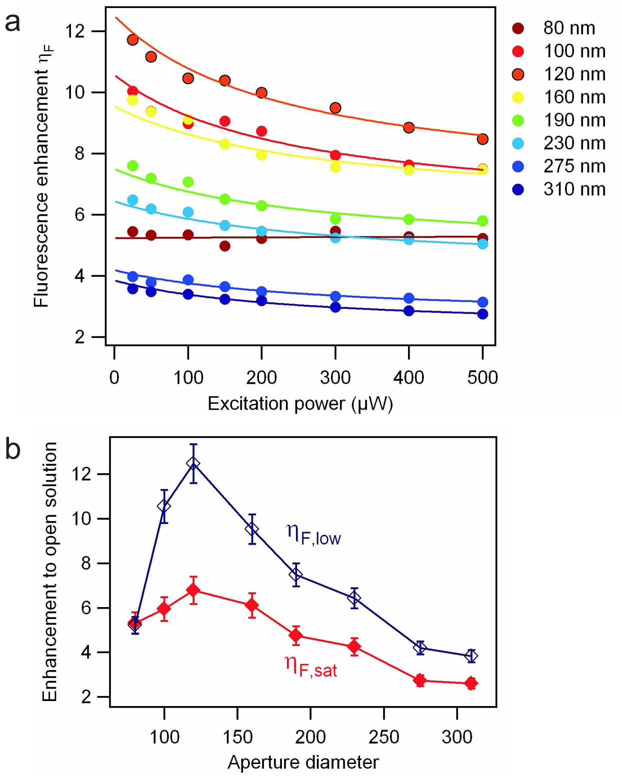

Fig. 4. (a) Fluorescence enhancement η_F derived from Fig. 3. (b) Fluorescence enhancement below saturation $\eta_{F,low}$ (empty markers) and at saturation $\eta_{F,sat}$ (filled markers) deduced from the numerical fits in Fig. 3 according to Eqs. (2), (4) and (6).

the average number of molecules N and fluorescence count rate per molecule *CRM*. Please note that special care has been taken to characterize the level of background noise and the dark state

#92310 - $15.00 USD Received 31 Jan 2008; revised 15 Feb 2008; accepted 15 Feb 2008; published 20 Feb 2008

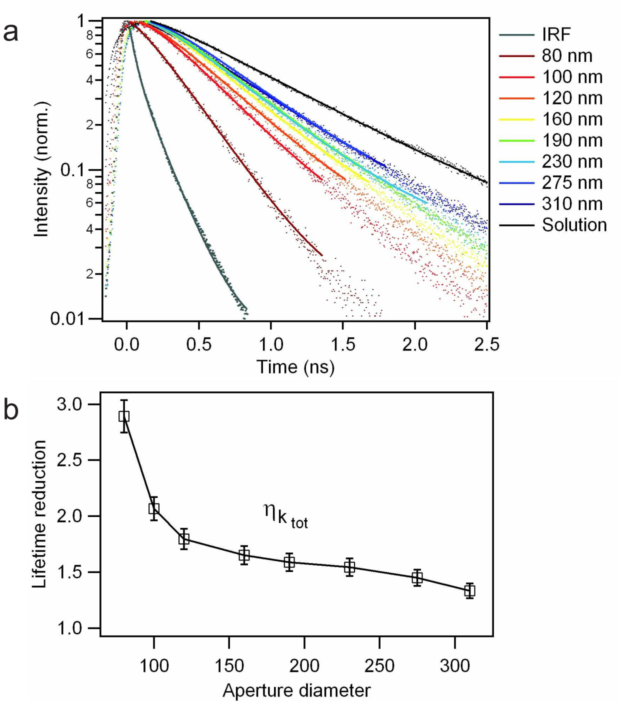

Fig. 5. (a) Normalized fluorescence decay traces measured in open solution (black dots) and in single nanoapertures. Dots are experimental data, lines are numerical fits following the procedure described in Sec. 3.3. The shorter decay trace (grey) is the overall instrument response function (IRF). (b) Fluorescence lifetime reduction versus the aperture diameter (as compared to open solution), deduced from the numerical fits in (a) using Eq. (8).

amplitude for each excitation power.

Figure 3 displays the evolution of the detected fluorescence rate per molecule *CRM* versus the excitation power for the different aperture diameters. Solid lines are numerical fits according to Eq. (2), which agree well to our experimental data. As the aperture diameter decreases, the fluorescence rate *CRM* increases before reaching an optimum for a diameter of 120 nm, which was previously assessed to give the largest fluorescence enhancement [23]. For smaller apertures (100 and 80 nm diameters), we show that *CRM* is decreased. Figure 3 also indicates that high count rates larger than 400,000 counts per second and per molecule are readily obtained in nanoapertures at high excitation power, while in open solution, the count rate saturates to values below 180,000 counts per second.

Count rates displayed on Fig. 3 were used to compute the corresponding fluorescence enhancement factors $\eta_F = CRM_{aper}/CRM_{sol}$. The results are displayed on Fig. 4(a) versus the excitation power, with an optimum diameter at 120 nm. Then, we use the numerical fits of *CRM* versus I_e according to Eqs. (2), (4) and (6) to infer the fluorescence enhancement well below saturation $\eta_{F,low}$ and at saturation $\eta_{F,sat}$. For clarity, we present these figures versus the aperture diameter in Fig. 4(b). The lower value for $\eta_{F,sat}$ as compared to $\eta_{F,low}$ results from the respective influence of the excitation intensity enhancement and lifetime reduction, as indicated in Eqs. (4) and (6). We point out that the reported fluorescence enhancement factors account for spectral averaging over the 650-690 nm detection window. Spectral dependence of the fluorescence enhancement has been investigated in [23], and was shown to cover the entire dye emission spectrum with only slight spectral variations.

Along with the FCS measurements, for the same nanoaperture sample and the same Alexa Fluor 647 solution, we conducted TCSPC experiments to investigate the fluorescence lifetime alteration inside the nanoapertures. Figure 5(a) shows the measured fluorescence decay curves (dots) and their numerical fits (lines) for Alexa 647 molecules in single nanoapertures of diameters ranging from 80 up to 310 nm. As the aperture diameter is decreased, a clear reduction in the fluorescence lifetime is seen. To quantify this reduction, we fitted the data according to Eq. (8), and normalized the measured decay rate to the decay rate in open solution. This yields the ratio $\eta_{k_{tot}} = k_{tot-aper}/k_{tot-sol}$ displayed on Fig. 5(b). $\eta_{k_{tot}}$ increases as the aperture diameter is decreased, and as the metal comes closer to the average position of the molecules. We measure a clear lifetime reduction of about 3 for a 80 nm aperture.

5. Discussion

The different experimental results on Fig. 4 and 5 are now combined to estimate the alteration of the fluorescence photokinetics rates. We use the different steps described in section 2 : according to Eq. (6), the fluorescence enhancement at saturation $\eta_{F,sat}$ gives the emission rate enhancement $\eta_{k_{em}}$, which denotes the gain in radiative rate and collection efficiency. Then, following Eq. (4), the excitation rate enhancement is obtained from the fluorescence enhancement below saturation and the lifetime reduction as $\eta_{I_e} = \eta_{F,low}\,\eta_{k_{tot}}/\eta_{k_{em}}$. For completeness, all these results are presented on one single figure for each aperture diameter (Fig. 6(a) to (d)). We also compute the ratio $\eta_{k_{em}}/\eta_{k_{tot}}$ (Fig. 6(e)). This displays the gain in the factor $k_{em}/k_{tot} = \kappa k_{rad}/k_{tot} = \kappa\phi$ which is the product of the collection efficiency κ with the dye's quantum yield ϕ. Last, to comment on these results, we display the propagation constant γ of the fundamental guided mode inside an infinitely long aperture as a function of the aperture diameter (Fig. 6(f)), the aperture being filled with water [23].

A general comment on Fig. 6 is that the nanoaperture affects both emission and excitation in the fluorescence process. Both effects contribute to the large fluorescence enhancement observed. Hereafter, we will relate these effects to the local density of states (LDOS) increase induced by the nanoaperture. The global consideration of the graphs on Fig. 6 leads to the introduction of three regions as indicated by the dashed vertical lines on Fig. 6. Region (1) is for aperture diameters below 100 nm, region (2) for diameters between 100 and 175 nm, and region (3) stands for diameters above 175 nm. These regions are only intended to guide the following discussion, there are obviously no strict borders between them.

Starting from region (3), the general trend is an increase in the photokinetic rates as the aperture diameter is decreased. To compare with the propagation constant γ (Fig. 6(f)) we point out that in this region, the real part of the propagation constant is large while the imaginary part is low, corresponding to a propagative excitation field. As the aperture diameter is decreased, the imaginary part of the propagation constant grows, leading to more electromagnetic confinement at the aperture entrance. This translates into an increase in the emission enhancement along with the excitation enhancement (Fig. 6(b) and (d)).

On the other hand, region (1) shows a decrease in the fluorescence enhancement as the aperture diameter is reduced. This is linked to a large increase in k_{tot} (Fig. 6(c)), while at the same time, the emission and the excitation rates tend to decrease with the aperture diameter. Consequently, the apparent quantum yield k_{em}/k_{tot} decreases (Fig. 6(e)). These effects are strong evidences for fluorescence quenching, which we relate to a too close vicinity between the dyes and the metal. Let us also point out that region (1) corresponds to a large imaginary part of the propagation constant γ and thus to strongly evanescent fields inside the aperture and large losses. This contributes to the reduction in emission and excitation enhancement (Fig. 6(b) and (d)).

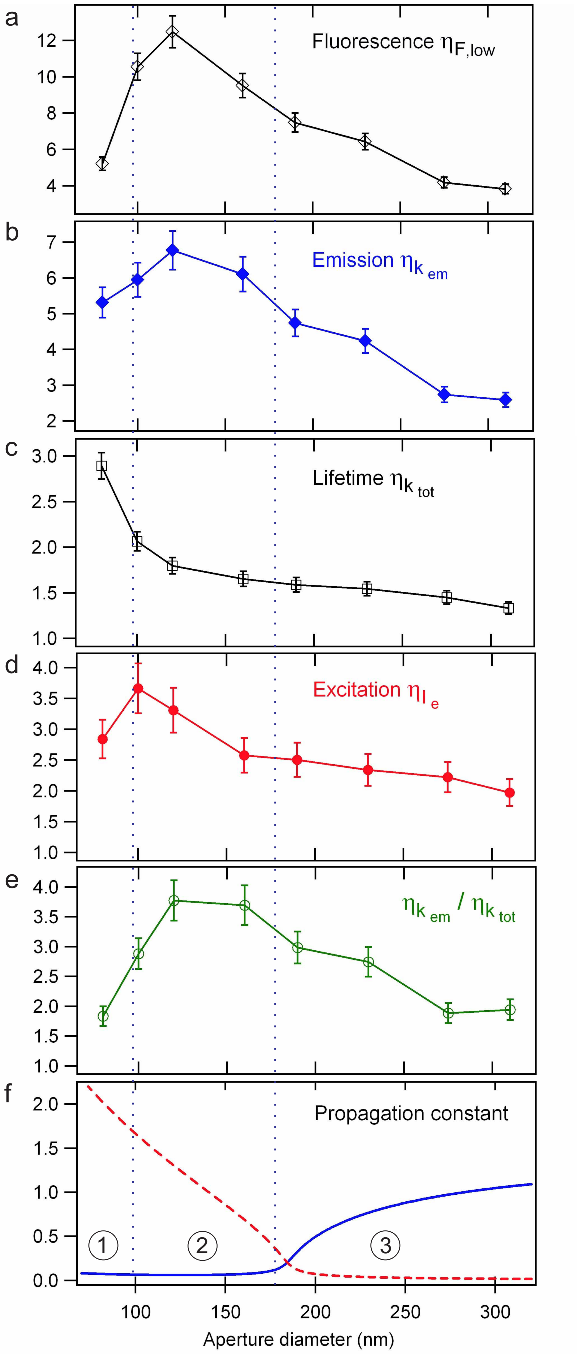

Fig. 6. Physical contributions to nanoaperture enhanced fluorescence, plotted versus the aperture diameter and normalized to the open solution case. (a) Fluorescence enhancement below saturation $\eta_{F,low}$, (b) Emission rate enhancement $\eta_{k_{em}}$, (c) Lifetime reduction $\eta_{k_{tot}}$, (d) Excitation enhancement η_{I_e}, (e) Ratio $\eta_{k_{em}}/\eta_{k_{tot}}$, (f) Propagation constant γ of the fundamental mode inside the aperture (solid line: real part, dashed line: imaginary part).

#92310 - $15.00 USD Received 31 Jan 2008; revised 15 Feb 2008; accepted 15 Feb 2008; published 20 Feb 2008

Last, region (2) appears as a trade-off between cases (1) and (3). This region is close to the cutoff of the fundamental mode that may propagate through the aperture and to the position where the group velocity is minimum (found for a diameter of 120 nm). These conditions lead to a maximum of the photonic density of states [1], and therefore to a maximum in the emission and excitation rates (Fig. 6(b) and (d)). Moreover, the metal-dielectric interface set by the aperture may allow fluorescence energy transferred to a surface plasmon to be coupled out into the radiated field at the aperture edge, contributing to the emission [2, 3]. At the same time, we infer that the molecules stay (on average) far enough from the metal layer, so that the relative influence of quenching to the metal is limited. This is supported by a plateau in the apparent quantum yield (Fig. 6(e)).

Finally, we point out that our experimental results stand in good agreement with the numerical predictions based on the finite elements method [37, 23] and differential theory [38].

6. Conclusion

We have detailed the influence of single nanometric apertures on the fluorescence of Alexa Fluor 647 molecules, and determined the respective contributions of excitation and emission in the observed enhanced fluorescence. The procedure has been conducted for a broad range of nanoapertures with diameters from 80 to 310 nm, which allowed us to discriminate between different physical effects and relate the photokinetics enhancements to the local photonic density of states. Let us emphasize that the characterization procedure combining FCS and TCSPC can be straightforwardly extended to other types of plasmonic nanostructures.

Finally, this study shows that nanoapertures bear many interesting properties for biophotonics, such as light localization, sub-femtoliter observation volume, and an increase in the excitation and emission yield. These properties are of great interest to increase the effectiveness of fluorescence-based single molecule detection.

Acknowledgments

The authors acknowledge stimulating discussions with S. Blair. This work has been funded by the French Agence Nationale de la Recherche under contract ANR-05-PNANO-035-01 “CO-EXUS” and ANR-07-NANO-006-03 “ANTARES”.

Appendix A: Fluorescence photokinetics notations

Symbol	Quantity
S_0	Molecular ground state
S_1	Excited single state
D	Dark state
σI_e	Excitation rate to S_1
σ	Excitation cross-section
I_e	Excitation intensity
k_{rad}	Rate constant for radiative emission
k_{nrad}	Rate constant for non-radiative deexcitation from S_1 to the ground state
k_{isc}	Rate constant for inter-system crossing to the dark state D
k_d	Rate constant for relaxation from D to S_0
k_{tot}	Total deexcitation rate from S_1: $k_{tot} = k_{rad} + k_{nrad} + k_{isc}$
τ_{tot}	Fluorescence lifetime $\tau_{tot} = 1/k_{tot}$
N	Average number of detected molecules
$\langle F \rangle$	Average total fluorescence signal per second
CRM	Fluorescence rate per molecule $CRM = \langle F \rangle / N$
κ	Collection efficiency
ϕ	Quantum yield $\phi = k_{rad}/k_{tot}$
I_s	Saturation intensity $I_s = k_{tot}/(\sigma(1 + k_{isc}/k_d))$
k_{em}	Effective emission rate $k_{em} = \kappa k_{rad}$
η_F	Fluorescence rate enhancement $\eta_F = CRM_{aper}/CRM_{sol}$
$\eta_{F,low}$	Fluorescence rate enhancement below saturation ($I_e \ll I_s$)
$\eta_{F,sat}$	Fluorescence rate enhancement at saturation ($I_e \gg I_s$)
$\eta_{k_{em}}$	Emission rate enhancement $\eta_{k_{em}} = k_{em-aper}/k_{em-sol}$
$\eta_{k_{tot}}$	Decay rate enhancement, lifetime reduction $\eta_{k_{tot}} = k_{tot-aper}/k_{tot-sol}$
η_{I_e}	Excitation rate enhancement $\eta_{I_e} = \sigma I_{e-aper}/\sigma I_{e-sol}$
η_κ	Collection efficiency enhancement $\eta_\kappa = \kappa_{aper}/\kappa_{sol}$

#92310 - $15.00 USD   Received 31 Jan 2008; revised 15 Feb 2008; accepted 15 Feb 2008; published 20 Feb 2008

PHYSICAL REVIEW B **77**, 045413 (2008)

Nanoaperture-enhanced fluorescence: Towards higher detection rates with plasmonic metals

Davy Gérard, Jérôme Wenger, Nicolas Bonod, Evgeni Popov, and Hervé Rigneault
Institut Fresnel, CNRS UMR 6133, Domaine Universitaire de Saint-Jérôme, 13397 Marseille Cedex 20, France

Farhad Mahdavi and Steve Blair
Electrical and Computer Engineering Department, University of Utah, 50 S. Central Campus Drive, Room 3280, Salt Lake City, Utah 84112, USA

José Dintinger and Thomas W. Ebbesen
Institut de Science et d'Ingénierie Supramoléculaire, CNRS UMR 7006, Université Louis Pasteur, 8 allée G. Monge, 67000 Strasbourg, France

(Received 6 November 2007; published 17 January 2008)

A bare nanometric aperture milled in a metallic film forms a simple nanophotonic device that can strongly enhance the optical properties of nearby emitters such as fluorescent molecules. In this paper, we experimentally and numerically compare the properties of circular apertures milled in gold and aluminum, and discuss the influence of a noble metal holding plasmonic resonances in the visible range such as gold. We report that nanometric apertures milled in gold exhibit significantly higher fluorescence enhancement factors than apertures in aluminum. We relate this effect to a larger enhancement of the excitation intensity and radiative rate for an aperture milled in gold. A spectrally resolved analysis of the fluorescence emission from apertures is also presented. Comparison with numerical simulations shows that the enhancement factor is maximum when the photonic density of modes is maximum. Altogether, these results provide crucial knowledge for the design of nanoapertures towards high-efficiency single-molecule analysis.

DOI: 10.1103/PhysRevB.77.045413 PACS number(s): 78.67.−n, 33.50.−j, 82.37.−j, 42.50.−p

I. INTRODUCTION

A bare subwavelength aperture milled in a metallic film forms a simple nanophotonic device. However, in spite of its conceptual simplicity, it exhibits complex and interesting optical properties. As soon as one is dealing with nanosized apertures pierced in a finite-thickness real metal, Bethe's theory[1] is no longer valid and a rigorous diffraction theory must be employed. A number of intriguing phenomena have been experimentally observed, such as the so-called extraordinary transmission through arrays of holes or slits,[2,3] directivity of the transmission through a single structured aperture,[4] or electromagnetic field enhancement and confinement inside and in the vicinity of the aperture.[5,6] All these phenomena are of practical significance to develop new applications in photonics, nano-optics, and biophotonics. In the years immediately following the first report of extraordinary transmission,[2] most of the attention was attracted by the properties of periodic arrays of holes or slits. More recently, there has been a growing interest around the properties of single (i.e., isolated) nanoapertures.[7] Indeed, a single nanoaperture can exhibit a surprisingly high transmission; it also supports highly confined and enhanced electromagnetic fields. Both properties arise from the existence, even for very small holes, of guided modes inside the aperture.[8–12]

The presence of high amplitude electromagnetic fields inside nanoapertures makes them promising for enhancing the fluorescent emission from molecules or nanocrystals. Many groups have already reported fluorescent emission enhancement from emitters located in the vicinity of different types of metallic nanostructures: metallic nanoparticles,[13–19] nanoporous gold,[20] gold "nanopockets,"[21] hole arrays and metallic gratings,[22–26] and single nanoapertures.[27–29] In this paper, we will focus our attention on subwavelength apertures. Such nanostructures present a certain number of advantages. First, they can be fabricated with robust nanofabrication techniques; consequently, the size and shape of the apertures are controlled and reproducible. Second, rigorous simulation algorithms of the electromagnetic properties of apertures are available. The last advantage is linked to the geometry of the aperture: it acts as a small reaction chamber and is a convenient platform that allows highly parallel solution analysis[30,31]—a crucial issue for biological applications.[32,33]

The fluorescence emission of an emitter located inside a nanoaperture may be affected in two ways: (i) by the local enhancement of the excitation intensity, and (ii) by the modification of the electromagnetic environment of the emitter, changing its quantum efficiency and radiation pattern. In both effects, surface plasmons can play a positive role to yield larger fluorescence rates.[13,34] In previous experiments,[28,29] only apertures milled in aluminum films were studied, yet aluminum does not sustain significant plasmonic effects in the visible range. Can we expect an increase of the enhancement factor in the case of a metal supporting strong surface plasmon resonances in the visible range, such as gold? To address this issue, we report in this paper a detailed comparison between the fluorescence emission enhancement factors for two metals: aluminum and gold. We set the excitation wavelength to 633 nm and use Alexa-Fluor 647 as a fluorescent reporter (Alexa-Fluor 647 is a commonly used dye with emission spectrum ranging from 650 to 710 nm and peak emission at 670 nm).

In order to get an accurate estimation of the fluorescence enhancement factor, it is of crucial importance to quantify the total fluorescence intensity *and* the number of emitters. Fluorescence correlation spectroscopy (FCS) is a robust method that answers this issue.[35] FCS provides access to the count rate per molecule, that is, the average number of photons emitted by a *single* fluorescent molecule. In this paper, we use FCS to directly compare the fluorescent enhancement from different nanostructures without making any implicit hypothesis on the number of fluorescent molecules.

The paper is outlined as follows. In Sec. II, we present the materials and methods used throughout the paper. A more detailed presentation of the FCS technique is provided. Experimental results are presented in Sec. III. Section IV is devoted to a discussion of the results and to a comparison with electromagnetic calculations. The respective roles of the reinforcement of the excitation intensity and of the modification of the emission characteristics are also discussed. Finally, in Sec. V, we summarize our conclusions.

II. MATERIALS AND METHODS

Optically thick metallic films (thickness of 200 nm) of gold and aluminum were coated on conventional microscope coverslips (thickness of 150 μm) by thermal evaporation. A 15 nm thick chromium layer ensures adhesion between the gold film and the borosilicate glass substrate. No chromium adhesion layer was used for the aluminum samples. Circular apertures with diameters ranging from 80 to 310 nm were then milled by focused ion beam (FEI Strata DB235, using Ga^+ ions exhibiting a 5 nm nominal beam diameter). A sample aperture milled in a gold film is displayed in the inset of Fig. 1(a).

As discussed above, for a rigorous characterization of the fluorescence enhancement, it is necessary to estimate the number of emitting molecules, motivating the use of the FCS technique. The temporal fluctuations $F(t)$ of the fluorescence signal are recorded, and the autocorrelation of this signal is computed:

$$g^{(2)}(\tau) = \frac{\langle F(t) \cdot F(t+\tau)\rangle}{\langle F(t)\rangle^2}, \tag{1}$$

where $\langle \cdot \rangle$ stands for time averaging. A sample correlogram $g^{(2)}(\tau)$ recorded in a nanoaperture is given in Fig. 1(b). The analysis of the experimental data relies on a numerical fit based on a three-dimensional Brownian diffusion model:

$$g^{(2)}(\tau) = 1 + \frac{1}{N}\left(1 - \frac{\langle B\rangle}{\langle F\rangle}\right)^2 \left[1 + n_T \exp\left(-\frac{\tau}{\tau_{b_T}}\right)\right] \times \frac{1}{(1+\tau/\tau_d)\sqrt{1+s^2\tau/\tau_d}}, \tag{2}$$

where N is the total number of molecules, $\langle F\rangle$ the total signal, $\langle B\rangle$ the background noise, n_T the amplitude of the dark state population, τ_{b_T} the dark state blinking time, τ_d the mean diffusion time, and s the ratio of transversal to axial dimensions of the analysis volume. Note that, strictly speaking, the assumption of a free three-dimensional diffusion model is not fulfilled within an aperture. However, this discrepancy can be taken into account by setting the aspect ratio s as a free parameter: it converges to a value close to unity for each run. It is clear from Fig. 1(b) that this model fits remarkably well the experimental data. From the correlogram and Eq. (2), it is possible to compute the count rate per molecule (i.e., the average number of photons emitted by a single molecule) as $\mathrm{CR} = (\langle F\rangle - \langle B\rangle)/N$. Then, the fluorescence enhancement η is given by the ratio of the count rate per molecule measured in the case of an aperture and in the case of an open solution. We point out that all the presented fluorescence data are spatially averaged over all the possible molecule orientations and positions inside the detection volume.

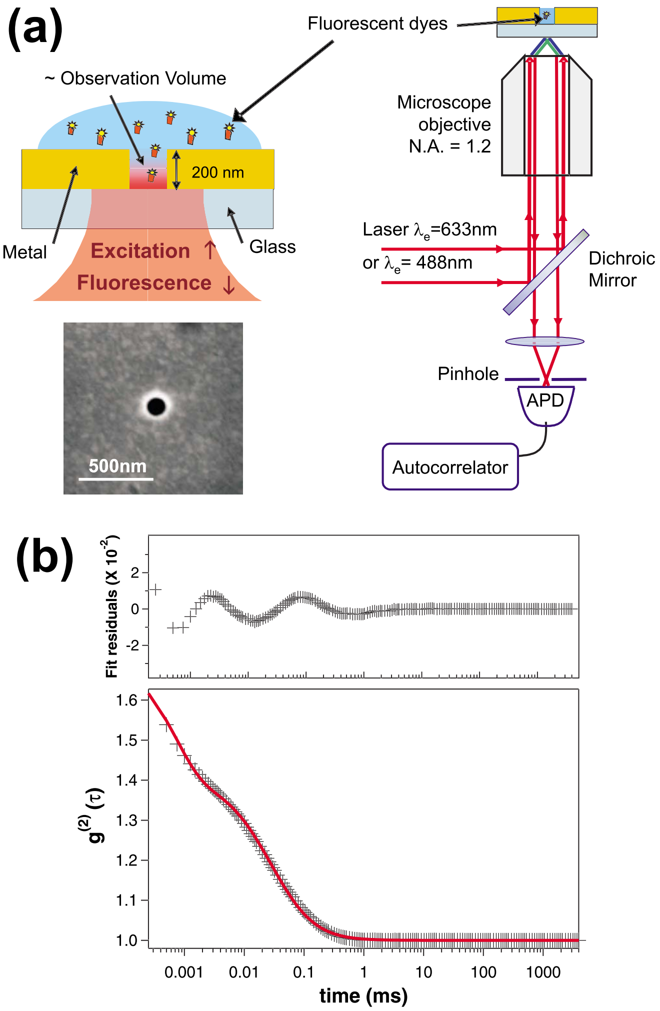

FIG. 1. (Color online) (a) Schematics of the experimental setup (APD, avalanche photodiode). Inset: Micrograph of a single nanoaperture milled in a gold film. (b) Sample correlogram recorded on a nanoaperture: autocorrelation function of the fluorescence emission signal recorded from A647 dyes in a 120 nm circular gold aperture. On the upper part of the graph are plotted the fit residuals.

Our experimental setup has already been presented in Ref. 28, but it is recalled in Fig. 1(a) for completeness. It is based on an inverted microscope (Zeiss Axiovert 35M) with a NA=1.2 water-immersion objective (Zeiss C-Apochromat). For experiments in solution, a 50 μm pinhole defines a three-dimensional detection volume. Nanopositioning of the aperture inside this confocal volume is performed with a multiaxis piezoelectric stage (Polytek PI P527). After the pinhole, the fluorescence signal passes through a 50/50

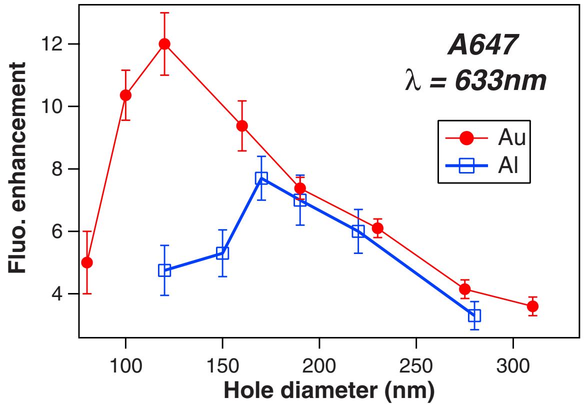

FIG. 2. (Color online) Enhancement factor as a function of the aperture diameter for Alexa-Fluor 647 dyes at $\lambda_e = 633$ nm (excitation power of 40 μW) for nanoapertures milled in aluminum (squares) and gold (circles) films.

beamsplitter and is focused on two avalanche photodiodes (Perkin-Elmer SPCM-AQR-13) with 670 ± 20 nm fluorescence bandpass filters (Omega Filters 670DF40). The fluorescence intensity fluctuations are analyzed by cross correlating the signal of each photodiode with an ALV6000 hardware correlator. This configuration eliminates correlations due to the dead time of the photodiodes (50 ns) and avoids artifacts. Each individual FCS measurement was obtained by averaging ten runs of 10 s duration.

For experiments in apertures, a droplet of solution containing Alexa-Fluor 647 fluorescent molecules (A647) is deposited onto the top of the aperture, with typically micromolar concentration. Note that the droplet acts as a reservoir of "fresh" molecules, which are constantly diffusing from the droplet to the aperture. This strongly limits photobleaching effects. Let us also emphasize that in all the following experiments, the signal-to-noise ratio was kept at values better than 10.

III. EXPERIMENTAL RESULTS

A. Fluorescence rate enhancement

We have measured the fluorescence count rate enhancement factor η as a function of the diameter of the aperture for two sets of apertures: the first set milled in an aluminum film, and the other set milled in gold (Fig. 2). The excitation wavelength is set to $\lambda_e = 633$ nm. We stress that all the values of η presented in Fig. 2 have been measured at low excitation intensity (40 μW) to ensure that the dyes are well below saturation. Both curves have a similar shape: starting from relatively low (~4) enhancement factors for small apertures, the curves quickly rise to a maximum and then decrease for larger aperture diameters. However, regardless of the aperture size, gold always gives a higher enhancement than aluminum. Most interestingly, it reaches a maximum value that is 55% higher than the value observed for aluminum ($\eta_{\max} \sim 12$ for gold and $\eta_{\max} \sim 7.7$ for aluminum). It should also be noted that the optimal diameter is shifted towards significantly smaller hole sizes for gold (120 nm) compared to aluminum (170 nm). The physics behind this behavior will be discussed in Sec. IV. It can, however, already be concluded that working with apertures milled in gold rather than aluminum brings two advantages. First, the fluorescence emission enhancement factor is significantly higher. Second, it allows us to work at smaller diameters and, consequently, at higher concentrations while keeping single molecule resolution.

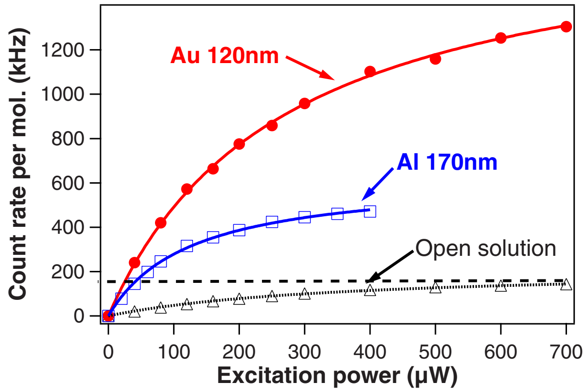

FIG. 3. (Color online) Count rate per molecule as a function of the excitation power at $\lambda_e = 633$ nm, for A647 dyes diffusing in a 120 nm diameter aperture in a gold film (circles), in a 170 nm diameter aperture in aluminum (squares), or in open solution (triangles). Solid lines are numerical fits by a three-level system (see text). Fitting parameters are for open solution, $A = 0.6$ kHz/μW and $I_s = 390$ μW; for aluminum, $A = 5.0$ kHz/μW and $I_s = 130$ μW; and for gold, $A = 6.8$ kHz/μW and $I_s = 260$ μW.

Nanoapertures allow for high count rates per molecule, even at moderate incoming excitation powers. We have performed a set of measurements of the count rate per molecule while increasing the excitation power. Please note that special care has been taken to characterize the level of background noise and the dark state fraction n_T for each excitation power. Results are presented in Fig. 3, in the case of an open solution and in the case of apertures milled in gold or aluminum. For aluminum, we limited the excitation power to 400 μW to avoid damaging the sample, as aluminum has a damage threshold about ten times lower than gold. Without the nanostructure, the count rates are limited to values below 180 000 counts per second (cps) per molecule (horizontal line in Fig. 3). In contrast, a striking count rate better than 1 200 000 cps/molecule is obtained in the nanoaperture milled in gold at high excitation power. For aluminum, the maximum rate reaches about 400 000 cps/molecule. Therefore, at fluorescence saturation, a three times higher count rate per molecule can be extracted in gold apertures as compared to aluminum.

To model this experimental data, we use the standard expression of the fluorescence rate of a three level system summarized by $F = A\frac{I_e}{1+Ie/I_s}$, where I_e is the excitation intensity, I_s is the saturation intensity, and A is a constant proportional to the dye absorption cross section, its quantum yield, and the setup collection efficiency.[35] Good agreement between this model and the experimental data is found. This analysis brings some insights in the photokinetic rate enhancements induced by the nanostructure, as we will discuss in Sec. IV. Before we move on to that discussion, we describe further experimental investigations towards alterations of the spectrum and directivity of the detected fluorescence beam.

B. Spectral analysis

When an emitter is placed near an arbitrary object or inside a cavity, its emission spectrum may be altered.[26,39] The data reported in Fig. 2 correspond to a spectral integration from 650 to 690 nm, which covers most of the dye emission spectrum but prevents any indirect observation of an alteration of the emission spectrum. To detail the fluorescence spectrum, we first performed a FCS measurement to quantify the average number of molecules inside the nanoaperture. Then, with a flipping mirror, the fluorescence beam was sent to a spectrograph (Jobin-Yvon SPEX 270M) equipped with a nitrogen-cooled charge coupled device (CCD) detector. The raw spectrum is eventually normalized by the number of molecules given by FCS. This procedure allows us to directly compare the intensities obtained *per single molecule* for different aperture sizes.

Normalized fluorescence spectra per A647 molecule measured in open solution and on several apertures in a gold film are presented in Fig. 4(a). The detected count rate per molecule is significantly enhanced over the whole A647 emission spectrum, with a maximum enhancement for 120 nm diameter apertures, as observed in FCS. Interestingly, the shapes of the spectra do not change noticeably between open solution and the different apertures. The same behavior has been observed for apertures in aluminum (data not shown). In Fig. 4(b), we plot the spectrally dependent enhancement factor (that is, the ratio of the spectrum recorded for an aperture by the reference spectrum in open solution). Within the range of 650–690 nm, the apparent value of η slightly increases with the wavelength, showing a higher enhancement for redshifted wavelengths. Our data also indicate that the optimal emission wavelength yielding the larger enhancement tends to be redshifted while increasing the aperture size, hereby confirming an intuitively expected scaling effect.

As already pointed out for nanoaperture arrays,[26] no direct correlation can be found between the white light transmission through the aperture and the fluorescence spectra. In the case of our study, we point out that white light transmission measurements through a single aperture of diameter 120–300 nm yielded transmission curves almost flat over the 650–710 nm spectral range covered by the dye emission. This range, therefore, seems too narrow to monitor any clear spectral link between white light transmission and fluorescence.

C. Fluorescence radiation pattern

A nanoaperture may strongly modify the radiation pattern of emitters placed inside it. For instance, Lezec *et al.*[4] have reported an unusual "beaming" effect in the transmitted light from nanoapertures decorated with a periodic set of grooves. In our case, a beaming effect—by concentrating light in a reduced emission cone[36,37]—would increase the molecular detection efficiency and, thus, the enhancement factors exhibited by gold and aluminum. In order to check experimentally the directivity of the fluorescence emission, we have modified our setup to image the microscope objective back focal plane on a CCD camera equipped with fluorescence filters.[38] This configuration allows us to directly monitor the fluorescence radiation pattern from an aperture. It should be emphasized that the numerical aperture of the microscope objective limits the collection to a cone of 64° half-angle. We present in Fig. 5 pictures of the A647 fluorescence beam from a 130 nm diameter hole milled in gold and a 170 nm hole milled in aluminum—these diameters correspond to the maximum enhancement factors. In both cases, the dye's emission fills the back aperture of the microscope objective. Within the collection angle of the microscope, we could not detect any clear effect.

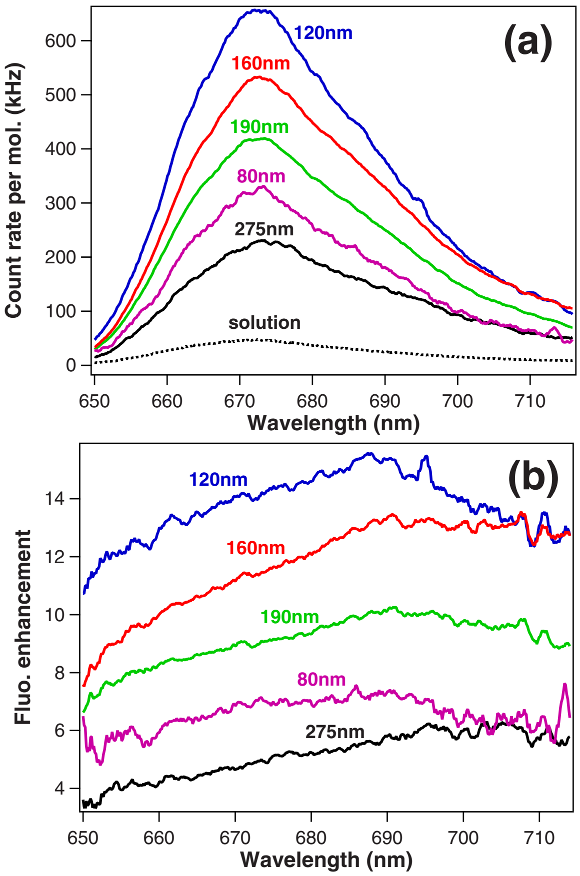

FIG. 4. (Color online) Spectral analysis of the fluorescence enhancement for A647 dyes diffusing in apertures milled in a gold film. (a) Integrated count rate per molecule vs emission wavelength, for a 10 s acquisition time. (b) Fluorescence enhancement factor vs emission wavelength.

According to recent calculations,[40] the far-field directivity of the beam transmitted through a single subwavelength aperture is highly dependent on the hole size and on the permittivity of the material surrounding the aperture. The directivity of the beam tends to increase when the modulus of the permittivity decreases and when the aperture size increases. In the case of Fig. 5, gold has a lower permittivity than aluminum, but the hole milled in gold is smaller than the one

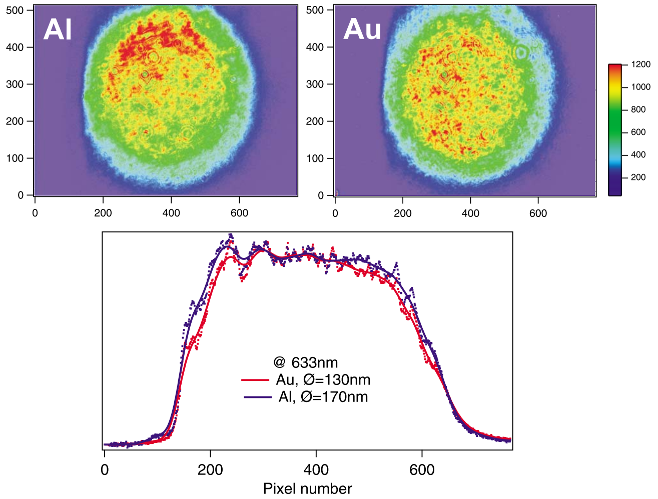

FIG. 5. (Color online) Images of the fluorescence emission beam in the microscope objective back focal plane. Up: CCD pictures of the beam emitted from a 170 nm hole milled in aluminum and a 130 nm hole milled in gold. Bottom: Line cuts of these pictures along a horizontal line (dots, raw experimental data; solid lines, smoothing of the raw data).

milled in the aluminum film. Altogether, the competition between these two effects leads to a similar far-field directivity for both apertures.

IV. DISCUSSION

A natural question while comparing the properties of gold versus aluminum apertures addresses the origin of the higher fluorescence count rates observed for gold. As stated in the Introduction, the fluorescence enhancement observed in Fig. 2 can be induced by a locally increased excitation intensity, by a larger quantum efficiency of the emitter (increased radiative rate vs nonradiative decays), and by a better collection of the emitted light within the objective's numerical aperture. For this last effect, our measurements of the fluorescence radiation pattern indicate that both metals show a similar behavior, with almost identical collection efficiencies. This invalidates any beaming effect linked with gold.

The trends shown by the molecular count rate versus the excitation power yield more insights. At saturation, the fluorescence rate is proportional to the radiative rate and no longer depends on the excitation rate. Therefore, the behavior seen in Fig. 3 for excitation powers above 300 μW shows a net enhancement of the radiative rate for gold apertures versus aluminum. Numerical fitting of the data displayed in Fig. 3 indicates a gain in emission of 7.8 for gold and 2.8 for aluminum. We, thus, conclude that a metal holding plasmonic resonances in the visible range allows for higher emission rates, even if the emission spectra are not significantly modified by the nanostructure.

Things get more intricate at low excitation powers (well below fluorescence saturation), as the fluorescence signal is proportional to the quantum yield of the dye and the excitation power. Previous theoretical analysis on aluminum apertures has shown that excitation enhancement played a critical role in the overall fluorescence gain.[5] From an experimental point of view, it is extremely difficult to estimate the relative weight of the contributions from the excitation and quantum yield. Therefore, we conducted a numerical analysis based on the finite element method using COMSOL MULTIPHYSICS version 3.3.[42] The size of the computational space is $1.0\times1.0\times1.1$ μm^3, with radiation boundary conditions on all six faces. A quartz substrate is assumed, on top of which a 200 nm thick layer of gold or aluminum is placed, the upper region being water. Dielectric properties of gold and aluminum are incorporated via the complex dielectric constant, as measured by spectroscopic ellipsometry from 300 to 1600 nm.[42] A single nanoaperture is placed in the center of the metal layer. To simplify the numerical computations, we restricted the observation area to a plane 15 nm inside the aperture. This provides the trends for the relative contribution of emission and excitation, and avoids normalization issues over the entire aperture volume. Quantitative comparison between experimental data and numerical computations integrated over the entire aperture volume will form the basis of a future communication.

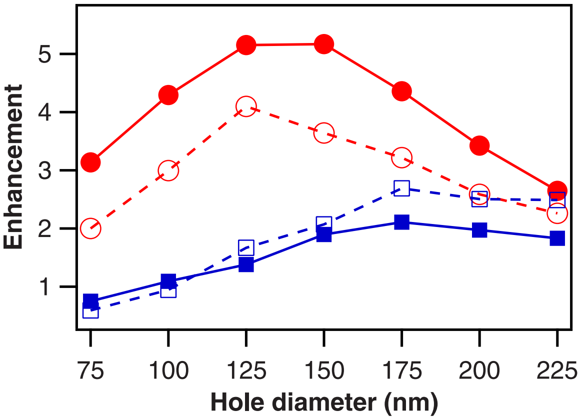

FIG. 6. (Color online) Enhancement factors versus the aperture diameter computed by the finite element method and averaged over a plane 15 nm inside the aperture. Circles refer to gold, squares to aluminum. Empty markers denote excitation gains, filled markers stand for emission.

To estimate the increase of the excitation intensity over the nanoaperture, a plane wave at 633 nm is launched 500 nm below the structure, incoming from the glass side. Light intensity is measured and averaged over the plane 15 nm inside the aperture. This result is then normalized by the integrated intensity within the same surface with no metal layer. Results for gold and aluminum films are displayed in Fig. 6 versus the aperture diameter (empty markers). These curves are qualitatively consistent with the experimental data found in Fig. 2, and show a remarkable agreement with the aperture diameters found for maximum fluorescence enhancement. A clear increase of the excitation intensity is found to occur inside the aperture for a diameter below the half-wavelength as already known from Ref. 5. Remarkably, the averaged excitation intensity is about 40% higher for a 120 nm aperture in gold as compared to a 170 nm aperture in aluminum (comparable to 55% observed experimentally). This factor directly contributes to the better fluorescence enhancement measured for gold apertures at low excitation powers.

For the emission calculations, a 1 nm dipole is positioned at various locations in the plane 15 nm inside the aperture. The radiative emission is estimated from the quartz side by integrating the z component of Poynting vectors across a plane located 20 nm below the metal surface. This power is then compared to the emission in the absence of the nanoaperture. Calculations are performed for x, y, and z dipole orientations, and the reported radiative enhancement is an average for these orientations. Figure 6 displays the emission enhancement factors versus the aperture diameters for gold and aluminum films (filled markers). A clear effect is seen between gold and aluminum, with 2.5 times more favorable emission enhancement in the case of gold. This is fully consistent with the higher count rates observed for gold at fluorescence saturation (a factor of 2.8 experimental). This factor is also in agreement with the two times larger saturation intensity found for gold in Fig. 3 (the saturation intensity is proportional to the ratio of the total decay rate to the excitation cross section, hereby indicating a larger increase of decay rate than excitation power when comparing gold to aluminum). At low excitation powers (below fluorescence saturation), the gain due to emission in the overall detected signal is lower, as it depends on the fluorophore quantum yield which interplays radiative and nonradiative rates. Starting from the gain in emission rate presented in Fig. 6 and given the quantum yield of A647 in solution of 30%, we infer a maximum quantum yield of 70% for A647 in a 120 nm gold aperture, and 50% for A647 in a 170 nm aluminum aperture. Therefore, the relative difference between the quantum yield gains for gold and aluminum is estimated to be about 40%. Again, this factor directly contributes to the better fluorescence enhancement obtained for gold apertures.

To predict the optimal diameter for aperture-enhanced fluorescence, we computed the propagation constant γ of the fundamental guided mode inside an infinitely long cylindrical aperture as a function of the aperture diameter (Fig. 7). The inner medium was taken to be water (refractive index of 1.33). The computation is based on the differential method written in a cylindrical geometry.[41] γ is defined as $\gamma = k_z / k_0$, where $k_0 = 2\pi/\lambda$. For apertures through a perfectly conducting metal, the cutoff is defined as the size of the aperture where the real part of the propagation constant γ vanishes. If the aperture is smaller than the cutoff, γ becomes imaginary and no propagative guided mode exists. Moreover, at the cutoff, the group velocity v_g equals zero. In the presence of absorption, γ becomes complex valued and, strictly speaking, there is no cutoff as the propagation constant never equals zero. A cutoff can still be defined, though. Following the intuitive definition of Baida *et al.*,[11] we define the cutoff as the size where the imaginary part of γ becomes higher than its real part: this corresponds to the crossing point of the curves plotted in Fig. 7. The corresponding position is shown in Fig. 7 as vertical dashed lines. Also indicated with arrows in Fig. 7 is the position of the maximum fluorescence emission enhancement $\eta_{\max}$ (taken from Fig. 2). Surprisingly, the optimum diameter for fluorescence enhancement falls about 50 nm below the intuitive cutoff diameter. To clarify this discrepancy, it should be stressed that for absorbing materials, the crossing between the real and imaginary parts of γ does not correspond anymore to a zero group velocity. For a real metal, v_g never vanishes, but passes through a minimum when the real part of γ is minimum. This corresponds to a maximum of the photonic density of modes.[43] This point is shown in Fig. 7 as a black dot. It appears that the observed position of $\eta_{\max}$ is very close to the position of the minimum group velocity. Therefore, we relate the maximum field enhancement inside the aperture to a maximum density of photonic modes and to a minimum group velocity. The significant shift of the optimum diameter as compared to the intuitive position of the cutoff has to be considered while designing nanoapertures for optimized single-molecule analysis.

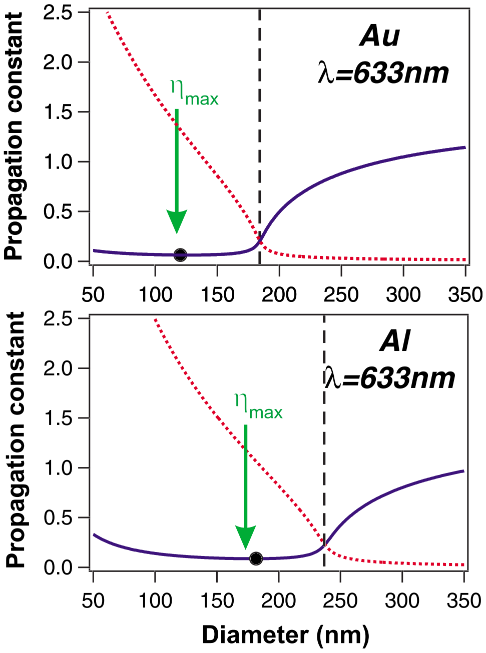

FIG. 7. (Color online) Propagation constant γ of the fundamental guided mode inside the aperture vs aperture diameter for gold and aluminum films, the aperture being filled with water. Solid line, real part of γ; dotted line, imaginary part of γ. The vertical dashed lines show the intuitive position of the cutoff, the arrows indicate the position of the observed maximum enhancement factor $\eta_{\max}$, and the dots show the position of the minimum group velocity [minimum value of Re(γ)].

As a final test experiment, we have performed measurements for gold apertures at $\lambda_e = 488$ nm excitation wavelength, using Rhodamine6G as a fluorescent molecule (Fig. 8). In this case, a rather low enhancement factor is found ($\eta \sim 2.5$) that only weakly depends on the aperture size. To understand these results, one has to recall that at this excitation wavelength, gold behaves more like a highly absorbing dielectric than like a metal. On the other hand, detection was performed in the range of 550–590 nm, where gold has a strong metallic behavior. Using the same experimental conditions, apertures milled in aluminum were shown to yield larger enhancement factors.[28] The inset of Fig. 8 presents the calculated propagation constants for the corresponding apertures: there is no cutoff as the real part of γ never approaches zero. Therefore, the group velocity never reaches low values.

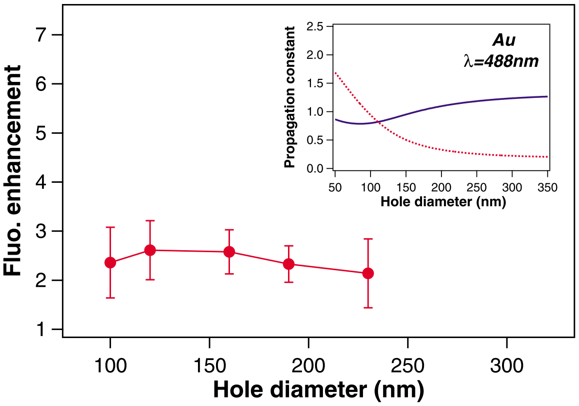

FIG. 8. (Color online) Enhancement factor as a function of the aperture diameter for Rhodamine 6G dyes excited at $\lambda_e = 488$ nm for nanoapertures milled in a gold film. Inset: Calculated propagation constant γ of the fundamental guided mode inside the gold aperture (solid, real part; dots, imaginary part).

This demonstrates the crucial importance of milling the nanoaperture in a material that exhibits a strong metallic character at the excitation wavelength. The strong electromagnetic field confinement induced by the metallic nanocavity is confirmed to be a key factor in the aperture-enhanced fluorescence process.

V. CONCLUSION

Using fluorescence correlation spectroscopy, we have rigorously characterized the fluorescence emission enhancement factors η for dyes freely diffusing in nanometric apertures milled in gold and aluminum films. We have observed that apertures milled in gold exhibit significantly higher fluorescence enhancement factors than apertures milled in aluminum. We demonstrate that the higher value of η for gold is related to a larger enhancement of the excitation intensity and radiative rate. The maximum enhancement for gold also occurs at a smaller aperture diameter, which is beneficial for single-molecule detection at high concentrations. Moreover, the enhancement covers the entire emission spectrum of the dye and shows only slight spectral variations. We have shown that the maximum value of η is obtained when the group velocity of the guided mode inside the aperture is close to zero, that is, when the photonic density of modes is maximum. This diameter is significantly shifted (up to 50 nm) as compared to the intuitive position of the cutoff of the fundamental guided mode. This effect has to be taken into account while designing nanoapertures for high-efficiency single-molecule analysis. Let us finally emphasize that nanoapertures, in spite of their conceptual simplicity, demonstrate unique and appealing properties for controlling fluorescence emission. These properties are of great interest to increase the effectiveness of fluorescence-based techniques.

ACKNOWLEDGMENTS

This work has been funded by Grant No. ANR-05-PNANO-035-01 “COEXUS” of the French National Research Agency. F.M. and S.B. were supported in part by National Science Foundation Grants No. ECS-0622225 and No. ECS-0637121.

---

[1] H. G. Bethe, Phys. Rev. **66**, 163 (1944).
[2] T. W. Ebbesen, H. J. Lezec, H. F. Ghaemi, T. Thio, and P. A. Wolff, Nature (London) **391**, 667 (1998).
[3] J. A. Porto, F. J. Garcia-Vidal, and J. B. Pendry, Phys. Rev. Lett. **83**, 2845 (1999).
[4] H. J. Lezec, A. Degiron, E. Devaux, R. A. Linke, L. Martin-Moreno, F. J. Garcia-Vidal, and T. W. Ebbesen, Science **297**, 820 (1998).
[5] E. Popov, M. Nevière, J. Wenger, P.-F. Lenne, H. Rigneault, P. Chaumet, N. Bonod, J. Dintinger, and T. W. Ebbesen, J. Opt. Soc. Am. A **23**, 2342 (2006).
[6] A. Naber, D. Molenda, U. C. Fischer, H.-J. Maas, C. Höppener, N. Lu, and H. Fuchs, Phys. Rev. Lett. **89**, 210801 (2002).
[7] C. Genet and T. W. Ebbesen, Nature (London) **445**, 39 (2007).
[8] H. Shin, P. B. Catrysse, and S. Fan, Phys. Rev. B **72**, 085436 (2005).
[9] M. Bai and N. Garcia, Appl. Phys. Lett. **89**, 141110 (2006).
[10] F. J. García-Vidal, L. Martin-Moreno, E. Moreno, L. K. S. Kumar, and R. Gordon, Phys. Rev. B **74**, 153411 (2006).
[11] F. I. Baida, A. Belkhir, D. Van Labeke, and O. Lamrous, Phys. Rev. B **74**, 205419 (2006).
[12] S. Collin, F. Pardo, and J.-L. Pelouard, Opt. Express **15**, 4310 (2007).
[13] J. R. Lakowicz, Anal. Biochem. **337**, 171 (2005).
[14] P. Anger, P. Bharadwaj, and L. Novotny, Phys. Rev. Lett. **96**, 113002 (2006).
[15] S. Kühn, U. Håkanson, L. Rogobete, and V. Sandoghdar, Phys. Rev. Lett. **97**, 017402 (2006).
[16] F. Tam, G. P. Goodrich, B. R. Johnson, and N. J. Halas, Nano Lett. **7**, 496 (2007).
[17] Y. Chen, K. Munechika, and D. S. Ginger, Nano Lett. **7**, 690 (2007).
[18] J. S. Biteen, L. A. Sweatlock, H. Mertens, N. S. Lewis, A. Polman, and H. A. Atwater, J. Phys. Chem. C **111**, 13372 (2007).
[19] P. Bharadwaj and L. Novotny, Opt. Express **15**, 14266 (2007).
[20] J. S. Biteen, D. Pacifici, N. S. Lewis, and H. A. Atwater, Nano Lett. **5**, 1768 (2005).
[21] G. L. Liu, J. Kim, and L. P. Lee, Appl. Phys. Lett. **89**, 241118 (2006).
[22] Y. Liu and S. Blair, Opt. Lett. **28**, 507 (2003).
[23] A. G. Brolo, S. C. Kwok, M. D. Cooper, M. G. Moffitt, C.-W. Wang, R. Gordon, J. Riordon, and K. L. Kavanagh, J. Phys. Chem. B **110**, 8307 (2006).
[24] Y.-J. Hung, I. I. Smolyaninov, C. C. Davis, and H.-C. Wu, Opt. Express **14**, 10825 (2006).
[25] G. Sun, J. B. Khurgin, and R. A. Soref, Appl. Phys. Lett. **90**,

111107 (2007).

[26] J. H. Kim and P. J. Moyer, Appl. Phys. Lett. **90**, 131111 (2007).

[27] U. C. Fischer, J. Opt. Soc. Am. B **3**, 1239 (1986).

[28] H. Rigneault, J. Capoulade, J. Dintinger, J. Wenger, N. Bonod, E. Popov, T. W. Ebbesen, and P.-F. Lenne, Phys. Rev. Lett. **95**, 117401 (2005).

[29] J. Wenger, B. Cluzel, J. Dintinger, N. Bonod, A.-L. Fehrembach, E. Popov, P.-F. Lenne, T. W. Ebbesen, and H. Rigneault, J. Phys. Chem. C **111**, 11469 (2007).

[30] M. J. Levene, J. Korlach, S. W. Turner, M. Foquet, H. G. Craighead, and W. W. Webb, Science **299**, 682 (2003).

[31] K. T. Samiee, M. Foquet, L. Guo, E. C. Cox, and H. G. Craighead, Biophys. J. **88**, 2145 (2005).

[32] H. G. Craighead, Nature (London) **442**, 387 (2006).

[33] J. T. Mannion and H. G. Craighead, Biopolymers **85**, 131 (2006).

[34] W. L. Barnes, J. Mod. Opt. **45**, 661 (1998).

[35] *Fluorescence Correlation Spectroscopy: Theory and Applications*, edited by R. Rigler and E. L. Elson (Springer-Verlag, Berlin, 2001).

[36] C. Obermüller and K. Karrai, Appl. Phys. Lett. **67**, 3408 (1995).

[37] A. Degiron, H. J. Lezec, N. Yamamoto, and T. W. Ebbesen, Opt. Commun. **239**, 61 (2004).

[38] L. Dai, I. Gregor, I. von der Hocht, T. Ruckstuhl, and J. Enderlein, Opt. Express **13**, 9409 (2005).

[39] F. Bordas, N. Louvion, S. Callard, P. C. Chaumet, and A. Rahmani, Phys. Rev. E **73**, 056601 (2006).

[40] E. Popov, M. Nevière, A. Sentenac, N. Bonod, A.-L. Fehrembach, J. Wenger, P.-F. Lenne, and H. Rigneault, J. Opt. Soc. Am. A **24**, 339 (2007).

[41] N. Bonod, E. Popov, and M. Nevière, J. Opt. Soc. Am. A **22**, 481 (2005).

[42] F. Mahdavi, Y. Liu, and S. Blair, Plasmonics **2**, 129 (2007).

[43] *Nanophotonics*, edited by H. Rigneault, J.-M. Lourtioz, C. Delalande, and A. J. Levenson (ISTE, London, 2006).

Chapitre 2

Nano-Ouvertures Métalliques Avec Corrugations

Détecter une molécule unique est une tâche difficile, en raison de la très faible quantité de lumière émise. Pour intensifier et contrôler la lumière émise par une seule molécule, nous utilisons des antennes métalliques de dimensions nanométriques, qui fonctionnent pour la lumière comme les antennes conventionnelles avec les ondes radio. La nanoantenne est formée d'une ouverture percée dans un film d'or, l'ouverture étant entourée de corrugations en sillons circulaires (figure 2.1 a et b).

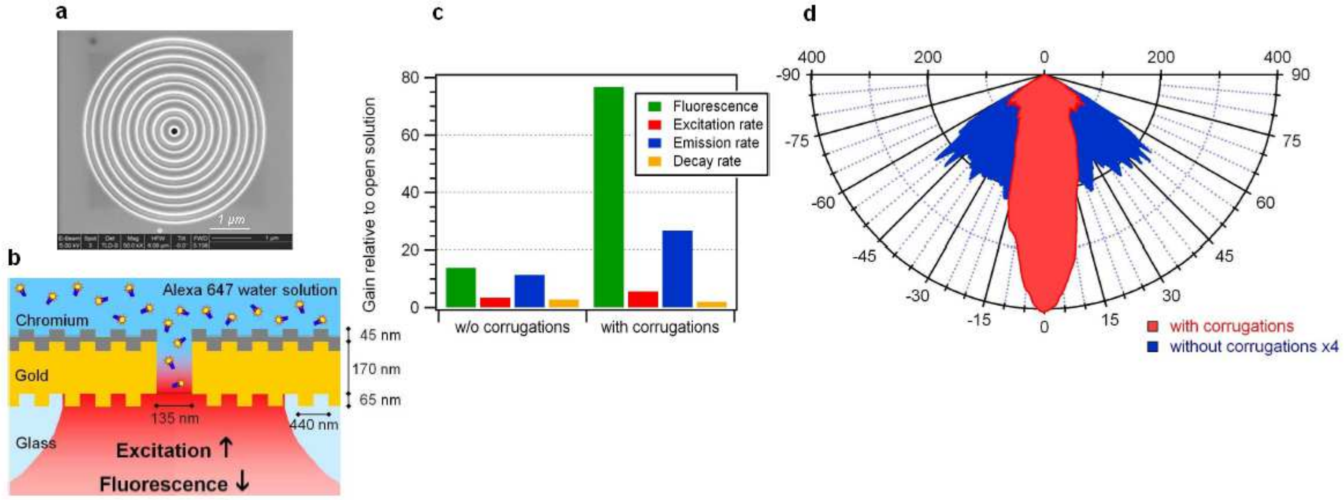

Fig. 2.1. (a) Nanouverture entourée de 5 corrugations circulaires. (b) Configuration expérimentale. (c) Facteurs d'exaltations mesurés. (d) Diagramme de rayonnement normalisé par émetteur.

Cette antenne formée d'une ouverture corruguée transforme une molécule standard en une source de lumière intense et uni-directionnelle [1] : l'intensité de fluorescence est augmentée de 75 fois, et quasiment toute la lumière est émise dans un cône dont la largeur angulaire peut être inférieure à 10° (figure 2.1 c et d). Les détails expérimentaux sont indiqués dans l'article publié dans Nano Letters et inclus ci-après (ainsi que ses suppléments d'information). L'intensité lumineuse et la direction d'émission sont contrôlées simultanément à l'échelle d'une molécule unique, ce qui constitue une première mondiale.

---

[1] H. Aouani, et al, Bright unidirectional fluorescence emission of molecules in a nanoaperture with plasmonic corrugations, Nano Lett. 11, 637-644 (2011).

L’étude du diagramme de rayonnement de molécules individuelles placées dans des nanoouvertures avec corrugations a été poussée plus loin en étudiant notamment l’influence de la phase entre le rayonnement de fluorescence émis directement depuis la nanoouverture, et le rayonnement de fluorescence diffusé par les corrugations [2]. Cette différence de phase est contrôlée expérimentalement lors de la fabrication des échantillons en réglant la distance entre l’ouverture centrale et la première corrugation. Nous avons montré que l’émission dans la direction normale à l’échantillon est maximale lorsque ces rayonnements sont en phase, et que l’émission présente un creux lorsque les rayonnements sont en opposition de phase. Ceci constitue une démonstration claire de l’origine par interférences de la directivité d’une antenne plasmonique munie des sources fluorescentes.

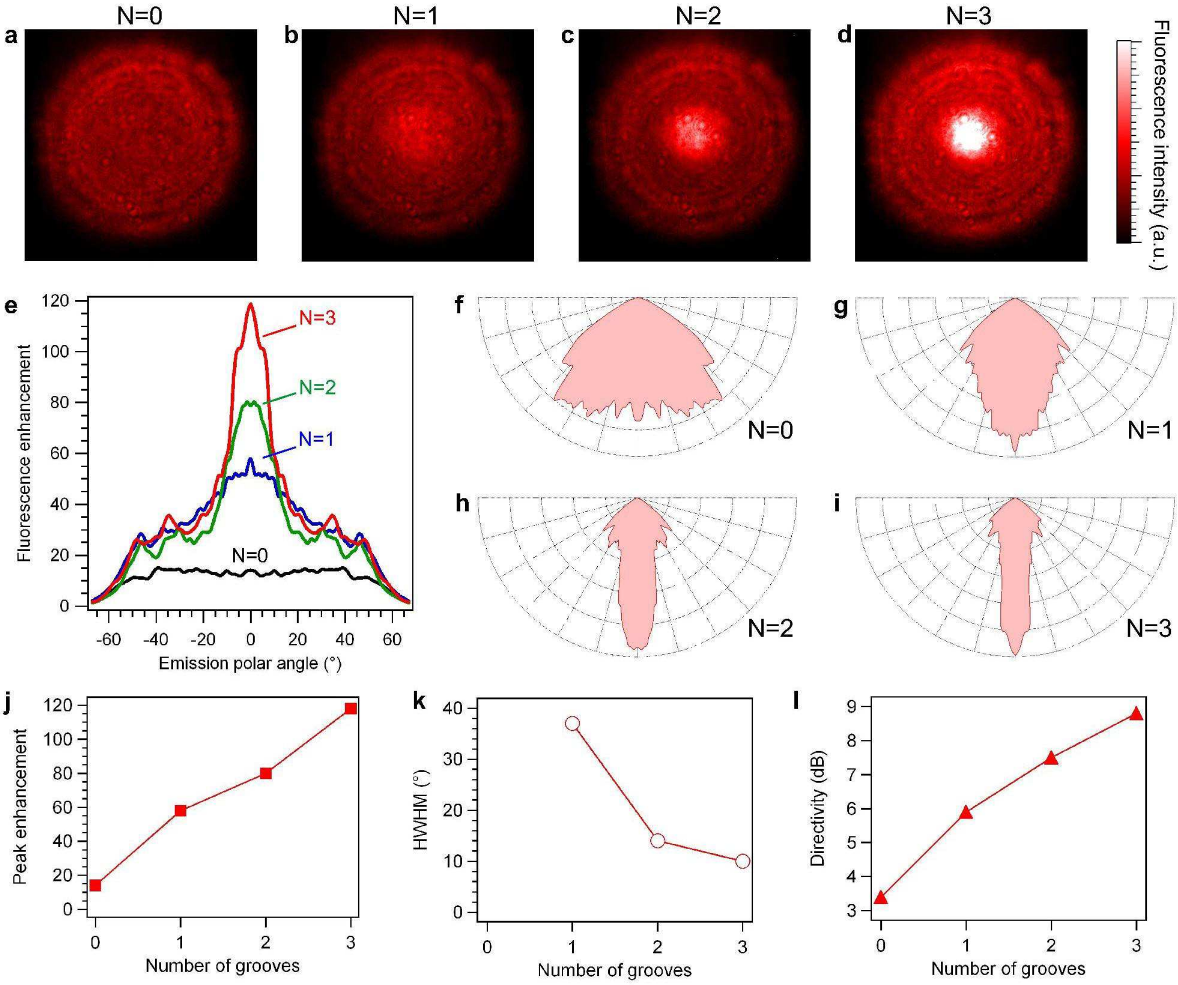

Fig. 2.2. Cas où la distance ouverture –première corrugation est multiple de la longueur d’onde (émission en phase à 0°). (a-d) Images dans le plan focal arrière de l’objectif (plan de Fourier), ici N désigne le nombre de corrugations cirulaires entourant l’ouverture centrale. (e) Facteur d’exaltation de fluorescence en fonction de l’angle d’émission et du nombre de corrugations. (f-i) diagramme polaire

---

[2] H. Aouani, et al, Plasmonic antennas for directional sorting of fluorescence emission, Nano Lett. 11, 2400-2406 (2011).

de rayonnement pour les différentes antennes. (j) Facteur d'exaltation au pic d'émission angulaire. (k) Demi-largeur angulaire d'émission. (l) Directivité IEEE de l'antenne en fonction du nombre de corrugations circulaires.

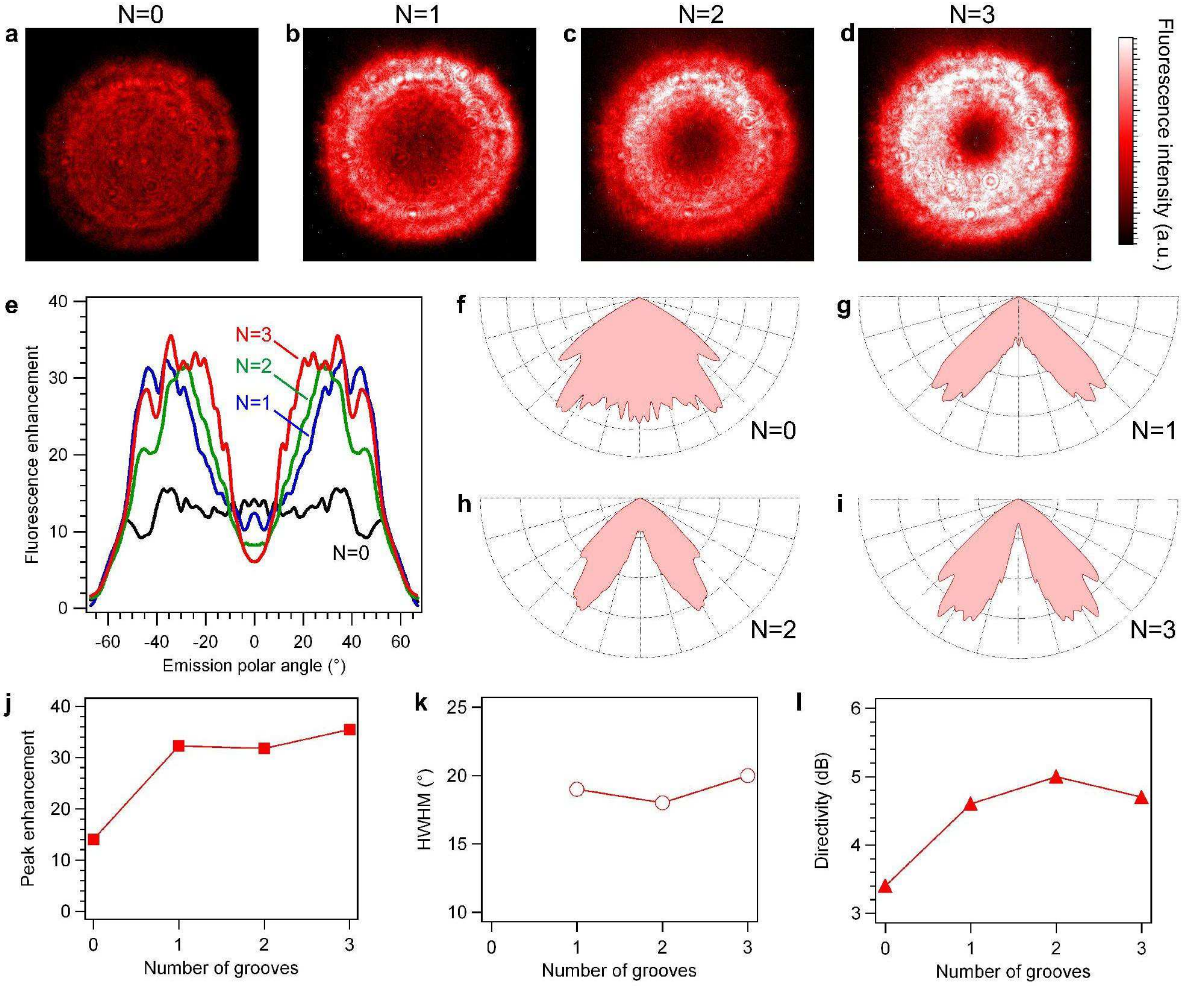

Fig. 2.3. Cas où la distance ouverture –première corrugation est multiple impair de la demi longueur d'onde (émission en opposition de phase à 0°). (a-d) Images dans le plan focal arrière de l'objectif (plan de Fourier), ici N désigne le nombre de corrugations cirulaires entourant l'ouverture centrale. (e) Facteur d'exaltation de fluorescence en fonction de l'angle d'émission et du nombre de corrugations. (f-i) diagramme polaire de rayonnement pour les différentes antennes. (j) Facteur d'exaltation au pic d'émission angulaire. (k) Demi-largeur angulaire d'émission. (l) Directivité IEEE de l'antenne en fonction du nombre de corrugations circulaires.

Les propriétés d'émission directive ont été étudiées en fonction du nombre de corrugations circulaires entourant l'ouverture centrale (figures 2.2 et 2.3). En particulier, nous montrons qu'un nombre de deux ou trois corrugations est un excellent compromis entre exaltation et complexité de réalisation [3]. Ces travaux quantifient également pour la première fois la caractéristique de directivité de l'antenne et son évolution en fonction des paramètres de design de l'antenne (voir les figures 2.2 l et 2.3 l).

En particulier, nous montrons qu'une seule corrugation apporte un gain supplémentaire d'un facteur 2.5x par rapport à une ouverture sans corrugation [3]. Ceci constitue la première démonstration du phénomène prédit numériquement dans la référence [4]. Cet effet montre le couplage plasmonique obtenu entre la corrugation (canal de forme coaxiale) et l'ouverture centrale. Il ouvre des perspectives nouvelles pour augmenter l'interaction entre les modes de plasmons de surface et la nano-ouverture (un brevet a été déposé sur cette thématique).

Le contrôle de la directivité a permis de démontrer la première séparation angulaire de photons de fluorescence spectralement distincts directement au niveau de la nanoantenne, donc dans un dispositif de nanophotonique intégré (figure 2.4). Le contrôle simultané de l'intensité et de la directivité permet la détection efficace de molécules uniques avec un microscope de faible complexité. Cette démonstration est une étape importante pour le développement de nouvelles méthodes d'analyse biochimique, les nanosources de lumière et le traitement de l'information quantique.

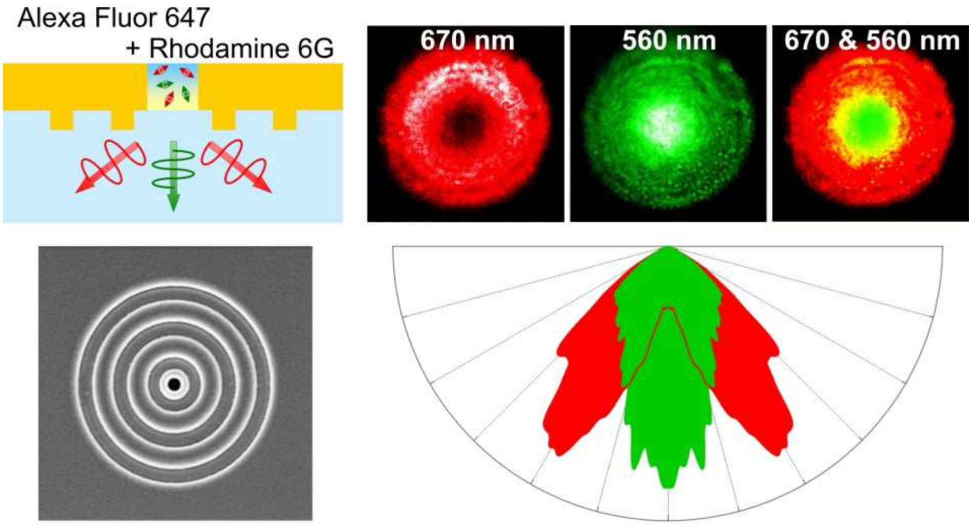

Fig. 2.4. Nanouverture entourée de deux corrugations circulaires, optimisée pour une émission de fluorescence centrée autour de +/- 30° pour une longueur d'onde de 670nm (molécule Alexa Fluor 647). La fluorescence de molécules de Rhodamine 6G centrée autour de 560nm est émise dans une direction normale à l'antenne.

---

[3] H. Aouani, et al, Large molecular fluorescence enhancement by a nanoaperture with plasmonic corrugations, Opt. Express 19, 13056-13062 (2011).

[4] N. Bonod, et al, Field enhancement in a circular aperture surrounded by a single channel groove, Opt. Express 16, 2276-2287 (2008).

NANO LETTERS
LETTER
pubs.acs.org/NanoLett

Bright Unidirectional Fluorescence Emission of Molecules in a Nanoaperture with Plasmonic Corrugations

Heykel Aouani,[†] Oussama Mahboub,[‡] Nicolas Bonod,[†] Eloïse Devaux,[‡] Evgeny Popov,[†] Hervé Rigneault,[†] Thomas W. Ebbesen,[‡] and Jérôme Wenger*[,†]

[†]Institut Fresnel, Aix-Marseille Université, CNRS, Ecole Centrale Marseille, Campus de St Jérôme, 13397 Marseille, France
[‡]Institut de Science et d'Ingénierie Supramoléculaires, Université de Strasbourg, CNRS, 8 allée G. Monge, 67000 Strasbourg, France

S *Supporting Information*

ABSTRACT: Controlling the fluorescence emission from nanoscale quantum emitters is a key element for a wide range of applications, from efficient analytical sensing to quantum information processing. Enhancing the fluorescence intensity and narrowing the emission directivity are both essential features to achieve a full control of fluorescence, yet this is rarely obtained simultaneously with optical nanoantennas. Here we report that gold nanoapertures surrounded by periodic corrugations transform standard fluorescent molecules into bright unidirectional sources. We obtain enhancement factors of the fluorescence count rate per molecule up to 120 fold simultaneously with a directional emission of the fluorescence into a narrow angular cone in the direction normal to the sample plane. The bright emission and narrow directionality enable the detection of single molecules with a low numerical aperture objective, and improve the effectiveness of fluorescence-based applications. We thoroughly quantify the increased light-matter coupling as well as the radiation pattern intensity. These results are highly relevant for the development of single molecule sensing, single-photon sources, and light emitting devices.

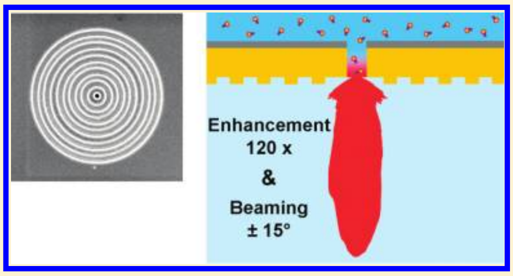

KEYWORDS: Plasmonics, nanoantennas, metal nanoapertures, fluorescence enhancement, fluorescence correlation spectroscopy, nanofabrication

Efficiently detecting the generally weak fluorescence signal emitted by a single molecule is of great interest due to the widespread use of fluorescence-based techniques in chemistry, molecular biology, materials science, and medicine.[1,2] For instance, applications on DNA sequencing, early diagnosis, or drug screening directly rely on the detected signal per molecule.[3] To overcome the detection limits set by the optical diffraction phenomenon, the environment surrounding the molecule can be tailored to control both the fluorescence intensity and the angular radiation pattern.[4] This leads to the concept of optical antennas, which reversibly convert the propagating optical energy into localized energy in nanoscale volumes, and are the counterparts of radio and microwave antennas in the optical regime.[5] Optical antennas provide new conceptual routes to locally enhance and direct the electromagnetic fields with major applications in molecular sensing and spectroscopy,[6] light-emitting devices,[7] and photovoltaics.[8]

To improve the detection of single molecules using optical antennas, both the antenna's enhancement factor and directivity are essential characteristics. The enhancement denotes the ability to locally increase the fluorescence count rate and the light-matter interaction, while the directivity measures the ability to concentrate the radiated power into a certain direction.[5] The enhancement aspect has received a considerable interest, mainly driven by the opportunity of improving the efficiencies of biomolecular sensing and spectroscopies.[2,6,9,10] The directivity aspect of optical nanoantennas has received much less experimental attention until very recently,[11] owing to the difficulty to realize plasmonic structures achieving directional control of the radiation from single quantum emitters.[12−16] Both enhancement factor and directivity of nanoantennas are essential features for the improvement of light-matter interaction and its wide applications. However, to the best of our knowledge there is no clear demonstration of nanoantennas to improve the fluorescence count rates per molecule and simultaneously provide directional control on the emission. There is currently a strong demand for experimental realizations of nanoantennas able to reach simultaneously a strong gain in the fluorescence signal, together with a unidirectional emission into a narrow angular cone.

In this Letter, we report the demonstration of bright unidirectional photon sources from fluorescent molecules. We obtain enhancement factors of the fluorescence count rate per molecule up to 120 fold, simultaneously with a directional emission of the fluorescence into a cone of ±15° in the direction normal to the

Received: October 25, 2010
Revised: January 7, 2011
Published: January 19, 2011

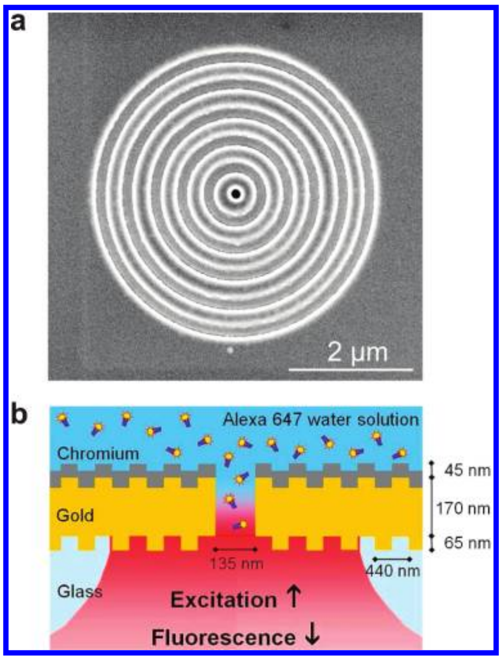

Figure 1. (a) Scanning electron microscopy image of the fabricated nanoaperture with five corrugations. (b) Configuration to enhance and control the fluorescence emission of molecules diffusing in the central aperture.

sample plane. To achieve this, we couple fluorescent molecules to a single nanoaperture surrounded by periodic corrugations milled in a thick gold film (Figure 1). The periodic circular corrugations act as a grating antenna to reversibly couple light to surface electromagnetic waves, as pioneered by Lezec and coworkers while studying the transmission of light through a single subwavelength aperture.[17] All measured signals are calculated back to average signal per molecule thanks to a calibration of the average number of molecules in the central nanoaperture by fluorescence correlation spectroscopy (FCS).

Nanoapertures surrounded by periodic corrugations (also known as “bull’s eyes” apertures) have received a considerable interest in the photonics community.[18,19] Much higher transmission can be achieved through these corrugated apertures than with standard noncorrugated apertures.[20] Moreover, if the output surface surrounding the aperture is also corrugated, a surprisingly narrow beam can be transmitted, having a divergence of less than a few degrees, which is far smaller than that of a simple aperture.[17] The antenna capacity of the corrugations to concentrate the photons at the tiny central aperture has also been used to realize novel applications in nonlinear optics,[21] ultrafast detectors,[22] optical data storage and nanolithography,[23] optical filters and sorters,[24] and semiconductor lasers.[25] The present study explores the use of corrugated nanoapertures for fluorescence sensing applications. This is the first study where single apertures surrounded by periodic corrugations are used to enhance the fluorescence count rate of molecules and control the emission directionality. The results are of high importance to improve the effectiveness of single molecule fluorescence detection[26,27] with applications in molecular sensing,[28,29] DNA sequencing,[30,31] high throughput screening,[32] or optical trapping.[33]

The average number of fluorescent molecules can be more than 2 orders of magnitude smaller in a nanoaperture than in a diffraction-limited classical confocal volume.[34] Therefore, the sole measurement of the total fluorescence intensity from the sample is not sufficient to accurately quantify the antennas properties of enhancement factor and directivity. The fluorescence intensity has to be normalized by the number of emitters that actually contribute to the signal to assess the fluorescence count rate per molecule CRM, which is the relevant figure to assess the enhancement on the fluorescence signal. We address this issue using FCS, which is an elegant method to directly and accurately quantify the average number of emitters N contributing to the detected fluorescence signal.[34,35] In FCS, the temporal fluctuations of the fluorescence signal $F(t)$ are recorded, and the temporal correlation of this signal is computed $g^{(2)}(\tau) = \langle F(t)F(t+\tau)\rangle/\langle F(t)\rangle^2$, where τ is the delay (lag) time, and $\langle\ \rangle$ stands for time averaging. The amplitude of the correlation function quantifies the average number of molecules N and provides access to the fluorescence count rate per molecule CRM = $\langle F\rangle/N$. Full details of the FCS analysis procedure are given in the Supporting Information, together with raw experimental FCS data. We point out that as a consequence of the stochastic nature of the FCS technique, all the presented fluorescence data are spatially averaged over all the possible molecule orientations and positions inside the detection volume. While FCS is not a “true” single molecule method, it nevertheless quantifies the average fluorescence emission characteristics of a single emitter. Hereafter, we use the FCS method to characterize the fluorescence emission per Alexa Fluor 647 molecules diffusing within the central nanoaperture. The emission count rate per molecule is the key to thoroughly analyze the fluorescence enhancement and the angular radiation pattern molecules in corrugated nanoapertures. Moreover, the method is able to specifically quantify the respective contributions of excitation and emission processes in the observed enhanced fluorescence.[35,36] We demonstrate that the periodic corrugations improve the local excitation intensity inside the central nanoaperture, while simultaneously increasing the directional emission count rate.

Figure 1 presents the doubly corrugated nanoapertures under investigation. The different nanostructures are fabricated by direct focused ion beam (FIB) milling, using optimized design parameters derived from the thorough characterization published in ref 37. The fabrication protocol is detailed in the Supporting Information. The inner aperture diameter is 135 nm and is chosen to be close to the optimum diameter leading to maximum fluorescence enhancement.[38] The groove period is 440 nm, width 200 nm, depth 65 nm, and there are 5 grooves. The periodic grooves provide the necessary momentum to match the far-field radiation with surface electromagnetic waves. As the Stokes shift between the laser and the fluorescence wavelengths is relatively small, these design parameters can be sufficiently close to resonance conditions for both the laser excitation and the fluorescence emission.[37] A spectral study shown in the Supporting Information does not reveal any major spectral resonance effect.

An unwanted phenomenon consecutive to the use of periodic corrugations on both sides of the gold film is the enhanced transmission through the central aperture.[17] Even the fluorescence from molecules diffusing above the nanoaperture could be detected, which would confuse the analysis. To solve this problem, we cover the gold film with an optically thick (45 nm) chromium layer, following the investigations in reference[39] on bowties nanoantennas. The high absorption losses of chromium efficiently damp the transmission through the corrugated nanoaperture and avoid detecting a fluorescence signal from the top of the nanoaperture sample. We demonstrate in the Supporting

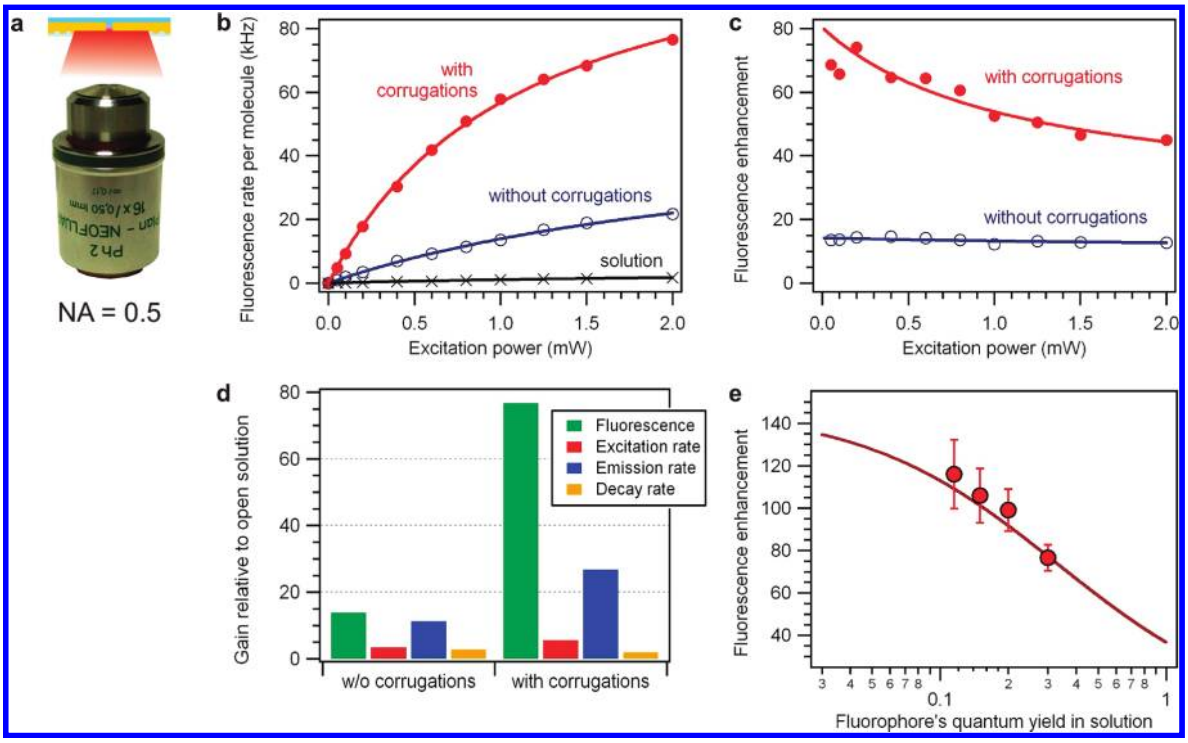

Figure 2. (a) Investigations of the detected fluorescence count rate per molecule with a 0.5 NA water immersion microscope objective. (b) Fluorescence count rate per molecule versus the excitation power. Markers are experimental data, solid lines are numerical fits using a model detailed in the main text. The fitting parameters are summarized in the Supporting Information. (c) Fluorescence enhancement factors relative to the standard confocal case (open solution), as deduced from the data in (b). (d) Contribution of excitation and emission gains to the overall fluorescence enhancement. Decay rate corresponds to the reduction of the fluorescence lifetime. The experimental values are summarized in the main text. (e) Evolution of the fluorescence enhancement factor versus Alexa Fluor 647 measured quantum yield ϕ in a water-methyl viologen solution. From right to left, the methyl viologen concentration increases from 0 up to 60 mM. The continuous line is a model based solely on the data displayed in (d). It is not a numerical fit of the experimental data points, there are no free parameters.

Information that similar numbers of molecules are detected for nanoapertures with and without corrugations thanks to the supplementary chromium layer. Without the chromium layer, the difference in the numbers of molecules can be larger than a factor of 6 fold.

The excitation is incident from below the sample (glass coverslip substrate) with linear polarization and 632.8 nm wavelength. It is focused by a 0.5 NA water-immersion objective (Zeiss Neofluar, see Figure 2a) to a spot diameter of about 1.5 μm largely covering the first three concentric corrugations. The same microscope objective is used to collect the fluorescence light emitted from Alexa Fluor 647 molecules (A647, Invitrogen, Carlsbad, CA) diffusing in the central aperture region. Alexa Fluor 647 is a common fluorescent molecule with maximum absorption/emission peaks at 650/672 nm, and a quantum yield of 30% in water solution. Unless otherwise stated, A647 molecules are diluted in a standard water-based phosphate-buffered saline (PBS) solution. The salt composition of the PBS buffer is expected to compensate for the local electrical charging of the nanoaperture surface acquired during the FIB fabrication process. For all the experiments reported here, a solution of A647 molecules at micromolar concentration is deposited on top of the sample to ensure that on average 10 molecules are present in the aperture volume, as calibrated by FCS for each experimental run (see the raw experimental data in the Supporting Information). The molecules are constantly diffusing in and out the aperture, this configuration strongly limits observing the negative effects of photobleaching in our data set.

The fluorescence count rates per molecule measured by FCS are plotted as function of the excitation power in Figure 2b for the three cases of (i) free solution (no nanostructure), (ii) gold nanoaperture without corrugations, and (iii) gold nanoaperture with the periodic corrugations. It is apparent from this set of data that the periodic corrugations have a strong influence in further enhancing the fluorescence emission. The experimental points are numerically fitted following the general model of the fluorescence count rate $\mathrm{CRM} = AI_e/(1 + I_e/I_s)$, where I_e is the excitation power, I_s the saturation power, and A is a constant proportional to the molecular absorption cross-section, quantum yield, and setup collection efficiency.[35] The fitting parameters are summarized in the Supporting Information and will be used hereafter to quantify the influence of excitation and emission gains in the fluorescence enhancement process.

These measurements unambiguously quantify the enhancement of the fluorescence intensity, which is the first essential feature of the nanoantenna. We define the fluorescence enhancement factor η_F as the direct ratio of the fluorescence count rates per molecule for the nanostructure and the reference (open) solution at a given excitation power: $\eta_F = \mathrm{CRM}_{\mathrm{aper}}/\mathrm{CRM}_{\mathrm{sol}}$. Figure 2c presents a clear evolution of the fluorescence enhancement factor with the excitation power. For both apertures with and without corrugations, the enhancement η_F decreases with the excitation power, as the fluorescence process tends to saturate.[35] In the low excitation regime ($I_e < 200$ μW), the corrugated nanoaperture provides a enhancement factor of $\eta_F = 77$, while the enhancement factor of the noncorrugated nanoaperture is 14. Adding plasmonic corrugations enables achieving close to 2 orders of magnitude enhancement factor, while using a standard fluorophore. Compared to the use of a noncorrugated aperture, the corrugations provide a supplementary gain of 5.5. These measurements also demonstrate that single molecule fluorescence analysis can be efficiently performed by a simple 0.5 NA water immersion objective, or equivalently 0.4 NA dry air objective.

The evolution of the fluorescence enhancement versus the excitation power (Figure 2c) allows to quantify the respective contributions of excitation and emission gains and unravel the origins of the fluorescence enhancement following a procedure developed in references.[35,36] From the interpolation of the fluorescence count rates per molecule CRM versus the excitation power, we deduce the fluorescence enhancements at the two extreme cases below saturation $I_e \ll I_s$ and at saturation $I_e \gg I_s$. In the asymptotic limit of the saturation regime, the fluorescence enhancement corresponds to the gain in emission η_{em}, as there is obviously no dependence anymore on the excitation power. The emission enhancement η_{em} can be expressed as the product of the radiative rate enhancement η_{rad} times the collection efficiency enhancement η_κ, $\eta_{em} = \eta_{rad}\eta_\kappa$. While most numerical simulations focus on the radiative rate enhancement, the experimental characterization procedure is only sensitive to the photons that are collected by the setup, and accesses to the product of the radiative decay rate k_r times the collection efficiency κ. In the low excitation regime $I_e \ll I_s$, the fluorescence enhancement η_F is proportional to the gains in emission η_{em} and local excitation intensity η_{exc}, and inversely proportional to the modification in total fluorescence decay rate η_{tot}, $\eta_F = \eta_{em}\eta_{exc}/\eta_{tot}$.[5] This expression can be rewritten as $\eta_F = \eta_\kappa\eta_\phi\eta_{exc}$, where η_κ is the collection efficiency enhancement, and $\eta_\phi = \eta_{rad}/\eta_{tot}$ is the quantum efficiency enhancement. This expression of the fluorescence enhancement explicitly indicates that in the low excitation regime, the fluorescence enhancement is proportional to the gains in collection efficiency, quantum yield, and excitation intensity. We determine experimentally the alteration in the total fluorescence decay rate η_{tot} by fluorescence lifetime (start−stop) measurements. We can thus extract the gain in local excitation intensity from the fluorescence enhancement in the low excitation regime, knowing η_{tot} and η_{em} (the latter corresponds to the fluorescence enhancement factor in the saturation regime). This procedure separates the excitation and emission contributions from the total fluorescence enhancement and is used here to investigate the influence of the periodic corrugations surrounding single nanoapertures.

The periodic grating structure acts as an antenna to reversibly couple far-field light radiation to near-field electromagnetic energy. Our characterization procedure is able to quantify this effect clearly, as shown in Figure 2d. For the nanoaperture without corrugations, we measure the different enhancement factors relative to the reference in open solution (no aperture): total fluorescence $\eta_F = 14$, excitation $\eta_{exc} = 3.2$, emission $\eta_{em} = 11$, and total decay rate $\eta_{tot} = 2.5$ (this increase in total decay rate corresponds to the reduction of the fluorescence lifetime). These values stand in good agreement with the values previously reported from FCS measurements[35] or from quantum dot photoluminescence dynamics.[40] For the corrugated nanoaperture, we find that the enhancement factors are significantly greater: fluorescence $\eta_F = 77$, excitation $\eta_{exc} = 5.5$, emission $\eta_{em} = 27$, while the total decay rate modification is almost unchanged $\eta_{tot} = 1.9$. Here again, the values for the excitation and emission correspond well to what can be inferred from transmission measurements and simulations on corrugated nanoapertures.[17,20] We note that the emission enhancement η_{em} is always larger than the excitation enhancement η_{exc}. This is because the emission enhancement is the product of the radiative rate enhancement η_{rad} times the collection efficiency enhancement η_κ. By reciprocity, we expect the radiative rate enhancement η_{rad} to be close to the excitation enhancement η_{exc}.[41] Consequently, the emission enhancement η_{em} is larger than the excitation enhancement η_{exc} by a factor that is close to the collection efficiency enhancement η_κ.

The characterization of the fluorescence enhancement shows that (i) both excitation and emission gains contribute to the overall fluorescence enhancement, and (ii) the periodic corrugations increase each gain in excitation and emission by roughly a factor of 2, as compared to a nanoaperture without corrugations. The grating structure acts as an antenna to concentrate the photons at the central nanoaperture with an increase in excitation intensity from 3.2 to 5.5 fold. The periodic corrugations also reversibly couple the near-field electromagnetic energy into far-field light radiation, with an gain in emission count rate from 11 to 27 fold. The simultaneous increase in both η_{exc} and η_{em} is permitted by the Stokes shift between the laser and the fluorescence wavelengths remaining on the order of $\lambda/20$. The periodic corrugations can thus be close to resonance conditions for both the laser excitation and the fluorescence emission.

The fluorescence enhancement factor obviously depends strongly on the fluorophore's quantum yield in solution; for a perfect emitter (quantum yield of one), all the fluorescence enhancement comes from the excitation intensity or collection efficiency, as there is no possible gain on the quantum yield. The lower the quantum yield in solution, the higher the gain on a plasmonic nanostructure can be, up to a certain extend where the losses are going to limit the enhancement factor.[42] To illustrate this, remarkably large single molecule fluorescence enhancements up to 1340 have been reported while studying TDQPI molecules.[10] These nonwater-soluble molecules have a relatively low quantum yield of ∼2.5%, which can be favorable to obtain large enhancement values. Here, we experimentally address the evolution of the fluorescence enhancement factor versus the fluorophore's quantum yield in solution. To control the A647 quantum yield, we add a growing fraction of methyl viologen (1,1′-dimethyl-4,4′-bipyridinium dichloride, Sigma-Aldrich) with concentrations up to 60 mM. Methyl viologen acts as a controllable quencher of the A647 fluorescence. A Stern−Volmer analysis shown in the Supporting Information quantifies this effect: in the presence of methyl viologen with concentration $[MV^{2+}]$, the quantum yield ϕ of A647 is decreased according to the formula $\phi_0/\phi = 1 + k_q\, \tau_0\, [MV^{2+}]$, where $\phi_0 = 30\%$ and $\tau_0 = 1.0$ ns are the unquenched quantum yield and fluorescence lifetime of A647 in water PBS solution, and $k_q = 2.4 \times 10^{10}\ s^{-1}\cdot M^{-1}$ is the quenching rate determined experimentally (see Supporting Information).

The A647 and methyl viologen mixture forms the ideal basis to check the evolution of the fluorescence enhancement factor while varying the initial quantum yield in solution. Our results are summarized in Figure 2e, showing a net increase in the fluorescence enhancement factor from 77 to 120 while the A647 quantum yield is quenched from 30 to 11% (added methyl viologen concentration up to 60 mM). This experimental data is analyzed using only the enhancement factors in Figure 2d, which we detail hereafter. Without the nanostructure, the fluorescent molecule has a radiative decay rate k_r, a nonradiative decay rate $k_{nr_0} + k_q\,[MV^{2+}]$, and a quantum yield $\phi = k_r/(k_r + k_{nr_0} + k_q\,[MV^{2+}])$. The setup collection efficiency is κ and the excitation rate is k_e. With the introduction of the nanostructure, the radiative rate is modified to k_r^*, the collection efficiency is κ^*, and the excitation rate k_e^*. The quantum yield now reads $\phi^* = k_r^*/(k_r^* + k_{nr_0} + k_q\,[MV^{2+}] + k_{abs}^*)$, where a new nonradiative decay route k_{abs}^* is introduced to take into account the ohmic losses into the metal and nonradiative energy transfers to the free electrons in the metal.[10] We also assume that the rates k_{nr_0} and k_q are unaffected by the nanostructure. At moderate excitation powers (below fluorescence saturation), the fluorescence count rate per molecule CRM is proportional to the excitation rate k_e, the collection efficiency κ, and the emission quantum yield ϕ.[35] The fluorescence enhancement with the nanoaperture can thus be explicitly written as

$$\eta_F = \frac{k_e^*}{k_e}\frac{\kappa^*}{\kappa}\frac{\phi^*}{\phi} \tag{1}$$

After some basic algebra, this equation can be rewritten:

$$\eta_F = \frac{k_e^*}{k_e}\frac{\kappa^*}{\kappa}\frac{k_r^*}{k_r}\frac{1}{(1-\phi)+\phi\zeta} = \eta_{exc}\eta_{em}\frac{1}{(1-\phi)+\phi\zeta} \tag{2}$$

with $\zeta = (k_r^* + k_{abs}^*)/k_r$. Hereafter, we set the quantity ζ to the value obtained from the characterization of A647 with no methyl viologen (Figure 2d). The linear curve in Figure 2e displays the awaited fluorescence enhancement factors η_F while varying the quantum yield in solution ϕ based on eq 2. Let us emphasize that this is not a numerical fit of the experimental data points, as there are no free parameters. This curve is only based on the values of the gains in excitation, emission, and total decay rates as deduced from the fluorescence characterization of A647 with no methyl viologen (Figure 2d). The satisfactorily agreement with the data points in Figure 2e is another confirmation of the validity of the fluorescence characterization procedure (see more characterization with a 1.2 NA objective in the Supporting Information). Besides, the theoretical predictions indicate that no fluorescence enhancement factor higher than 150 could be reached with this experimental configuration, whatever the choice of the fluorophore's quantum yield in solution. Further reducing the aperture diameter is not expected to significantly improve the fluorescence enhancement, as the diameter of 135 nm is already close to the optimum diameter leading to maximum enhancement for a noncorrugated aperture, independently on the fluorophore's quantum yield in solution.[43] Higher enhancement values seem restricted to plasmonic nanoantennas with higher electromagnetic field confinement and lightning rod effect, such as bowties nanoantennas,[10] which is not surprising at all. However, the corrugated nanoapertures have another crucial advantage, which deals with the ability to control the fluorescence emission directivity.

After the fluorescence enhancement parameter, the second essential feature of the nanoaperture antenna is the directivity, which measures the antenna's ability to concentrate the radiated power into a certain direction. To characterize the directivity of the corrugated nanoaperture, we switch the microscope objective to a 1.2 NA water immersion objective (Zeiss C-apochromat). This is essential to provide enough range for the angular detection, with a present detection limit set by the numerical aperture to ±64° around the optical axis. To characterize the angular emission, we record the fluorescence intensity distribution on the back focal plane of the high NA microscope objective on a charge-coupled device CCD camera with microlenses (Kodak KAF-1603).[44] These images represent the intensity emitted for different angular directions from the antenna, we call them radiation patterns (this corresponds formally to the emission diagram in the Fourier plane or equivalently the momentum space).[11] Typical radiation patterns for a single nanoaperture without and with periodic corrugations are presented in Figure 3a,b. Let us emphasize that as the FCS measurements provide an accurate estimation of the numbers of molecules N contributing to the overall fluorescence signal, we can normalize the intensities in the radiation pattern images by the actual number of molecules N for each experiment, which is the case in Figure 3. Therefore, the intensity scaling is to be understood as the normalized fluorescence per molecule. This is very important to provide an accurate picture of the radiation pattern and to be able to compare between different radiation patterns. Not only the shape of the radiation patterns in Figure 3 are important, the intensities are here fully relevant too.

For the noncorrugated aperture, the radiation pattern image contains a single circle representing the maximum collection angle at 64°. However, for the corrugated aperture, the image contains an additional bright spot with an extension of 15° (half-width at half-maximum) centered on the optical axis. This directly reveals that the emission from a noncorrugated aperture is almost omni-directional with no privileged direction, while the emission from the corrugated aperture can be tuned to high directionality in the direction normal to the sample. A first step to quantify the antenna's directionality is to introduce the "directional performance" as the ratio of the fluorescence intensity along the peak direction ($\theta = 0°$) relative to the fluorescence intensity emitted strongly off-axis (which we take at $\theta = 50°$ in the present case). For the noncorrugated aperture, the directional performance is roughly 0 dB, as expected for a subwavelength circular structure. For the corrugated aperture in Figure 3b, the directional performance is 7.3 dB, which appears similar to the performance of a recent Yagi-Uda antenna demonstration.[11] The periodic corrugations thus efficiently control the emission directionality. Moreover, the emission directionality is achieved along all azimuthal orientations (it is circularly symmetric in the back focal plane image), and the main emission direction is normal to the sample plane, contrarily to Yagi-Uda antennas.[11,45]

In antenna theory, "directivity" is a figure of merit for an antenna corresponding to the ratio of the radiated power density along the direction of strongest emission, relative to the power density radiated by an ideal isotropic emitter radiating the same amount of total power. As we quantify the radiation pattern intensity per molecule, we can estimate the directivity figure of merit and assess the fluorescence enhancement versus the emission angle. Figure 3c directly quantifies the fluorescence enhancement per molecule along each emission direction relative to an open water environment. To obtain this figure, we first calibrate the integrated fluorescence enhancement with the 1.2 NA objective in the case of the nanoaperture without corrugations. Data shown in the Supporting Information indicate an integrated value over the whole objective NA of 13.6. This value directly corresponds to the fluorescence enhancement found for each emission direction from a noncorrugated aperture, as the angular emission is uniform within the limit of ±64° set by our objective. In the case of the nanoaperture with the periodic corrugations, we use the ratio of the fluorescence intensities per molecule in Figure 3a,b and the known fluorescence

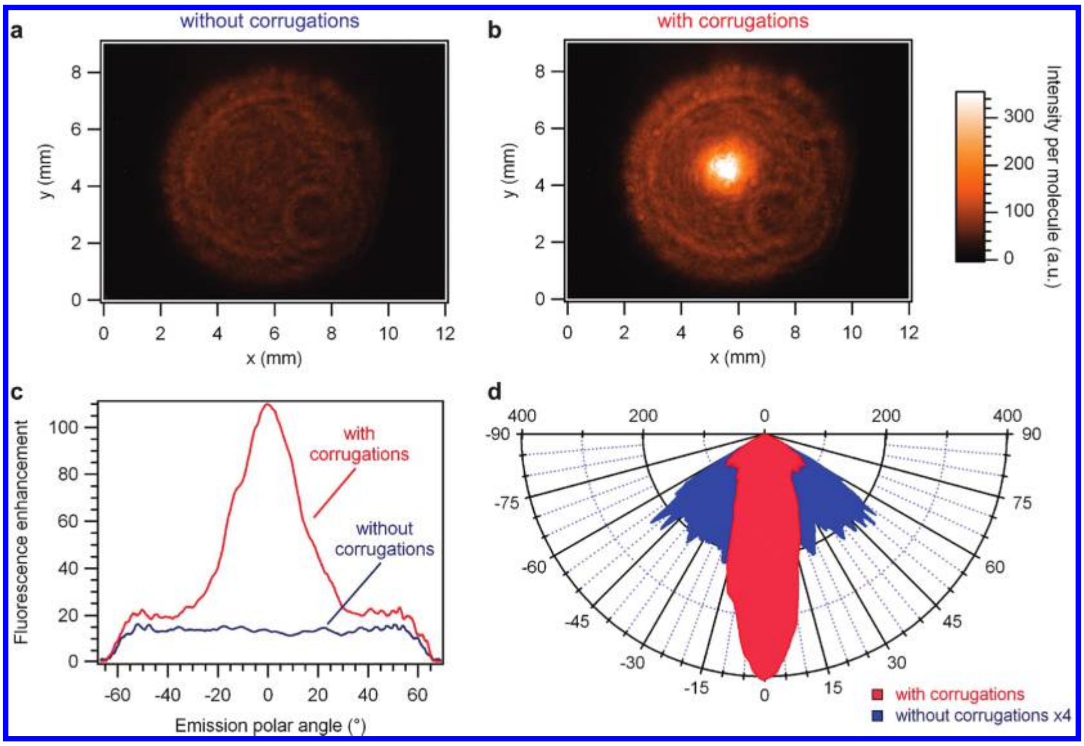

Figure 3. Radiation patterns (intensity distribution in the back focal plane of the 1.2 NA objective) for a single nanoaperture without (a) and with (b) periodic corrugations. The excitation power is 120 μW in both cases. The intensities presented here are normalized by the average number of detected molecules, as measured by FCS. Therefore, the intensity scaling in (a) and (b) corresponds to the normalized fluorescence intensity *per molecule*. The larger circle seen for instance in image (a) corresponds to the maximum detectable angle of ±64° set by our 1.2 NA water immersion objective. (c) Fluorescence intensity enhancement per single molecule as function of the emission polar angle, relative to the open solution reference case. (d) Angular radiation patterns in the polar angle, as deduced from the images in (a,b). The intensity per molecule in the case of the noncorrugated aperture is multiplied here by a factor of 4 to ease viewing the figure.

enhancement factor of 13.6 for an aperture without corrugations to calibrate the fluorescence enhancement versus the emission angle (Figure 3c). A clear peak centered at 0° (direction normal to the sample plane) is seen in Figure 3c with a peak enhancement up to 110 fold, or 20.5 dB. To quantify the antenna directivity, one needs to normalize this peak enhancement by the average enhancement integrated over all emission directions (directivity is defined relative to an isotropic source radiating the same total power). We estimate average enhancement integrated over all emission directions by the fluorescence enhancement of 23.8 found in the case of the 1.2 NA collection objective, divided by 2 to account for the emission occurring in the lower half-space only (see Supporting Information). As a result, the corrugated aperture directivity is estimated to 110/(23.8/2) = 9.2, or equivalently 9.7 dB.

For the corrugated aperture, the peak seen in Figure 3c has a half-width at half-maximum of ±15°, where most of the angular fluorescence enhancement is to be found. This value corresponds nicely to the ±22° collection cone of our 0.5 NA water-immersion objective. Almost all the energy of the central peak in the radiation pattern is thus collected by the 0.5 NA objective. This effect directly contributes to the high fluorescence enhancement found with the corrugated apertures, and to the ability to efficiently detect the fluorescence from a single molecule with a 0.5 NA objective. The radiation patterns are also shown in polar diagrams (Figure 3d), which are more intuitive to view. To complete this picture, the Supporting Information provides a comprehensive graph of the collected fluorescence per molecule versus the objective numerical aperture.

Lastly, we investigate the antenna capacity to couple the electromagnetic energy to the central aperture via surface electromagnetic waves. To this end, we perform the experiment depicted in Figure 4a; the fluorescence from the central aperture is measured while the excitation laser spot focused by a 1.2 NA water immersion objective is scanned over the corrugated nanoaperture sample. We emphasize that the fluorescence detection path is not scanned, only the emission from the fixed central aperture is collected while the excitation spot is moved. This type of image measurement directly notifies the occurrence of coupling through surface waves. It is also sensitive to the polarization coupling, as the laser light is linearly polarized and the corrugations grating has circular symmetry. Figure 4b,c represents the fluorescence images for horizontal and vertical polarization of the excitation field, while only the excitation spot is scanned over the corrugated nanoaperture. These pictures represent the direct image space (they must not be confused with radiation patterns in the reciprocal Fourier plane as in Figure 3a). The butterfly shape is characteristic to selective coupling when the field polarization is aligned along the transverse magnetic (TM) direction respective to the circular corrugations grating. This is directly representative of coupling to TM-sensitive surface waves such as surface plasmon polaritons. In the Supporting Information, we show an image scan of a single nanoaperture without corrugations. The characteristic butterfly shape is absent, as nothing (except the aperture edge) provides the necessary momentum to couple the far-field radiation to surface waves.

Gold nanoapertures surrounded by periodic corrugations transform standard fluorescent molecules into bright unidirectional

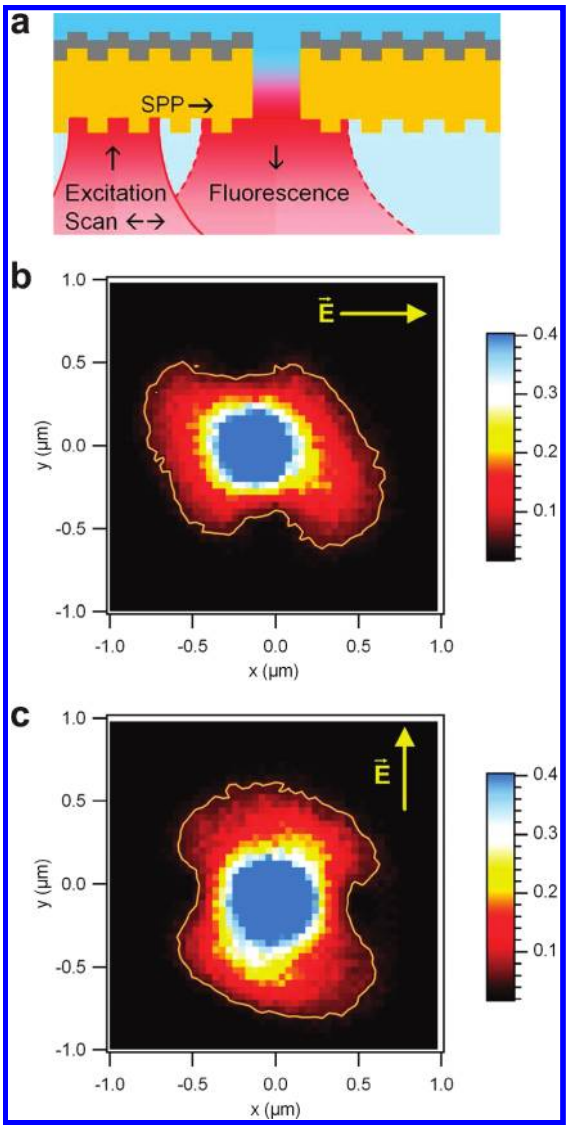

Figure 4. (a) Schematic of the experiment: the fluorescence from the central aperture is collected while the excitation laser spot focused by a 1.2 NA water immersion objective is scanned over the corrugated nanoaperture sample. The fluorescence detection path is not scanned, only the emission from the fixed central aperture is measured while the excitation spot is moved. (b,c) The fluorescence images for horizontal and vertical polarization of the excitation field. These pictures are in the direct image space (not reciprocal Fourier plane as in Figure 3a). We deliberately saturate the signal stemming from the center of the aperture (normalized to 1) to better display the intensity distribution near the periodic corrugations. The butterfly shape is characteristic to selective coupling when the field polarization is aligned along the transverse magnetic (TM) direction respective to the circular corrugations grating.

sources. The corrugated nanoaperture simultaneously increases the emission count rate and redirects the fluorescence radiation; our study reports enhancement factors of the fluorescence count rate per molecule up to 120 fold simultaneously with a directional emission of the fluorescence into a cone of ±15° in the direction normal to the sample. Corrugated nanoapertures thus provide a source for intense fluorescence light with very narrow directionality. There is still plenty of room for further optimization of the many antenna parameters, according to the design characterizations at hand.[37,46] On the basis of the very narrow directionality of ±3° achieved for the transmitted light beam,[17] we believe that similar angular divergences can be realized for the fluorescence beam using optimized parameters design. Even though such directionality performance comes at the expense of a larger foot print of the structure, we point out that several corrugated apertures can be strongly overlapped,[24] hereby providing a way toward integration of corrugated apertures in compact device architecture. Our study also demonstrates that a simple 0.5 NA water immersion objective can efficiently detect a single fluorescent molecule, hereby releasing the need for high NA microscope objectives. Another remarkable point is that the structure is insensitive to the incoming polarization direction. We believe that the present demonstration is of high relevance for the development of advanced single molecule sensing, bright single-photon sources for quantum information processing, and light emitting devices.

■ ASSOCIATED CONTENT

Ⓢ Supporting Information. Fabrication procedure, experimental setup and analysis methods descriptions, raw experimental data acquired with 0.5 and 1.2 NA objectives, fluorescence enhancement characterization with a 1.2 NA objective, Stern–Volmer analysis of A647 quenching, spectral analysis of the fluorescence emission, influence of the numerical aperture for collection, image scan of a single nanoaperture, and photon antibunching experiment with a corrugated nanoaperture. This material is available free of charge via the Internet at http://pubs.acs.org.

■ AUTHOR INFORMATION

Corresponding Author

*E-mail: jerome.wenger@Fresnel.fr.

■ ACKNOWLEDGMENT

The authors acknowledge stimulating discussions with Davy Gérard and Steve Blair. This research is partly funded by the French Agence Nationale de la Recherche under Contract ANR-07-NANO-006-03 "ANTARES" and by the European Research Council under Contract 227577 "Plasmonics".

■ REFERENCES

(1) Walter, N. G.; Huang, C. Y.; Manzo, A. J.; Sobhy, M. A. *Nat. Methods* **2008**, *5*, 475–489.
(2) Lal, S.; Link, S.; Halas, N. J. *Nat. Photonics* **2007**, *1*, 641–648.
(3) Craighead, H. G. *Nature* **2006**, *442*, 387–393.
(4) Barnes, W. L. *J. Mod. Opt.* **1998**, *45*, 661–699.
(5) Bharadwaj, P.; Deutsch, B.; Novotny, L. *Adv. Opt. Photonics* **2009**, *1*, 438–483.
(6) Fu, Y.; Lakowicz, J. R. *Laser Photonics Rev.* **2009**, *3*, 221–232.
(7) Schuller, J. A.; Barnard, E. S.; Cai, W. S.; Jun, Y. C.; White, J. S.; Brongersma, M. L. *Nat. Mater.* **2010**, *9*, 193–204.
(8) Atwater, H. A.; Polman, A. *Nat. Mater.* **2010**, *9*, 205–213.
(9) Anger, P.; Bharadwaj, P.; Novotny, L. *Phys. Rev. Lett.* **2006**, *96*, No. 113002.
(10) Kinkhabwala, A.; Yu, Z. F.; Fan, S. H.; Avlasevich, Y.; Mullen, K.; Moerner, W. E. *Nat. Photonics* **2009**, *3*, 654–657.
(11) Curto, A.; Volpe, G.; Taminiau, T. H.; Kreuzer, M.; Quidant, R.; Van Hulst, N. F. *Science* **2010**, *329*, 930–933.
(12) Taminiau, T. H.; Stefani, F. D.; Segerink, F. B.; Van Hulst, N. F. *Nat. Photonics* **2008**, *2*, 234–237.
(13) Koenderink, A. F. *Nano Lett.* **2009**, *9*, 4228–4233.

(14) Pakizeh, T.; Käll, M. *Nano Lett.* **2009**, *9*, 2343–2349.
(15) Esteban, R.; Teperik, T. V.; Greffet, J. J. *Phys. Rev. Lett.* **2010**, *104*, No. 026802.
(16) Devilez, A.; Stout, B.; Bonod, N. *ACS Nano* **2010**, *4*, 3390–3396.
(17) Lezec, H. J.; Degiron, A.; Devaux, E.; Linke, R. A.; Martin-Moreno, L.; Garcia-Vidal, F. J.; Ebbesen, T. W. *Science* **2002**, *297*, 820–822.
(18) Genet, C.; Ebbesen, T. W. *Nature* **2007**, *445*, 39–46.
(19) Garcia-Vidal, F. J.; Martin-Moreno, L.; Ebbesen, T. W.; Kuipers, L. *Rev. Mod. Phys.* **2010**, *82*, 729–787.
(20) Martin-Moreno, L.; Garcia-Vidal, F. J.; Lezec, H. J.; Degiron, A.; Ebbesen, T. W. *Phys. Rev. Lett.* **2003**, *90*, No. 167401.
(21) Nahata, A.; Linke, R. A.; Ishi, T.; Ohashi, K. *Opt. Lett.* **2003**, *28*, 423–425.
(22) Ishi, T.; Fujikata, J.; Ohashi, K. *Jpn. J. Appl. Phys.* **2005**, *44*, L364–L366.
(23) Srituravanich, W.; Pan, L.; Wang, Y.; Sun, C.; Bogy, D. B.; Zhang, X. *Nat. Nanotechnol.* **2008**, *3*, 733–737.
(24) Laux, E.; Genet, C.; Skauli, T.; Ebbesen, T. W. *Nat. Photonics* **2008**, *2*, 161–164.
(25) Yu, N.; Fan, J.; Wang, Q. J.; Plügl, C.; Diehl, L.; Edamura, T.; Yamanishi, M.; Kan, H.; Capasso, F. *Nat. Photonics* **2008**, *2*, 564–570.
(26) Moran-Mirabal, J. M.; Craighead, H. G. *Methods* **2008**, *46*, 11–17.
(27) Lenne, P. F.; Rigneault, H.; Marguet, D.; Wenger, J. *Histochem. Cell Biol.* **2008**, *130*, 795–805.
(28) Levene, M. J.; Korlach, J.; Turner, S. W.; Foquet, M.; Craighead, H. G.; Webb, W. W. *Science* **2003**, *299*, 682–686.
(29) Chansin, G. A. T.; Mulero, R.; Hong, J.; Kim, M. J.; deMello, A. J.; Edel, J. B. *Nano Lett.* **2007**, *7*, 2901–2906.
(30) Eid, J.; Fehr, A.; Gray, J.; Luong, K.; Lyle, J.; Otto, G.; Peluso, P.; Rank, D.; Baybayan, P.; Bettman, B.; Bibillo, A.; Bjornson, K.; Chaudhuri, B.; Christians, F.; Cicero, R.; Clark, S.; Dalal, R.; Dewinter, A.; Dixon, J.; Foquet, M.; Gaertner, A.; Hardenbol, P.; Heiner, C.; Hester, K.; Holden, D.; Kearns, G.; Kong, X. X.; Kuse, R.; Lacroix, Y.; Lin, S.; Lundquist, P.; Ma, C. C.; Marks, P.; Maxham, M.; Murphy, D.; Park, I.; Pham, T.; Phillips, M.; Roy, J.; Sebra, R.; Shen, G.; Sorenson, J.; Tomaney, A.; Travers, K.; Trulson, M.; Vieceli, J.; Wegener, J.; Wu, D.; Yang, A.; Zaccarin, D.; Zhao, P.; Zhong, F.; Korlach, J; Turner, S. *Science* **2009**, *323*, 133–138.
(31) McNally, B.; Singer, A.; Yu, Z.; Sun, Y.; Weng, Z.; Meller, A. *Nano Lett.* **2010**, *10*, 2237–2244.
(32) Wenger, J.; Gérard, D.; Aouani, H.; Rigneault, H.; Lowder, B.; Blair, S.; Devaux, E.; Ebbesen, T. W. *Anal. Chem.* **2009**, *81*, 834–839.
(33) Juan, M. L.; Gordon, R.; Pang, Y.; Eftekhari, F.; Quidant, R. *Nat. Phys.* **2009**, *5*, 915–919.
(34) Rigneault, H.; Capoulade, J.; Dintinger, J.; Wenger, J.; Bonod, N.; Popov, E.; Ebbesen, T. W.; Lenne, P. F. *Phys. Rev. Lett.* **2005**, *95*, No. 117401.
(35) Wenger, J.; Gérard, D.; Bonod, N.; Popov, E.; Rigneault, H.; Dintinger, J.; Mahboub, O.; Ebbesen, T. W. *Opt. Express* **2008**, *16*, 3008–3020.
(36) Aouani, H.; Wenger, J.; Gérard, D.; Rigneault, H.; Devaux, E.; Ebbesen, T. W.; Mahdavi, F.; Xu, T.; Blair, S. *ACS Nano* **2009**, *3*, 2043–2048.
(37) Mahboub, O.; Carretero Palacios, S.; Genet, C.; Garcia-Vidal, F. J.; Rodrigo, S. G.; Martin-Moreno, L.; Ebbesen, T. W. *Opt. Express* **2010**, *18*, 11292–11299.
(38) Gérard, D.; Wenger, J.; Bonod, N.; Popov, E.; Rigneault, H.; Mahdavi, F.; Blair, S.; Dintinger, J.; Ebbesen, T. W. *Phys. Rev. B* **2008**, *77*, No. 045413.
(39) Jiao, X.; Goeckeritz, J.; Blair, S.; Oldham, M. *Plasmonics* **2009**, *4*, 37–50.
(40) Aouani, H.; Itzhakov, S.; Gachet, D.; Devaux, E.; Ebbesen, T. W.; Rigneault, H.; Oron, D.; Wenger, J. *ACS Nano* **2010**, *4*, 4571–4578.
(41) Bharadwaj, P.; Novotny, L. *Opt. Express* **2007**, *15*, 14266–14274.
(42) Bharadwaj, P.; Novotny, L. *J. Phys. Chem. C* **2010**, *114*, 7444–7447.
(43) Wenger, J.; Aouani, H.; Gérard, D.; Blair, S.; Ebbesen, T. W.; Rigneault, H. *Proc. SPIE* **2010**, *7577*, 75770J.
(44) Huang, C.; Bouhelier, A.; Colas des Francs, G.; Bruyant, A.; Guenot, A.; Finot, E.; Weeber, J.-C.; Dereux, A. *Phys. Rev. B* **2008**, *78*, No. 155407.
(45) Kozako, T.; Kadoya, Y.; Hoffmann, H. F. *Nat. Photonics* **2010**, *4*, 312–315.
(46) Popov, E.; Nevière, M.; Fehrembach, A. L.; Bonod, N. *Appl. Opt.* **2005**, *44*, 6141–6154.

Supporting Information for
Bright unidirectional fluorescence emission of molecules in a nanoaperture with plasmonic corrugations

Heykel Aouani, Oussama Mahboub, Nicolas Bonod, Eloïse Devaux,
Evgeny Popov, Hervé Rigneault, Thomas W. Ebbesen, Jérôme Wenger

Abstract

This document contains the following supplementary information:

- Fabrication procedure
- Experimental setup and analysis method descriptions
- Raw experimental data presentation
- Fluorescence enhancement characterization with a 1.2 NA objective
- Stern-Volmer analysis of A647 quenching with methyl viologen
- Spectral analysis of the fluorescence emission
- Influence of the numerical aperture for collection
- Image scan of a single nanoaperture
- Photon antibunching experiment with a corrugated nanoaperture

1 Fabrication procedure

The preparation procedure of the corrugated nanoapertures is based on two-step direct focused ion beam milling (FIB). The procedure is schematically presented in Figure 1. First, the glass substrate is coated with a thin chromium adhesion layer and a 50 nm thick gold layer to make the substrate conductive and avoid charge accumulation during the fabrication process. Then, the periodic concentric corrugations are milled into this gold-coated substrate. Two optically thick layers of gold and chromium are then deposited on top of the corrugated substrate to obtain the final gold thickness with a chromium layer on top. As final step, the central nanoaperture is opened with FIB milling. The electron microscope imaging capability of our FIB machine (FEI Strata DB235) enables us to accurately center the ion beam respectively to the corrugations.

Satisfactorily reproducibility is achieved, as the fluorescence measurements have a variability of less than 8% from aperture to aperture. This variation results from minor fabrication deficiencies.

Figure 2 presents typical scanning electron microscopy (SEM) images of the fabricated samples, at the end of the fabrication process (a) and at step 4, to better show the periodic corrugations (b).

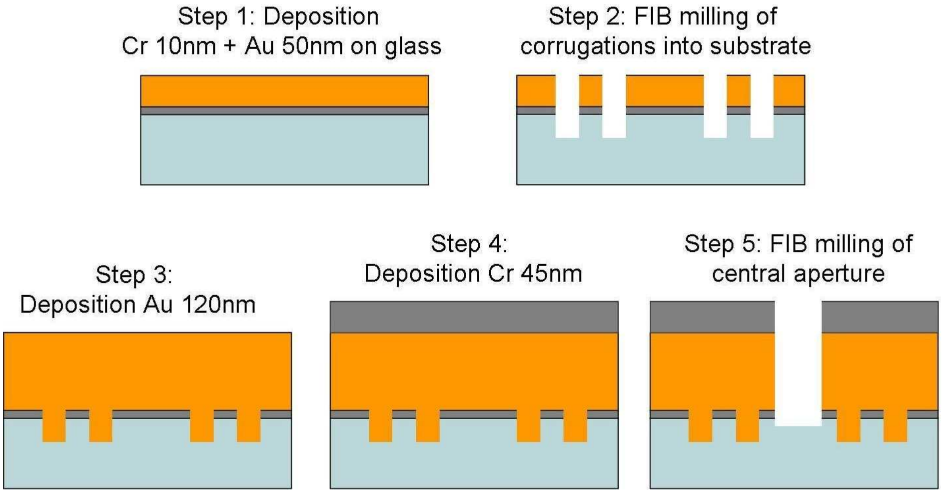

Figure 1: Nanofabrication procedure to realize the corrugated nanoaperture samples.

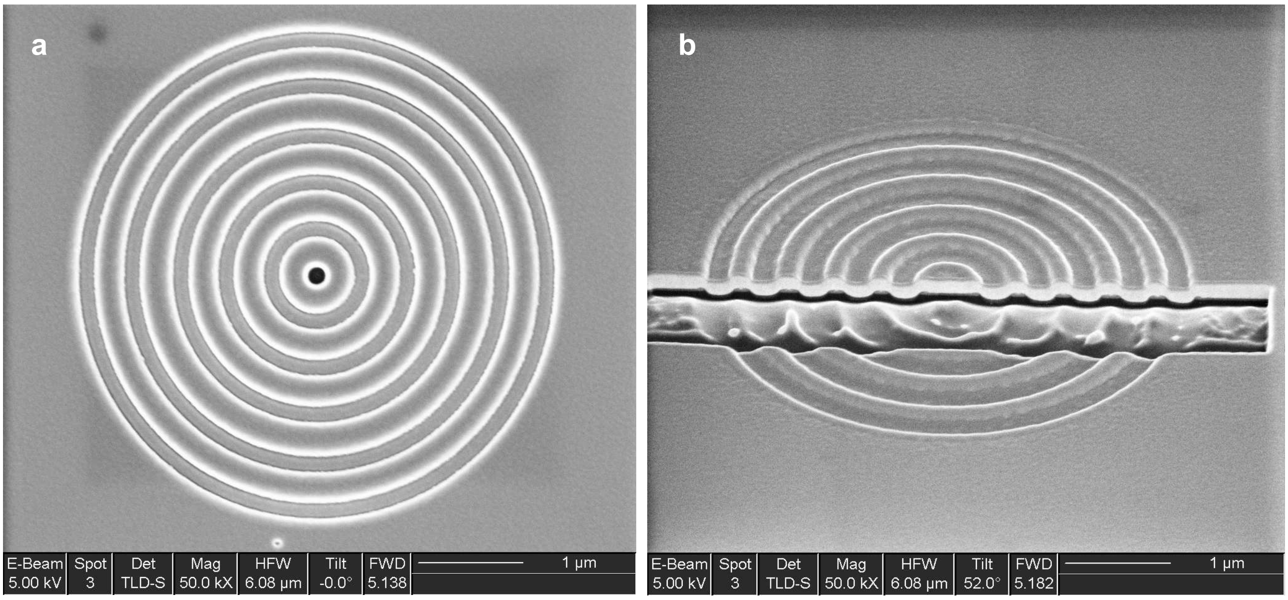

Figure 2: Typical scanning electron microscopy images of the corrugated nanoapertures. (a) is the final structure after milling the central aperture, (b) is a side view of the corrugations on a sacrificed sample where a deep trench has been milled over one half of the structure to allow for angle viewing (this stage is before milling the central aperture, corresponding to step 4 of the nanofabrication procedure).

2 Experimental setup

Our experimental set-up is based on a confocal inverted microscope allowing single aperture studies (Figure 3). It combines FCS and time-correlated lifetime measurements facilities on the same setup to determine the complete photokinetics alteration in a nanoaperture following the procedure derived in reference [1]. We emphasize that for all experiments, a droplet of solution containing Alexa-Fluor 647 molecules is deposited on top of the sample. This droplet acts as a reservoir of molecules, that are constantly diffusing inside the aperture, which strongly limits the effects of photobleaching on our observations. For FCS measurements, the excitation source is a CW He-Ne laser operating at 633 nm. For lifetime measurements, the excitation source is a picosecond laser diode operating at 636 nm (PicoQuant LDH-P-635, repetition rate 80 MHz). A single-mode optical fiber (Thorlabs P3-630A-FC-5) ensures a perfect spatial overlap between the pulsed laser diode and the CW HeNe laser. This guarantees the same excitation spot for FCS and TCSPC and almost same wavelength. Accurate positioning of the nanoaperture at the laser focus spot is obtained with a multi-axis piezoelectric stage (Polytech PI P-517.3CD). A dichroic mirror (Omega Filters 650DRLP) and a long pass filter (Omega Filters 640AELP) separate the fluorescence light from the epi-reflected laser and elastically scattered light. After a 30 μm confocal pinhole conjugated to the sample plane, the detection is performed by two avalanche photodiodes (Micro Photon Devices by PicoQuant MPD-5CTC, with timing jitter about 50 ps and active area 50 μm) with 670 ± 20 nm fluorescence bandpass filters. For FCS, the fluorescence intensity temporal fluctuations are analyzed with a ALV6000 hardware correlator. Each individual FCS measurement is obtained by averaging 10 runs of 10 s duration. For fluorescence lifetime measurements, the photodiode output is coupled to a fast time-correlated single photon counting module (PicoQuant PicoHarp 300). The temporal resolution of our setup for fluorescence lifetime measurements is 120 ps FWHM.

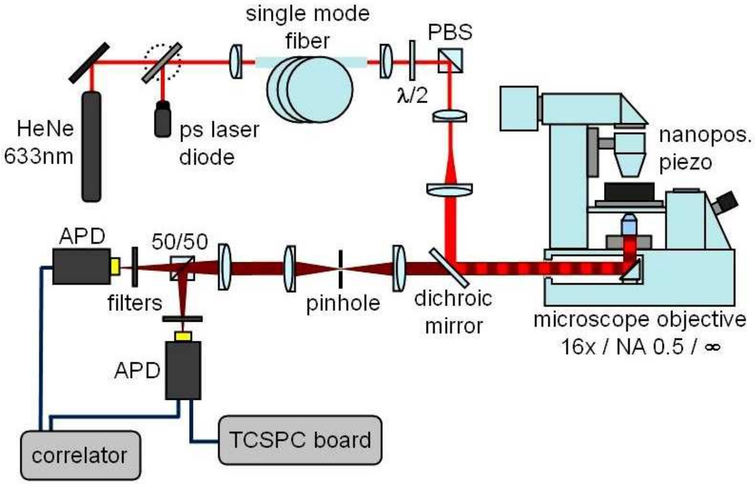

Figure 3: Schematic view of the experimental setup.

The analysis of the FCS data relies on a numerical fit based on a three dimensional Brownian diffusion model [1, 2]:

$$g^{(2)}(\tau) = 1 + \frac{1}{N}\left(1 - \frac{\langle B\rangle}{\langle F\rangle}\right)^2 \left[1 + n_T \exp\left(-\frac{\tau}{\tau_{b_T}}\right)\right] \frac{1}{(1+\tau/\tau_d)\sqrt{1+s^2\,\tau/\tau_d}} \tag{1}$$

where N is the total number of molecules, $\langle F\rangle$ the total signal, $\langle B\rangle$ the background noise, n_T the amplitude of the dark state population, τ_{b_T} the dark state blinking time, τ_d the mean diffusion time and s the ratio of transversal to axial dimensions of the analysis volume, which we set to $s = 1$ for the nanoapertures and $s = 0.2$ for the open solution reference.[2] Numerical fit of the FCS data following Equation (1) provides the average number of molecules N which is used to compute the fluorescence count rate per molecule $CRM = (\langle F\rangle - \langle B\rangle)/N$. The background noise $\langle B\rangle$ originates mainly from the back-reflected laser light and from gold autofluorescence. At 500 μW excitation powers, it typically amounts to $\langle B\rangle = 1$ kHz, which is almost negligible as compared to the count rates per molecule in the nanoapertures in the range 10-30 kHz.

The assumption of a free diffusion model is obviously not fulfilled within a nanoaperture. However, as already demonstrated in references [1, 2] this model suffices to determine the average number of molecules N and the fluorescence count rate per molecule CRM. The key point is that to reliably determine N, one only needs to focus on the amplitude of the correlation function as the lag time goes to zero. Basically, the number of detected molecules N is proportional to the inverse of the correlation function amplitude at origin $g^{(2)}(0)$. The expression of $g^{(2)}(0)$ given by Equation (1) is independent of the shape of the excitation field and the type of diffusion statistics, and is therefore sufficient to reliably estimate N. This is a direct consequence of the Poissonian nature of the probability to find a molecule in the observation volume at a given time. This procedure holds for a stationary system and a dilute solution where the spatial correlation length of concentration fluctuations is much smaller than the detection volume, which is clearly the case for our study. To fully take into account the fast photokinetics of a real dye (photoisomerization and triplet blinking), one has to consider the first channels of the correlogram (with characteristic times below 10 μs), yet the knowledge of the shape of the correlation function at larger times is not necessary.

As shown in Figure 4, the agreement between the expression in Equation (1) and the experimental data is very good. Using a more elaborate model would mostly result in introducing more noise in the data analysis, without bringing much more insights. Determining the molecular diffusion coefficient in the case of the nanoapertures is a complex task, as it requires to take into account various artifacts brought by the non-Gaussian observation volume. The restriction of the range available for diffusion affects the diffusion time (millisecond time range), but leaves unaffected the correlation amplitude and the fast components of the correlogram (triplet photokinetics). Still, we point out that relative measurements of variations in diffusion times are always possible, and are sufficient to assess enzymatic activity, chemical rate constants, or binding rates.

To measure the fluorescence decay rate, we use the following procedure that takes into account the limited resolution of our setup. Careful analysis of the instrument response function (IRF) reveals a double exponential decay : $IRF(t) \propto A_1 \exp(-k_1 t) + A_2 \exp(-k_2 t)$ with $A_1 = 0.516$, $A_2 = 0.484$, $k_1 = 5.7\ 10^9\ \mathrm{s}^{-1}$ and $k_2 = 20.7\ 10^9\ \mathrm{s}^{-1}$, as already determined in reference [1]. The output signal $O(t)$ of the TCSPC card corresponds to the convolution of the system IRF with the averaged fluorescence decay, which is assumed to be mono-exponential. Convolving a mono-exponential fluorescence decay with a double exponential IRF results in a triple exponential :

$$O(t) \propto \left(\frac{A_1}{k_1 - k_{tot}} + \frac{A_2}{k_2 - k_{tot}}\right) \exp(-k_{tot} t) - \frac{A_1}{k_1 - k_{tot}} \exp(-k_1 t) - \frac{A_2}{k_2 - k_{tot}} \exp(-k_2 t) \qquad (2)$$

where k_{tot} is the molecular total deexcitation rate, and A_1, A_2, k_1 and k_2 are fixed parameters set by the IRF analysis. While analyzing the experimental decay curves, k_{tot} is thus kept as the only free varying parameter. This procedure yields a fluorescence lifetime of 1.0 ns for Alexa Fluor 647 in open water solution, which corresponds well to the data in the literature.

3 Raw experimental data with the 0.5 NA objective

Figure 4 presents a typical set of raw experimental data, taken with the microscope objective of 0.5 NA (average excitation power of 1 mW) on the confocal reference on open A647 solution, the nanoaperture without corrugations, and the corrugated nanoaperture. Numerical analysis of this data following the models of Equations (1) and (2) yield the folowing results: for the open solution case, number of molecules $N = 110$ (concentration diluted 100x compared to the concentration used for the nanoapertures), diffusion time $\tau_d = 664$ μs, triplet amplitude $n_T = 0.65$, triplet blinking time $\tau_T = 1.8$ μs, count rate per molecule $CRM = 1.08$ kHz, fluorescence lifetime 1.01 ns. For the nanoaperture without corrugations, $N = 5.4$, $\tau_d = 61$ μs, $n_T = 0.77$, $\tau_T = 0.8$ μs, $CRM = 11.9$ kHz, fluorescence lifetime 377 ps. For the nanoaperture with corrugations, $N = 12.7$, $\tau_d = 64$ μs, $n_T = 0.48$, $\tau_T = 0.7$ μs, $CRM = 56.9$ kHz, fluorescence lifetime 551 ps.

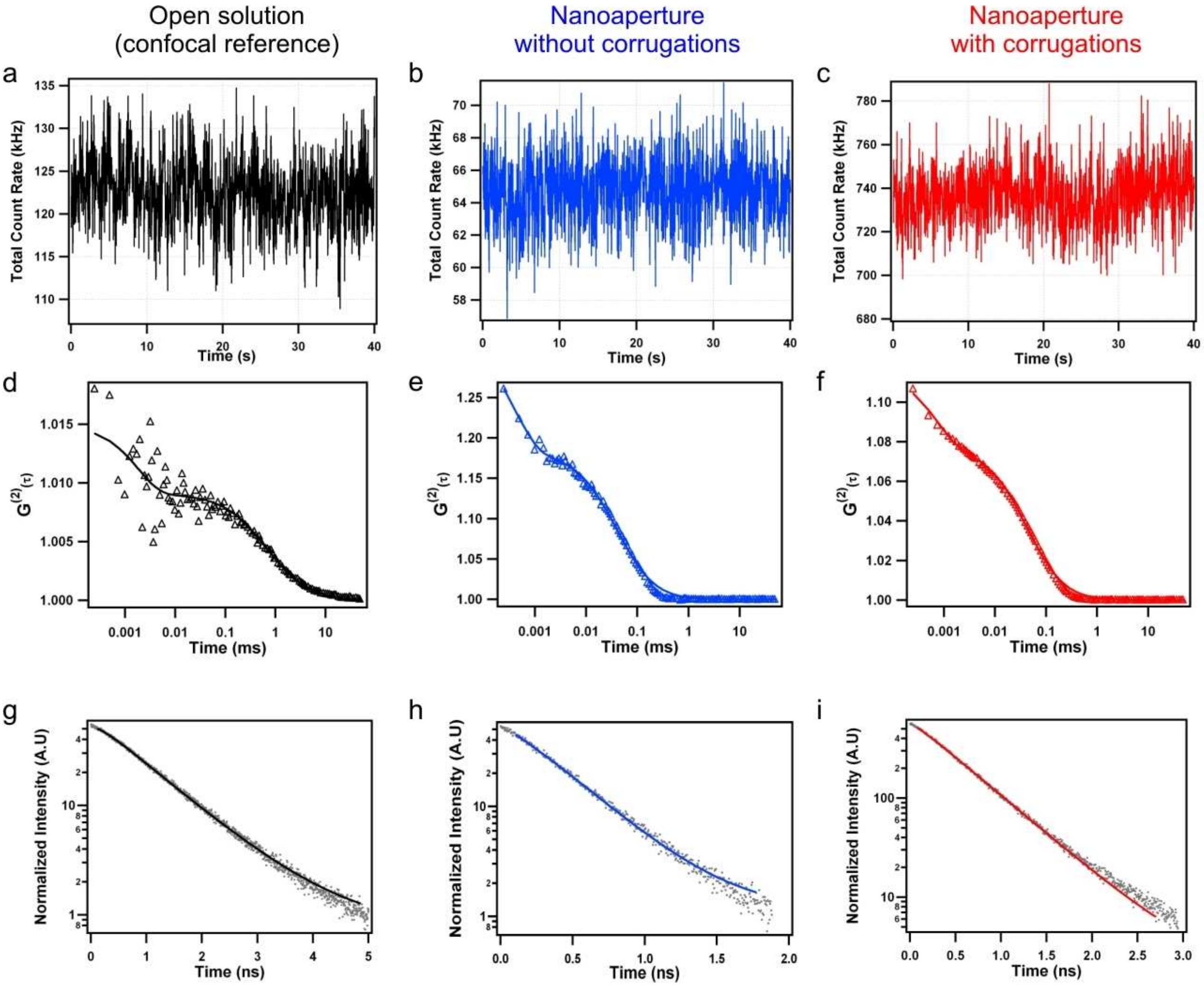

Figure 4: Raw experimental data for the confocal reference on open A647 solution (a),(d),(g), the nanoaperture without corrugations (b),(e),(h) and the corrugated nanoaperture (c),(f),(i), while using the microscope objective of 0.5 NA. All data displayed here are taken with an average excitation power of 1 mW. (a)-(c) represent the raw fluorescence time trace. (d)-(f) are the corresponding fluorescence intensity correlation function, and the numerical fits using Equation (1). (g)-(i) are the fluorescence intensity distributions used to determine the fluorescence lifetime.

4 Fluorescence enhancement characterization for NA=0.5

To complete the data presentation of Figure 2 of the main document, Table 1 summarizes the fitting parameters A, I_s for the fluorescence count rate per molecule $CRM = A\, I_e/(1 + I_e/I_s)$, in the case a 0.5 NA water immersion objective is used. Table 2 presents the enhancement factors relative to open solution for the fluorescence signal η_F, the excitation rate η_{exc}, the emission rate η_{em} and the total decay rate η_{tot} (inverse of fluorescence lifetime).

	Aperture with corrugations	Aperture w/o corrugations	Reference solution
A (kHz/μW)	0.105	1.89 $\times 10^{-2}$	1.37 $\times 10^{-3}$
I_s (μW)	1190	2795	3420

Table 1: Fitting parameters of the fluorescence count rate per molecule with the 0.5 NA objective (Figure 2(b) of the main document).

	Fluorescence η_F	Excitation η_{exc}	Emission η_{em}	Decay rate η_{tot}
Aperture with corrugations	76.6	5.5	26.7	1.9
Aperture without corrugations	13.8	3.2	11.3	2.5

Table 2: Enhancement factors relative to open solution with the 0.5 NA objective (Figure 2(d) of the main document).

5 Fluorescence enhancement characterization for NA=1.2

Figure 5 presents the same analysis as for Figure 2 of the main document, but for a 1.2 NA water immersion microscope objective, instead of the 0.5 NA used previously. As a consequence of the smaller spot size of the excitation laser spot and larger fluorescence collection efficiency with a 1.2 NA, the enhancement factors are lower comparing a corrugated nanoaperture to an aperture without corrugations or to the reference open solution case. In the case of a 1.2 NA excitation, the laser spot size is about 530 nm in diameter, so that less than one corrugation is illuminated by the laser spot. The fitting parameters for the fluorescence count rate per molecule and the enhancement factors relative to open solution are respectively presented in Tables 3 and 4.

	Aperture with corrugations	Aperture w/o corrugations	Reference solution
A (kHz/μW)	2.26	1.29	0.095
I_s (μW)	126	266	510

Table 3: Fitting parameters of the fluorescence count rate per molecule with the 1.2 NA objective (Figure 5(b)).

	Fluorescence η_F	Excitation η_{exc}	Emission η_{em}	Decay rate η_{tot}
Aperture with corrugations	23.8	7.7	5.9	1.9
Aperture without corrugations	13.6	3.7	7.0	1.9

Table 4: Enhancement factors relative to open solution with the 1.2 NA objective (Figure 5(d)).

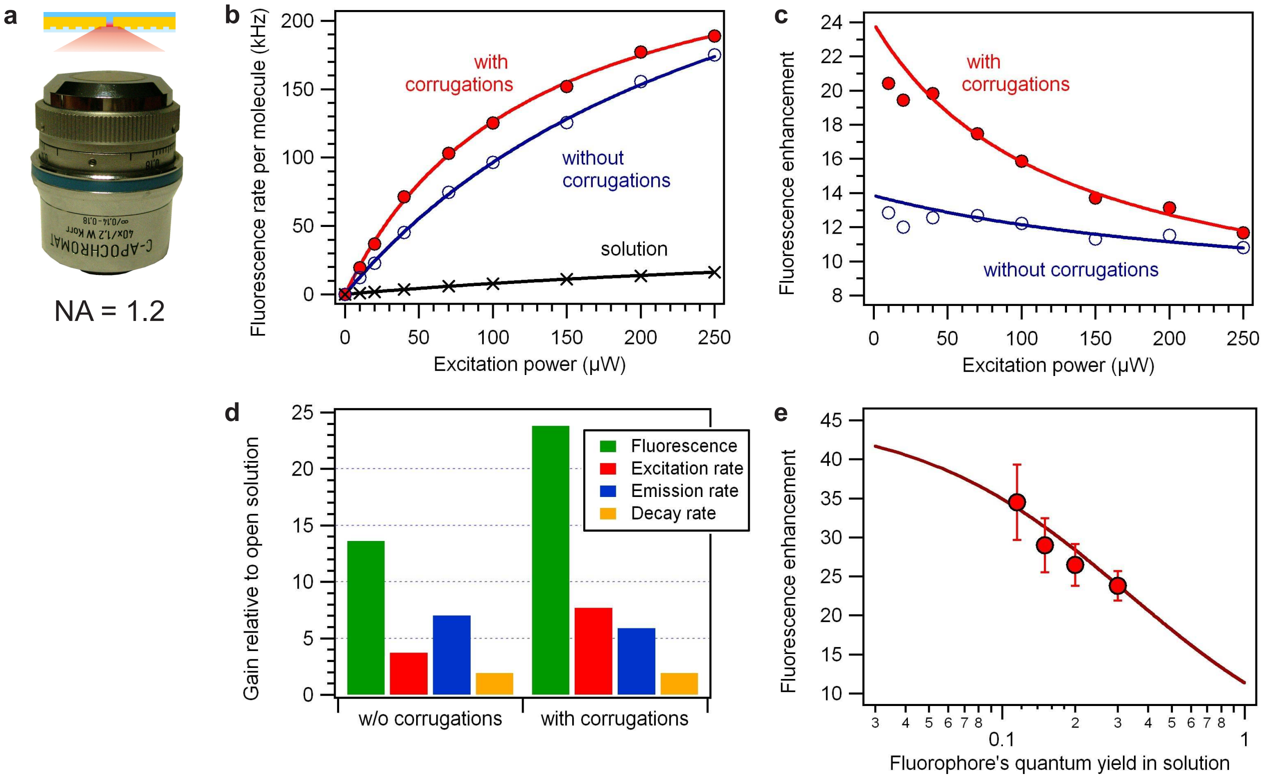

Figure 5: (a) Investigations of the detected fluorescence count rate per molecule with a 1.2 NA water immersion microscope objective, instead of the 0.5 NA used in the main document. (b) Fluorescence count rate per molecule versus the excitation power. Markers are experimental data, solid lines are numerical fits. (c) Fluorescence enhancement factors relative to the standard confocal case (open solution), as deduced from the data in (b). (d) Contribution of excitation and emission gains to the overall fluorescence enhancement. Decay rate corresponds to the reduction of the fluorescence lifetime. (e) Evolution of the fluorescence enhancement factor versus Alexa Fluor 647 measured quantum yield ϕ in a water-methyl viologen solution. From right to left, the methyl viologen concentration increases from 0 up to 60 mM. The continuous line is a model based solely on the data displayed in (d). It is not a numerical fit of the experimental data points, there are no free parameters.

6 Raw experimental data with the 1.2 NA objective

Figure 6 presents a typical set of raw experimental data, taken with the microscope objective of 1.2 NA (average excitation power of 70 μW) on the confocal reference on open A647 solution, the nanoaperture without corrugations, and the corrugated nanoaperture. Numerical analysis of this data following the models of Equations (1) and (2) yield the folowing results: for the open solution case, number of molecules $N = 98.7$ (concentration diluted 100x compared to the concentration used for the nanoapertures), diffusion time $\tau_d = 109$ μs, triplet amplitude $n_T = 0.89$, triplet blinking time $\tau_T = 1.8$ μs, count rate per molecule $CRM = 5.9$ kHz, fluorescence lifetime 989 ps. For the nanoaperture without corrugations, $N = 5.6$, $\tau_d = 26$ μs, $n_T = 0.67$, $\tau_T = 0.8$ μs, $CRM = 73.9$ kHz, fluorescence lifetime 507 ps. For the nanoaperture with corrugations, $N = 16$, $\tau_d = 39$ μs, $n_T = 0.67$, $\tau_T = 1.0$ μs, $CRM = 105.1$ kHz, fluorescence lifetime 525 ps.

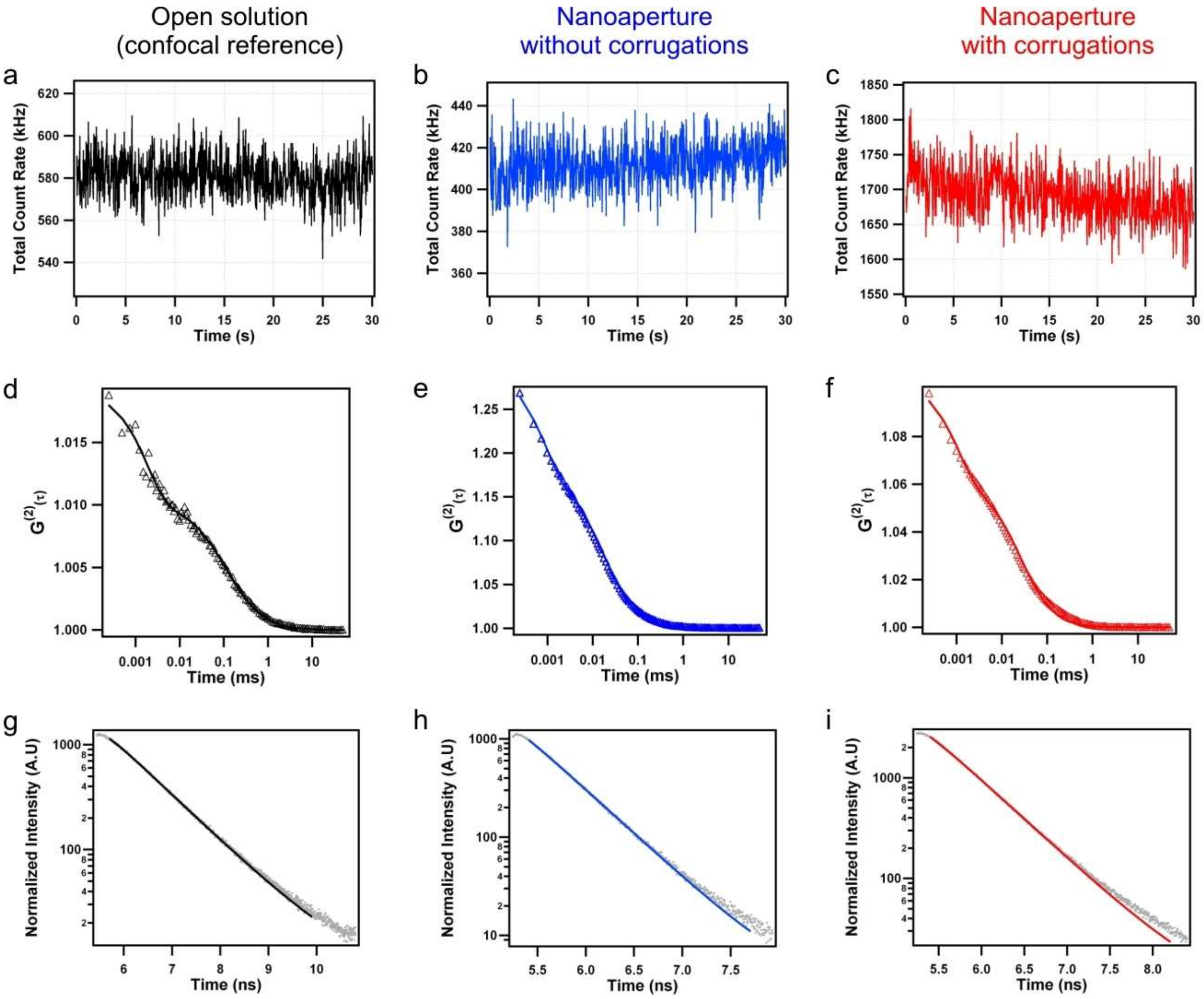

Figure 6: Raw experimental data for the confocal reference on open A647 solution (a),(d),(g), the nanoaperture without corrugations (b),(e),(h) and the corrugated nanoaperture (c),(f),(i), while using the microscope objective of 1.2 NA. All data displayed here are taken with an average excitation power of 70 μW. (a)-(c) represent the raw fluorescence time trace. (d)-(f) are the corresponding fluorescence intensity correlation function, and the numerical fits using Equation (1). (g)-(i) are the fluorescence intensity distributions used to determine the fluorescence lifetime.

7 Methyl viologen as a fluorescence quencher

We report here a standard Stern-Volmer analysis of the quenching effect of methyl viologen on the fluorescence emission of the Alexa Fluor 647 dye. We measure the evolution of the total fluorescence intensity I_f and the fluorescence lifetime τ while the methyl viologen concentration $[\mathrm{MV}^{2+}]$ is increased, and we compare these values to the reference intensity I_{f0} and lifetime τ_0 when no quencher is present. For a standard dynamic quenching of A647 fluorescence, the intensity and lifetime ratios follow the Stern-Volmer relationship:

$$\frac{I_{f0}}{I_f} = \frac{\tau_0}{\tau} = 1 + k_q\, \tau_0\, [\mathrm{MV}^{2+}] \tag{3}$$

where k_q is the quenching rate. Figure 7 presents our experimental results, which follow nicely the Stern-Volmer relation. This confirms the dynamic quenching of A647 by the methyl viologen with a rate of $k_q = 2.4 \times 10^{10}$ s^{-1}.M^{-1}. We use the Stern-Volmer relation derived experimentally to calibrate the A647 quantum yield in the methyl viologen solution for the experiments reported in Figure 2(e) (main document) and Figure 5(e). We carefully checked that A647 emission spectrum and absorption coefficient remained unchanged within the range of methyl viologen concentration used here.

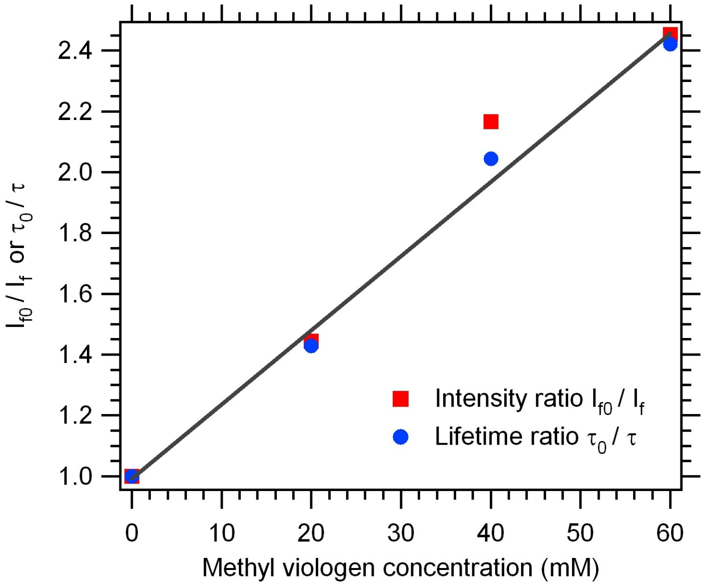

Figure 7: Stern-Volmer plot of the fluorescence intensity and fluorescence lifetime ratios versus the methyl viologen concentration.

8 Spectral analysis

The periodic corrugations around the nanoaperture act as a grating, which may influence the emission spectrum of the molecules due to the wavelength-dependent resonant conditions. The data reported in the main document correspond to a spectral integration from 650 to 690 nm. This covers most of the dye emission spectrum but prevents any observation of an alteration of the emission spectrum, especially if resonant gratings are used. To detail the fluorescence spectrum, the fluorescence beam was sent to a spectrograph (Jobin-Yvon SPEX 270M) equipped with a nitrogen-cooled CCD detector. The raw spectrum is then normalized by the number of molecules given by FCS. This procedure allows to directly compare the intensities obtained *per single molecule* for different apertures with and without periodic corrugations. It directly yields the average fluorescence spectrum per single emitter.

Fluorescence spectra per A647 molecule are presented on Figure 8(a). The detected count rate per molecule is significantly enhanced over the whole A647 emission spectrum. Interestingly, the shapes of the spectra do not change noticeably between open solution and the different apertures. No clear spectral resonance is visible while using nanoapertures with periodic corrugations. As expected for this type of sample, the resonance is sufficiently wide spectrally to cover the 630-700 nm region. This spectral range is also further enlarged by the extra chromium layer used to reduce the transmission through the corrugated aperture.

As we are able to measure the fluorescence spectrum per molecule, we can directly deduce the fluorescence enhancement for each emission wavelength. This provides the spectral enhancement factors displayed in Figure 8(b), which are the ratio of the spectrum recorded for an aperture by the reference spectrum in open solution. Within the range 650-690 nm, the apparent value of the fluorescence enhancement slightly increases with the wavelength, showing a higher enhancement for red-shifted wavelengths, as already observed.[2] Both curves with and without corrugations show qualitatively the same behavior. Our data also indicate that the optimal emission wavelength yielding the larger enhancement tends to be red-shifted, hereby confirming the expected scaling effect.[2]

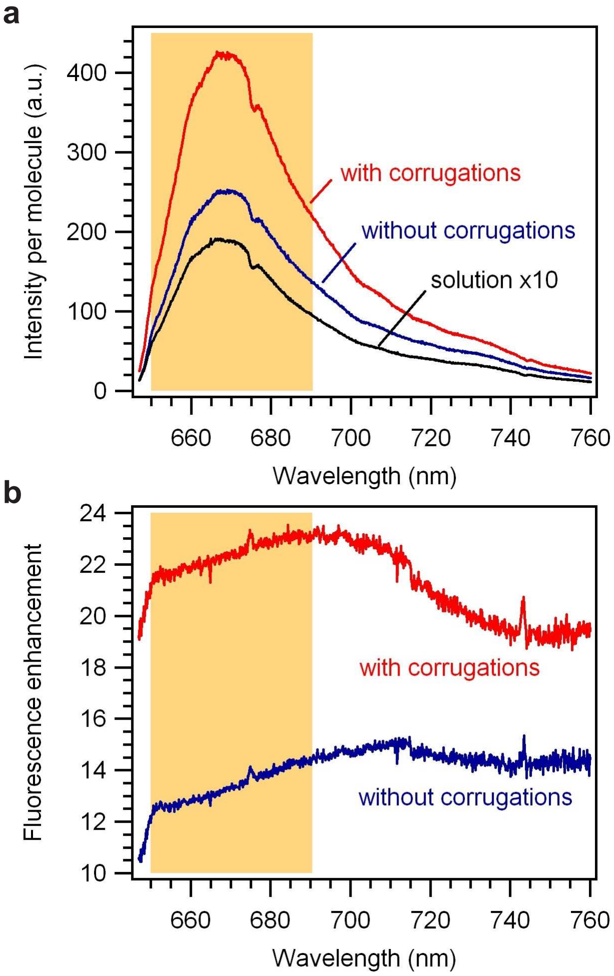

Figure 8: Spectral analysis of the fluorescence enhancement for A647 dyes diffusing in nanoapertures with and without corrugations, for 1.2 NA illumination. (a) Integrated fluorescence signal *normalized per molecule* vs. emission wavelength, for a 10 s acquisition time. (b) Fluorescence enhancement factor vs. emission wavelength. The orange region correspond to the 650-690 nm region used for fluorescence integration in the data presented in the main document.

9 Influence of numerical aperture used for collection

The radiation patterns as displayed in Figure 3 of the main document contain all the necessary information to fully represent the fluorescence emission dependence on (i) the emission angle and (ii) the numerical aperture used for collection. Figure 9 presents the results of the calculation of the total integrated power for a single nanoaperture within an angular cone of extension $\pm\alpha$, where α is given by the numerical aperture used for collection NA=$n \sin\alpha$, with $n = 1$ for dry (air) objectives and $n = 1.33$ for water immersion objectives. If $I_f(\theta)$ denotes the fluorescence radiated power along the direction given by the polar angle θ, then the data presented in Figure 9 corresponds to the integrated power

$$P_f = \int_0^{\alpha} I_f(\theta)\, 2\pi\theta d\theta \tag{4}$$

The term in $2\pi\theta d\theta$ is a consequence that the fluorescence is integrated over the bi-dimensional circular surface of the fluorescence beam. There is no term in $\sin(\theta)$ as we assume the microscope objective is perfectly corrected from spherical aberrations and is hence transforming a spherical wavefront into a planar wavefront (which is detected by the CCD camera in the objective's back focal plane).

As expected, the integrated fluorescence power grows with the collection angle. We note that the integrated fluorescence with the corrugated aperture is significantly higher than for the non-corrugated sample. This is a direct consequence of the beaming observed for the fluorescence light towards the angles close to the normal of the sample. Moreover, the ratio of the curves for a given NA in Figure 9 directly yield the enhancement factor in collection brought by the periodic corrugations.

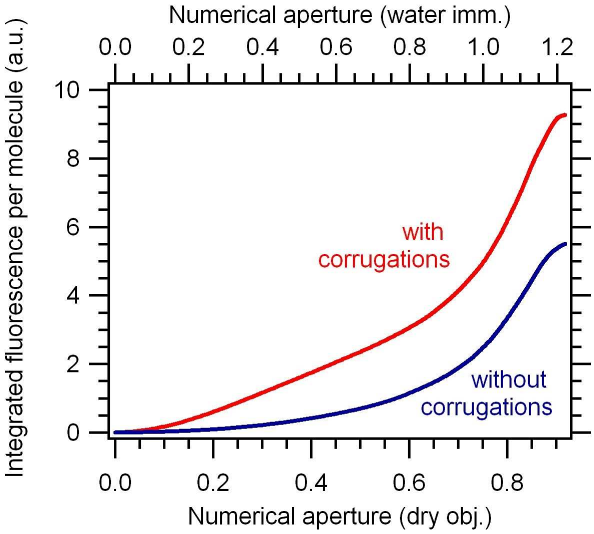

Figure 9: Integrated fluorescence power *per molecule* P_f versus the numerical aperture used for collection.

10 Image scan of a single nanoaperture

To complete the data presented in Figure 4 of the main document, we show here the results of the same experiment for a single nanoaperture without corrugations (Figure 10). The fluorescence from the central aperture is measured (fixed detection path) while the excitation laser spot focused by a 1.2 NA water immersion objective is scanned over the sample. The characteristic butterfly shape obtained for corrugated apertures is absent for an aperture without corrugations. Let us emphasize that we use the same settings for the image intensity display of each image (linear scale, normalization to 1, saturation level at 0.4), so that the different images can be directly compared. The lack of periodic corrugations does not provide the momentum necessary to launch surface electromagnetic waves while the laser excitation spot is scanned over the sample. This further confirms the antenna capacity of the corrugations.

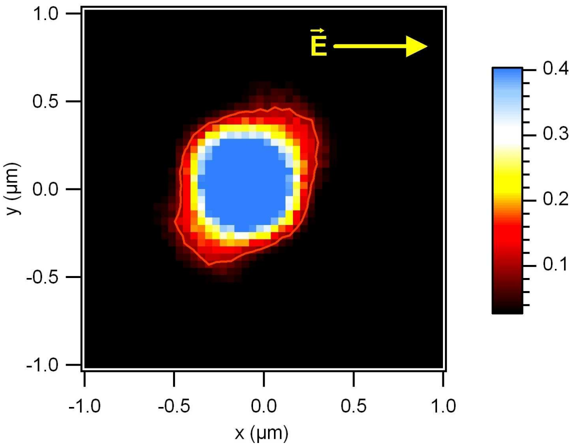

Figure 10: Same as Figure 4 of the main document, for a single nanoaperture with no corrugations, using the same image settings. The fluorescence from the central aperture is collected while the excitation laser spot focused by a 1.2 NA water immersion objective is scanned over the sample. The fluorescence detection path is not scanned, only the emission from the fixed central aperture is measured while the excitation spot is moved.

11 Photon antibunching experiment

The experimental setup used for fluorescence lifetime measurements can easily be modified to realize a Hanbury-Brown-Twiss type of photon detection experiment, where the two photodiodes are connected to the start and stop inputs of the fast photon counting module (PicoHarp 300).[3] This type of detection is commonly used to investigate the photon emission statistics, specially to reveal photon antibunching. The photon antibunching corresponds to the property that individual quantum emitters generate photons one by one, which are separated by a characteristic time interval.

As we are dealing here with diffusing molecules that have a stochastic Brownian motion, the fluorescence emission will bear additional fluctuations due to the random presence of the molecular emitters.[3] Consequently, the fluorescence intensity correlation function $g^{(2)}(\tau)$ will never go below unity, which means that the emission statistics will always follow a classical distribution. However, it can be shown that $g^{(2)}(0) = 1$, and that $g^{(2)}(\tau) > g^{(2)}(0)$ for $\tau > 0$.[3] This corresponds to the interesting case where photon antibunching is clearly present, but the statistics are not sub-Poisson. The physical origin of this effect is to be found in the fact that the photon contributing to the distribution at $\tau > 0$ originates from a different molecule than the initial photon that defined $\tau = 0$.

The high fluorescence count rates detected in the case of the corrugated nanoaperture are specially appealing to investigate this antibunching effect for molecules in solution. In order to obtain the highest contrast in the correlation function $g^{(2)}(\tau)$, we set the A647 concentration so that the average number of molecules diffusing inside the nanoaperture is close to one, $N \approx 1$. Figure 11 presents the recorded correlation function in the case of a corrugated nanoaperture under pulsed excitation. The detected count rates have been normalized so that the value at $\tau = 0$ equals to unity. In that framework, the data displayed in Figure 11 can directly be analyzed as the fluorescence intensity correlation function $g^{(2)}(\tau)$ for different lag times τ in the nanosecond regime. The different peaks at $\tau = 12.5$, 25, 37.5 ns are a direct consequence of the pulsed laser excitation with 80 MHz repetition rate. A fluorescence photon can be emitted only when an excitation photon is present. The lower peak at $g^{(2)}(0)$ than $g^{(2)}(12.5)$, $g^{(2)}(25)$,... reveals the presence of antibunching on the emission, even if the photon statistics are not sub-Poissonian. The differences between the peaks at $\tau \neq 0$ and the peak at $\tau = 0$ corresponds to the inverse of the number of molecules $1/N$. It is well close to one, as expected from the FCS calibration of the molecular concentration.

This antibunching experiment further confirms the single molecule nature of our observations, independently on the FCS method. The high signal to noise ratio in Figure 11 can only be achieved thanks to the large fluorescence count rates per molecule in a corrugated nanoaperture. It is a supplementary witness of the bright single molecule fluorescence emission in nanoapertures.

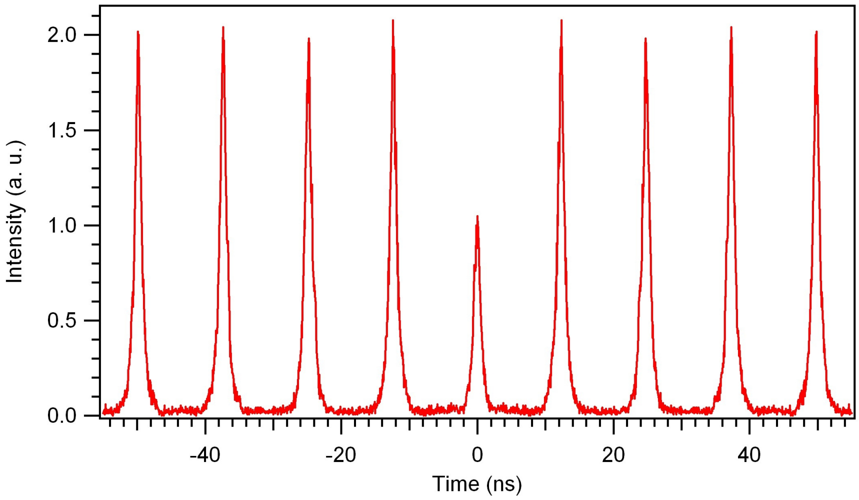

Figure 11: Normalized fluorescence intensity correlation function $g^{(2)}(\tau)$ in a Hanbury Brown Twiss experiment with a corrugated nanoaperture and an average $N \approx 1$ A647 molecule in the nanoaperture observation volume. The microscope objective has 1.2 NA, the average excitation power is 150 μW, the pulse repetition rate is 80 MHz, and the total integration time is 200 s.

References

[1] Wenger, J.; Gérard, D.; Bonod, N.; Popov, E.; Rigneault, H.; Dintinger, J.; Mahboub, O.; Ebbesen, T. W. *Opt. Express* **2008**, *16*, 3008-3020.

[2] Gérard, D.; Wenger, J.; Bonod, N.; Popov, E.; Rigneault, H.; Mahdavi, F.; Blair, S.; Dintinger, J.; Ebbesen, T. W. *Phys. Rev. B* **2008**, *77*, 045413.

[3] Mets, Ü. Antibunching and rotational diffusion in FCS, in *Fluorescence correlation spectroscopy: theory and applications*, edited by Rigler, R. ; Elson, E. S. (Springer, Berlin, 2001).

Chapitre 3

Microsphères diélectriques

Ces travaux portent sur l'étude de la focalisation de la lumière par des sphères micrométriques diélectriques, et sur leur exploitation potentielle en microscopie de fluorescence. Comparativement aux nano-ouvertures métalliques, les microsphères proposent une structure de très faible coût (elles sont disponibles commercialement à grande échelle avec un excellent contrôle de forme). De façon surprenante, nous montrons que l'efficacité de telles microstructures peut s'avérer très bonne, et qu'il est possible sous certaines conditions de dépasser les limites imposées par la diffraction en microscopie confocale classique.

Lorsqu'une microsphère en verre synthétique de quelques microns de diamètre est éclairée par un faisceau de lumière, un phénomène spécial se produit. La microsphère focalise la lumière en agissant comme une lentille micrométrique, mais en plus le minuscule jet de lumière produit possède des propriétés optiques bien particulières : un très faible diamètre, égal à une longueur d'onde et une faible divergence. Ainsi, ce faisceau (appelé nanojet photonique) conserve une excellente concentration lumineuse sur une distance relativement longue de plusieurs micromètres. Des performances exceptionnelles qui surpassent celles de systèmes optiques bien plus évolués, alors qu'une microsphère est très un élément très simple.

Nous avons effectué la première observation directe de ce faisceau, et quantifié ses propriétés optiques (largeur transverse, divergence) grâce à un montage de microscopie confocale à balayage [1]. Ceci a permis la première confrontation théorie-expérience de ce phénomène (figure 3.1).

---

[1] P. Ferrand, et al., Direct imaging of photonic nanojets, Opt. Express 16, 6930-6940 (2008).

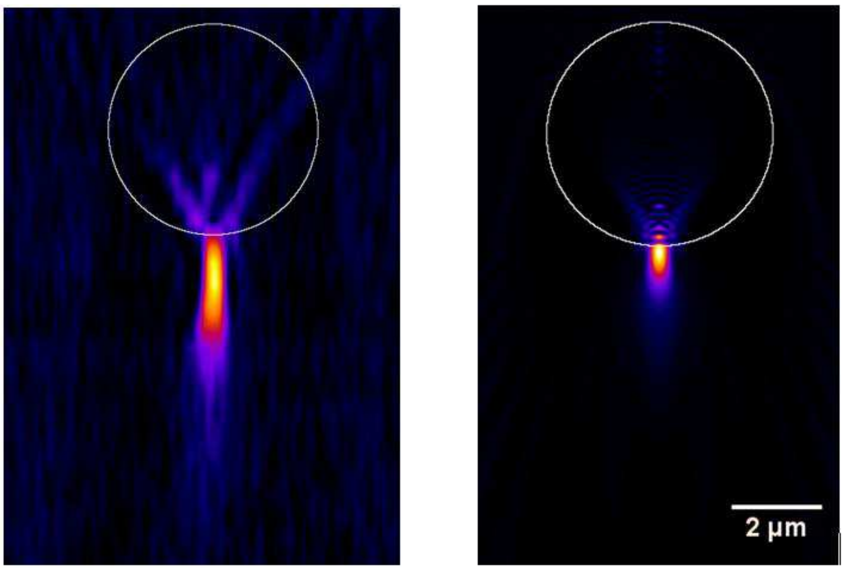

Fig. 3.1. Comparaison expérience (gauche) et théorie (droite) pour la focalisation d'une onde plane par une microsphère en polystyrène de 5µm de diamètre.

Nous avons également mis en évidence un phénomène nouveau de confinement électromagnétique à 3 dimensions sous la limite de diffraction [2,3]. Lorsqu'une microsphère est éclairée par un faisceau gaussien fortement focalisé, si le décalage entre la microsphère et le point de focalisation du faisceau laser est correctement choisi, des interférences entre le champ incident et le champ diffusé par la sphère permettent de confiner la lumière dans un volume de l'ordre de $(\lambda/n)^3$. Ce faible volume optique est associé à un renforcement de l'intensité locale d'un facteur 2,5 (figure 3.2).

Ces propriétés optiques remarquables ont été utilisées pour améliorer très significativement la détection de molécules individuelles par fluorescence [2] (article Optics Express ci-après). De plus, les molécules fluorescentes servent de sondes locales pour caractériser (i) le confinement lumineux et (ii) l'exaltation locale d'intensité optique. En agissant comme une lentille positionnée directement dans le voisinage proche des molécules, la microsphère permet de mieux éclairer et de mieux collecter la lumière produite par les molécules. Nous avons pu quantifier une réduction d'un facteur 10 du volume sondé, ainsi qu'une exaltation x5 du signal de fluorescence par molécule [2]. Ces valeurs sont en bon accord avec les simulations numériques par méthode de Mie ou FDTD [3]. Nous avons également montré qu'une combinaison de microsphères permet d'atteindre des résultats similaires à partir d'une onde plane, réduisant ainsi la contrainte de disposer d'un objectif de forte ouverture numérique en amont de la microsphère [4].

---

[2] D. Gérard, et al, Strong electromagnetic confinement near dielectric microspheres to enhance single-molecule fluorescence, Opt. Express 16, 15297-15303 (2008).

[3] A. Devilez, et al., Three-dimensional subwavelength confinement of light with dielectric microspheres, Opt. Express 17, 2089-2094 (2009).

[4] A. Devilez, et al, Transverse and longitudinal confinement of photonic nanojets by compound dielectric microspheres, Proc. of SPIE, Vol. 7393, pp.73930E-1 (2009)

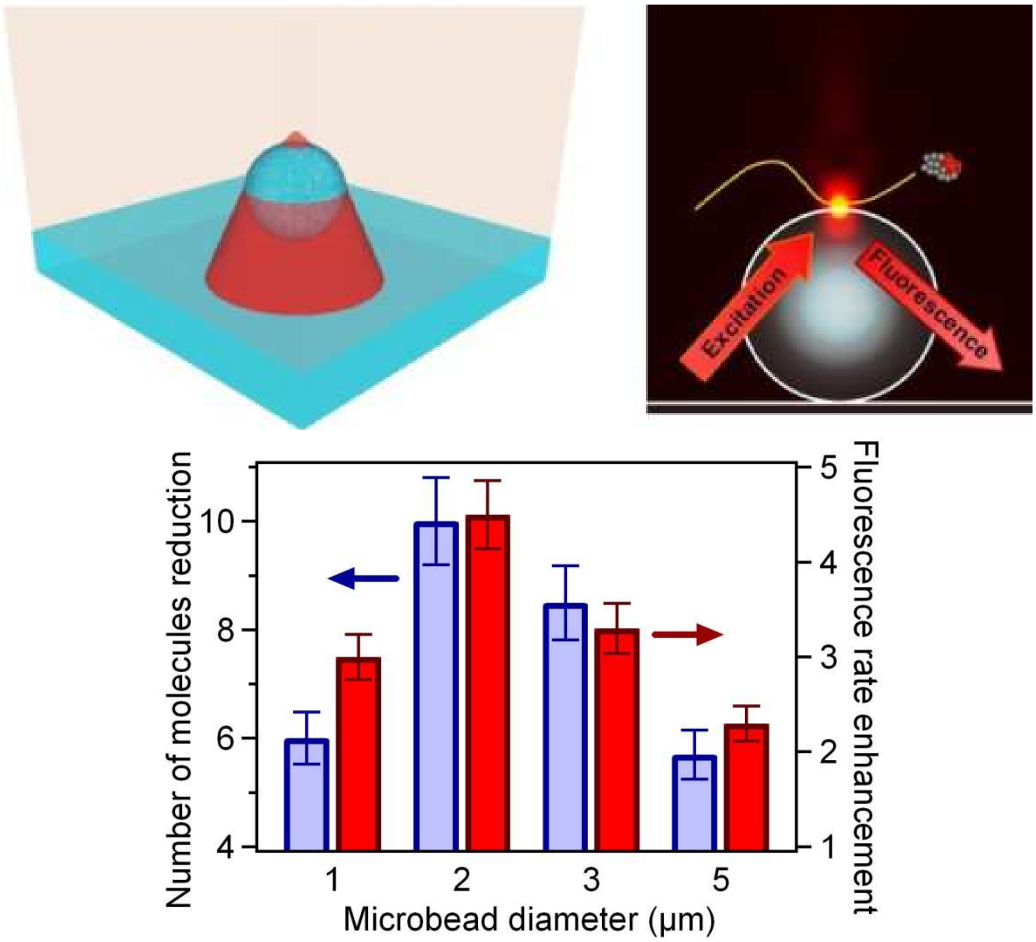

Fig. 3.2. Principe de l'utilisation d'une microsphère de polystyrène pour exalter l'émission de fluorescence d'une molécule individuelle, la carte de champ en fond correspond à un calcul pour une sphère de 2 µm de diamètre.

Une étude plus détaillée a ensuite été menée dans la référence [5] en utilisant la procédure de caractérisation par FCS et mesure de temps de vie qui avait été développée pour les nano-ouvertures métalliques (article JOSA B ci-après). Cette procédure permet de quantifier précisément les renforcements d'intensité d'excitation (mesuré à x2,5 pour les conditions optimales), ainsi que le renforcement en efficacité de collection (x2 pour la meilleure configuration). Dans le cas des microsphères diélectriques, la modification du rendement quantique est négligeable (mesurée pour une variation relative à moins de 8%), aucun transfert non-radiatif d'énergie ne vient affecter les mesures (contrairement au cas des antennes plasmoniques).

---

[5] D. Gérard, et al., Efficient excitation and collection of single molecule fluorescence close to a dielectric microsphere, J. Opt. Soc. Am. B 26, 1473-1478 (2009).

Ces démonstrations ouvrent de nouvelles perspectives pour l'amélioration des dispositifs de détection de molécules et de caractérisation de fluorescence allant bien au-delà des limites de diffraction. Un brevet a été publié sur cette technologie.

Nous avons également étendu cette technologie au cas de l'illumination à deux photons [6]. Grâce au renforcement quadratique sur l'intensité pompe, les gains peuvent être plus forts que dans le cas de la fluorescence à un photon. Nous avons ainsi pu obtenir des gains de fluorescence par molécule supérieurs à 10 avec une microsphère optimisée de 3 µm de diamètre. Il est à noter que ces gains ne s'accompagnent d'aucune augmentation notable du bruit de fond de photoluminescence, contrairement au cas des antennes métalliques. En proposant une structure simple, robuste et de très bas coût, les microsphères diélectriques sont des concurrents pertinents aux nanoantennes plasmoniques dans le cas de la fluorescence moléculaires. Les gains sont moins importants avec des microsphères, mais ceci est compensé par des pertes quasi-négligeables, et une absence de bruit de photoluminescence de la structure.

---

[6] H. Aouani, et al, Two-photon fluorescence correlation spectroscopy with high count rates and low background using dielectric microspheres, Biomed. Opt. Express 1, 1075-1083 (2010)

Strong electromagnetic confinement near dielectric microspheres to enhance single-molecule fluorescence

**Davy Gérard, Jérôme Wenger *, Alexis Devilez, David Gachet,
Brian Stout, Nicolas Bonod, Evgeny Popov, and Hervé Rigneault**

Institut Fresnel, Aix-Marseille Université, CNRS, 13397 Marseille, France
* *Corresponding author: jerome.wenger@fresnel.fr*

Abstract: Latex microspheres are used as a simple and low-cost means to achieve three axis electromagnetic confinement below the standard diffraction limit. We demonstrate their use to enhance the fluorescence fluctuation detection of single molecules. Compared to confocal microscopy with high numerical aperture, we monitor a detection volume reduction of one order of magnitude below the diffraction limit together with a 5-fold gain in the fluorescence rate per molecule. This offers new opportunities for a broad range of applications in biophotonics, plasmonics, optical data storage and ultramicroscopy.

OCIS codes: (180.0180) Microscopy; (170.6280) Spectroscopy, fluorescence and luminescence; (290.4020) Mie theory; (230.3990) Micro-optical devices

References and links

1. H. G. Craighead, “Future lab-on-a-chip technologies for interrogating individual molecules,” Nature (London) **442**, 387-393 (2006).
2. E. Fort and S. Grésillon, “Surface enhanced fluorescence,” J. Phys. D: Appl. Phys. **41**, 013001 (2008).
3. H. Blom, L. Kastrup, and C. Eggeling, “Fluorescence Fluctuation Spectroscopy in Reduced Detection Volumes,” Curr. Pharm. Biotechnol. **7**, 51-66 (2006).
4. X. Li, Z. Chen, A. Taflove, and V. Backman, “Optical analysis of nanoparticles via enhanced backscattering facilitated by 3-D photonic nanojets,” Opt. Express **13**, 526-533 (2005).
5. P. Ferrand, J. Wenger, M. Pianta, H. Rigneault, A. Devilez, B. Stout, N. Bonod, and E. Popov, “Direct imaging of photonic nanojets,” Opt. Express **16**, 6930–6940 (2008).
6. A. Heifetz, K. Huang, A. V. Sahakian, X. Li, A. Taflove, V. Backman, “Experimental confirmation of backscattering enhancement induced by a photonic jet,” Appl. Phys. Lett. **89**, 221118 (2006).
7. S. Lecler, S. Haacke, N. Lecong, O. Crégut, J.-L. Rehspringer, C. Hirlimann, “Photonic jet driven non-linear optics: example of two-photon fluorescence enhancement by dielectric microspheres,” Opt. Express **15**, 4935-4942 (2007).
8. K. Koyama, M. Yoshita, M. Baba, T. Suemoto, and H. Akiyama, “High collection efficiency in fluorescence microscopy with a solid immersion lens,” Appl. Phys. Lett. **75**, 1667-1669 (1999).
9. B. Stout, M. Nevière, E. Popov, “Light diffraction by a three-dimensional object: differential theory,” J. Opt. Soc. Am. A, **22**, 2385-2404 (2005).
10. R. Rigler, and E. S. Elson, *Fluorescence correlation spectroscopy : theory and applications* (Springer, Berlin, 2001).
11. A. Gennerich and D. Schild, “Fluorescence Correlation Spectroscopy in Small Cytosolic Compartments Depends Critically on the Diffusion Model used,” Biophys. J. **79**, 3294-3306 (2000).
12. T. Ruckstuhl, J. Enderlein, S. Jung, and S. Seeger, “Forbidden Light Detection from Single Molecules,” Anal. Chem. **72**, 2117-2123 (2000).
13. J. Wenger, D. Gérard, A. Aouani, and H. Rigneault, “Disposable Microscope Objective Lenses for Fluorescence Correlation Spectroscopy using Latex Microspheres,” Anal. Chem. **80**, 6800-6804 (2008).
14. J. Wenger, *et al*, “Emission and excitation contributions to enhanced single molecule fluorescence by gold nanometric apertures,” Opt. Express **16**, 3008-3020 (2008).

#100422 - $15.00 USD Received 21 Aug 2008; revised 10 Sep 2008; accepted 10 Sep 2008; published 12 Sep 2008

1. Introduction

The common strategy to detect single molecule fluorescence uses a confocal microscope with a high numerical aperture (NA) objective to maximize the collected signal and reject the scattered light. Optical diffraction limits this approach to rather large detection volumes of typically 0.5 fL ($= 0.5\ \mu\text{m}^3$) and low detection rates per molecule. Nanophotonics offer new opportunities to overcome these limits [1, 2]. A major goal is to tailor the molecular electromagnetic environment, so as to simultaneously enhance the collected fluorescence and decrease the detection volume to reduce background noise and enlarge the practicable domain of concentrations for single-molecule analysis. Among the many different nanophotonic techniques that have been implemented recently, nanometric apertures, super-critical angle collection, microfluidic channels, and stimulated emission depletion stand out as promising tools (see [3] and references therein). Despite recent progress in nanotechnologies, a fundamental limitation on the existing techniques is that they rely either on complex optical instrumentation, and/or expensive nanofabrication facilities. Therefore, simple and highly parallel optical systems allowing light manipulation at the nanoscale are currently in high demand.

Here, we propose a simple, low-cost method to focus light on a spot presenting sub-wavelength dimensions in both transverse and axial dimensions. We demonstrate that a three-axis sub-wavelength light confinement can be obtained by illuminating a single dielectric microsphere with a tightly focused Gaussian beam (Fig. 1(a)). This system is exploited to enhance the detection of single fluorescent molecules : we report a simultaneous decrease of the confocal observation volume by an order of magnitude and an enhancement of the fluorescence brightness by a factor of five. This offers new opportunities for applications in biophotonics, plasmonics, and optical data storage. It also raises a number of fundamental questions regarding the interaction between the microsphere, the focused laser beam and the molecular emission.

Our findings appear very different to the previous investigations of the electromagnetic distribution close to a dielectric microsphere. Previous studies did all consider plane wave illumination. In this case, the beam that emerges from the microsphere has a high intensity, sub-wavelength transverse dimensions and low divergence, and was termed “photonic nanojet” [4]. Photonic nanojets have been experimentally characterized in [5], and have been demonstrated to enhance nanoparticle backscattering at microwave frequencies [6], and two-photon fluorescence with floating microspheres added to the analyte solution [7]. Due to its large dimension along the optical axis (typically about 2-3 μm), a photonic nanojet generated by plane wave illumination is not suitable for single molecule fluorescence analysis, as it will not yield better optical confinement than standard confocal microscopy. Quite surprisingly, we show below that a microsphere under focused Gaussian illumination can outperform classical confocal microscopy and simultaneously significantly enhance the fluorescence from a single emitter. This concept has strong connections with solid immersion lenses (SIL) [8], but with a much simpler and cost-effective system based on isolated latex microspheres.

2. Numerical simulations

To study the interaction between a highly focused laser beam and a dielectric microsphere, we have performed three dimensional numerical simulations using the Mie theory with analytic expressions for the incident and scattered fields on a basis of multipolar wave functions [9]. The sphere is characterized by a refractive index of $n = 1.6$ and a 2 μm diameter, with a water embedding medium ($n = 1.33$). A circularly polarized Gaussian laser beam of wavelength 633 nm is focused from the glass side with NA = 1.2. Without the microsphere, the incident beam focuses a few microns above the glass substrate with a waist of 280 nm (Fig. 1(b)), corresponding to the normal confocal microscopy situation. With the microsphere (Fig. 1(c)), a high intensity region is introduced, with reduced dimensions in both axial and transverse directions.

#100422 - $15.00 USD Received 21 Aug 2008; revised 10 Sep 2008; accepted 10 Sep 2008; published 12 Sep 2008

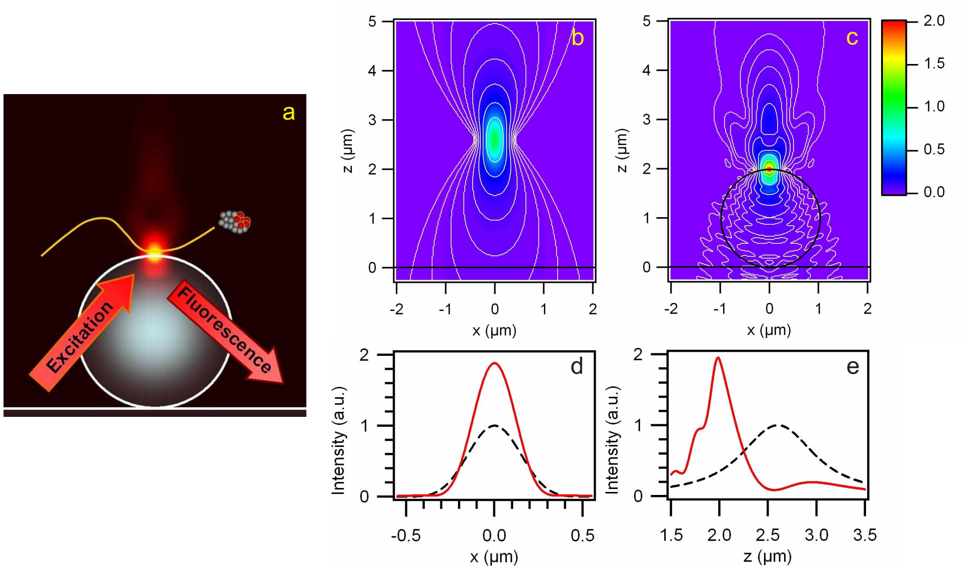

Fig. 1. (a) Microsphere configuration for single molecule detection enhancement. Numerical simulations are computed without (b) and (c) in the presence of a 2 μm sphere illuminated by a focused Gaussian beam at $\lambda = 633$ nm with NA= 1.2 (factor of 2 between adjacent contours). Cuts along the horizontal and vertical axis at best focus outside the sphere are given in (d) and (e). Dashed lines correspond to a Gaussian illumination without the sphere, solid lines are for the resulting beam with the microsphere.

The focus of the incident beam respective to the microsphere was set to the position numerically yielding the best electromagnetic confinement. A remarkable property is that focused Gaussian illumination of a microsphere can achieve strong three-axis electromagnetic confinement, with a large reduction of the beam extent along the optical axis. From Fig. 1(d) and (e), we estimate the transverse FWHM of 270 nm and axial half decay length in water of 180 nm. Both values are well below those of the unperturbed Gaussian illumination. Moreover, numerical results indicate a factor 2 intensity enhancement at the focus with the microsphere. We explain this phenomenon by the combination of two effects : (i) the microsphere overfocuses the beam, creating large transverse wave-vectors by refraction on the microsphere, and (ii) interferences between the incident beam passing outside the sphere and the transmitted and refracted light. The interferences are destructive a few hundred nanometers above the sphere upper surface, which efficiently reduces the axial extension of the spot. These processes produce an enlarged effective numerical aperture and spatial confinement along the longitudinal axis.

3. Materials and methods

To investigate the electromagnetic distribution close to a microsphere illuminated by a tightly focused laser beam, we monitored the fluorescence intensity of single molecular dyes that diffuse around the structure (Fig. 2(a)). Latex microspheres (refractive index 1.6) of calibrated diameters from 1 to 5 μm (dispersion below 0.1%) were taken as purchased from Fluka Chemie GmbH (Buchs, Switzerland), diluted in pure water and dispersed on a cleaned microscope coverslip (refractive index 1.51, thickness 150 μm). Slowly drying the water solvant overnight is a simple and efficient way to ensure electrostatic adhesion between the microsphere and the

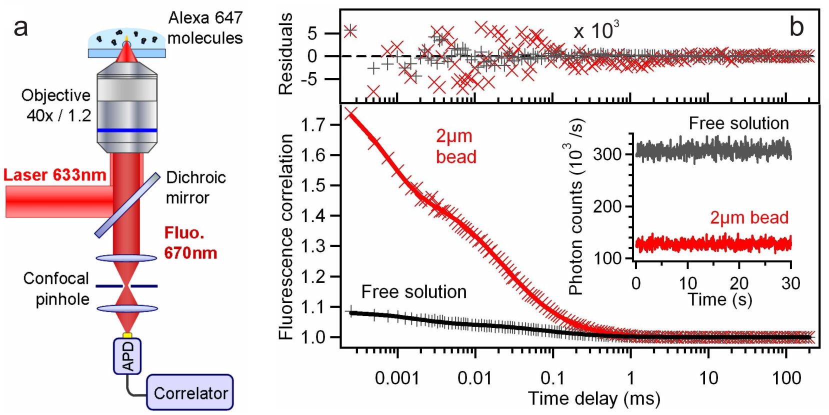

Fig. 2. (a) Schematics of the experimental set-up. (b) Correlation functions recorded in free solution and on a 2 μm sphere, using the same A647 solution (crosses: raw data ; lines: numerical fits). Analysis based on Eq. (1) yields for the free solution : $N = 21.3$, $\tau_d = 71$ μs, $n_T = 0.80$, $\tau_{b_T} = 1.9$ μs, $CRM = 14.5$ kHz, and for the 2 μm sphere : $N = 2.06$, $\tau_d = 22.6$ μs, $n_T = 0.76$, $\tau_{b_T} = 0.8$ μs, $CRM = 62.0$ kHz. The insert shows a snapshot of the raw total fluorescence signal.

glass slide. Concentration was set to isolate one single sphere per 10x10 μm^2. Our experimental setup is based on an epifluorescence microscope with a 40x, NA= 1.2 water-immersion objective (Zeiss C-Apochromat). Alexa-Fluor 647 dyes (A647) diluted in pure water are excited by a focused linearly polarized CW He-Ne laser beam at 633 nm, with a power of 40 μW. The microsphere sample is positioned at the objective focus with nanometric resolution using a 3 axis piezoelectric stage (Polytek PI P517). The fluorescence is collected via the same microscope objective, and filtered from the scattered laser light by a dichroic mirror. A 30 μm confocal pinhole conjugated to the microscope object plane rejects out-of-focus light, and defines a three-dimensional detection volume calibrated to 0.5 μm^3 for experiments on free solution. Lastly, the fluorescence is focused on avalanche photodiodes (Perkin-Elmer SPCM-AQR-13) with 670 ± 20 nm bandpass filters. To analyse the fluorescence signal, we implemented fluorescence correlation spectroscopy (FCS) [10]. FCS is a robust method that provides access to the average number of detected molecules N together with the average count rate per molecule CRM. The fluorescence intensity temporal fluctuations $F(t)$ are recorded to compute the intensity correlation : $g^{(2)}(\tau) = \langle F(t).F(t+\tau)\rangle / \langle F(t)\rangle^2$, where $\langle . \rangle$ stands for time-averaging. This operation is performed by a hardware correlator (ALV-GmbH ALV6000), each FCS measurement was obtained by averaging 10 runs of 10 s duration.

To analyse the FCS data we used a three dimensional Brownian diffusion model [10]:

$$g^{(2)}(\tau) = 1 + \frac{1}{N} \frac{[1 + n_T \exp(-\tau/\tau_{b_T})]}{(1+\tau/\tau_d)\sqrt{1+s^2\,\tau/\tau_d}} \ , \tag{1}$$

where N stands for the average number of molecules, n_T the amplitude of the dark state population, τ_{b_T} the dark state blinking time, τ_d the mean diffusion time and s the ratio of transversal to axial dimensions of the analysis volume, calibrated to $s = 0.2$ for free solution. For 40 μW excitation, the background noise was less than 2,000 counts/second, which can be safely neglected when compared to the total fluorescence signal (insert of Fig. 2).

We note that strictly speaking, the assumption of a free diffusion model is not fulfilled close to a latex microsphere. For the discussion presented here, we need to estimate the size of the

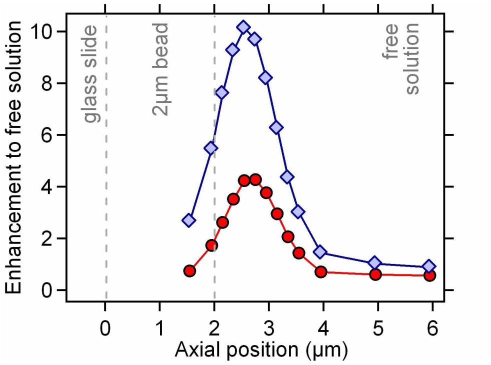

Fig. 3. Observation volume reduction (blue diamonds) and *CRM* enhancement (red circles) versus the focus position with respect to the 2 μm sphere.

observation volume and the count rate per molecule. Both are obtained from the number of detected molecules N, which is proportional to the inverse of the correlation function amplitude at origin $g^{(2)}(0)$. To fully take into account the fast photokinetics of a real dye (photoisomerization and triplet blinking), one has to consider the first channels of the correlogram (with characteristic times below 10 μs), yet the knowledge of the shape of the correlation function at larger times is not necessary. We point out that the expression of $g^{(2)}(0)$ given by Eq. (1) is independent of the shape of the excitation field and the type of diffusion statistics, and is therefore sufficient to reliably estimate N. This is a consequence of the Poissonian nature of the probability to find a molecule in the observation volume at a given time. This procedure holds for a stationary system and a dilute solution where the spatial correlation length of concentration fluctuations is much smaller than the detection volume, which is clearly the case for our study. As shown by the residuals of the fit displayed in Fig. 2(b), the agreement between the expression in Eq. (1) and the experimental data is very good.

Determining the molecular diffusion coefficient in the case of the microsphere is a complex task, as it requires to take into account various artifacts brought by the non-Gaussian observation volume [11]. The restriction of the range available for diffusion affects the diffusion time (millisecond time range), but leaves unaffected the correlation amplitude and the fast components of the correlogram (triplet photokinetics). Still, we point out that relative measurements of variations in diffusion times are always possible, and are sufficient to assess enzymatic activity, chemical rate constants, or binding rates.

4. Experimental results

Figure 2(b) presents raw correlation functions recorded in free solution and at the optimum position on a 2 μm sphere. To avoid for possible calibration errors, the same fluorophore solution was used for both acquisitions. Numerical analysis of the FCS data provides the average number of molecules N inside the detection volume. The ratio of the total fluorescence signal by N yields the fluorescence count rate per molecule *CRM*, which accounts for spatial averaging over all molecular orientations and positions in the detection volume. Analysis of the data displayed in Fig. 2(b) reveals a 10x reduction of the number of molecules, together with a 4.3x *CRM* increase and 3.1x diffusion time reduction. This clearly assesses the gain brought by the microsphere as compared to conventional confocal microscopy : reduced observation volume and increased molecular brightness. We explain the fluorescence enhancement as resulting from two effects : (i) a local intensity enhancement due to extra focusing by the microsphere

#100422 - $15.00 USD Received 21 Aug 2008; revised 10 Sep 2008; accepted 10 Sep 2008; published 12 Sep 2008

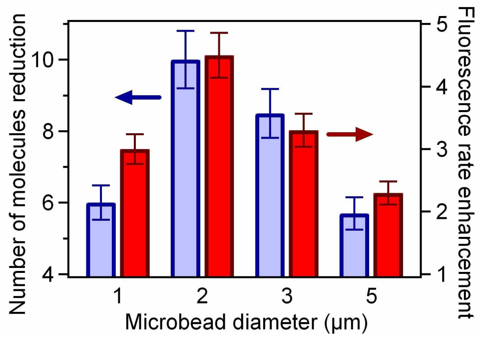

Fig. 4. *CRM* enhancement and observation volume reduction vs. diameter.

(see Fig. 1), together with (ii) an improved fluorescence detection efficiency related to a better collection of light emitted at high incidence angles [12]. Detailed analysis of this phenomenon will form the basis of a future communication.

To study the axial positioning dependence, we report a set of measurements taken while varying the focus position of the incident beam with respect to the 2 μm microsphere. The blue diamonds in Fig. 3 represent the corresponding observation volume reduction $\eta_V = (N_{sphere}/N_{sol})^{-1}$, where N_{sphere} is the number of molecules measured using the sphere and N_{sol} the free solution reference. We simultaneously display the count rate per molecule enhancement $\eta_{CRM} = CRM_{sphere}/CRM_{sol}$ (red circles). To ensure the optimum observation volume reduction and *CRM* enhancement, an accurate ±150 nm axial positioning is necessary, which is readily within the reach of modern translation stages. A similar analysis was performed with spheres of different diameters. We report the best values for η_V and η_{CRM} in Fig. 4, with a clear optimum for 2 μm diameter. We also point out that factor 5 volume reductions and factor 2 fluorescence enhancements are readily obtained with diameters from 1 to 5 μm. Lastly, we considered the case of a bare glass/water interface. At the optimum position, we obtained $\eta_V = 2.1$ and $\eta_{CRM} = 1.2$, showing a modest influence from the plane interface.

5. Conclusion

We have demonstrated that a dielectric microsphere under focused Gaussian illumination can achieve strong three-axis optical confinement, and significantly enhance the fluorescence from a single emitter. This configuration outperforms the results obtained using standard confocal microscopy with a high numerical aperture objective. Since the electromagnetic enhancement is maximum at the microsphere top surface, the present technique can be straightforwardly extended to the detection of luminescent probes bound to the functionalized sphere surface or embedded in lipid membranes deposited on top of the microspheres. Furthermore, microspheres can be combined with low NA objectives to form high performance optical systems, as an alternative to the expensive and complex high NA objectives [13]. Lastly, let us point out that the values reported here are quite similar to results obtained with more complex metallic nanostructures [2, 14], where the electromagnetic enhancement can be much higher, but quenching and absorption can play a negative counterbalancing role. We thus believe that microspheres open new opportunities for low-cost and highly parallel means to develop new microscopy techniques.

#100422 - $15.00 USD Received 21 Aug 2008; revised 10 Sep 2008; accepted 10 Sep 2008; published 12 Sep 2008

Efficient excitation and collection of single-molecule fluorescence close to a dielectric microsphere

Davy Gérard,[1,2,3] Alexis Devilez,[1] Heykel Aouani,[1] Brian Stout,[1] Nicolas Bonod,[1] Jérôme Wenger,[1,*] Evgeny Popov,[1] and Hervé Rigneault[1]

[1]*Institut Fresnel, CNRS, Aix-Marseille Université, Ecole Centrale Marseille, Campus de Saint-Jérôme, 13013 Marseille, France*

[2]*Present address: Laboratoire de Nanotechnologie et d'Instrumentation Optique, Institut Charles Delaunay, Université de Technologie de Troyes, France*

[3] *davy.gerard@utt.fr*

**Corresponding author: jerome.wenger@fresnel.fr*

Received April 20, 2009; accepted May 28, 2009;
posted June 4, 2009 (Doc. ID 110228); published June 30, 2009

Dielectric microspheres illuminated by a tightly focused Gaussian beam can focus light on a tiny spot with subwavelength dimensions along the three directions of space. We report here a detailed experimental and theoretical study of the interaction between a single fluorescent molecule and this peculiar electromagnetic distribution. The microsphere increases the excitation intensity sensed by the molecule up to a factor of 2.2, while at the same time it allows for a collection efficiency of up to 60% by redirecting the light emitted at large incidences toward the optical axis. By combining these two effects, the number of collected fluorescence photons can be increased up to a factor of 5. We quantify the evolution of the excitation and collection contributions with the microsphere dimensions and compare our experimental findings with numerical simulations. © 2009 Optical Society of America

OCIS codes: 260.2510, 240.3990, 170.6280, 350.3950, 290.4020.

1. INTRODUCTION

A crucial issue for many applications in biophotonics is to enhance the detected signal of fluorescent molecules or quantum dots. This can be done by increasing the local excitation intensity, the emission rate, or the radiation collection efficiency. All these properties can be controlled by properly tailoring the electromagnetic environment [1]; microstructures and nanostructures thus offer new opportunities for highly efficient detection of single emitters. In this perspective, strong attention has been devoted to metallic nanostructures (see [2,3] for reviews). These structures are known to generate strong electromagnetic fields in their vicinity, allowing a more efficient excitation of molecules. However, metals are also known to quench the fluorescence or luminescence emission, and a delicate balance has to be found between field enhancement and losses [4,5].

An alternative to enhancing the excitation intensity is to improve the detected fluorescence by increasing the collection efficiency. Already, a flat dielectric interface significantly modifies the angular emission of a dipole if the emitter is sufficiently close to the interface [6–8]. For a dipole bound to a glass–water interface with averaged dipole orientations, up to 72% of the total fluorescence is emitted into the glass half-space of refractive index 1.5. However, the angular distribution shows a significant emission maximum around the direction of the critical angle of total internal reflection, with about 34% of the fluorescence being emitted into the glass above the critical angle [9–11]. This radiation is not collected by classical microscope objectives and is therefore called forbidden light [8]. To achieve fluorescence collection efficiencies of more than 50%, it is necessary to collect light above the critical angle, as done for instance by a parabolic collector [9,10,12] or by a solid immersion lens [13–15].

In a recent publication [16], we have shown that dielectric microspheres can be a viable alternative for enhanced fluorescence detection in solution. When a latex microsphere is illuminated with a tightly focused Gaussian beam, it overfocuses light in a region with subwavelength dimensions in both the transverse and longitudinal directions, creating high local intensities (see Fig. 1, right panel). This effect stems from interferences between the field scattered by the sphere and the high angular components of the incident Gaussian beam passing aside the sphere [17]. Microspheres therefore appear as an attractive and cost-effective route to enhance the fluorescence emission up to five times without requiring expensive nanofabrication facilities. Let us point out that this phenomenon differs from the so-called "photonic nanojets" arising when a dielectric microsphere is illuminated by a plane wave [18–20]. Under plane wave illumination, no subwavelength confinement is obtained along the axial direction, and thus the resulting focal volume does not outperform the diffraction limit obtained with a high numerical aperture (NA) objective. This largely lowers the interest of such standard nanojets for fluorescence detection.

In this Letter, we provide a detailed experimental and theoretical analysis of the interaction between an emitter

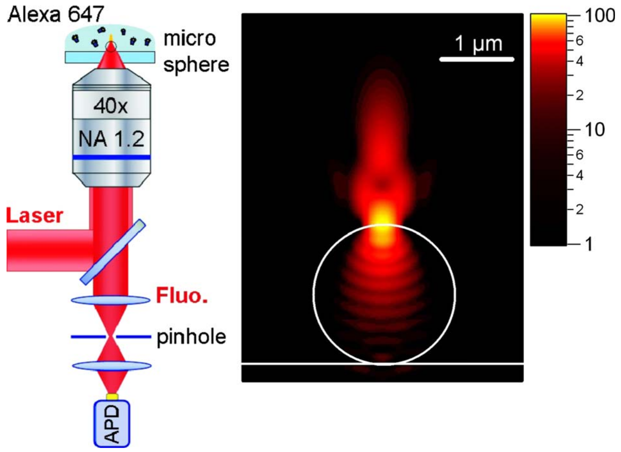

Fig. 1. (Color online) Schematic view of the experimental setup for confocal single molecule detection enhanced by a single microsphere (left panel) and numerical simulation of the electric field intensity distribution near a dielectric microsphere (diameter 2 μm, refractive index 1.59) illuminated with a tightly focused Gaussian beam at $\lambda = 633$ nm with 1.2 NA (right panel, note the logarithmic scale). The outer medium refractive index is set to 1.33; the glass slide refractive index is 1.5.

and a microsphere under tightly focused Gaussian illumination. We thoroughly investigate the origins of the fluorescence enhancement close to a dielectric microsphere and quantify the gains in excitation and collection efficiencies. Both experimental observations and numerical simulations show that the microsphere increases the excitation intensity sensed by the molecule up to a factor of 2.2, while at the same time it allows for a gain in collection efficiency up to 60% by redirecting the light emitted at large incidences toward the optical axis.

2. EXCITATION AND COLLECTION EFFICIENCIES CHARACTERIZATION

The presence of a microsphere affects the fluorescence signal via three phenomena: (i) local enhancement of the excitation intensity inside the focused spot, (ii) improvement of the emitter's quantum yield, and (iii) modification of the emitter's radiation pattern, directing more energy toward the detectors. We have recently developed an experimental procedure to distinguish between the respective weights of these contributions by employing fluorescence correlation spectroscopy (FCS) combined with fluorescence lifetime measurements. This procedure has already been used to quantify the fluorescence alteration by gold nanometric apertures [21] and is briefly reviewed here.

In steady state, the detected fluorescence count rate per molecule (CRM) is given by [22]

$$\mathrm{CRM} = \kappa\phi \frac{\sigma I_e}{1 + I_e/I_s}, \tag{1}$$

where κ is the fluorescence collection efficiency and $\phi = k_{\mathrm{rad}}/k_{\mathrm{tot}}$ is the quantum yield with k_{rad} as the radiative emission decay rate and k_{tot} as the total decay rate. σ is the absorption cross section, I_e is the excitation intensity, and $I_s \propto (k_{\mathrm{tot}}/\sigma)$ is the saturation intensity. Please note that the I_e and I_s are given here as the number of photons per second and per surface unit. The FCS technique allows one to reliably estimate this CRM, which corresponds to the average number of photons emitted by a single molecule [22,23].

The fluorescence enhancement η_F near a microsphere is defined as the ratio of the detected fluorescence CRM near the microsphere with respect to the open solution for a fixed excitation power, $\eta_F = \mathrm{CRM}_{\mathrm{sphere}}/\mathrm{CRM}_{\mathrm{sol}}$. Let us consider the two extreme excitation regimes depending on the relative values of I_e and I_s. In the low excitation regime $I_e \ll I_s$, the CRM and the fluorescence enhancement reduces to

$$\mathrm{CRM}_{\mathrm{low}} = \kappa\phi\sigma I_e \quad (I_e \ll I_s), \tag{2}$$

$$\eta_{F,\mathrm{low}} = \eta_\kappa \eta_\phi \eta_{I_e} \quad (I_e \ll I_s), \tag{3}$$

where η_κ, η_ϕ, and η_{I_e} are the enhancements in the collection efficiency, quantum yield, and excitation rate, respectively. In the saturation regime $I_e \gg I_s$, the dependence on the excitation intensity disappears in Eq. (1), and the fluorescence rate enhancement is expressed [21] as

$$\eta_{F,\mathrm{sat}} = \eta_\kappa \eta_{k_{\mathrm{rad}}} \quad (I_e \gg I_s), \tag{4}$$

which indicates that the fluorescence enhancement at saturation is determined only by the gains in collection efficiency η_κ and radiative emission rate $\eta_{k_{\mathrm{rad}}}$.

In our specific case, it is possible to further simplify the above equations. A nonabsorbing dielectric microstructure is expected to only marginally modify the dye's photophysics, since the absence of absorption losses does not open new nonradiative deexcitation routes. We confirm this assumption by the report in Section 4 of experimental evidence based on time-correlated fluorescence measurements that the fluorescence lifetime of the dye is not affected by the presence of the microsphere. Consequently, we consider that $\eta_{k_{\mathrm{rad}}} = \eta_\phi = 1$. Equations (3) and (4) then become

$$\eta_{F,\mathrm{low}} = \eta_\kappa \eta_{I_e} \quad (I_e \ll I_s), \tag{5}$$

$$\eta_{F,\mathrm{sat}} = \eta_\kappa \quad (I_e \gg I_s). \tag{6}$$

This set of equations provides the guidelines for distinguishing between the gains in collection efficiency η_κ and excitation intensity η_{I_e} brought by the photonic structure. The procedure can be summarized as follows: the fluorescence rates per molecule CRM are measured by FCS for increasing excitation powers in open solution and in the case of a microsphere. The resulting data points are fitted according to Eq. (1) to deduce the fluorescence enhancements $\eta_{F,\mathrm{low}}$ and $\eta_{F,\mathrm{sat}}$ taken at the asymptotic limits where $I_e \to 0$ and $I_e \to \infty$, respectively. According to Eq. (6), the value of $\eta_{F,\mathrm{sat}}$ at saturation gives the collection efficiency enhancement η_κ. The excitation intensity enhancement is obtained as $\eta_{I_e} = \eta_{F,\mathrm{low}}/\eta_{F,\mathrm{sat}}$ [Eq. (5)]. This unambiguously separates the excitation and emission contributions to the total fluorescence enhancement.

3. EXPERIMENTAL METHODS

Our experimental setup is based on an inverted confocal microscope with a NA=1.2 water-immersion objective (Fig. 1, left panel). A single latex microsphere of well calibrated diameter (Fluka Chemie GmBH: $d_s=1$, 1.5, 2, or 3 μm; dispersion $<0.1\%$; refractive index 1.59) is set at the microscope objective focus with nanometer resolution using a three axis piezoelectric stage. For the microsphere sample preparation, the spheres are diluted in pure water and dispersed on a cleaned microscope glass coverslip before air drying to ensure adhesion to the substrate. The concentration is set to isolate a single sphere per 10 μm $\times 10$ μm. Adhesion onto the glass surface is sufficient to ensure that the sphere remained stuck on the substrate for the duration of the experiment.

A 50 μL droplet of Alexa Fluor 647 fluorescent molecules diluted in pure water to a concentration of 40 nM is deposited on top of the microsphere sample. Alexa Fluor 647 are purchased from Invitrogen, Carlsbad, Calif., and have peak absorption and emission at 650 and 668 nm, respectively. The molecules are excited by a linearly polarized He–Ne laser beam at 633 nm focused by the combination of the microscope objective and the microsphere. The backward-emitted fluorescence is collected via the same combination of microsphere and microscope objective, and filtered from the scattered laser light by a dichroic mirror (Omega Filters 650DRLP) and a long-pass filter (Omega Filters 640AELP). A 30 μm confocal pinhole conjugated to the microscope objective focal plane rejects out-of-focus light. After the pinhole, the fluorescence is detected by an avalanche photodiode with 670 ± 20 nm bandpass filter (Omega Filters 670DF40).

For FCS, the fluorescence intensity temporal fluctuations $F(t)$ are analyzed by a hardware correlator (ALV-GmbH ALV6000) to compute the temporal correlation, $g^{(2)}(\tau)=\langle F(t)F(t+\tau)\rangle/\langle F(t)\rangle^2$, where $\langle\ \rangle$ stands for time averaging over the experiment duration [22,23]. Each FCS measurement is obtained by averaging ten runs of 10 s duration. Numerical fit of the FCS data provides the average number of molecules N and, therefore, the fluorescence CRM. We refer the reader to [16] for a detailed discussion on FCS analysis close to a latex microsphere.

For lifetime measurements, we use a time-correlated single photon counting card (PicoQuant PicoHarp 300). The excitation is switched to a picosecond laser diode operating at 636 nm. Perfect spatial overlap between the modes of the pulsed laser diode and the CW He–Ne laser is obtained by coupling to a single-mode optical fiber prior to focusing in the microscope [21]. Overall, the temporal resolution of the setup is 120 ps, well below the 1.0 ns fluorescence lifetime recorded for Alexa Fluor 647 in water solution.

We emphasize that the value of the fluorescence enhancement is extremely sensitive to the position of the microsphere. An accurate positioning of the focus with ± 150 nm precision is required along the axial direction [16]. In what follows we only present the results obtained at the optimal position. Note that the values for each diameter have been averaged over several microspheres to ensure the reproducibility of the results. Finally, let us point out that owing to the statistical approach used here, all our results have to be understood as spatially averaged values over all the possible molecular orientations and positions inside the confocal detection volume.

4. RESULTS AND DISCUSSION

Figure 2(a) shows the measured CRMs versus the excitation power for the different sphere diameters and for the reference case in free solution. Solid curves indicate numerical fits using Eq. (1), which stand in good agreement with the experimental data. CRM enhancements with the different microsphere diameters are clearly observed at all excitation powers. Let us also emphasize that CRMs larger than 100 kHz are readily obtained with the microsphere, while these values remain unreachable in free solution. From the numerical fits we deduce the values of the fluorescence enhancement factors in the limits of low excitation $\eta_{F,\text{low}}$ and saturation $\eta_{F,\text{sat}}$. The results are displayed in Fig. 2(b) versus the sphere diameter, showing an optimum for a diameter of 1.5 μm. It is worth noticing that with a 1.5 μm latex microsphere it is possible to reach a five times enhancement of the molecular fluorescence, a value that is comparable to the enhancement factors reported with some metallic nanostructures [3].

Along with FCS experiments, we perform fluorescence lifetime measurements to quantify the alteration of the molecule total decay rate close to the microsphere. Typical decay curves are plotted in Fig. 3 in the case of the reference solution [black dots (free solution)] and for a 2 μm diameter sphere (red dots). A numerical fit taking into account the 120 ps instrument resolution indicates a lifetime reduction near the sphere of less than 4%. For the other sphere diameters, we observed even smaller varia-

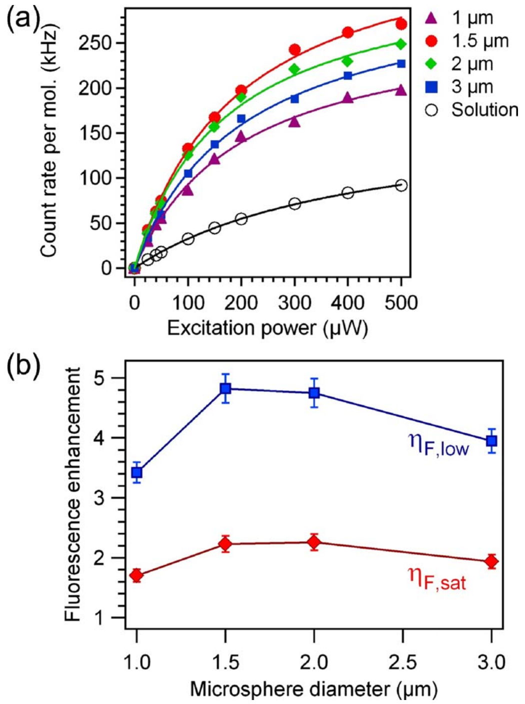

Fig. 2. (Color online) (a) CRM versus excitation power for the different sphere diameters and for the reference solution. Dots: experimental data; solid curves: numerical fit using Eq. (1). (b) Fluorescence enhancement factors in the low excitation regime $\eta_{F,\text{low}}$ and at saturation $\eta_{F,\text{sat}}$, as deduced from the numerical fits in (a).

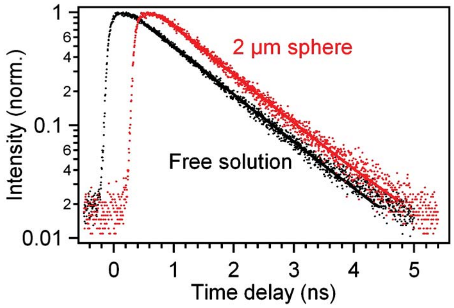

Fig. 3. (Color online) Fluorescence lifetime measurements. Dots: experimental data; solid curves: numerical fits taking into account the resolution of the setup. The curves are horizontally shifted for clarity.

tions in the fluorescence lifetime, which are limited by the statistical accuracy of our measurements. Thus, we consider that for the range of diameters tested here, the microsphere has a negligible influence on the fluorescence lifetime. Since the nonabsorbing microsphere obviously does not open new nonradiative de-excitation routes, our observations of an unchanged fluorescence lifetime mean that the dye's radiative rate and consequently its quantum yield are also unaffected by the microsphere. This validates the assumption $\eta_{k_{\mathrm{rad}}}=\eta_{\phi}=1$ made in Section 2.

We can now distinguish the excitation and emission contributions to the overall fluorescence enhancement. Following Eq. (6), the collection efficiency enhancement η_κ is given by the value of $\eta_{F,\mathrm{sat}}$ at saturation. The excitation intensity enhancement is obtained as $\eta_{I_e}=\eta_{F,\mathrm{low}}/\eta_{F,\mathrm{sat}}$ [Eq. (5)]. According to this procedure, Fig. 4 shows the excitation and collection enhancement factors corresponding to the experimental results in Fig. 2(b). It appears from these results that excitation and collection effects are both involved in the global fluorescence enhancement. For the optimal microsphere diameter of 1.5 μm, the excitation intensity sensed by the molecule is enhanced by a factor of 2.2, while at the same time the collection efficiency is increased by the same factor. Given the collection efficiency of 30% for the 1.2 NA objective with no microsphere, the enhancement brought by the microsphere amounts to a collection efficiency of about 66%. Such a large collection efficiency can only be obtained by redirecting the so-called forbidden light emitted at large incidence angles toward the optical axis [8,10], which shows that the microsphere acts as an efficient light collector. The microsphere can thus be seen as a microlens placed in the emitter's near field, allowing a more efficient focusing of the incident beam as well as increasing the collection of the fluorescence light.

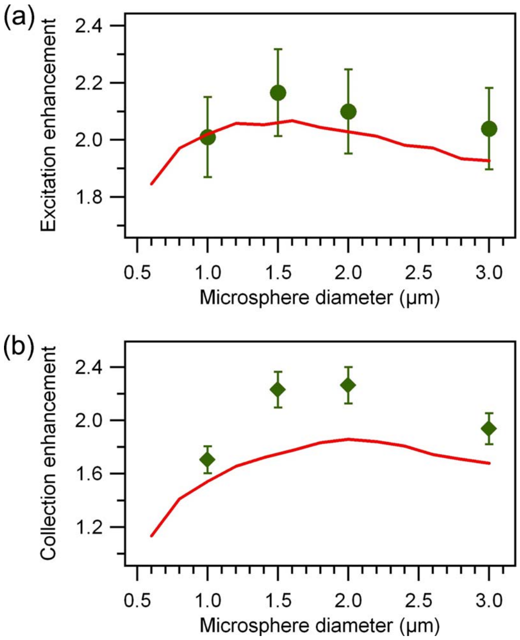

Fig. 4. (Color online) Contributions of (a) excitation and (b) collection enhancements close to a single microsphere (random dipole orientation). Markers are experimental data; curves result from numerical computation (see text).

To support the experimental data, we perform three-dimensional numerical simulations of the field distribution near a microsphere using the Lorentz–Mie theory [24]. The incident linearly polarized Gaussian beam is simulated using first-order Davis coefficients with the beam shape parameter corresponding to the experimental configuration of NA=1.2 [17]. A typical electromagnetic field intensity distribution in the case of a 2 μm diameter sphere is plotted on the right panel of Fig. 1. To compute the excitation intensity enhancement, we introduce the intensity density ϱ_e as the total excitation intensity I_V per unit of effective volume V_{eff}, $\varrho_e=I_V/V_{\mathrm{eff}}$, where the excitation intensity is given by [22,25]

$$I_V=\int_V |E|^2 \mathrm{d}V, \tag{7}$$

and the effective volume is defined as

$$V_{\mathrm{eff}}=\frac{\left(\int_V |E|^2 \mathrm{d}V\right)^2}{\int_V |E|^4 \mathrm{d}V}. \tag{8}$$

The numerical integration of the field intensity is made over the region outside the microsphere where the intensity is larger than $I_{\max}/10$, with $I_{\max}$ being the maximum intensity of the excitation field. Finally, we obtain the excitation intensity enhancement as the ratio of ϱ_e for the microsphere to the reference value of ϱ_e without the sphere. The theoretical results are plotted versus the microsphere diameter in Fig. 4(a) and are found to be in good agreement with the experimental data, with a relative difference comparable to the experimental statistical errors.

To numerically compute the gain in collection efficiency brought by the microsphere, we set a single dipole close to the surface of the sphere at the position corresponding to the maximum intensity found in the excitation field distribution in Fig. 1. We compute the average Poynting vector flux in the far field over a spherical surface of 20 μm radius located underneath the microsphere, with a center at the dipole location and a maximum half-angle of 60° corresponding to the microscope objective NA. The collection efficiency is then obtained as the ratio of this Poynting vector flux to the flux computed over all directions of space (4π sr). Finally, the collection efficiency enhancement is derived by normalizing the collection efficiency found with a microsphere to the reference one found without the sphere. To reproduce the random dipole orientation in the experimental observations, we average the collection efficiencies found for dipole orientations along each direction x, y, and z. Figure 4(b) displays our results versus the microsphere diameter. These numerical results stand again in good qualitative agreement with the experimental findings, although we did not consider spatial averaging over various dipole locations as in the FCS experiments. Altogether, the numerical simulations confirm that gains in both local excitation intensity and collection efficiency contribute in about equal parts to the overall fluorescence enhancement. These simulations also confirm the drop in the fluorescence enhancement found experimentally for microsphere diameters below 1 μm.

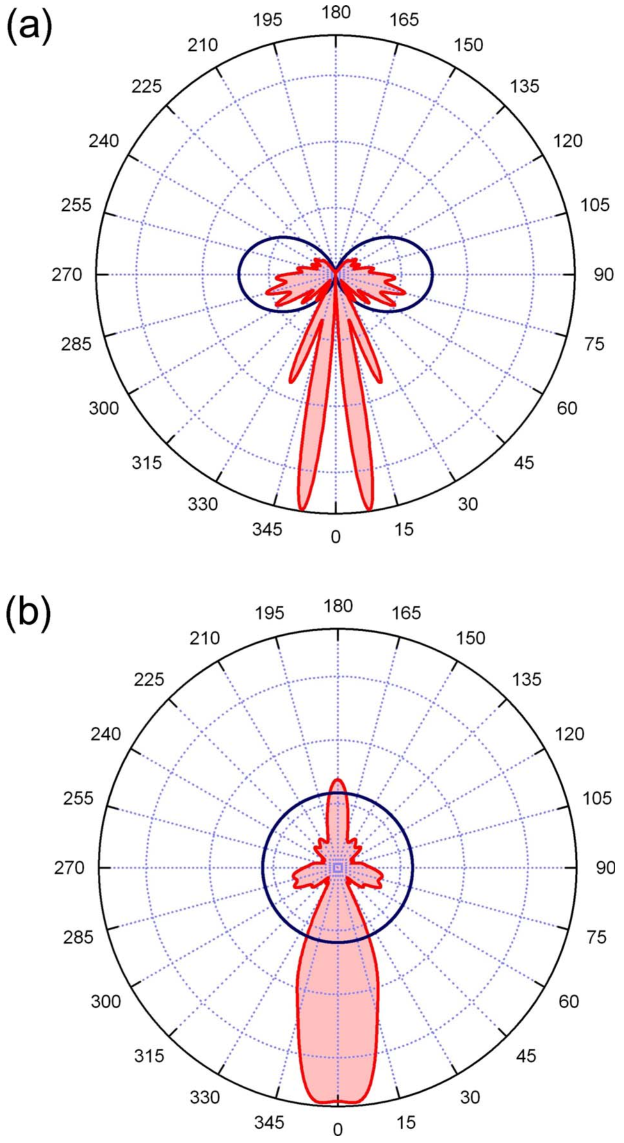

Fig. 5. (Color online) Angular distribution of the fluorescence intensity of a molecule located at 100 nm above a 2 μm polystyrene microsphere in water (red curve) for a dipole oriented along the Z axis (a) and averaged over all orientations (b). The nonfilled curves correspond to the dipole emission without the microsphere.

To illustrate the increased collection efficiency brought by the microsphere, we compute the radiation pattern for a dipole located at 100 nm on top of a 2 μm polystyrene microsphere in water. This radiation pattern is computed in the far field at a distance of 20 μm from the dipole; it fully takes into account the microsphere refractive effects. Figure 5 displays the angular distributions for a dipole oriented along the Z axis and for an average over all orientations. It is apparent that light emitted above the critical angle of 57° in the case of the polystyrene–water interface is largely redirected toward the optical axis, allowing efficient detection of the fluorescence radiation. This gives the picture of the microsphere acting as a magnifying lens directly in the emitter's vicinity.

5. CONCLUSION

We report a detailed experimental and theoretical study of the fluorescence emission alteration close to a dielectric microsphere illuminated with a tightly focused Gaussian beam. The microsphere increases the excitation intensity sensed by the emitter up to a factor of 2.2, while at the same time it allows for a collection efficiency up to 60% by redirecting the light emitted at large incidences toward the optical axis. Altogether, these effects contribute to an increase in the number of collected fluorescence photons up to a factor of 5. The microsphere is shown to act as a microlens placed in the emitter's near field, allowing a more efficient focusing of the incident beam as well as increasing the radiation collection efficiency. Let us point out that the microsphere can be designed so that the gains in excitation and collection efficiencies are maximized at the microsphere's top surface by properly choosing the microsphere radius and refractive index [17,18,26]. This extends the potential of dielectric microspheres to detect luminescent probes immobilized on the sphere surface, which can eventually be chemically functionalized [27]. Dielectric microspheres are thus found to offer a cheap, conceptually simple, and highly efficient way to enhance both excitation and harvesting of light from emitters. Further applications include optical microscopy [28], Raman spectroscopy [29], photolithography [30,31], or optical data storage [32].

ACKNOWLEDGMENT

The authors acknowledge funding from the French Centre National de la Recherche Scientifique (CNRS).

REFERENCES

1. W. L. Barnes, "Fluorescence near interfaces: the role of photonic mode density," J. Mod. Opt. **45**, 661–699 (1998).
2. J. R. Lakowicz, "Radiative decay engineering 5: metal-enhanced fluorescence and plasmon emission," Anal. Biochem. **337**, 171–194 (2005).
3. E. Fort and S. Grésillon, "Surface enhanced fluorescence," J. Phys. D **41**, 013001 (2008).
4. P. Anger, P. Bharadwaj, and L. Novotny, "Enhancement and quenching of single-molecule fluorescence," Phys. Rev. Lett. **96**, 113002 (2006).

5. R. Carminati, J.-J. Greffet, C. Henkel, and J.-M. Vigoureux, "Radiative and non-radiative decay of a single-molecule close to a metallic nanoparticle," Opt. Commun. **261**, 368–375 (2006).
6. W. Lukosz and R. E. Kunz, "Light emission by magnetic and electric dipoles close to a plane interface. I. Total radiated power," J. Opt. Soc. Am. **67**, 1607–1615 (1977).
7. W. Lukosz and R. E. Kunz, "Light emission by magnetic and electric dipoles close to a plane interface. II. Radiation patterns of perpendicular oriented dipoles," J. Opt. Soc. Am. **67**, 1615–1619 (1977).
8. L. Novotny, "Allowed and forbidden light in near-field optics. I. A single dipolar light source," J. Opt. Soc. Am. A Opt. Image Sci. Vis. **14**, 91–104 (1997).
9. J. Enderlein, T. Ruckstuhl, and S. Seeger, "Highly efficient optical detection of surface-generated fluorescence," Appl. Opt. **38**, 724–732 (1999).
10. T. Ruckstuhl, J. Enderlein, S. Jung, and S. Seeger, "Forbidden light detection from single molecules," Anal. Chem. **72**, 2117–2123 (2000).
11. J. Mertz, "Radiative absorption, fluorescence, and scattering of a classical dipole near a lossless interface: a unified description," J. Opt. Soc. Am. B **17**, 1906–1913 (2000).
12. J. Ries, T. Ruckstuhl, D. Verdes, and P. Schwille, "Supercritical angle fluorescence correlation spectroscopy," Biophys. J. **94**, 221–229 (2008).
13. K. Koyama, M. Yoshita, M. Baba, T. Suemoto, and H. Akiyama, "High collection efficiency in fluorescence microscopy with a solid immersion lens," Appl. Phys. Lett. **75**, 1667–1669 (1999).
14. A. Serov, R. Rao, M. Gösch, T. Anhut, D. Martin, R. Brunner, R. Rigler, and T. Lasser, "High light field confinement for fluorescent correlation spectroscopy using a solid immersion lens," Biosens. Bioelectron. **20**, 431–435 (2004).
15. R. Rao, J. Mitic, A. Serov, R. A. Leitgeb, and T. Lasser, "Field confinement with aberration correction for solid immersion lens based fluorescence correlation spectroscopy," Opt. Commun. **271**, 462–469 (2007).
16. D. Gérard, J. Wenger, A. Devilez, D. Gachet, B. Stout, N. Bonod, E. Popov, and H. Rigneault, "Strong electromagnetic confinement near dielectric microspheres to enhance single-molecule fluorescence," Opt. Express **16**, 15297–15303 (2008).
17. A. Devilez, N. Bonod, B. Stout, D. Gérard, J. Wenger, H. Rigneault, and E. Popov, "Three-dimensional subwavelength confinement of photonic nanojets," Opt. Express **17**, 2089–2094 (2009).
18. Z. Chen, A. Taflove, and V. Backman, "Photonic nanojet enhancement of backscattering of light by nanoparticles: a potential novel visible-light ultramicroscopy technique," Opt. Express **12**, 1214–1220 (2004).
19. A. Heifetz, K. Huang, A. V. Sahakian, X. Li, A. Taflove, and V. Backman, "Experimental confirmation of backscattering enhancement induced by a photonic jet," Appl. Phys. Lett. **89**, 221118 (2006).
20. P. Ferrand, J. Wenger, M. Pianta, H. Rigneault, A. Devilez, B. Stout, N. Bonod, and E. Popov, "Direct imaging of photonic nanojets," Opt. Express **16**, 6930–6940 (2008).
21. J. Wenger, D. Gérard, N. Bonod, E. Popov, H. Rigneault, J. Dintinger, O. Mahboub, and T. W. Ebbesen, "Emission and excitation contributions to enhanced single molecule fluorescence by gold nanometric apertures," Opt. Express **16**, 3008–3020 (2008).
22. C. Zander, J. Enderlein, and R. A. Keller, *Single-Molecule Detection in Solution—Methods and Applications* (VCH-Wiley, 2002).
23. W. W. Webb, "Fluorescence correlation spectroscopy: inception, biophysical experimentations, and prospectus," Appl. Opt. **40**, 3969–3983 (2001).
24. B. Stout, M. Nevière, and E. Popov, "Light diffraction by a three-dimensional object: differential theory," J. Opt. Soc. Am. A Opt. Image Sci. Vis. **22**, 2385–2404 (2005).
25. E. Popov, M. Nevière, J. Wenger, P.-F. Lenne, H. Rigneault, P. Chaumet, N. Bonod, J. Dintinger, and T. W. Ebbesen, "Field enhancement in single subwavelength apertures," J. Opt. Soc. Am. A Opt. Image Sci. Vis. **23**, 2342–2348 (2006).
26. A. Devilez, B. Stout, N. Bonod, and E. Popov, "Spectral analysis of three-dimensional photonic jets," Opt. Express **16**, 14200–14212 (2008).
27. J. R. Epstein and D. R. Walt, "Fluorescence-based fibre optic arrays: a universal platform for sensing," Chem. Soc. Rev. **32**, 203–214 (2003).
28. J. Wenger, D. Gérard, H. Aouani, and H. Rigneault, "Disposable microscope objective lenses for fluorescence correlation spectroscopy using latex microspheres," Anal. Chem. **80**, 6800–6804 (2008).
29. A. Desmedt, D. Talaga, and J.-L. Bruneel, "Enhancement of the Raman scattering signal due to a nanolens effect," Appl. Spectrosc. **61**, 621–623 (2007).
30. E. McLeod and C. B. Arnold, "Subwavelength direct-write nanopatterning using optically trapped microspheres," Nat. Nanotechnol. **3**, 413–417 (2008).
31. S. Li, C. Du, X. Dong, L. Shi, X. Luo, X. Wei, and Y. Zhang, "Superlens nano-patterning technology based on the distributed polystyrene spheres," Opt. Express **16**, 14397–14403 (2008).
32. S.-C. Kong, A. Sahakian, A. Taflove, and V. Backman, "Photonic nanojet-enabled optical data storage," Opt. Express **16**, 13713–13719 (2008).

Chapitre 4

Quelques Applications en Biophotonique

Le premier domaine d'application en biophotonique des recherches exposées ci-dessus porte sur l'amélioration et l'extension des techniques de spectroscopie par corrélation de fluorescence (figure 4.1). Grâce aux faibles volumes mis en œuvre, l'analyse de réactions de clivage enzymatique d'ADN peuvent être conduites à de très fortes concentrations de plusieurs dizaines de micromolaires, alors que les mesures standard sont limitées à des concentrations dans la gamme de 10-100 nanomolaires. De plus, le bruit lié à la diffusion éalstique et inélastique dans le volume d'analyse est réduit.

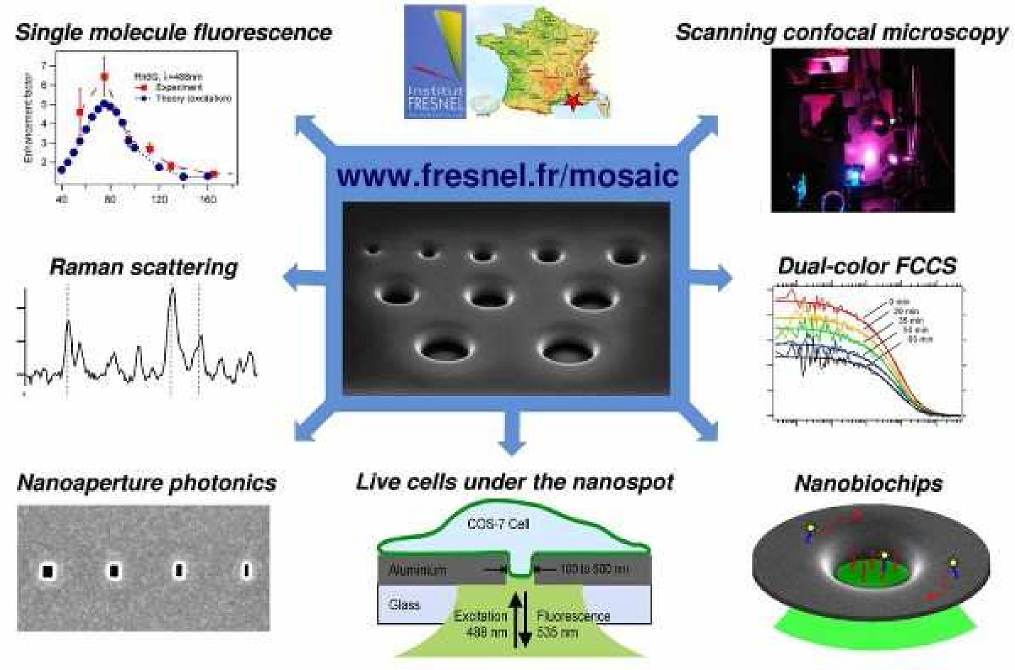

Fig. 4.1. Applications biophotoniques et nanophotoniques de nano-ouvertures individuelles.

Trois articles de revues ont été publiés concernant les applications en biologie et biochimie des structures nanophotoniques. Le premier traite de l'analyse de fluorescence dans des nano-ouvertures métalliques [1]. Le second porte plus généralement sur les applications biophotoniques des nano-

---

[1] P.-F. Lenne, et al, Fluorescence fluctuations analysis in nanoapertures: physical concepts and biological applications, HistoChem. Cell. Biol. 130, 795-805 (2008)

ouvertures (individuelles ou en réseau) [2]. Le troisième décrit les principaux systèmes nanophotoniques pour la détection exaltée de molécules fluorescentes en solution [3].

L'exaltation électomagnétique de la fluorescence améliore également le rapport signal à bruit pour le suivi de réactions moléculaires. En FCS, le rapport signal à bruit est proportionnel au taux de comptage de fluorescence *par molécule*, et à la racine carrée du temps total d'intégration. Ainsi, un gain de 10 sur la fluorescence par molécule se traduit par une augmentation de 10 du rapport signal à bruit, ou de manière équivalente, à la possibilité de réduire d'un facteur $10^2 = 100$ le temps total d'intégration. Ceci est particulièrement bénéfique pour le suivi rapide de réactions enzymatiques à forte concentration. Nous avons démontré expérimentalement ces principes dans l'étude [4] (article Analytical Chemistry ci-après), où le clivage de double brins d'ADN a été suivi à des concentrations micromolaires avec une résolution de la seconde (figure 4.2). Jusqu'alors, l'état de l'art de la FCS fonctionnait pour des concentrations nanomolaires et des résolutions temporelles de l'ordre de la minute. Les fortes exaltations du signal par molécule dans le cas des nano-ouvertures ou des microsphères ouvrent des nouvelles approches pour l'analyse rapide d'un grand nombre de réactions biochimiques.

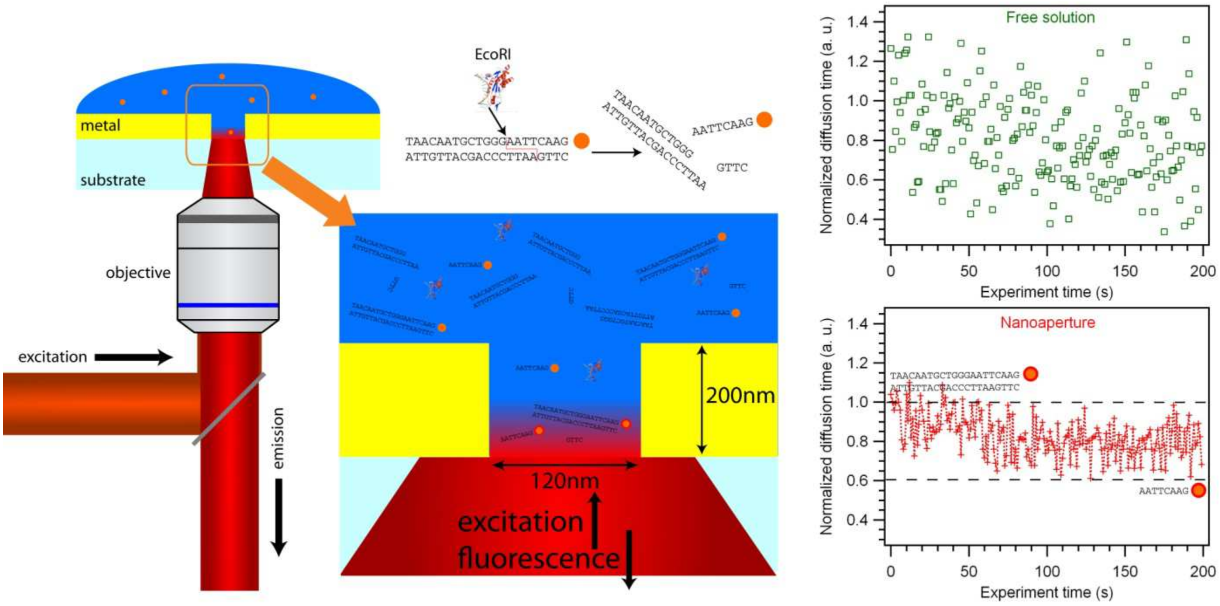

Fig. 4.2. L'exaltation et le confinement dans le cas d'une nano-ouverture permettent le suivi rapide d'une réaction de clivage de double brins d'ADN par une enzyme EcoRI à forte concentration.

---

[2] J. Wenger, et al, Biophotonics applications of nanometric apertures, Int. J. Materials and Product Technology 34, 488-506 (2009)

[3] J. Wenger, H. Rigneault, Photonic Methods to Enhance Fluorescence Correlation Spectroscopy and Single Molecule Fluorescence Detection, Int. J. Mol. Sci. 11, 206-221 (2010)

[4] J. Wenger, et al, Nanoaperture-Enhanced Signal-to-Noise Ratio in Fluorescence Correlation Spectroscopy, Anal. Chem. 81, 834-839 (2009).

Un autre domaine important d'application de l'analyse de molécules fluorescentes concerne l'étude des fonctions biologiques des cellules. La compréhension de l'architecture fine de membranes cellulaires nécessite le développement de nouvelles méthodes d'investigation pour dépasser les limites de résolution et de sensibilité imposées par le phénomène de diffraction. Nous avons utilisé des ouvertures nanométriques isolées dans des films métalliques pour réduire le volume d'observation en microscopie optique sous la limite de diffraction d'un champ propagatif. En agissant comme un trou de filtrage placé directement dans le plan objet, la nanoouverture autorise une observation d'une zone sous la limite de diffraction optique (figure 4.3).

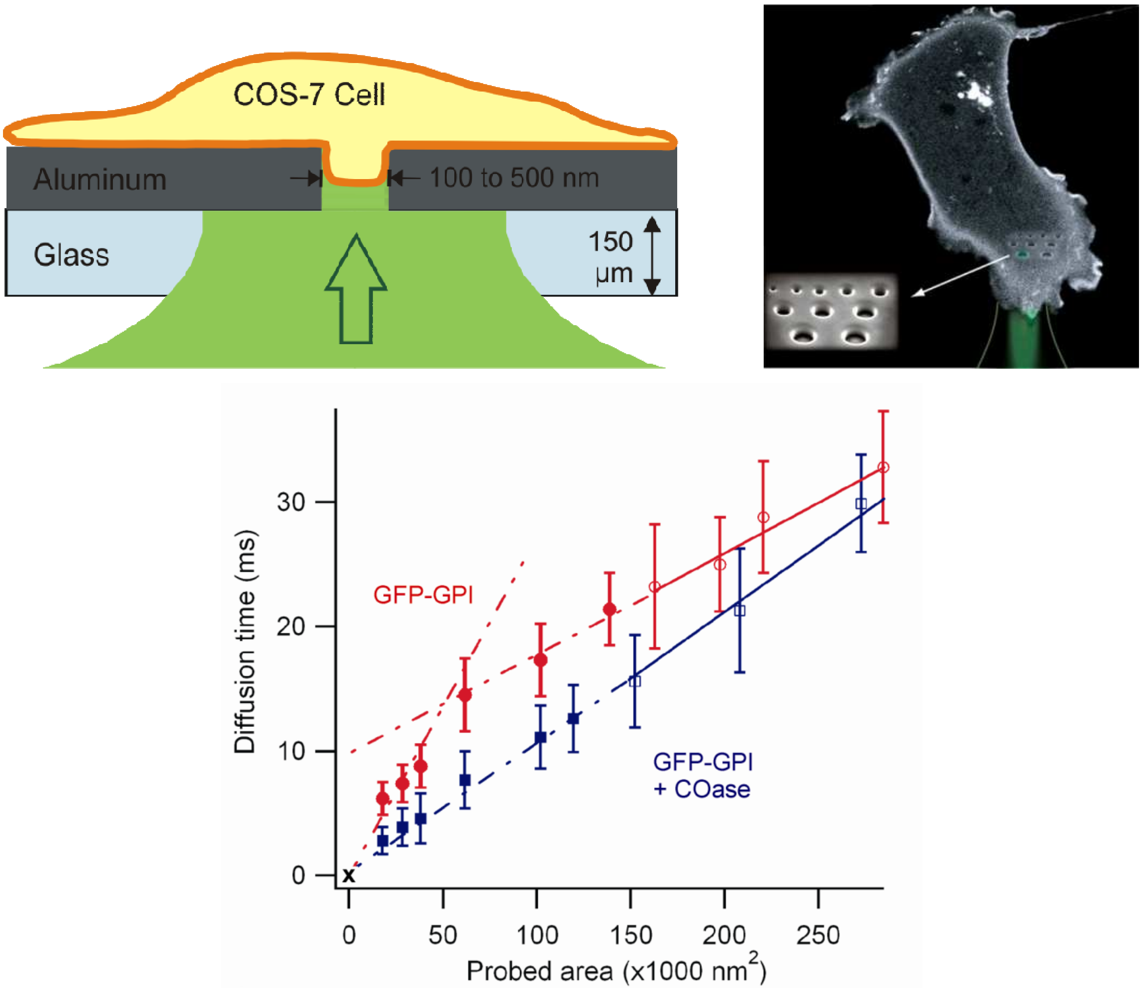

Fig. 13 Principe de l'utilisation d'une nano-ouverture pour sonder la diffusion latérale de molécules fluorescentes dans la membrane cellulaire.

Cette ultra-résolution est mise à profit pour étudier la diffusion latérale de marqueurs individuels dans des membranes biologiques de cellules vivantes [5] (articler Biophysical Journal ci-après). La comparaison des comportements pour différentes espèces révèle la présence d'hétérogénéités de dimensions nanométriques qui contraignent la diffusion membranaire. On voit par exemple dans la

---

[5] J. Wenger, et al, Diffusion analysis within single nanometric apertures reveals the ultrafine cell membrane organization, Biophys. J. 92, 913-919 (2007).

figure 4.3 un comportement non-linéaire du temps de diffusion en fonction de la surface membranaire éclairée. Ce comportement s'explique par la présence de nanodomaines moléculaires (enrichis en lipides, cholestérol, protéines…) qui altèrent le processus de diffusion des marqueurs fluorescents. Nous avons ainsi pu mettre en évidence des domaines de dimensions de l'ordre de 50 nm, bien en dessous de la limite de résolution de microscopes optiques.

Un aspect plus technologique de mes recherches porte sur le développement de systèmes simples, compacts et efficaces pour la détection et l'analyse de molécules fluorescentes, en particulier avec la méthode de corrélation temporelle FCS. Cette technique est très polyvalente, mais elle nécessite une forte sensibilité de fluorescence, pour être capable de sonder des molécules individuelles. Ceci explique que tous les dispositifs actuels emploient des objectifs de microscope de forte ouverture numérique, qui sont à la fois chers et complexes. En conséquence, la parallélisation et la portabilité de la FCS (comme de l'analyse de molécules individuelles) sont limitées.

En exploitant la focalisation introduite par la microphère, nous avons montré qu'une combinaison {microsphère+lentille de faible ouverture numérique} permet de détecter efficacement le signal de fluorescence d'une molécule individuelle, en dépit d'un système optique extrêmement simple [6]. Nous avons en particulier démontré la détection d'une seule molécule fluorescente avec une lentille plastique jetable de lecteur de disque optique CDrom. Ces travaux ouvrent des perspectives d'application pour la détection exaltée de particules dans des dispositifs opto-fluidiques intégrés.

En combinant la focalisation induite par une microsphère avec une fibre optique, nous avons réalisé le premier dispositif de corrélation de fluorescence en mode endoscope avec la sensibilité d'une molécule individuelle [7] (figure 4.4, article Optics Express ci-après). Ces travaux étendent le domaine d'application de la FCS aux systèmes d'endoscopie, offrant ainsi de nouvelles méthodes d'analyse (fluorescence, pH, température, agrégation moléculaire…) dans un dispositif compact et portable. Un brevet a été déposé.

---

[6] Wenger J., et al, Disposable Microscope Objective Lenses for Fluorescence Correlation Spectroscopy Using Latex Microspheres, Anal. Chem. 80, 6800-6804 (2008).

[7] H. Aouani, et al, Optical-fiber-microsphere for remote fluorescence correlation spectroscopy, Opt. Express 17, 18912-18919 (2009).

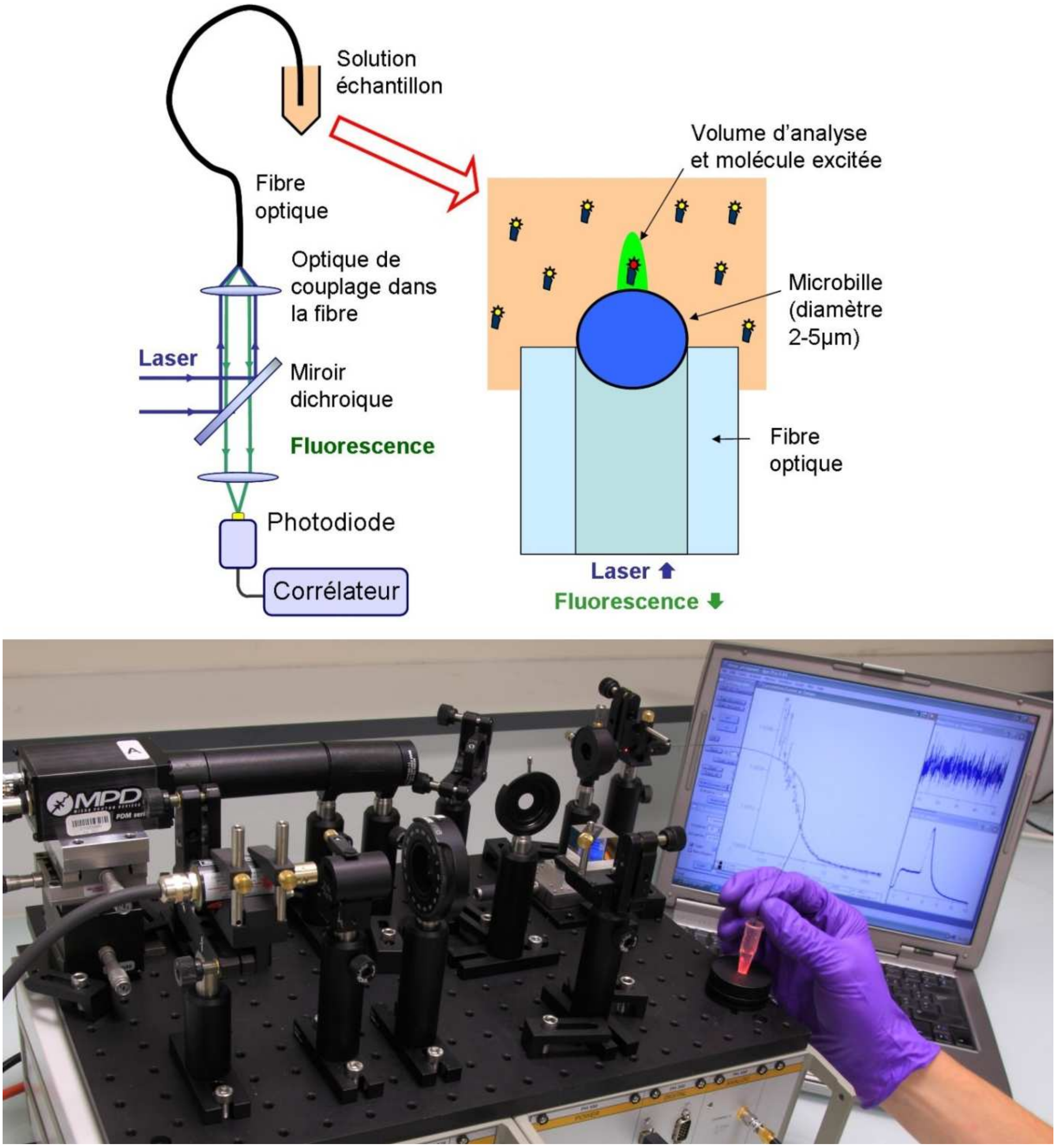

Fig. 14. Plus petit dispositif de spectroscopie FCS, et premier système assurant une sensibilité à la molécule individuelle. La fibre optique microstructurée remplace l'objectif de microscope.

Anal. Chem. **2009,** *81,* 834–839

Nanoaperture-Enhanced Signal-to-Noise Ratio in Fluorescence Correlation Spectroscopy

Jérôme Wenger,* Davy Gérard, Heykel Aouani, and Hervé Rigneault

Institut Fresnel, Aix-Marseille Université, CNRS, Domaine Universitaire de Saint-Jérôme,
13397 Marseille Cedex 20, France

Bryan Lowder and Steve Blair

University of Utah, Electrical and Computer Engineering Department, 50 South Central Campus Drive,
Room 3280, Salt Lake City, Utah

Eloïse Devaux and Thomas W. Ebbesen

Institut de Science et d'Ingénierie Supramoléculaire, Université Louis Pasteur, CNRS, 8 Allée G. Monge,
67000 Strasbourg, France

The fluorescence enhancement found in gold nanoapertures is demonstrated to increase the signal-to-noise ratio (SNR) in fluorescence correlation spectroscopy (FCS). Starting from a general discussion on noise in FCS experiments, we show that fluorescence enhancement leads to a dramatic increase in the SNR. This prediction is confirmed by experiments where we report an experimental gain in SNR of about 1 order of magnitude, corresponding to a 100-fold reduction of the experiment duration. This technique is then applied to monitor the kinetics of a fast enzymatic cleavage reaction. This set of experiments evidence the feasibility of FCS analysis with fast integration times of about 1 s, opening the way to the monitoring of a variety of biochemical reactions at reduced time scales.

Fluorescence correlation spectroscopy (FCS) is a powerful and versatile tool for the analysis of biomolecular interactions.[1,2] FCS can in principle provide information about any molecular dynamic process that induces a change in fluorescence intensity, including translational and rotational diffusion, molecular concentrations, chemical kinetics, and binding reactions.[3,4] It is based on the statistical analysis of fluorescence intensity fluctuations and is commonly performed by computing the second order temporal correlation of the fluorescence trace to construct the so-called autocorrelation function (ACF). The two detection events involved in the ACF have nonzero physical correlations only if they originate from the same molecule. This highlights the single molecule nature of FCS, even though this technique does not rely on the explicit tracking of individual molecules.

Noise and statistical accuracy in FCS are important considerations. First, the understanding of signal-to-noise ratio enables optimization of the experimental apparatus. Second, proper weighting procedures based on statical estimates for the noise enable more accurate analysis. Therefore, several authors have considered the issue of determining the expected noise in FCS since Koppel's seminal contribution in 1974.[5−13] Two physical phenomena contribute to the noise in FCS: the quantum nature of light that induces shot noise and the stochastic nature of the fluorescence fluctuation process itself. A major result from Koppel's work is that the signal-to-noise ratio (SNR) in FCS does not depend>on the total detected fluorescence but on the fluorescence count rate per molecule (CRM) times the square root of the total experiment acquisition time T_{tot} and the correlator channel minimum width $\Delta\tau$: $\mathrm{SNR} \propto \mathrm{CRM}\,(T_{\mathrm{tot}}\Delta\tau)^{1/2}$. This further emphasizes the single molecule nature of FCS and provides guidelines to improve the statistical accuracy in FCS. For a fixed experimental apparatus, one can either increase the excitation power to raise the CRM or wait for longer integration times T_{tot}. However, both of these strategies have significant practical limitations. First, saturation and photobleaching limit the CRM increase to a certain extent. Second, because of the square root dependence of the SNR on the acquisition time, increasing T_{tot} to a few hundred seconds has only a minor influence on the SNR.

---

* To whom correspondence should be addressed. E-mail: jerome.wenger@fresnel.fr.

(1) Eigen, M.; Rigler, R. *Proc. Natl. Acad. Sci. U.S.A.* **1994**, *91*, 5740–5747.
(2) Briddon, S. J.; Hill, S. J. *Trends Pharmacol. Sci.* **2007**, *28*, 637–645.
(3) Rigler, R.; Elson, E. S. *Fluorescence Correlation Spectroscopy, Theory and Applications*; Springer: Berlin, Germany, 2001.
(4) Zander, C. Enderlein, J.; Keller, R. A. *Single-Molecule Detection in Solution: Methods and Applications*; VCH-Wiley: New York, 2002.
(5) Koppel, D. E. *Phys. Rev. A* **1974**, *10*, 1938–1945.
(6) Geerts, H. *J. Biochem. Biophys. Methods* **1983**, *7*, 255–261.
(7) Qian, H. *Biophys. Chem.* **1990**, *38*, 49–57.
(8) Kask, P.; Günther, R.; Axhausen, P. *Eur. Biophys. J.* **1997**, *25*, 163–169.
(9) Meseth, U.; Wohland, T.; Rigler, R.; Vogel, H. *Biophys. J.* **1999**, *76*, 1619–1631.
(10) Wohland, T.; Rigler, R.; Vogel, H. *Biophys. J.* **2001**, *80*, 2987–2999.
(11) Saffarian, S.; Elson, E. L. *Biophys. J.* **2003**, *84*, 2030–2042.
(12) Enderlein, J.; Gregor, I.; Patra, D.; Fitter, J. *J. Fluoresc.* **2005**, *15*, 415–422.
(13) Rao, R.; Langoju, R.; Gösch, M.; Rigler, P.; Serov, A.; Lasser, T. *J. Phys. Chem. A* **2006**, *110*, 10674–10682.

10.1021/ac8024015 CCC: $40.75

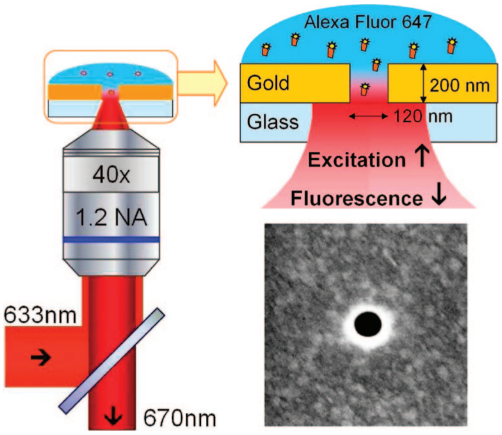

Figure 1. Schematics of the experimental setup and electron micrograph of a 120 nm aperture milled in a gold film.

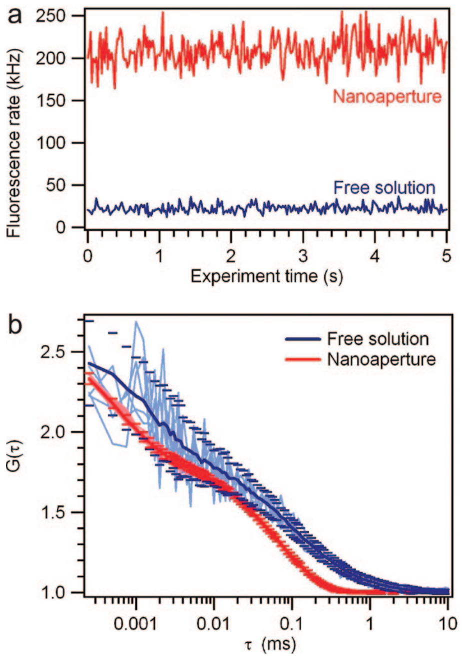

Figure 2. (a) Total fluorescence trace for 40 μW excitation power in the case of free solution and 120 nm diameter gold aperture. (b) ACFs corresponding to the traces in part a. Thick solid lines are ACFs for $T_{\mathrm{tot}} = 200$ s, thin lines correspond to different ACFs acquired with 1 s integration time. The horizontal bars indicate the standard deviation for each point of the ACF computed from the stack of 200 independent ACFs. Analysis of the average ACF (corresponding to $T_{\mathrm{tot}} = 200$ s) using eq 2 yields for the free solution: $N = 1.18$, $\tau_{\mathrm{d}} = 97.5$ μs, $n_{\mathrm{T}} = 0.74$, $\tau_{\mathrm{b_T}} = 2.2$ μs, $s = 0.2$, CRM = 18.1 kHz. For the nanoaperture: $N = 1.15$, $\tau_{\mathrm{d}} = 66$ μs, $n_{\mathrm{T}} = 0.73$, $\tau_{\mathrm{b_T}} = 0.8$ μs, $s = 1$, and CRM = 181 kHz.

Nanophotonics offers new opportunities to further improve the detection of single fluorescent molecules.[14] The CRM can be increased more than 10 times by tailoring the photonic environment.[15] Simultaneously, the detection volume can be reduced to lower the background noise and provide an enlarged domain of molecular concentrations for FCS. Among the many different nanophotonics techniques that have been implemented recently (see ref 16 for a review), nanometer-size apertures milled in an opaque metallic film stand out as promising tools.[17,18] As illustrated on Figure 1, the nanoaperture acts as a pinhole filter directly placed into the object plane of a standard inverted microscope. When the aperture diameter is reduced below the cutoff diameter of the excitation mode in the aperture, the light inside the structure is confined to a rapidly decaying evanescent mode, with a decay length of a few tens of nanometers. Although the concept appears very simple, such nanoapertures exhibit attractive properties for biophotonics, such as localization of excitation light,[17,19,20] strong isolation from emission produced by species located outside the aperture,[21,22] and an increase in the fluorescence signal.[23,24]

Studies on nanoaperture-enhanced fluorescence point out that for a properly tailored aperture, CRM greater than a few hundreds of thousands photons per second can be readily obtained,[25,26] whereas for a single molecule in open solution, fluorescence saturation prevents the count rate from exceeding a few tens of thousands of counts per second. It is therefore anticipated that the nanoaperture-enhanced CRM will yield a much higher SNR in FCS experiments. However, no experimental demonstration has hitherto been presented. In this article, we present the first detailed discussion on the SNR increase when performing FCS in a properly designed nanoaperture. We report an experimental gain in SNR of about 1 order of magnitude and discuss the evolution of the SNR for an arbitrary lag time. Last, we apply this SNR increase to follow the kinetics of a fast enzymatic cleavage reaction.

The paper is outlined as follows. In the Theory section, we give a theoretical background on the noise in FCS. Noise measurements corresponding to a generic situation in FCS are presented in Noise in FCS with Nanoapertures. A specific application to an enzymatic cleavage reaction is described in Application to Enzymatic Cleavage Reaction. Finally in Conclusion we summarize our contributions.

THEORY

In an FCS experiment, the temporal fluctuations $F(t)$ of the fluorescence signal are recorded, and the autocorrelation (ACF) of this signal is computed:

$$G(\tau) = \frac{\langle F(t)\,.\,F(t+\tau)\rangle}{\langle F(t)\rangle^2} \tag{1}$$

---

(14) Craighead, H. G. *Nature* **2006**, *442*, 387–393.
(15) Fort, E.; Grésillon, S. *J. Phys. D: Appl. Phys.* **2008**, *41*, 013001.
(16) Blom, H.; Kastrup, L.; Eggeling, C. *Curr. Pharm. Biotechnol.* **2006**, *7*, 51–66.
(17) Levene, M. J.; Korlach, J.; Turner, S. W.; Foquet, M.; Craighead, H. G.; Webb, W. W. *Science* **2003**, *299*, 682–686.
(18) Lenne, P. F.; Rigneault, H.; Marguet, D.; Wenger, J. *Histochem. Cell Biol.* **2008**, *130*, 795–805.
(19) Samiee, K. T.; Moran-Mirabal, J. M.; Cheung, Y. K.; Craighead, H. G. *Biophys. J.* **2006**, *90*, 3288–3299.
(20) Wenger, J.; Gérard, D.; Lenne, P.-F.; Rigneault, H.; Dintinger, J.; Ebbesen, T. W.; Boned, A.; Conchonaud, F.; Marguet, D. *Opt. Express* **2006**, *14*, 12206–12216.
(21) Liu, Y.; Bishop, J.; Williams, L.; Blair, S.; Herron, J. *Nanotechnology* **2004**, *15*, 1368–1374.
(22) Moran-Mirabal, J. M.; Torres, A. J.; Samiee, K. T.; Baird, B.; Craighead, H. G. *Nanotechnology* **2007**, *18*, 195101.
(23) Liu, Y.; Blair, S. *Opt. Lett.* **2003**, *28*, 507–509.
(24) Rigneault, H.; Capoulade, J.; Dintinger, J.; Wenger, J.; Bonod, N.; Popov, E.; Ebbesen, T. W.; Lenne, P.-F. *Phys. Rev. Lett.* **2005**, *95*, 117401.
(25) Gérard, D.; Wenger, J.; Bonod, N.; Popov, E.; Rigneault, H.; Mahdavi, F.; Blair, S.; Dintinger, J.; Ebbesen, T. W. *Phys. Rev. B* **2008**, *77*, 045413.
(26) Wenger, J.; Gérard, D.; Bonod, N.; Popov, E.; Rigneault, H.; Dintinger, J.; Mahboub, O.; Ebbesen, T. W. *Opt. Express* **2008**, *16*, 3008–3020.

where τ is the delay (lag) time, and $\langle . \rangle$ stands for time averaging. For free Brownian three-dimensional diffusion and Gaussian molecular detection efficiency, the ACF can be expressed as[3,4]

$$G(\tau) = 1 + \frac{1}{N}\left(1 - \frac{\langle B \rangle}{\langle F \rangle}\right)^2 \left[1 + n_{\mathrm{T}} \exp\left(-\frac{\tau}{\tau_{\mathrm{b_T}}}\right)\right] g(\tau) \qquad (2)$$

with

$$g(\tau) = \frac{1}{(1 + \tau/\tau_{\mathrm{d}})\sqrt{1 + s^2\tau/\tau_{\mathrm{d}}}} \qquad (3)$$

where N is the total number of fluorescent molecules, $\langle F \rangle$ the total signal, $\langle B \rangle$ the background noise, n_{T} the amplitude of the dark state population, $\tau_{\mathrm{b_T}}$ the dark state blinking time, τ_{d} the mean diffusion time, and s the ratio of transversal to axial dimensions of the analysis volume. We note that strictly speaking, the assumption of a free 3D-diffusion model is not fulfilled within an aperture. However, this discrepancy can be taken into account by setting the aspect ratio s as a free parameter: it converges to a value close to unity for each run. As already pointed out in refs 25 and 26, this model fits the experimental data remarkably well. Lastly, the count rate per molecule is computed as $\mathrm{CRM} = (\langle F \rangle - \langle B \rangle)/N$.

Koppel considered the case of a large number of molecules in the observation volume $N \gg 1$, small duration of the counting interval compared to the diffusion time $\Delta\tau \ll \tau_{\mathrm{d}}$, negligible background, uniform illumination, and exponential form of the ACF. Under these assumptions, the signal-to-noise ratio for the first channel of the ACF is obtained from Koppel's eq 40:

$$\mathrm{SNR}_{\tau\to 0} = \frac{\mathrm{CRM}\sqrt{T_{\mathrm{tot}}\Delta\tau}}{(1 + 4\mathrm{CRM}\Delta\tau + 2\mathrm{CRM}^2\tau_{\mathrm{d}}\Delta\tau^2)^{1/2}} \simeq \mathrm{CRM}\sqrt{T_{\mathrm{tot}}\Delta\tau} \qquad (4)$$

As discussed in the introduction, the SNR is proportional to the count rate per molecule times the square root of the total measurement time.

To compute the noise in the ACF at longer lag times, we use the same procedure as Meseth and co-workers,[9] and Wohland and co-workers.[10] The standard deviation of the experimental points in the ACF are computed according to a generalization of Koppel's eq 34 with proper normalization:

$$\sigma^2(G(\tau)) = \frac{1}{MN^2}\left[\frac{(1 + g^2(\Delta\tau))(1 + g^2(\tau))}{1 - g^2(\Delta\tau)} + 2mg^2(\tau)\right] + \frac{1}{M}\left[\frac{2(1 + g^2(\tau))}{N\langle n \rangle} + \frac{1}{\langle n \rangle^2}\left(1 + \frac{g(\tau)}{N}\right)\right] \qquad (5)$$

where $M = T_{\mathrm{tot}}/\Delta\tau$, $m = \tau/\Delta\tau$, and $\langle n \rangle$ the average count rate per correlator channel of width $\Delta\tau$. This estimation of the standard deviation is only an approximation of the real noise, but it has previously been demonstrated to be qualitatively correct.[9,10] We point out that care must be taken to model the case of multitau correlators commonly used in FCS, as $\Delta\tau$ is a nonlinear function of the lag time τ.

Interestingly, taking eq 5 in the limit where $\tau \to 0$ and $\Delta\tau \to 0$ provides a formula for the generalized SNR for the first channel of the ACF for the most common experimental conditions for FCS: Gaussian molecular detection efficiency, 3D Brownian diffusion, negligible background, and small width of the counting interval but without any assumption on the number of molecules N. After some basic algebra, one obtains

$$\mathrm{SNR}_{\tau\to 0} \simeq \frac{\mathrm{CRM}\sqrt{T_{\mathrm{tot}}\Delta\tau}}{(1 + 1/N)^{1/2}} \qquad (6)$$

This formula is very close to eq 4 derived by Koppel; although the supplementary $1/N$ term in the denominator accounts for the dependence on the number of molecules. Similar scaling was already obtained by Qian:[7] $\mathrm{SNR} \propto N^{1/2}$ if $N \ll 1$. The physical interpretation of this term is that when $N \ll 1$, a significant fraction of the measurement time is wasted waiting for a detection event. In the next section, we will present noise measurements corresponding to three-dimensional Brownian diffusion of a molecular dye, which is a common case in FCS.

NOISE IN FCS WITH NANOAPERTURES

For the FCS experiments in nanoapertures, we coated 200 nm thick gold films on conventional glass microscope coverslips (thickness 150 μm) by thermal evaporation. A 15 nm thick chromium layer ensures adhesion between gold and the glass substrate. Circular apertures of 120 nm diameter were then milled by a focused ion beam (FEI Strata DB235). This diameter was chosen so as to yield the optimum fluorescence enhancement for Alexa Fluor 647 (A647) dyes excited at 633 nm.[25] Our custom FCS setup is based on an inverted confocal microscope with a 1.2 NA microscope objective. The setup has already been detailed in refs 25 and 26, and it is schematically recalled in Figure 1 for completeness. A droplet of 50 μL of water solution containing A647 molecules was deposited either on top of the nanoaperture sample or on a standard microscope coverslip for the reference case of free solution. As usual in confocal FCS, the droplet acts as a reservoir of molecules that are constantly diffusing in and out of the observation volume. This strongly limits photobleaching effects. The excitation power was set to 40 μW at 633 nm wavelength. We stress that all the data presented here have been measured at this rather low excitation intensity to ensure that the dyes are well below saturation. The detection was performed within the 650−690 nm spectral window, covering about 70% of A647 fluorescence spectrum. The experimental ACFs were computed with a ALV-GmbH ALV6000 hardware multitau correlator, with a minimum channel width of 250 ns.

To investigate the SNR in FCS while using nanoapertures, we conducted 200 successive acquisitions of $T_{\mathrm{tot}} = 1$ s duration. Figure 2a presents a snapshot of the raw fluorescence signal for the free solution and the nanoaperture. Figure 2b displays several ACFs for $T_{\mathrm{tot}} = 1$ s integration, together with the average ACF corresponding to $T_{\mathrm{tot}} = 200$ s. To ensure a direct comparison between the SNRs for both cases, we kept the average number of molecules in each observation volume as close as possible by choosing appropriate dilutions. We obtained $N = 1.18$ molecules for the free solution and $N = 1.15$ for the nanoaperture. This avoids artifacts brought by the dependence of the

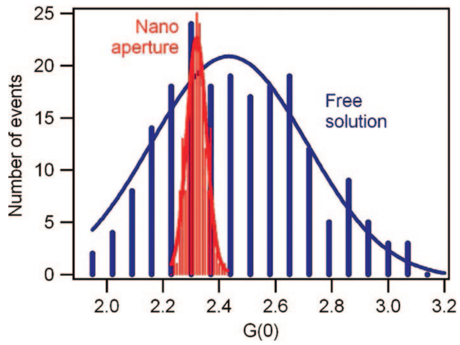

Figure 3. Experimental histograms (bars) for $G(0)$ in the cases corresponding to Figure 2 and numerical fits based on a Gaussian distribution. $T_{\text{tot}} = 1$ s.

SNR on N, as shown by eq 6. With comparison of the fluorescence levels in Figure 2a and given that the number of molecules probed by FCS are equivalent, it is clear that the CRM is dramatically increased within the nanoaperture, which testifies to the fluorescence enhancement brought by the nanoaperture. Numerical analysis of the average ACF using eq 2 yields CRM = 18.1 kHz for the free solution and CRM = 181 kHz for the nanoaperture, corresponding to a fluorescence rate enhancement of 10. It is also apparent from the raw ACFs in Figure 2 that the SNR in the case of $T_{\text{tot}} = 1$ s is far better for the nanoaperture than for the free solution. Hereafter, we will focus on the quantitative evaluation of the SNR increase while using the nanoaperture.

Figure 3 provides a closer look at the statistical distribution of the first channel of the ACF $G(0)$. Histograms of $G(0)$ obtained for 200 runs on free solution or 120 nm aperture are presented. From this data, the mean and the standard deviation of $G(0)$ can be inferred, yielding a SNR of 8.7 for free solution, while SNR = 65.4 for the nanoaperture. The nanostructure brings therefore a gain on SNR of 7.5, which immediately contributes to better FCS data analysis. These figures are to be compared to the theoretical predictions according to Koppel's generalized formula eq 6 which yields a SNR of 6.7 for free solution and 66.2 for the nanoaperture, in very good agreement with the experimental measurements.

The noise on the ACF at longer lag times can be determined by computing the standard deviation for each point $G(\tau)$ from the stack of 200 independent ACFs. These results are presented as markers in Figure 4a. Alternatively, the standard deviation can be analytically approximated by eq 5 (lines in Figure 4a), which stand in good agreement with the measured values. As the lag time τ increases, the average count rate per correlator channel $\langle n \rangle$ increases. The shot noise contribution to the ACF noise is proportional to $\langle n \rangle^{-1}$.[11] Therefore, the higher the count rate, the lower the relative shot noise contribution, which explains why the standard deviation decreases in Figure 4a as τ increases.

Lastly, Figure 4b displays the experimental SNR computed by dividing the average ACFs in Figure 2b by the standard deviation in Figure 4a. It also shows the theoretical SNR awaited from eq 5. As pointed out already in ref 10, eq 5 is a pretty good approximation at short lag times τ but it fails to accurately predict the SNR behavior at longer lag times. One has to keep in mind that eq 5 is a numerical generalization of Koppel's work to account for a Gaussian molecular detection efficiency and an hyperbolic ACF. It has to be understood rather as a (qualitatively correct) approximation of the real noise than as a pure theoretical prediction.[9]

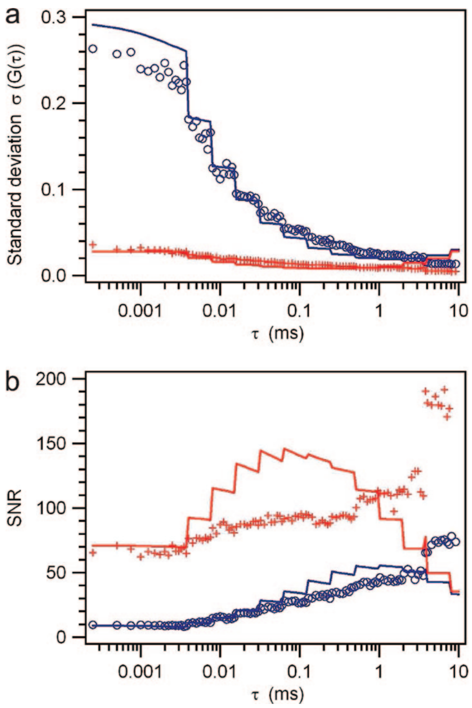

Figure 4. (a) Standard deviations in FCS. Markers denote the experimental points (blue circles, free solution; red crosses, 120 nm aperture), lines are theoretical predictions based on eq 5. (b) SNR deduced from the average ACFs in Figure 2 and the standard deviations in Figure 4a. $T_{\text{tot}} = 1$ s.

Very nicely, the experimental SNR in Figure 4b is always about 1 order of magnitude higher for the nanoaperture than the free solution. This means that the determination of the diffusion time τ_d also benefits from the higher SNR. We estimate an SNR for the determination of τ_d of 25 for the experiments in free solution, while SNR = 95 for the nanoaperture.

Of course, a straightforward way to further increase the SNR in FCS is to wait for longer acquisition times T_{tot}. However, as we already pointed out in the introduction, this strategy may be inappropriate in some applications where speed and time resolution are important or when the CRM are especially low. Hereafter, we will focus on such an application.

APPLICATION TO ENZYMATIC CLEAVAGE REACTION

As part of a molecular immune system, bacteria and archea possess enzymes that cut foreign nucleic acids at specific recognition sequences. The discovery and exploitation of these restriction endonucleases (REs) has been a boon to researchers, enabling targeted cleavage of DNA and thus modern genetic engineering.[27] The most frequently used REs are the so-called "orthodox" type II REs, each of which cuts double stranded DNA at a specific 4−8 base pair palindromic sequence, i.e., a sequence that reads the same from 5′ to 3′ on either strand. The most thoroughly

---

(27) Pingoud, A.; Fuxreiter, M.; Pingoud, V.; Wende, W. *Cell. Mol. Life Sci.* **2005**, *62*, 685–707.

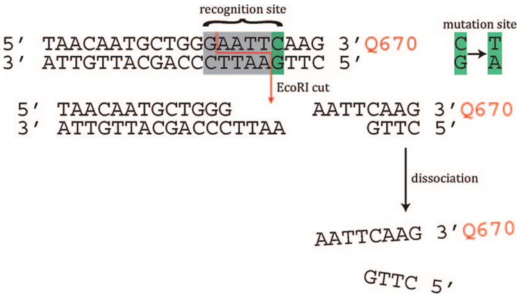

Figure 5. Sequence of the DNA substrate with Quasar 670 (Q670) fluorescent label. The *Eco*RI recognition sequence is shadowed. The mutation site within the recognition region is shaded in green.

studied RE[28] is the orthodox type II RE *Eco*RI.[29] *Eco*RI cuts the sequence GAATTC between the G and A on both strands (Figure 5); the enzyme first binds nonspecifically to the DNA, then diffuses in one dimension along the double helix until it reaches its recognition sequence. The link between binding and catalytic activity is still poorly understood, and more thermodynamic and kinetic measurements are required to elucidate this link.

For kinetic measurements via FCS, we designed an *Eco*RI-cleavable synthetic oligonucleotide substrate (and its complement) as shown in Figure 5. It should be noted that the oligonucleotide sequence corresponds to a portion of the human gene *fucA1*. When *fucA1* is mutated from C to T at nucleotide 1264 (in the translated region), the single *Eco*RI cut site in the gene is eliminated, and codon position 422 is changed from glutamine (CAA) to the ochre stop (TAA) codon. The resulting protein truncation causes a severe form of fucosidosis, a rare neurodegenerative disorder leading to early mortality.[30]

In designing the substrate, we took into consideration the placement of the recognition sequence within the oligo. Ideally, since FCS is sensitive to the change in diffusion time, the cleaved portion (containing the fluorescence label) should be short relative to the entire sequence. A short cleaved duplex will dissociate readily at room temperature, further reducing the size of the product. Many REs have difficulty in cleaving a site that is too close to an end of the helix; however, studies by New England Biolabs suggest that *Eco*RI has little difficulty cleaving near the ends.[31] Further, the fluorescent label may cause steric hindrance of *Eco*RI's activity if placed too closely to the recognition sequence. DNA footprinting experiments[32] with *Eco*RI suggest that the label should be at least four nucleotides distant from the recognition sequence; however, a study of the crystal structure of *Eco*RI bound to its substrate[33] convinced us that a three-nucleotide separation was sufficient.

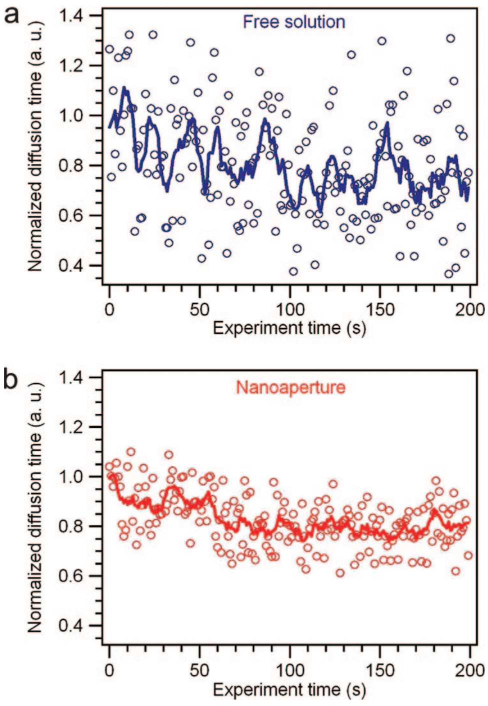

Figure 6. Normalized diffusion times τ_d monitored by FCS during enzymatic cleavage for free solution (a) and 120 nm aperture (b). Markers correspond to $T_{tot} = 1$ s integration time, lines to $T_{tot} = 7$ s.

*Eco*RI activity was recorded in a buffer containing 50 mM Tris-HCl (pH 8.0), 10 mM $MgCl_2$, and 100 mM NaCl. Experiments in free solution were performed on a droplet containing 100 μL of DNA substrate at 85 nM, plus 3 μL of *Eco*RI of activity 10 u/μL. This relatively high *Eco*RI concentration ensures fast cleavage kinetics.[34-36] For FCS on nanoapertures, we kept an equivalent ratio of *Eco*RI to DNA final concentrations, so that the cleavage kinetics are identical in both cases. For FCS in nanoapertures, we used a droplet containing 50 μL of DNA substrate at 1.7 μM, plus 20 μL of *Eco*RI of activity 10 u/μL. Enzyme and DNA solutions were diluted in the reaction buffer and added immediately before analysis.

During the cleavage reaction, *Eco*RI breaks the chemical link between the fluorophore and the double-stranded DNA, resulting in a decrease of the effective dye molecular mass and thus of the mean diffusion time as probed by FCS (Figure 6). Before cleavage, the double stranded DNA-Q670 molecule has a mass of about 14.6 kDa, while after cleavage the Q670 marked strand weighs 4.7 kDa. The anticipated diffusion time reduction scales as the cubic root of the ratio of molecular masses, namely, $(4.7/14.7)^{1/3} \approx 70\%$, which is close to the measured value after about 150 s reaction time (see Figure 6), which is assumed to be near completion.

The experimental results displayed in Figure 6 in free solution and in the nanoaperture show similar behavior, but the SNR in the case of the nanoaperture is about 2.7× better in the case of $T_{tot} = 1$ s. To get an SNR in free solution similar to the one on the nanoaperture, one must increase the integration time by a

---

(28) As measured by number of publications on REBASE database: http://rebase.neb.com. Accessed September 25, 2008. See also Roberts, R. J.; Vincze, T.; Posfai, J.; Macelis, D. *Nucleic Acids Res.* **2007**, *35*, D269–D270.

(29) Yoshimori, R.; Roulland-Dussoix, D.; Boyer, H. W. *J. Bacteriol.* **1972**, *112*, 1275–1279.

(30) Willems, P. J.; Seo, H.-C.; Coucke, P.; Tonlorenzi, R.; O'Brien, J. S. *Eur. J. Hum. Genet.* **1999**, *7*, 60–67.

(31) http://www.neb.com/nebecomm/tech_reference/restriction_enzymes/cleavage_olignucleotides.asp. Accessed September 25, 2008.

(32) Uchida, K.; Pyle, A. M.; Morii, T.; Barton, J. K. *Nucleic Acids Res.* **1989**, *17*, 10259–10279.

(33) Grigorescu, A.; Horvath, M.; Wilkosz, K.; Chandrasekhar, K.; Rosenberg, J. M. Restriction Endonucleases. In *Nucleic Acids and Molecular Biology*; Gross, H. J., Pingound, A., Eds.; Springer-Verlag: Berlin, Germany, 2004; Vol. 14, Chapter 6, pp 137–177.

(34) Kinjo, M.; Rigler, R. *Nucleic Acids Res.* **1995**, *23*, 1795–1799.

(35) Kinjo, M.; Nishimura, G.; Koyama, T.; Mets, U.; Rigler, R. *Anal. Biochem.* **1998**, *260*, 166–172.

(36) Kettling, U.; Koltermann, A.; Schwille, P.; Eigen, M. *Proc. Natl. Acad. Sci. U.S.A.* **1998**, *95*, 1416–1420.

factor $2.7^2 \approx 7$, thereby losing temporal resolution. Remarkably, the experimental data acquired on free solution with $T_{\mathrm{tot}} = 7$ s confirms this prediction.

CONCLUSION

Nanoapertures allow for high count rates per molecule, even at moderate incoming excitation powers. In this contribution, we presented the first demonstration of the signal-to-noise increase in FCS while using nanoapertures. Since the SNR in FCS scales by the product $\mathrm{CRM}(T_{\mathrm{tot}})^{1/2}$, a 10-fold CRM increase commonly observed in well designed nanoapertures amounts to a potential 100-fold reduction of the experiment duration, enabling fast FCS analysis. We believe that this opens new opportunities for probing of specific biochemical reactions that require fast sampling rates.

ACKNOWLEDGMENT

This work has been funded by the French Agence Nationale de la Recherche under Contract ANR-05-PNANO-035-01 “CO-EXUS” and ANR-07-NANO-006-03 “ANTARES. B.L. and S.B. were supported in part by National Science Foundation Grants ECS-0622225 and ECS-0637121.

Received for review November 12, 2008. Accepted November 28, 2008.

AC8024015

Diffusion Analysis within Single Nanometric Apertures Reveals the Ultrafine Cell Membrane Organization

Jérôme Wenger,*† Fabien Conchonaud,‡§¶ José Dintinger,‖** Laure Wawrezinieck,*†‡§¶
Thomas W. Ebbesen,‖** Hervé Rigneault,*† Didier Marguet,‡§¶ and Pierre-François Lenne*†
*Institut Fresnel, Mosaic Group, Université Paul Cézanne Aix-Marseille III, Domaine Universitaire de Saint Jérôme, Marseille Cedex, France; †CNRS UMR 6133, Marseille, France; ‡Centre d'Immunologie de Marseille Luminy, Université de la Méditerranée, Parc Scientifique de Luminy, Case 906, Marseille Cedex, France; §CNRS UMR 6102, Marseille, France; ¶INSERM UMR 631, Marseille, France; ‖ISIS, Université Louis Pasteur, Strasbourg, France; and **CNRS UMR 7006, Strasbourg, France

ABSTRACT We describe the development of a new methodology to probe the plasma membrane organization of living cells at the nanometric scale. Single nanometric apertures in a metallic film limit the observed membrane area below the optical diffraction barrier. The new approach performs fluorescence correlation spectroscopy with increasing aperture sizes and extracts information on the diffusion process from the whole set of data. In particular, transient diffusion regimes are clearly observed when the probed area comes close to the size of the confining structures. First, this strategy allows identification of the mechanism controlling the diffusion of various fluorescent lipid analogs and green fluorescent protein-tagged proteins. Second, it gives an estimate of the characteristic size of the nanometric membrane heterogeneities, allowing a quantitative study of membrane domains such as lipid rafts. Compared to other optical techniques, this method combines the advantages of high spatio-temporal resolution and direct statistical analysis.

INTRODUCTION

Understanding the cell membrane organization is a major biological issue, with implications in cell signaling, adhesion, and trafficking (1–3). Among the debated questions, most attention was paid to membrane heterogeneities, which are commonly investigated by monitoring the diffusion of lipids and membrane proteins. For years, most measurements of lateral diffusion have been made by fluorescence recovery after photobleaching (FRAP) (4,5), showing that membrane heterogeneities impede the diffusion of lipids and proteins (6). However, FRAP investigates an area at least ten times larger than the laser spot, so that it is therefore difficult to infer deviations from Brownian diffusion. Single particle tracking (SPT) offers a powerful alternative by tracking individual labeled molecules with a high spatial resolution of ~10–30 nm (7,8). SPT was successfully applied to reveal membrane corrals (9) and domains (10), but it appears presently limited by a low temporal resolution (often in the millisecond range) and a tedious data analysis. Fluorescence correlation spectroscopy (FCS) is a third method, used to monitor the mobility of individual fluorescent probes across a well-defined observation volume (11). Compared to SPT, FCS allows a better temporal resolution and also an easier data analysis, as statistical averaging is directly carried out in FCS. The main limitation of standard FCS is its spatial resolution of ~300 nm set by the diffraction of light. This drawback can be overcome by using nanometric apertures milled in a metallic film (12–14), but no quantitative application to the question of membrane organization has ever been demonstrated. Moreover, while performing FCS experiments with only a single nanoaperture size, it appears almost impossible to extract relevant information on membrane heterogeneities.

In this study, we describe the development of a methodology to probe the ultrafine organization of living cell membranes by combining FCS with single nanometric apertures of different sizes. The main innovation is that our strategy allows us to identify the mechanism controlling the diffusion of the different molecular components and also provides an estimate for the characteristic size of the nanometric membrane heterostructures. This yields a technique having both high spatial and temporal resolution together with a direct statistical analysis. Living cells with fluorescently labeled membrane components (lipid analogs and green fluorescent protein (GFP)-tagged proteins) are incubated over isolated nanoapertures milled in a metallic film with radii between 75 and 250 nm. The single apertures act as pinholes directly located under the cell membrane and restrict the observation area below the diffraction limit (this is illustrated in Fig. 1). Performing FCS experiments with increasing aperture sizes, we clearly demonstrate that transient regimes are observed when the probed area is close to the size of the confining structures, revealing nanometric membrane heterogeneities. Based on numerical simulations and previous theoretical work (15), we identify the mechanism controlling the diffusion and give an estimate of the characteristic size of the heterogeneities. To validate the method, we compare the diffusion behaviors of different membrane components. For every molecule that we probed, the data obtained within larger

---

Submitted September 4, 2006, and accepted for publication October 13, 2006.

Address reprint requests to Pierre-François Lenne, Institut Fresnel, Domaine Universitaire de Saint Jérôme, 13397 Marseille Cedex 20, France. Tel.: 33-491-288-494; Fax: 33-491-288-067; E-mail: lenne@fresnel.fr, jerome.wenger@fresnel.fr.

0006-3495/07/02/913/07 $2.00

doi: 10.1529/biophysj.106.096586

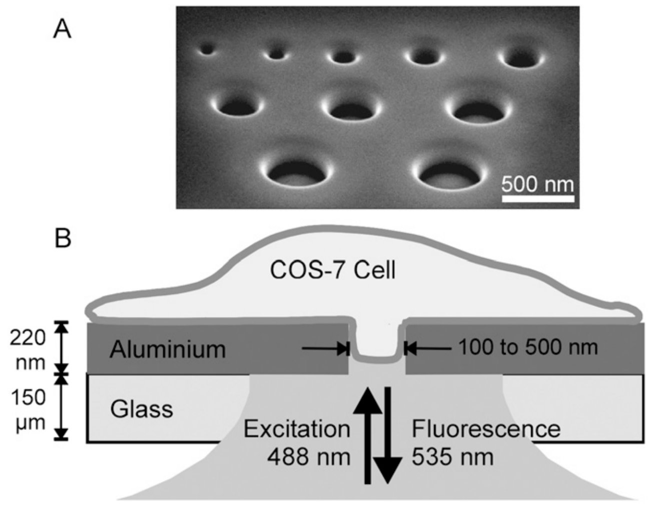

FIGURE 1 (*A*) Electron micrograph image of a set of nanoapertures of various diameters under oblique illumination. This set was only intended for display, as isolated apertures were used in this study. (*B*) Experimental arrangement of the sample.

nanoholes agrees well with the results using diffraction-limited spots and extensive drug treatments (16). This further rules out the possibility that the observed regimes are artifactual.

MATERIALS AND METHODS

Plasmid constructs, cell culture, and transfection

The GFP- glycosylphophatidylinositol (GPI) (gifted from A. LeBivic, IBDML, Marseille) and human transferrin receptor (TfR)-GFP constructs were previously described (16). All experiments were carried out on COS-7 cells (ATCC, CRL-1657). Cells were grown at 37°C, 7% CO_2, in DME supplemented with 10% fetal calf serum, glutamine, and sodium pyruvate. Transfections were performed with ExGen 500 as per the manufacturer's instructions (Euromedex, Souffelweyersheim, France) and stable expressing cells were cloned after selection for G418 resistance.

Cell culture over nanoapertures

Optically opaque aluminum films (thickness 220 nm) were deposited on standard microscope glass coverslips (thickness 150 μm). Focused ion beam technique (FIB) was then used to mill circular nanometric apertures with radii ranging from 75 to 250 nm. The samples were washed for 3 min in an ultrasonic cleaner before rinsing with diluted ethanol (70°) and evaporation of the alcohol residue. We placed a drop of culture medium containing trypsinized COS-7 (ATCC, CRL-1657) cells 40 h before the FCS experiments, to allow cell-substrate adhesion. Cells adhered to the metal surface and conformed to nanoapertures spontaneously.

Fluorescent staining with lipid analogs

Phosphatidylcholine (PC) and ganglioside (G_{M1}) lipids were labeled with the 4,4-difluoro-5,7-dimethyl-4-bora-3a,4a-diaza-s-indacene (BODIPY) fluorophore (Molecular Probes, Leiden, The Netherlands). Equimolar complexes of 0.05 μM BODIPY phosphatidylcholine PC (FL-PC) or BODIPY ganglioside G_{M1} (FL-G_{M1}) with defatted BSA were prepared in HBSS/HEPES buffer (Hanks' buffered salt solution containing 10 mM HEPES pH 7.4). Cell cultures were washed in HBSS/HEPES, incubated with the 0.05 μM lipid/BSA complex in HBSS/HEPES for 30 min at 20°C, rinsed and incubated subsequently in HBSS/HEPES at 37°C. FL-PC staining was done immediately previous to the FCS measurements and FL-G_{M1} staining at least 12 h before the measurements.

Cholesterol conversion

To modify the cholesterol composition of the plasma membrane, cells were treated with *Streptomyces sp.* cholesterol oxidase (COase, Calbiochem) in serum-free HBSS/HEPES buffer, incubated with COase at 1 U/mL for 60 min at 37°C and finally rinsed in HBSS/HEPES buffer. All FCS measurements were completed within 60 min after cellular treatments. In this condition, ~20% of the total cell cholesterol was converted into cholestenone (16). We think that the effect of cholesterol oxidation on raft disorganization originates from a combined effect of cholesterol concentration decrease and production of cholestenone bearing antagonizing action to ordered domains (17).

FCS apparatus

FCS experiments were performed on a custom setup based on an Axiovert 200M microscope (Zeiss, Jena, Germany) with a Zeiss C-Apochromat 40×, numerical aperture 1.2 objective lens and a three-axis piezo-scanner (Physik Instrument, Karlsruhe, Germany). The laser power was lowered to 2.5 μW to avoid cell damage and dye photobleaching. Fluorescence was collected by the same objective, filtered by a dichroic mirror and a confocal pinhole before detection by two avalanche photodiodes through a 50/50 splitter and 535 ± 20 nm bandpass filters. Cross correlations using a hardware correlator (ALV-GmBH, Langen, Germany) between the two photodiodes was used to reduce artifacts. For each aperture diameter, FCS measurements were performed on a minimum of 6 different cells. Each measurement was obtained from 20 runs of 5 s duration. For experiments with diffraction-limited beams, the observation areas were calibrated using FCS measurements on rhodamine-6G in aqueous solution (the diffusion coefficient was taken as 280 $\mu m^2/s$). Due to technical concerns with the microscope apparatus at the beginning of this study, FCS measurements on living cells were carried out at 27°C for lipid analogs and at 37°C for GFP-tagged proteins.

Fitting the autocorrelation functions

For free Brownian two-dimensional diffusion in the case of a Gaussian molecular detection efficiency, the fluorescence autocorrelation function (ACF) is given by

$$g^{(2)}(\tau) = 1 + \frac{1}{N}\frac{1}{1+\tau/\tau_d}, \tag{1}$$

where N denotes the average number of molecules in the observation area and τ_d the diffusion time. τ_d is linked to the laser beam transversal waist w and the molecular diffusion coefficient D by $\tau_d = w^2/(4D)$. In this case, τ_d also equals the ACF lag time at half-maximum.

For FCS measurements on lipids analogs, a single membrane component fit following Eq. 1 was implemented. Even for the smallest apertures used, this procedure efficiently fitted the experimental data, as shown on Fig. 2. In FCS experiments conducted on the chimeric proteins, two diffusive species were associated to the ACF, as already reported in (16). The faster component had diffusion times τ_{fast} of the order of 0.5–1 ms (linked to species diffusing in the intracellular pool), whereas the longer component experienced clearly distinct diffusion times τ_d of ~20 ms (two-dimensional diffusion across the membrane). This is taken into account in the ACF numerical fits by introducing a supplementary free variable A to account for the relative weight of the slow (membrane-bound) species:

$$g^{(2)}(\tau) = A\, g^{(2)}_{slow}(\tau) + (1-A) g^{(2)}_{fast}(\tau). \tag{2}$$

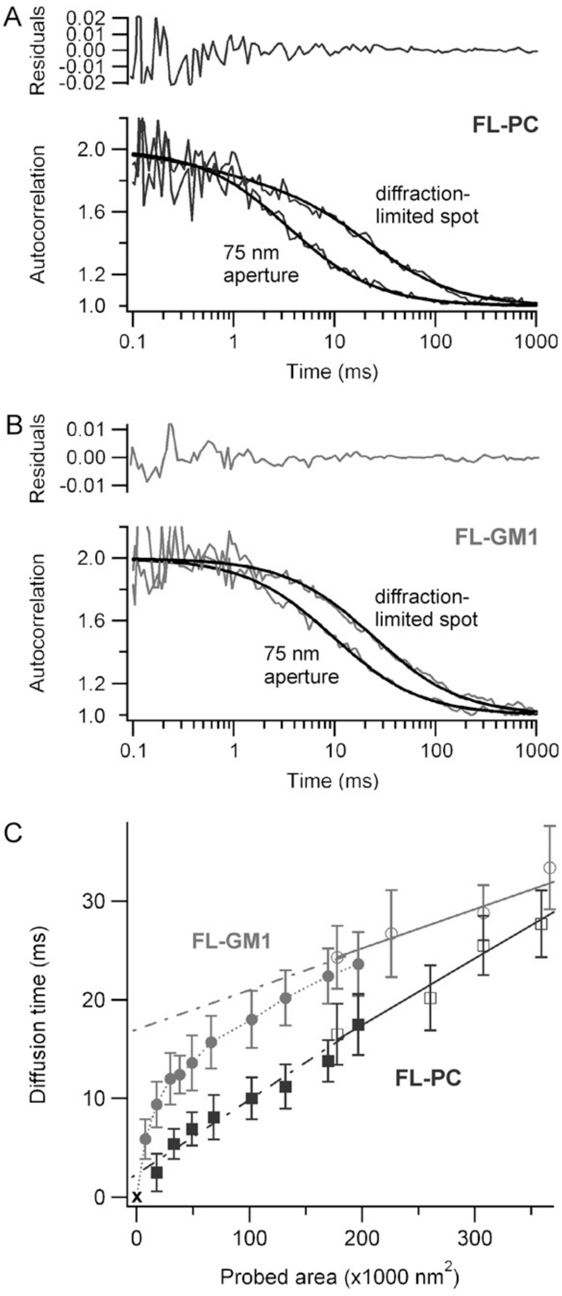

FIGURE 2 (*A*) Normalized autocorrelation functions and numerical fits obtained for FL-PC using an open diffraction-limited beam (240-nm waist) or a 75-nm radius aperture. The upper graph shows the residuals of the fit for the 75-nm aperture case. (*B*) Same as *A* for the FL-G_{M1} lipid analog. (*C*) FCS diffusion laws for FL-PC (*squares*) and FL-G_{M1} (*circles*). The open markers correspond to open beam measurements, whereas the solid markers refer to the nanoaperture experiments (the *dotted line* is to guide the eyes). Solid lines are numerical fits to the open-beam experiments; these lines are extended below the diffraction limit by the dash-dotted lines. Errors bars represent the mean standard deviation.

In open-beam FCS experiments and for the wider apertures, *A* was found to be of the order of 65–70%. When the aperture radius was reduced, the depth of field was also restricted, which limited the influence of the cytosolic fluorescing species. Typically, for a 150-nm radius aperture, *A* was ~75%. It increased to 85% for a 110-nm aperture, and to almost 100% for a 75-nm radius aperture. Thus for these smallest apertures, the diffusion time τ_d could be simply taken as the ACF lag time at half-maximum.

RESULTS

The method reveals different diffusion behaviors for lipid analogs FL-PC and FL-G_{M1}, indicating either free-like or hindered diffusion

We first examine the diffusion of the fluorescent phosphatidylcholine FL-PC in a COS-7 cell membrane. Fig. 2 *A* shows two fluorescence ACFs obtained for FL-PC using a 75-nm radius nanohole and a diffraction-limited spot of 240-nm waist. The ACFs were numerically fitted to determine the diffusion time τ_d (see the Methods section for a description of the fitting procedure). The extracted diffusion times were then plotted against the aperture area and against the laser spot area (as in (15,16), this curve is referred to as FCS diffusion law, see Fig. 2 *C*). Aperture radii varied from 75 to 250 nm in radius, whereas diffraction-limited spot waists were set from 240 to 350 nm by changing the microscope objective's filling factor (15). Fig. 2 *C* shows that the diffusion time τ_d for FL-PC varies almost linearly with the observation area over the whole range being probed. A small slope change may be pointed out around $r \sim 125$ nm (area $\sim 5 \times 10^4$ nm^2), but this comes close to the sensitivity of our apparatus, and appears a minor discrepancy compared to the transient regimes found for the other membrane components (see the discussion in the Supplementary Material online). Two conclusions can thus be drawn: i), FL-PC diffusion within the membrane is apparently unhindered by the nanoaperture; and ii), the observation volume is set by the aperture area.

Although cells, culture conditions and labeling methods were the same, ganglioside analogs FL-G_{M1} have a completely different diffusion behavior, as reported in Fig. 2 *C*. At aperture radii below 100 nm, τ_d increases almost linearly with the aperture area. FL-G_{M1} diffusion then experiences a marked transition at a characteristic radius of ~100 nm, before taking an affine regime. From the slope at $r < 80$ nm, expressing τ_d as $\tau_d = \text{area}/(4\pi D)$, we estimate an effective coefficient $D = 0.36 \pm 0.10$ μm^2/s. For larger observation areas ($r > 200$ nm), τ_d can be written as $\tau_d = \text{area}/(4\pi D) + t_0$, with $t_0 = 16.3 \pm 1.5$ ms and $D = 1.7 \pm 0.2$ μm^2/s. The difference between these regimes enlightens the transition between the diffusion behaviors, even if *D* cannot be straightforwardly interpreted as the exact diffusion coefficients before and after the transition.

The relative change of diffusion behaviors measured for FL-PC and FL-G_{M1} guarantees the relevance of the method. These lipid analogs exhibit very different diffusion laws, indicating that our observations depend on the probed component. For the range of nanoaperture diameters tested, this rules out the possibility that the observed regimes are artifactual. This point is reinforced by the fact that for every marker the diffusion times within larger nanoholes ($r > 200$

nm) agrees nicely with those obtained using diffraction-limited spots. It is probable that the membrane area within nanoholes does not equal the aperture area, but the correction could only account for slight changes of diffusion laws but cannot explain the different behaviors (see the discussion in the Supplementary Material online). Hereafter, we will extract information on the heterogeneities hindering the diffusion of FL-G_{M1}, but before we describe experimental data on the diffusion of GPI-anchored proteins.

The diffusion of GPI-anchored protein is hindered by cholesterol-dependent structures

We investigated the diffusion of the green fluorescent protein (GFP) anchored to a glycosylphophatidylinositol (GPI). Fig. 3 summarizes the results, showing a typical ACF function obtained for a 95-nm radius nanoaperture together with the corresponding curve of the average diffusion time versus the aperture area. Fig. S2 of the Supplementary Material shows nonnormalized ACFs in nanoapertures of various radii. The FCS diffusion law of GFP-GPI displays a marked transition at a characteristic radius of ~120 nm (Fig. 3 *B*). From the slope at $r < 100$ nm, we estimate an effective coefficient $D = 0.30 \pm 0.05\ \mu\text{m}^2/\text{s}$, whereas for $r > 140$ nm, we get $D = 0.9 \pm 0.2\ \mu\text{m}^2/\text{s}$, which is ~3 times the value found for $r < 100$ nm (expressing $\tau_d = \text{area}/(4\pi D) + t_0$, with $t_0 = 8.7 \pm 1.3$ ms). Again, the results obtained for the largest apertures match well with those obtained using diffraction-limited beams, indicating that the probed area is defined by the aperture area and that the aperture does not strongly alter the diffusion process.

We next modified the cholesterol composition of the plasma membrane, since this component is likely to play a significant role in the formation and stability of lipid domains. To achieve this, cholesterol was converted into cholestenone by a cholesterol oxidase (COase) treatment at 1 U/mL. This treatment had a dramatic effect on the diffusion of GFP-GPI, as a linear behavior of the diffusion time versus the probed area was recovered after COase treatment (see Fig. 3 *B*). This free-like two-dimensional diffusion held true for every spot size from 75 to 380 nm, with an effective coefficient $D = 0.72 \pm 0.05\ \mu\text{m}^2/\text{s}$ and an almost null intercept time at origin $t_0 = 0.1 \pm 0.3$ ms consistent with unhindered diffusion (16). This effect confirms that the observed diffusion regimes are not induced by the nanoapertures. The diffusion of GFP-GPI is clearly shown to be cholesterol-dependent, which is consistent with previous studies (16,18).

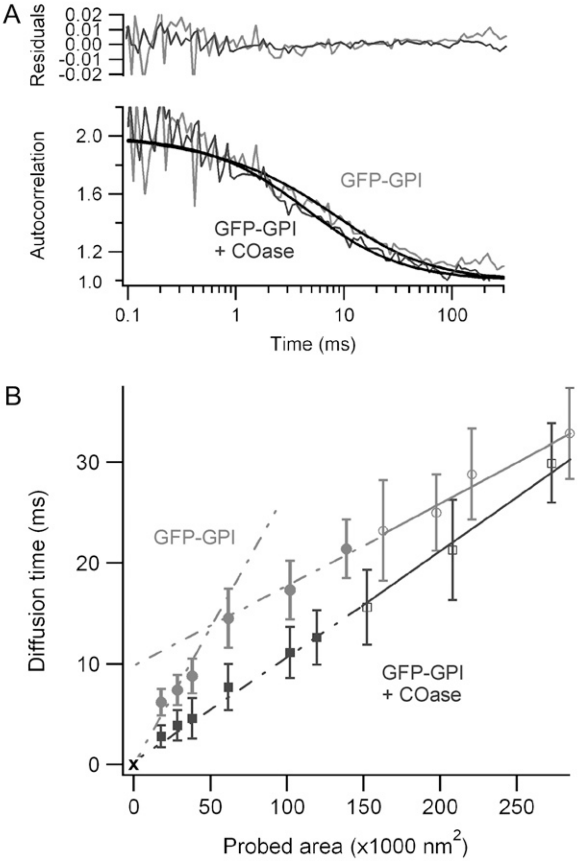

FIGURE 3 (*A*) Normalized autocorrelation functions and numerical fits for GFP-GPI in a 95-nm radius aperture with (*gray*) or without (*black*) 1U/mL COase treatment. The upper graph displays the residuals of the fits. (*B*) FCS diffusion laws for untreated GFP-GPI (*gray circles*) and GFP-GPI with 1 U/mL COase (*black squares*). Open markers correspond to open beam measurements, and solid markers refer to the nanoaperture experiments. Solid lines are numerical fits to the open-beam data. Errors bars represent the mean standard deviation.

Microdomain model simulations and estimates for the sizes of domains

We recently developed numerical models of diffusion into a membrane with confinement structures (15). These structures are areas which confine molecules transiently: their boundaries are sufficiently impenetrable so that the confinement time within the corral is longer than the diffusion time across it. We first consider the case of isolated domains, as indicated in Fig. 4 *A*. In a previous theoretical study, we have shown that diffusion in a such landscape leads to FCS diffusion laws with a marked transition from linear to affine with a positive shift (15). Briefly, isolated domains are assumed to be circular with radius *a*, periodically spaced and static. In this model, molecules can diffuse in and out of the domains with a prescribed probability. The simulations do not depend on the position of the observation area relative to the confining domains, as we averaged the simulated data for the different positions of the beam area. The simulated average diffusion time τ_d is displayed in Fig. 4 *B* versus the normalized area $X_c^2 = (\text{observed area})/(\text{domain area})$.

The features observed for FL-G_{M1} and GFP-GPI (slope change and transient regime) are nicely reproduced by this microdomain model, the transitions being understood as the crossover from confined to normal diffusion. The characteristic transition in our simulations occurs at an observation

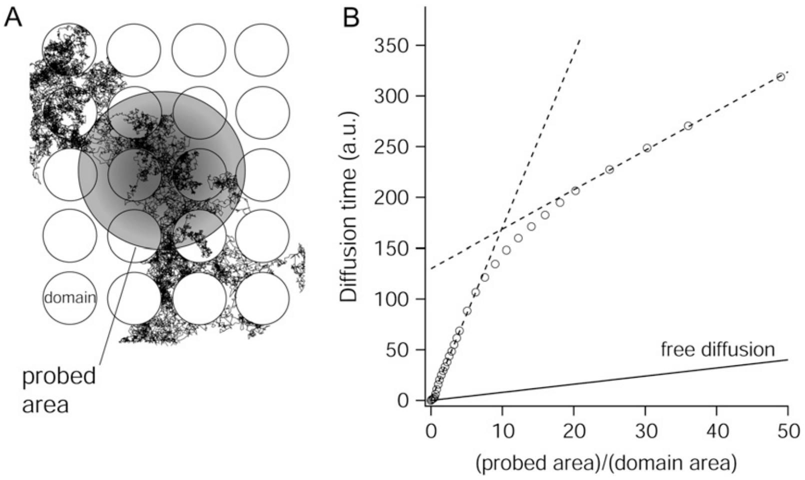

FIGURE 4 Simulated diffusion laws for isolated domains (*A*). The molecules diffuse inside and outside the domains, and are trapped transiently within them. Diffusion is measured by FCS within the probed area (*gray disk*), leading to the FCS diffusion law (*B*). Simulation parameters (15): domains density $d = 0.55$, $\tau_{\mathrm{conf}}/\tau_{\mathrm{d}}^{\mathrm{domain}} = 22$, $D_{\mathrm{in}}/D_{\mathrm{out}} = 1/5$.

area corresponding to $X_{\mathrm{c}}^2 = 10$. We can thus estimate the radii of the confining structures to be ~40 nm for GFP-GPI and 30 nm for FL-G_{M1}. These results come fully within the framework of lipid rafts (19,20).

Transferrin receptor TfR evidences that a cytoskeleton-mediated meshwork also contributes to the lateral compartmentalization in the cell membrane

A cytoskeleton-mediated meshwork also plays a critical role in the membrane lateral organization (9,21). We thus investigated the diffusion of the human transferrin receptor TfR, a transmembrane protein was tagged with the fluorescent protein EGFP (TfR-GFP) whose diffusion is sensitive to the actin cytoskeleton. Fig. 5 displays a typical ACF function obtained for a 210-nm radius nanoaperture, together with the corresponding FCS diffusion law. The results for TfR-GFP clearly differ from the diffusion laws found for GFP-GPI and FL-G_{M1}. Fig. 5 *B* shows two transitions, respectively at $r \sim 150$ nm and $r \sim 230$ nm. As the probed area increases, the diffusion time grows first with an apparent coefficient $D = 0.23 \pm 0.02\ \mu\mathrm{m}^2/\mathrm{s}$, then levels off to $D = 0.7 \pm 0.1\ \mu\mathrm{m}^2/\mathrm{s}$, before increasing again with an effective diffusion rate $D = 0.27 \pm 0.03\ \mu\mathrm{m}^2/\mathrm{s}$ and a negative time intercept at the origin $t_0 = -22 \pm 2$ ms.

To describe the diffusion within the cytoskeleton-mediated meshwork, we developed a numerical model including a network of barriers, as displayed in Fig. 6 . Molecules diffuse within corrals and hop between domains with a prescribed probability. As indicated in Fig. 6 *B*, the transition observed at large area for TfR-GFP comes well within the barrier network model, confirming that fences play a critical role in the compartmentalization of transmembrane proteins. For the meshwork model, the characteristic transition in the FCS law occurs at $X_{\mathrm{c}}^2 \approx 1$. From the measurements on TfR-GFP, the characteristic size of the network can be estimated to be ~230 nm, which appears consistent with the mesh size found for the actin meshwork in rat kidney fibroblast (21).

The shape of the FCS diffusion law in small radii nanoapertures suggests that confinement within discrete microdomains may also occur. This point is reinforced by previous studies using diffraction-limited laser beams (16), where it

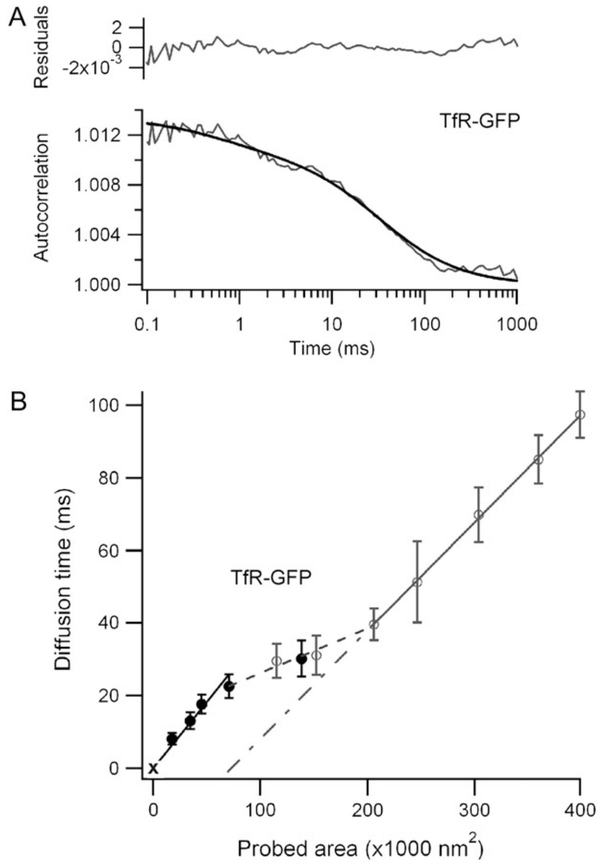

FIGURE 5 (*A*) Autocorrelation function and numerical fit for TfR-GFP in a 210-nm radius aperture, where the characteristic transition takes place. The upper graph displays the residuals of the fit. (*B*) FCS diffusion laws for TfR-GFP. The open markers correspond to open beam measurements, whereas the solid markers refer to the nanoaperture experiments (the *dotted lines* are to guide the eyes).

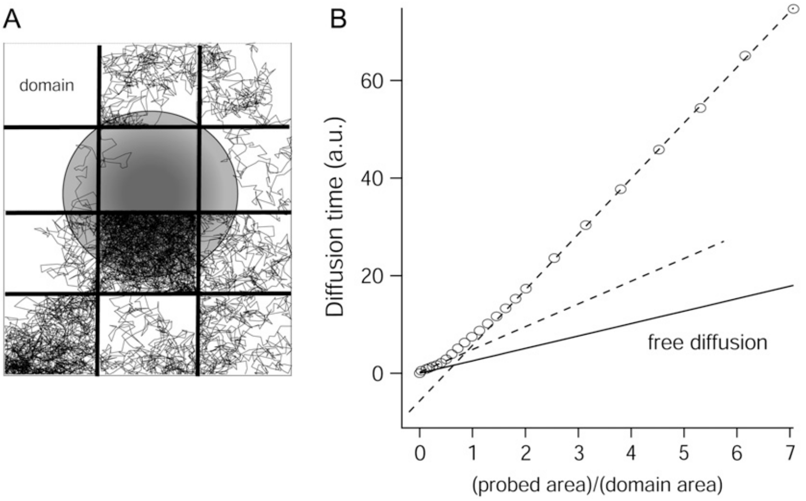

FIGURE 6 Simulated diffusion laws for a network of barriers defining contiguous corrals (*A*). Molecules diffuse within corrals and move from one domain to a neighbored one with a prescribed probability. Diffusion is measured by FCS within the probed area (*gray disk*), leading to the diffusion law (*B*). We considered $\tau_{\mathrm{conf}}/\tau_{\mathrm{d}}^{\mathrm{domain}} = 9$; details of simulations can be found in Wawrezinieck et al. (15).

was shown that high cytochalasin D concentrations disrupted the actin meshwork and led to a positive y-axis intercept t_0. When both actin-based fences and cholesterol were simultaneously modified, the diffusion time was found to be linear with the probed area, thus recovering free-like diffusion behavior. It thus seems likely that the effects of fences and microdomain confinement add each other. From the results displayed in Fig. 5 *B* for probed areas below 10^5 nm^2 and the microdomain numerical model, we can thus estimate the radii of the microdomain confining structures to be ~50 nm for TfR-GFP.

CONCLUSION

We described what we believe is a novel optical approach to explore the ultrafine organization of the plasma membrane. Combining single nanometric apertures of different sizes with FCS, we observe different diffusion regimes, which reveal the kind and the size of the nanometric membrane heterostructures. Compared to conventional FCS, our method has a high spatial resolution, necessary to quantify the size of membrane heterogeneities at the submicron scale. Alternatively to single particle tracking, our approach takes advantage of a high temporal resolution at the microsecond range together with a simple data analysis. Thanks to the recent technical progress in nanotechnology and the development of numerous nanofabrication facilities, the well-established method of FCS can be readily improved by this method. There is thus a high immediate practical relevance for the quantitative study of membrane domains and molecular interactions in membranes.

SUPPLEMENTARY MATERIAL

An online supplement to this article can be found by visiting BJ Online at http://www.biophysj.org.

We thank P. Sens, E. Popov, N. Bonod, and A. Talneau for fruitful discussions and E. Gallery for editing the English.

This work was supported by the ''ACI Nanosciences'' of the French Research ministry, specific grants from UE FEDER and institutional grants from CNRS and INSERM.

REFERENCES

1. Edidin, M. 2003. Lipids on the frontier: a century of cell-membrane bilayers. *Nat. Rev. Mol. Cell Biol.* 4:414–418.
2. Simons, K., and W. L. C. Vaz. 2004. Model systems, lipid rafts, and cell membranes. *Annu. Rev. Biophys. Biomol. Struct.* 33:269–295.
3. Marguet, D., P. F. Lenne, H. Rigneault, and H.-T. He. 2006. Dynamics in the plasma membrane: how to combine fluidity and order. *EMBO J.* 25:3446–3457.
4. Axelrod, D., D. E. Koppel, J. Schlessinger, E. L. Elson, and W. W. Webb. 1976. Mobility measurement by analysis of fluorescence photobleaching recovery kinetics. *Biophys. J.* 16:1055–1069.
5. Meder, D., M. Joao Moreno, P. Verkade, W. L. C. Vaz, and K. Simons. 2006. Phase coexistence and connectivity in the apical membrane of polarized epithelial cells. *Proc. Natl. Acad. Sci. USA.* 103:329–334.
6. Yechiel, E., and M. Edidin. 1987. Micrometer-scale domains in fibroblast plasma membranes. *J. Cell Biol.* 105:755–760.
7. Saxton, M. J., and K. Jacobson. 1997. Single-particle tracking: applications to membrane dynamics. *Annu. Rev. Biophys. Biomol. Struct.* 26:373–399.
8. Kusumi, A., C. Nakada, K. Ritchie, K. Murase, K. Suzuki, H. Murakoshi, R. S. Kasai, J. Kondo, and T. Fujiwara. 2005. Paradigm shift of the plasma membrane concept from the two-dimensional continuum fluid to the partitioned fluid: high-speed single-molecule tracking of membrane molecules. *Annu. Rev. Biophys. Biomol. Struct.* 34:351–378.
9. Sako, Y., and A. Kusumi. 1994. Compartmentalized structure of the plasma membrane for receptor movements as revealed by a nanometer-level motion analysis. *J. Cell Biol.* 125:1251–1264.
10. Dietrich, C., B. Yang, T. Fujiwara, A. Kusumi, and K. Jacobson. 2002. Relationship of lipid rafts to transient confinement zones detected by single particle tracking. *Biophys. J.* 82:274–284.
11. Bacia, K., S. A. Kim, and P. Schwille. 2006. Fluorescence cross-correlation spectroscopy in living cells. *Nat. Methods.* 3:83–89.
12. Levene, M. J., J. Korlach, S. W. Turner, M. Foquet, H. G. Craighead, and W. W. Webb. 2003. Zero-mode waveguides for single-molecule analysis at high concentrations. *Science.* 299:682–686.

13. Edel, J. B., M. Wu, B. Baird, and H. G. Craighead. 2005. High spatial resolution observation of single-molecule dynamics in living cell membranes. *Biophys. J.* 88:L43–L45.
14. Wenger, J., H. Rigneault, J. Dintinger, D. Marguet, and P.-F. Lenne. 2006. Single-fluorophore diffusion in a lipid membrane over a subwavelength aperture. *J. Biol. Phys.* 32:SN1–SN4.
15. Wawrezinieck, L., H. Rigneault, D. Marguet, and P. F. Lenne. 2005. Fluorescence correlation spectroscopy diffusion laws to probe the submicron cell membrane organization. *Biophys. J.* 89:4029–4042.
16. Lenne, P. F., L. Wawrezinieck, F. Conchonaud, O. Wurtz, A. Boned, X.-J. Guo, H. Rigneault, H.-T. He, and D. Marguet. 2006. Dynamic molecular confinement in the plasma membrane by microdomains and the cytoskeleton meshwork. *EMBO J.* 25:3245–3256.
17. Xu, X., and E. London. 2000. The effect of sterol structure on membrane lipid domains reveals how cholesterol can induce lipid domain formation. *Biochemistry.* 39:843–849.
18. Brown, D. A., and E. London. 1998. Functions of lipid rafts in biological membranes. *Annu. Rev. Cell Dev. Biol.* 14:111–136.
19. Pike, L. J. 2006. Rafts defined: a report on the Keystone symposium on lipid rafts and cell function. *J. Lipid Res.* 47:1597–1598.
20. Pralle, A., P. Keller, E. L. Florin, K. Simons, and J. K. Horber. 2000. Sphingolipid-cholesterol rafts diffuse as small entities in the plasma membrane of mammalian cells. *J. Cell Biol.* 148:997–1008.
21. Fujiwara, T., K. Ritchie, H. Murakoshi, K. Jacobson, and A. Kusumi. 2002. Phospholipids undergo hop diffusion in compartmentalized cell membrane. *J. Cell Biol.* 157:1071–1081.

Optical-fiber-microsphere for remote fluorescence correlation spectroscopy

Heykel Aouani[1], **Frédérique Deiss**[2], **Jérôme Wenger**[1,*],
Patrick Ferrand[1], **Neso Sojic**[2] **and Hervé Rigneault**[1]

[1] *Institut Fresnel, CNRS, Aix-Marseille Université, Ecole Centrale Marseille,*
Campus de St Jérôme, 13397 Marseille, France
[2] *Institut des Sciences Moléculaires, Université Bordeaux 1, ENSCPB, CNRS,*
16 Avenue Pey-Berland, 33607 Pessac, France
[*] *Corresponding author: jerome.wenger@fresnel.fr*

Abstract: Fluorescence correlation spectroscopy (FCS) is a versatile method that would greatly benefit to remote optical-fiber fluorescence sensors. However, the current state-of-the-art struggles with high background and low detection sensitivities that prevent the extension of fiber-based FCS down to the single-molecule level. Here we report the use of an optical fiber combined with a latex microsphere to perform FCS analysis. The sensitivity of the technique is demonstrated at the single molecule level thanks to a photonic nanojet effect. This offers new opportunities for reducing the bulky microscope setup and extending FCS to remote or in vivo applications.

OCIS codes: (120.0280) Remote sensing and sensors; (170.6280) Spectroscopy, fluorescence and luminescence; (350.3950) Micro-optics; (120.6200) Spectrometers and spectroscopic instrumentation

---

References and links

1. S. Maiti, U. Haupts, and W. W. Webb, “Fluorescence correlation spectroscopy: diagnostics for sparse molecules,” Proc. Natl. Acad. Sci. U.S.A. **94**, 11753-11757 (1997).
2. W. W. Webb, “Fluorescence correlation spectroscopy: inception, biophysical experimentations, and prospectus,” Appl. Opt. **40**, 3969-3983 (2001).
3. J. Wenger, D. Gérard, H. Aouani, H. Rigneault, B. Lowder, S. Blair, E. Devaux, T. W. Ebbesen, “Nanoaperture-Enhanced Signal-to-Noise Ratio in Fluorescence Correlation Spectroscopy,” Anal. Chem. **81**, 834-839 (2009).
4. F. Helmchen, “Miniaturization of fluorescence microscopes using fibre optics,” Exp. Physiol. **87**, 737-745 (2002).
5. J. R. Epstein and D. R. Walt, “Fluorescence-based fibre optic arrays: a universal platform for sensing,” Chem. Soc. Rev. **32**, 203-214 (2003).
6. O. S. Wolfbeis, “Fiber-optic chemical sensors and biosensors,” Anal. Chem. **78**, 3859-3873 (2006).
7. K. Garai, M. Muralidhar, and S. Maiti, “Fiber-optic fluorescence correlation spectrometer,” Appl. Opt. **45**, 7538-7542 (2006).
8. K. Garai, R. Sureka, and S. Maiti, “Detecting amyloid-beta aggregation with fiber-based fluorescence correlation spectroscopy,” Biophys. J. **92**, L55-L57 (2007).
9. Y.-C. Chang, J. Y. Ye, T. Thomas, Y. Chen, J. R. Baker, and T. B. Norris, “Two-photon fluorescence correlation spectroscopy through dual-clad optical fiber,” Opt. Express **16**, 12640-12649 (2008).
10. Z. Chen, A. Taflove, and V. Backman, “Photonic nanojet enhancement of backscattering of light by nanoparticles: a potential novel visible-light ultramicroscopy technique,” Opt. Express **12**, 1214-1220 (2004).
11. X. Li, Z. Chen, A. Taflove, and V. Backman, “Optical analysis of nanoparticles via enhanced backscattering facilitated by 3-D photonic nanojets,” Opt. Express **13**, 526-533 (2005).
12. P. Ferrand, J. Wenger, M. Pianta, H. Rigneault, A. Devilez, B. Stout, N. Bonod, and E. Popov, “Direct imaging of photonic nanojets,” Opt. Express **16**, 6930–6940 (2008).
13. A. Heifetz, K. Huang, A. V. Sahakian, X. Li, A. Taflove, V. Backman, “Experimental confirmation of backscattering enhancement induced by a photonic jet,” Appl. Phys. Lett. **89**, 221118 (2006).

#116295 - $15.00 USD Received 27 Aug 2009; accepted 5 Oct 2009; published 8 Oct 2009

14. D. Gérard, J. Wenger, A. Devilez, D. Gachet, B. Stout, N. Bonod, E. Popov, H. Rigneault, "Strong electromagnetic confinement near dielectric microspheres to enhance single-molecule fluorescence," Opt. Express **16**, 15297-15303 (2008).
15. D. Gérard, A. Devilez, H. Aouani, B. Stout, N. Bonod, J. Wenger, E. Popov, and H. Rigneault, "Efficient excitation and collection of single molecule fluorescence close to a dielectric microsphere," J. Opt. Soc. Am. B **26**, 1473-1478 (2009).
16. A. Devilez, N. Bonod, B. Stout, D. Gérard, J. Wenger, H. Rigneault, and E. Popov, "Three-dimensional subwavelength confinement of photonic nanojets," Opt. Express **17**, 2089-2094 (2009).
17. J. Wenger, D. Gérard, H. Aouani, and H. Rigneault, "Disposable microscope objective lenses for fluorescence correlation spectroscopy using latex microspheres," Anal. Chem. **80**, 6800-6804 (2008).
18. A. Gennerich and D. Schild, "Fluorescence Correlation Spectroscopy in Small Cytosolic Compartments Depends Critically on the Diffusion Model Used," Biophys. J. **79**, 3294-3306 (2000).
19. J. Wenger, D. Gérard, N. Bonod, E. Popov, H. Rigneault, J. Dintinger, O. Mahboub and T. W. Ebbesen,"Emission and excitation contributions to enhanced single molecule fluorescence by gold nanometric apertures," Opt. Express **16**, 3008-3020 (2008).
20. M. Pitschke, R. Prior, M. Haupt, and D. Riesner, "Detection of single amyloid β-protein aggregates in the cerebrospinal fluid of Alzheimer's patients by fluorescence correlation spectroscopy," Nature Medicine **4**, 832-834 (1998).
21. N. Opitz, P. J. Rothwell, B. Oeke, and P. Schwille, "Single molecule FCS-based oxygen sensor (O_2-FCSensor): a new intrinsically calibrated oxygen sensor utilizing fluorescence correlation spectroscopy (FCS) with single fluorescent molecule detection sensitivity," Sensors and Actuators B **96**, 460-467 (2003).
22. F. H. C. Wong, D. S. Banks, A. Abu-Arish, and C. Fradin, "A Molecular Thermometer Based on Fluorescent Protein Blinking," J. Am. Chem. Soc. **129**, 10302–10303 (2007).

---

1. Introduction

Fluorescence correlation spectroscopy (FCS) is a powerful and versatile method for the detection and characterization of fluorescent molecules [1, 2]. FCS is based on computing the temporal correlation of the fluorescence intensity fluctuations. It can in principle provide information about any molecular process that induces a change in the fluorescence intensity. Applications include determining translational and rotational diffusion, molecular concentrations, chemical kinetics, and binding reactions.

In contrast to other fluorescence techniques, the critical parameter in FCS is not the total fluorescence intensity, but the amplitude of the fluorescence fluctuations, which is directly related to the brightness of each molecule. While computing the temporal correlation of the fluorescence intensity, non-zero correlations will occur only if they originate from the same molecule. This highlights the single molecule nature of FCS, and the need to maximize the detected photons from each molecule [3].

Therefore, FCS is commonly implemented on a confocal microscope with a high numerical aperture objective. Despite its extreme sensitivity (down to the single molecule in a routine experiment), this approach remains expensive and difficult to integrate onto a lab-on-a-chip format because of the bulky optical arrangement.

Much attention is currently devoted to miniaturize optical devices and extend the detection capabilities to remote or in vivo applications. To this end, the use of an optical fiber probe for simultaneous excitation and detection of fluorescent molecules is a promising approach [4, 5, 6], which would be greatly extended if FCS was implemented for dynamics analysis.

Recently, the use of a single-mode [7, 8] or dual-clad [9] optical fiber has been investigated to perform FCS with one- or two-photon excitation respectively. However, due to low detected fluorescence rates per molecule and the high background in the fibers, these demonstrations were limited to detecting fluorescent nanospheres of at least 24 nm in diameter. Extending the technique to true single-molecule sensitivity remains a challenge.

Here, we circumvent the aforementioned limitations by combining the optical fiber endoscope with a polystyrene microsphere at the end of the fiber (figure 1). Selective wet-chemical etching of the distal face of an optical fiber bundle produces a microwell array. The microwells

Received 27 Aug 2009; accepted 5 Oct 2009; published 8 Oct 2009

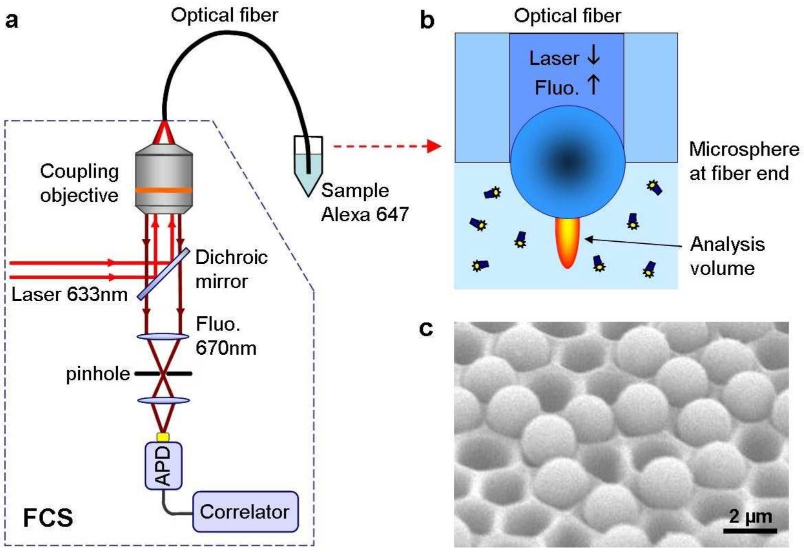

Fig. 1. (a) Schematic view of the experimental setup. (b) shows a close-up view of the end of the optical fiber core covered with the microsphere. (c) Electron microscope image of the optical fiber bundle output partly etched with polystyrene microspheres.

correspond to the etched optical cores, and are then filled with microspheres. This procedure enables correct alignment of the microsphere on top of the optical fiber.

We call this device OFM, which stands for Optical-Fiber-Microsphere. By acting as a microlens coupler directly set at the fiber end, the microsphere enables efficient excitation and detection of the fluorescence from standard single molecular dyes. This enables the first demonstration of remote fiber-based FCS at the single molecule level.

Our results are strongly related to the peculiar electromagnetic field distribution that emerges from a dielectric microsphere. Under plane wave illumination, several recent papers have theoretically and experimentally demonstrated the existence of a beam called “photonic nanojet” that emerges from the microsphere with high intensity, subwavelength transverse dimensions and low divergence [10, 11, 12]. Dielectric microspheres have appeared as effective devices to enhance nanoparticle backscattering [13], and single molecule fluorescence detection in a conventional confocal microscope setup [14, 15, 16].

We have recently demonstrated that a latex microsphere combined with a simple lens can form a high performance disposable optical system, offering a simple and low-cost alternative to the expensive microscope objectives used in FCS [17]. However, this method requires careful positioning of the microsphere respectively to the collection lens focus, and is not compatible with an integrated arrangement for remote sensing.

Here, we take advantage of the previous demonstrations to describe an optical fiber-microsphere (OFM) coupled system with single molecule sensitivy for FCS. This device has the advantage to operate without any positioning stage (except the fiber input coupler), and to offer remote sensing capabilities in a compact setup.

2. Numerical simulations of the optical fiber microsphere system

To investigate the interaction between the optical fiber mode and the microsphere, we have performed 2D finite-difference time-domain (FDTD) computations using RSoft Fullwave soft-

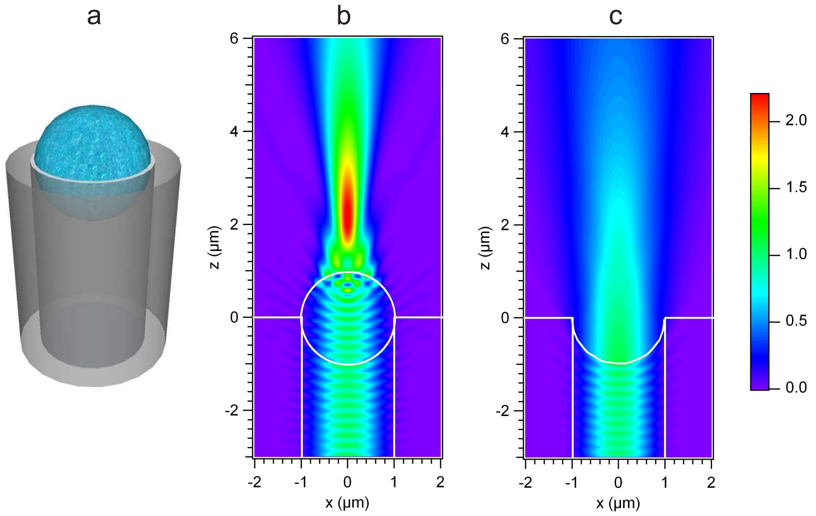

Fig. 2. (a) Experimental configuration of the fiber core-clad and microsphere configuration. FDTD-calculated electric field intensity with (b) and without (c) a 2 μm cylinder illuminated by the fundamental fiber mode at $\lambda = 633$ nm (see text for structure details).

ware (Fig. 2). These simulations are intended to give a vision of the peculiar electromagnetic distribution that emerges from this system.

The computational domain is set to 4×8 μm^2, with 10×10 nm^2 grid size and perfectly matched layers as boundary conditions. The microsphere is modelled by a dielectric cylinder with a 2 μm diameter and a refractive index corresponding to polystyrene in the visible range $n = 1.59$. The GeSiO$_2$-FSiO$_2$ core-clad optical fiber has a core diameter of 2 μm (refractive index 1.49) and cladding diameter of 3.4 μm (refractive index 1.43). The embedding medium is taken to be water (refractive index 1.33).

The fundamental mode of the optical fiber at 633 nm wavelength (in vacuum) is launched inside the fiber. When the microsphere is set on top of the fiber (Fig. 2(b)), the incident beam is focused in close fashion to photonic nanojets under plane wave illumination [10, 11]. When no sphere is present (Fig. 2(c)), the beam is just diverging from the chemically etched fiber output.

From Fig. 2(b), we estimate the transverse and axial FWHM of 480 nm and 2.7 μm respectively, which come close to the values typically reached with a high NA microscope objective. The specific focusing brought by the microsphere further confines the excitation light. Reciprocally, the microsphere also allows for collecting the fluorescence light [15]. Both effects contribute to the increased sensitivity of the OFM system.

3. Materials and methods

3.1. Optical fibers and microspheres

The bundles consist of 6000 individually cladded optical fibers coherently organized in an imaging area of 270 μm diameter (FIGH-06-300S, Fujikura Ltd). The two faces of the 50 cm imaging fiber are polished before use with 5-1-0.3 μm lapping films (Thorlabs). A microwell at each optical fiber core is realized by a 25 s chemical etching in a fluorhydric acid solution (use with caution: HF solutions are extremely corrosive), using the difference in wet-etching rates between the GeO$_2$-doped core and the fluorine-doped cladding. The reaction time was adapted to create wells fitting the 2 μm polystyrene spheres. The OFM is finally obtained by solvent

Received 27 Aug 2009; accepted 5 Oct 2009; published 8 Oct 2009

evaporation of a solution containing the microspheres: Small drops of this solution are successively deposited on the etched face and let dry to allow the microspheres to self-organize on the microwell array. Last, distilled water is used to wash out the unfixed microspheres.

3.2. FCS experimental setup

As molecular probe, we use Alexa Fluor 647 (A647, Invitrogen, Carlsbad, CA) which is a commonly used dye for FCS with absorption / emission maxima at 650 and 670 nm. Our experimental setup is based on an inverted microscope with a Zeiss C-Apochromat 40x/NA 1.2/ water-immersion objective, providing a state-of-the-art reference for confocal FCS setup. For experiments with the bundle of fibers, the same objective is used to couple the 633 nm excitation light into the fiber and collect the emitted fluorescence. However, to get a better coupling into a single fiber of the bundle, the size of the incident beam is reduced to obtain an effective NA of 0.3. Micrometer positioning of the fiber bundle with respect to the microscope objective focus enables exciting a single fiber. We emphasize that no cross-correlation between different fibers of the bundle was detected, thanks to a 4 μm separation between each individual fiber and 50 cm propagation length.

The fluorescence path after the fiber comprises a dichroic mirror (Omega Filters 650DRLP) followed by a confocal filter with a 50 μm pinhole. Detection is performed by two fast avalanche photodiodes (Micro Photon Devices by PicoQuant MPD-5CTC) separated by a 50/50 beamsplitter. Due to a strong Raman and fluorescence background from the optical fiber, A647 fluorescence measurements are spectrally integrated in a narrow window around 680 ± 10 nm by combining two bandpass filters (Omega Filters 670DF40 and 695AF55). This configuration is set to optimize the fluorescence signal-to-noise ratio.

Finally to perform FCS, the fluorescence intensity temporal fluctuations are analyzed by cross-correlating the signal of the two photodiodes with a ALV6000 hardware correlator. This computes the correlation function: $g^{(2)}(\tau) = \langle F(t).F(t+\tau)\rangle / \langle F(t)\rangle^2$, where $\langle . \rangle$ stands for time-averaging over the experiment duration [2]. This well-known configuration eliminates correlations due to the dead time of the photodiodes and avoids artifacts. Each individual FCS measurement was obtained by averaging at least 10 runs of 10 s duration each.

3.3. FCS analysis

To analyze the FCS data we use the analytical model established for Brownian three-dimensional diffusion in the case of a Gaussian molecular detection efficiency [2]:

$$g^{(2)}(\tau) = 1 + \frac{1}{N}\left(1 - \frac{B}{F}\right)^2 \left[1 + n_T \exp\left(-\frac{\tau}{\tau_T}\right)\right] \frac{1}{(1+\tau/\tau_d)\sqrt{1+s^2\,\tau/\tau_d}} \tag{1}$$

where N is the average number of molecules, F the total signal, B the background noise, n_T the amplitude of the dark state population, τ_T the dark state blinking time, τ_d the mean diffusion time and s the ratio of transversal to axial dimensions of the analysis volume, fixed here to $s = 0.2$ from the numerical simulations. Strictly speaking, the assumptions for the above model are not fulfilled close to a microsphere. However, let us point out that restriction of the range available for diffusion will only slightly affect the diffusion time (millisecond time range), and leave unaffected the correlation amplitude and the fast components of the correlogram [18]. Equation (1) model has successfully been applied in more complex systems [14, 19]. Lastly, we point out that relative measurements of variations in diffusion times are always possible, and are sufficient to assess enzymatic activity, chemical rate constants, or binding rates.

Received 27 Aug 2009; accepted 5 Oct 2009; published 8 Oct 2009

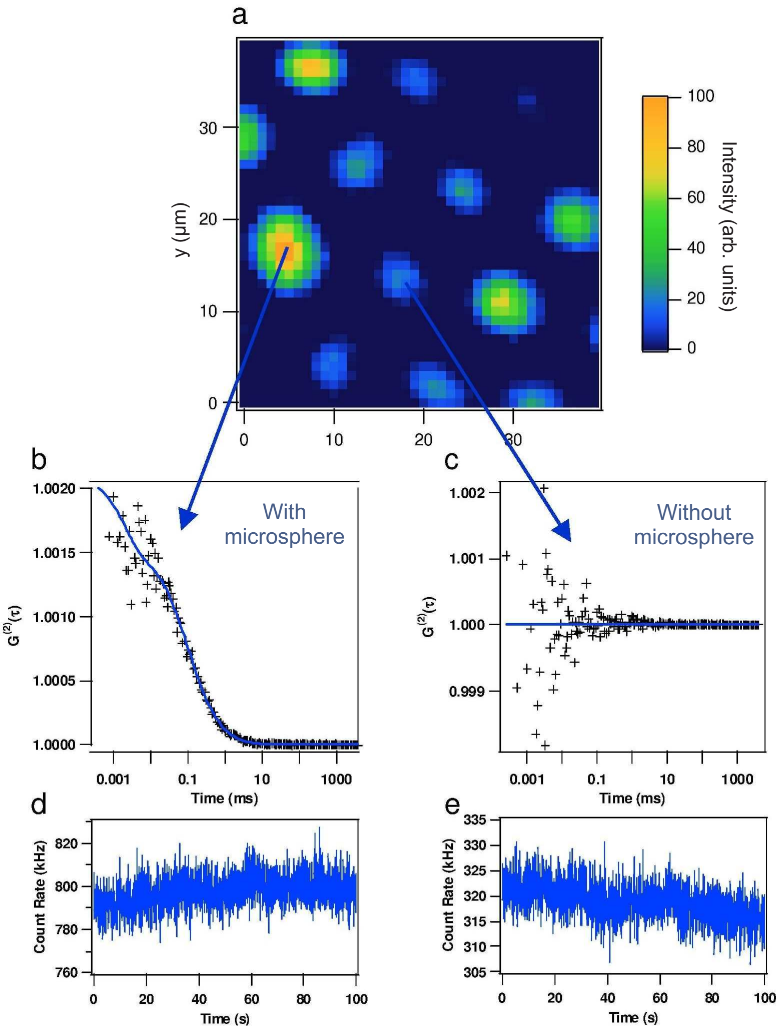

Fig. 3. (a) Scanning image of the bundle: bright areas correspond to the presence of microsphere, where autocorrelation function is obtained (b). Analysis of the correlation function in (b) yield: N = 284, τ_d = 123μs, s = 0.2, n_T = 0.39, τ_T = 2μs, CRM = 1.9kHz, the laser power being set to 0.6 mW at the entrance of the fiber. Without microsphere (dark areas), FCS measurements cannot be performed (c). (d) and (e) are the fluorescence signal traces corresponding respectively to (b) and (c).

4. Experimental results and discussion

We conduct FCS measurements by dipping the OFM bundle into a fluorescent solution of A647 molecules. Not all etched fibers are associated with a 2 μm polystyrene sphere, as the microsphere deposit step was not specifically optimized for this study. Scanning the coupling into the bundle is thus necessary to identify optical fiber-microsphere coupled systems (Fig. 3 (a)). The bright areas correspond to the presence of a 2 μm sphere on the fiber output where the fluorescence correlation function is clearly greater than one (Fig. 3 (b)) while in dark areas, no time correlation was found, corresponding to the absence of microsphere (Fig. 3 (c)).

Received 27 Aug 2009; accepted 5 Oct 2009; published 8 Oct 2009

From Figure 3 (b) it is apparent that thanks to the microsphere, the sensitivity is high enough to detect temporal correlations for FCS with standard organic fluorophores. As demonstrated in the negative control in Fig. 3 (c) and (e) and discussed further below, the correlations observed in the case of the microsphere are related to the detection of A647 molecules, and not to any fluctuation originating from technical noise on our setup.

To analyse the FCS data according to Eq. (1), it is crucial to accurately determine the background noise B. In our case, B originates mainly from fluorescence and Raman scattering from impurities or dopants in the fibers. Special care has been taken to evaluate the level of this background noise by dipping the fibers into pure water solution. The typical level of background noise corresponding to the situation of Fig. 3 is $B = 270$ kHz, the signal-to-noise ratio is typically about 1.9.

Table 1 summarizes the characteristics of the OFM system, and compares the results to the conventional confocal setup using a 1.2 NA microscope objective, with the same A647 solution. Very nicely, the measured numbers of molecules come very close for both systems. This demonstrates that the analysis volume with the OFM is comparable to the one obtained with a diffraction-limited state-of-the-art FCS microscope, and stands in good agreement with the numerical simulations performed in Section 2. Despite a much higher background in the case of the OFM, the sensitivity is still high enough to detect single A647 molecules within a reasonable integration time.

Table 1. Results of the numerical fits of the FCS data measured with the Zeiss objective and OFM. The observation volume V_{eff} is inferred from the number of molecules N and the dye concentration.

Objective	N	τ_d (μs)	V_{eff} (fL)	CRM (kHz)	P_{laser} (mW)
Zeiss 1.2NA	222	115	0.5	3.5	0.1
OFM	284	123	0.65	1.9	0.6

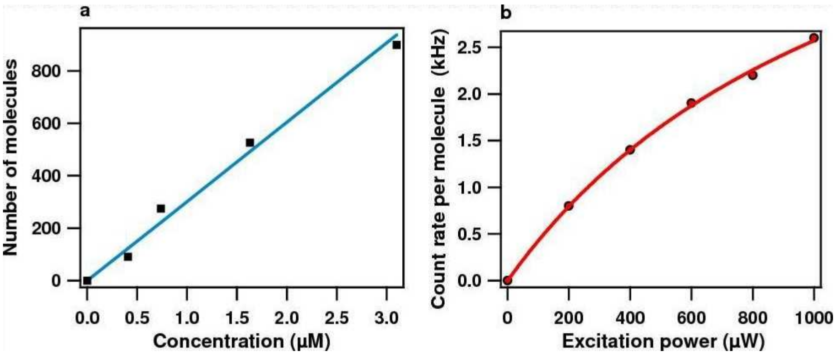

Fig. 4. (a) Evolution of the detected number of A647 molecules versus calibrated molecular concentration. (b) Count rate per molecule plotted versus excitation power (circle) and numerical fit (solid line).

To discuss the concentration sensitivity of the OFM, we carried out FCS measurements for different calibrated concentrations of A647 ranging from 0.4 to 3.1 μM. Figure 4 (a) displays the evolution of the total number of molecules detected with the OFM versus the concentration of A647 dye. As expected for FCS, the detected number of molecules follows a linear relationship with the concentration. Due to the high background noise, FCS measurements are presently limited to concentrations above 400 nM.

In addition, we performed a set of FCS measurements of the detected count rates per molecule *CRM* while increasing the excitation power from 200 to 1000 μW (Fig. 4 (b)). This experimental data follows the standard expression of the fluorescence rate of a three level system given by $CRM = A\, I_e/(1+I_e/I_s)$, where I_e is the excitation intensity, I_s the saturation intensity, and A a constant proportional to the dye's absorption cross section, its quantum yield, and the setup collection efficiency [19]. Results of the fit are: A = 0.05 kHz/μW, I_s = 1260 μW. This measurement provides another confirmation of the single-molecule sensitivity of the OFM.

5. Conclusions

We report the use of an Optical-Fiber-Microsphere (OFM) which combines an etched optical fiber with a latex microsphere to perform remote fiber-based FCS analysis at the single molecule level. Thanks to the microsphere, the excitation beam is further focused and the fluorescence collection efficiency is improved. This configuration circumvents the drawbacks introduced while performing remote FCS sensing with an optical fiber, and enables a sensitivity high enough to work with standard fluorescent molecules.

We point out that there is no need to use a bundle; a single optical fiber combined with a 2 μm sphere can achieve the same performances. FCS measurements have been performed by using an optical fiber combined with 3 μm latex sphere, but no correlation of the fluorescence signal was found due to a weaker focusing by these spheres. Currently, the main limitation of the OFM is the intrinsic background fluorescence of the fiber that makes FCS studies on A647 difficult below 400 nM concentration. Using fibers with less background noise and/or brighter dyes could further extend FCS studies at nanomolar concentration.

We believe that OFM offers new opportunities for remote or in vivo fluorescence characterization together with a miniaturization of bulky FCS setup. Compact portable systems for FCS analysis appear clearly feasible with this technique. We foresee new investigations for endoscopic applications, and opto-microfluidic lab-on-chips. Applications for remote sensing with FCS concern for instance early diagnosis of Alzheimer's disease [20], oxygen sensing [21], or temperature sensing [22].

Acknowledgments

The authors acknowledge stimulating discussions with D. Gérard, N. Bonod, A. Devilez, B. Stout, and E. Popov. This work is funded by contract ANR-07-NANO-006-03 "ANTARES".

Conclusion et Perspectives

La capacité de réaliser des nanostructures dont les formes sont contrôlées avec une résolution de quelques nanomètres ouvre des perspectives prometteuses pour la nanophotonique et la biophotonique. Des avancées récentes permettent de confiner et d'exalter le champ lumineux, et donnent accès à un contrôle de l'environnement électromagnétique d'une molécule individuelle. Ces nouvelles possibilités apportent des améliorations essentielles dans la détection de fluorescence, et ouvrent des perspectives d'applications innovantes en biochimie analytique à l'échelle d'une molécule individuelle.

L'emploi de nanoantennes plasmoniques optimisées ouvre la perspective de performances nettement améliorées. Des renforcement de l'ordre de la centaine et des volumes réduits de plus de trois ordres de grandeurs sous la limite de diffraction sont à portée en exploitant judicieusement les résonances plasmoniques à la surface de nanoparticules métalliques. Enfin, ces différentes structures peuvent être combinées en sortie de fibre optique pour former un dispositif portable pour l'analyse de molécules individuelles, et permettre l'endoscopie de fluorescence in situ avec une excellente sensibilité.

Les moyens technologiques actuels permettent une ingénierie de structures nanométriques interagissant fortement avec les champs optiques. Micro et nano-cavités, nano-antennes, guides et résonateurs plasmoniques ne supportant pas de coupure sont des objets capables de confiner les champs optiques sur des échelles bien inférieures à la longueur d'onde. Il est passionnant d'explorer comment ces résonances localisées peuvent être utilisées pour exalter les interactions molécule/lumière et ainsi réaliser une spectroscopie moléculaire à l'échelle de quelques molécules. Les applications concernent alors l'ultra-résolution optique mais également les bio-puces à forte intégration spatiale. Est également concerné le développement de sondes plasmoniques (nanoparticules) dont l'interaction lumière matière serait optimisée.

Le couplage entre structure plasmonique est, nous le savons, une des clefs pour optimiser les résonances électromagnétiques ; comment adresser de manière optimale de telles structures reste un champ à explorer. Il est aussi spectaculaire de constater que les multiples degrés de liberté du champ électromagnétique dans les structures plasmoniques complexes permettent un adressage spatial, contrôlable à une échelle sub-longueur d'onde, de la lumière par adaptation du profil spatio-temporel des champs incidents.

Projets financés

Ces projets s'inscrivent dans la prolongation thématique de mes recherches (nanoantennes plasmoniques, fluorescence moléculaire), mais les structures sondées et les techniques de mesures seront complètement originales, et en rupture avec les études passées (nanotrous, microsphères). De plus, un élargissement vers d'autres contrastes (diffusion Raman stimulé, optique non-linéaire) est en cours.

ERC Starting Grant « ExtendFRET »

Titre long : Extended fluorescence resonance energy transfer with plasmonic nanocircuits

Projet : exaltation du processus de transfert dipole-dipole dans des nanocircuits plasmoniques

Durée : 5 ans du 01/01/2012 au 31/12/2016

Rôle : principal investigateur

FP7 STREP ICP « NanoVISTA »

Titre long : Advanced photonic antenna tools for biosensing and cellular nanoimaging

Projet : développement de nanoantennes photoniques pour la détection exaltée de biomolécules et l'imagerie à haute résolution de membranes cellulaires

Durée : 4 ans du 01/11/2011 au 31/10/2015

Rôle : responsable du workpackage sur l'exaltation de fluorescence par des nanoantennes

ANR Blanc « TWINS »

Titre long : ToWards hybrid architectures for BrIght and directional NanoantennaS

Projet : développement de nanosources de photons uniques avec des nanoantennes plasmoniques auto-assemblées

Durée : 3 ans du 01/10/2011 au 30/09/2014

Rôle : partenaire en charge des expériences de corrélation de fluorescence

Nanoantennes plasmoniques et fluorescence moléculaire

La capacité de détecter efficacement une molécule individuelle est un enjeu majeur des nanotechnologies, avec des implications pour l'analyse chimique et biophysique. Cependant, deux défis majeurs limitent actuellement l'usage de méthodes de détection de molécules individuelles par fluorescence : (i) une limitation des concentrations utiles au domaine nanomolaire, et (ii) des niveaux de signaux par molécule généralement très faibles.

L'objectif principal de ce projet est d'étendre le domaine d'application des techniques de détection de molécules uniques par fluorescence, et de dépasser les limites imposées par le phénomène de diffraction. Les objectifs spécifiques sont (i) obtenir un volume d'analyse inférieur à 0,1 attolitre, et (ii) réaliser une exaltation du signal de fluorescence d'une molécule individuelle d'un facteur supérieur à 100.

Des nanoantennes plasmoniques (nanofils et assemblages de nanoparticules) seront utilisés pour exalter localement l'interaction lumière-émetteur moléculaire. L'utilisation de ces nanoantennes implique de repenser les méthodes d'analyse du signal de fluorescence. Ce projet met en œuvre quatre techniques innovantes : (i) une excitation délocalisée de la fluorescence, (ii) l'utilisation d'un désactivateur chimique (quencher) pour contrôler le rendement quantique de l'émetteur, (iii) une modulation de polarisation pour extraire le signal utile du bruit, et (iv) l'émission de fluorescence stimulée. L'optimisation de ces techniques et leur utilisation conjointe permettra une extension significative de l'utilisation des nanoantennes plasmoniques pour des applications biophotoniques.

Ce projet aura des applications directes:

- Nanofabrication, pour la réalisation de nanoantennes par des méthodes de synthèse par chimie douce (auto-assemblage),
- Nanophotonique, pour caractiser en profondeur l'interaction lumière-nanoantenne-molécule,
- Chimie analytique, pour améliorer la détection de molécules individuelles en solution (mesures de cinétiques rapides à forte concentration et détection d'espèces de faible rendement quantique),
- Biophysique, pour étudier l'organisation fine des membranes cellulaires.

Photodynamique de saturation de fluorescence : ultramicroscopie et nanoantennes

La détection rapide et spécifique de biomolécules est un enjeu majeur, où la nanophotonique permet des gains notables. Une question essentielle est de distinguer le signal du bruit de fond. Pour dépasser les limites de l'état de l'art, le projet proposé ici combine des avancées récentes dans les domaines de l'ultramicroscopie optique et des nanoantennes plasmoniques. Une microscopie optique ultra-résolue sera développée en exploitant la saturation de fluorescence. Ce système particulièrement robuste servira à sonder des nanostructures photoniques, pour améliorer la sensibilité de détection de molécules fluorescentes dans un environnement fortement concentré.

La première partie de projet vise à modifier le montage de microscopie optique existant pour ajouter une modulation d'intensité et une détection synchrone. Les gains en résolution optique sous la limite de diffraction seront caractérisés. La seconde partie du projet porte sur la réalisation de nano-antennes plasmoniques dans un film d'or pour extraire le signal exalté d'une molécule individuelle dans un environnement de forte concentration. En combinant la localisation lumineuse induite par la nanoantenne avec l'analyse dynamique par la détection synchrone, le signal a bruit est augmenté. On peut ainsi bénéficier pleinement des exaltations électromagnétiques pour détecter l'activité de molécules individuelles dans un environnement fortement concentré, et permettre de suivre des cinétiques de réactions qui ne se déclenchent qu'au delà de concentration typiquement micromolaires.

Polymères thermosensibles, et nanoantennes plasmoniques

Le développement de plate-forme structurées à l'échelle nano- ou micrométrique de type biopuce suscite un intérêt grandissant depuis quelques années pour des applications dans le domaine de la culture cellulaire, de l'ingénierie tissulaire, ou de l'étude des interactions récepteurs-ligands biologiques. Bien que des progrès considérables aient été réalisés ces dernières années, le développement de nouvelles méthodes de structuration chimiques ou physiques de surface permettant l'adhésion confinée (à l'échelle nano- ou micrométrique) et réversible de protéines ou de cellules dans des conditions expérimentales douces, demeure un défi important.

Pour répondre à la fois aux critères d'adhésion nano-confinée et d'immobilisation réversible de bio-(objets), le couplage entre polymères thermosensibles et nano-optique, ou plus précisément plasmonique, apparaît comme une stratégie originale et intéressante. En effet, les nanoparticules de métaux nobles sont capables d'offrir un contrôle précis de la lumière et de la chaleur à l'échelle nanométrique, ce qui est particulièrement avantageux pour le développement de dispositifs intégrés miniaturisés.

Nous proposons de combiner des nanoparticules d'or, utilisées comme nanosources ponctuelles de lumière et de chaleur avec des brosses de polymères thermosensibles employés comme couche primaire d'adhésion afin d'obtenir des plateformes bioactives « intelligentes » offrant des propriétés de surface réversibles et contrôlées à l'échelle nanométrique. L'idée principale repose sur le caractère thermostimulable des polymères thermosensibles qui peut favoriser/défavoriser l'adhésion d'une protéine ou d'une cellule par simple changement de température. En effet, ces polymères présentent une transition de phase thermo-induite, accompagnée de modifications importantes de leurs propriétés chimiques, correspondant à une commutation hydrophile/hydrophobe. La conversion d’énergie opto-thermique fournie par les nanoparticules supportées conduira à un confinement spatial de la transition de phase du polymère permettant ainsi un contrôle précis des propriétés de mouillabilité de la surface et d’adhésion à l’échelle nanométrique, celles-ci étant contrôlables à distance sous l’effet d’une irradiation laser.

Nous évaluerons la capacité des substrats nanoparticules d’or/polymères thermosensibles à favoriser l’adhésion de particules modèles, de protéines ou de cellules puis à les relâcher de façon réversible après avoir couper l’irradiation laser. En balayant le spot laser d’un point à l’autre de la plate-forme, on pourra envisager d’adsorber différents types de bio(objets) dans des régions distinctes. De plus, le fort confinement du champ électromagnétique au voisinage des nanostructures plasmoniques permettra d’exalter les signaux Raman et de fluorescence des biomatériaux adsorbés pour une détection ultra-sensible.

Le système hybride constitué de nanoparticules d’or fonctionnalisées par des brosses de polymères thermosensibles offrira les propriétés uniques de (i) fort confinement du champ électromagnétique et augmentation de chaleur sur des régions sub-microniques; (ii) transition de phase du polymère induite par effet opto-thermique conduisant à des surfaces hautement structurées et présentant des propriétés chimiques stimulables, et (iii) un contrôle local et réversible de l’adhésion par le biais de la transition hydrophile/hydrophobe du polymère sous irradiation laser.

Le contrôle actif de la température à l’échelle nanométrique et ses implications dans le domaine de la biophysique est un champ de recherche important qui sera exploré par le consortium à travers ce projet, dont l’objectif principal est le développement d’une nouvelle génération de plateformes bioadhésives pour l’obtention de laboratoires sur puces « intelligents ».

Annexe A
Résumé des Travaux de Recherche

J’étudie comment des nanostructures photoniques permettent d’exalter l'émission optique de molécules. L’objectif est de dépasser les limites imposées par la diffraction en microscopie optique pour améliorer la détection de nano-émetteurs. Mes travaux combinent recherche fondamentale et applications. L’axe recherche fondamentale porte sur la compréhension des phénomènes électromagnétiques mis en jeu dans des antennes de dimensions nanométriques. L’axe recherche appliquée porte sur le développement de nouvelles techniques de détection et d’analyse de biomolécules. Ces travaux s’inscrivent dans les thématiques très actives actuellement des nano-antennes plasmoniques et des capteurs pour la biophotonique.

Axe 1. Nanophotonique : interaction lumière-matière exaltée par des nano-antennes

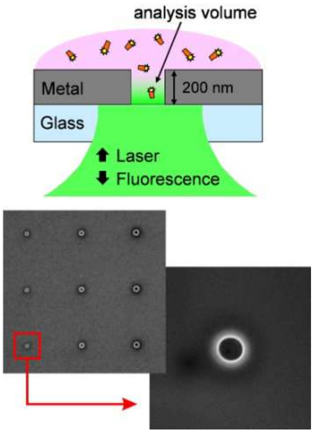

Exaltations électromagnétiques dans des nano-ouvertures métalliques. La diffraction par une ouverture est un sujet étudié depuis des siècles en électromagnétisme. Cependant, un défi persistant concerne la compréhension des phénomènes physiques intervenant lorsque le diamètre de l’ouverture est réduit en-dessous de la demi-longueur d’onde. L’approche développée utilise des molécules luminescentes pour sonder localement les interactions lumière-matière au voisinage de nano-ouvertures percées dans un film métallique. Différentes techniques ont été introduites pour quantifier les renforcements de champs électromagnétiques : spectroscopie de corrélation de fluorescence, suivi de dynamique temporelle de boîtes quantiques, spectroscopie sous saturation de fluorescence. Pour la première fois, ces expériences mesurent l’importance de la densité locale d’états photoniques. Une optimisation du design de la nano-ouverture a également permis un gain significatif (x25) sur l’émission de fluorescence de molécules individuelles.

Contrôler la directivité d’un nano-émetteur par une antenne plasmonique. Un nouveau type de nanoantenne a été étudié pour intensifier et contrôler la lumière émise par une seule molécule. La nanoantenne est formée d’une ouverture percée dans un film d’or, l’ouverture étant entourée de corrugations en sillons circulaires. Cette antenne transforme une molécule standard en une source de lumière intense et uni-directionnelle : l’intensité de fluorescence est

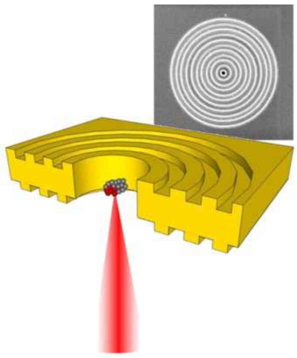

augmentée de 120 fois, et quasiment toute la lumière est émise dans un cône étroit. L'intensité lumineuse et la direction d'émission sont contrôlées simultanément à l'échelle d'une molécule unique, ce qui constitue une première mondiale. Cette démonstration est une étape importante pour le développement de nouvelles méthodes d'analyse biochimique, les nanosources de lumière et le traitement de l'information quantique.

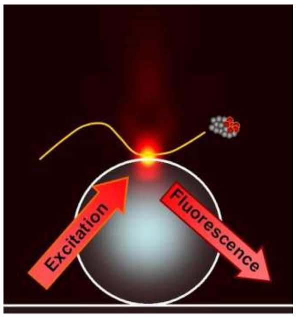

Dépasser la limite de diffraction avec des microsphères diélectriques. Un nouveau phénomène de confinement électromagnétique à 3 dimensions a été mis en évidence en exploitant la focalisation de la lumière par des sphères diélectriques de dimensions micrométriques. Sous certaines conditions des interférences entre le champ incident et le champ diffusé permettent le confinement de la lumière dans un volume de l'ordre de (□/n)^3, ce qui constitue un record pour un système purement diélectrique. Des molécules fluorescentes ont été utilisées comme sondes locales pour caractériser le confinement lumineux et l'exaltation locale d'intensité optique. En agissant comme une lentille positionnée directement dans le voisinage proche des molécules, la microsphère permet de mieux éclairer et de mieux collecter la lumière produite par les molécules, avec une exaltation x5 du signal de fluorescence par molécule. Ces démonstrations ouvrent de nouvelles perspectives pour l'amélioration des dispositifs de détection de molécules.

Axe 2. Applications biophotoniques : détection exaltée de biomolécules

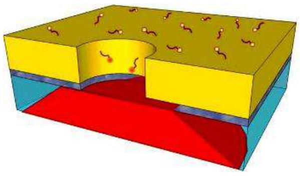

Détection exaltée de biomolécules. Grâce aux faibles volumes mis en œuvre dans les nanoouvertures, des réactions enzymatiques peuvent être analysées à de très fortes concentrations de plusieurs dizaines de micromolaires, alors que les mesures standard sont limitées à des concentrations dans la gamme de 10-100 nanomolaires. L'exaltation électomagnétique de la fluorescence améliore également grandement le rapport signal à bruit pour le suivi de réactions moléculaires, avec une possibilité de réduire le temps total d'intégration d'un facteur supérieur à 100. Les fortes exaltations du signal par molécule dans le cas des nano-ouvertures ou des microsphères ouvrent des nouvelles approches pour l'analyse rapide d'un grand nombre de réactions biochimiques. Ces travaux ont donné lieu au dépôt d'un brevet. Un transfert de technologie est en cours avec la société PixInBio basée à Gardanne.

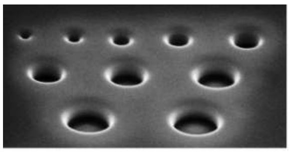

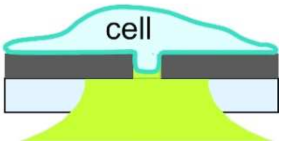

Analyse de l'architecture fine des membranes cellulaires. Les ouvertures nanométriques dans des films métalliques ont été utilisées pour réduire le volume d'observation en microscopie optique sous la limite de diffraction. En agissant comme un trou de filtrage placé directement sous l'objet, la nanoouverture autorise l'observation d'une zone sous la limite de diffraction optique. Cette ultra-résolution est mise à profit pour étudier la diffusion latérale de marqueurs individuels dans des membranes biologiques de cellules vivantes. La comparaison des comportements pour différentes espèces révèle la présence d'hétérogénéités de dimensions nanométriques qui contraignent la diffusion membranaire. Les dimensions de ces domaines sont de l'ordre de 50 nm, ce qui se situe bien en dessous de la limite de résolution de microscopes optiques.

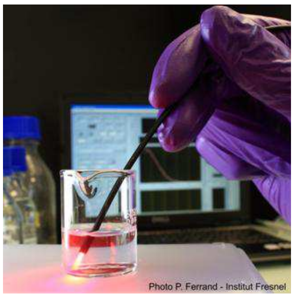
Photo P. Ferrand - Institut Fresnel

Capteurs bas coût pour l'analyse de molécules individuelles. Cet aspect des recherches porte sur le développement de systèmes compacts et efficaces pour l'analyse de molécules fluorescentes. En exploitant la focalisation introduite par la microphère, le signal de fluorescence d'une molécule fluorescente individuelle peut être détecté avec une lentille plastique jetable de lecteur de disque optique CDrom. Ces travaux ouvrent des perspectives d'application pour la détection exaltée de particules dans des dispositifs opto-fluidiques intégrés. En combinant une microsphère avec une fibre optique, nous avons réalisé le premier dispositif de corrélation de fluorescence en mode endoscope avec la sensibilité d'une molécule individuelle. Ces travaux étendent le domaine d'application de l'analyse de molécules individuelles aux systèmes d'endoscopie, offrant ainsi de nouvelles méthodes d'analyse (fluorescence, pH, température, agrégation moléculaire…) dans un dispositif compact et portable. Deux brevets ont été déposés.

Annexe B

Autres Activités

B1- Enseignement, formation et diffusion de la culture scientifique

Thèses, post-doctorats et stages encadrés

Post-doctorants :

- **Richard Hostein**, novembre 2009 – août 2010, recruté Maître de Conférences à l'université Pierre et Marie Curie - Paris VI.
- **Nadia Djaker,** novembre 2008 – octobre 2009, recrutée Maître de Conférences à l'université de Paris XIII Villetaneuse.
- **Davy Gérard**, septembre 2006 **-** août 2008, recruté Maître de Conférences à l'université de technologies de Troyes.
- **Benoît Cluzel**, mars 2006 - août 2006, recruté Maître de Conférences à l'université de Bourgogne.

Doctorant :

- **Heykel Aouani**, octobre 2008 – septembre 2011, 11 publications dans des revues internationales à comité de lecture durant la thèse, recruté post-doctorant à l'Imperial College

Stagiaires :

- **Joël Lepape**, stage de 2^{e} année Ecole Centrale Lyon, mai-juillet 2011.
- **Heykel Aouani**, stage de M2, mars-juillet 2008.
- **Wilfried Glastre**, stage de première année de l'école supérieure d'optique, juillet 2007.

Enseignement

2011

Cours magistral : Lasers : physique et applications, Ecole Supérieure des Mines de St Etienne, 48 heures, niveau M2

Encadrement de projet personnel : optical antennas, université Aix Marseille III Paul Cézanne, 28 heures, niveau M1, Master Erasmus Mundus

Encadrement de projet laboratoire : numerical simulations & single molecule spectroscopy, université Aix Marseille III Paul Cézanne, 15 heures, niveau M1, Master Erasmus Mundus

Travaux dirigés : microscopie de Fourier, université Aix Marseille III Paul Cézanne, 2 heures, niveau M1, Master Erasmus Mundus
Travaux dirigés : microscopie de Fourier, IUT université Aix Marseille, 2 heures, niveau L1
Cours magistral : Nanobioplasmonics, université Aix Marseille III Paul Cézanne, 2 heures, niveau doctorat

2010
Cours magistral : Lasers : physique et applications, Ecole Supérieure des Mines de St Etienne, 48 heures, niveau M2
Travaux dirigés : microscopie de Fourier, université Aix Marseille III Paul Cézanne, 4 heures, niveau M2
Cours magistral : Nanophotonics to improve single molecule fluorescence detection, université Aix Marseille III Paul Cézanne, 2 heures, niveau doctorat

2009
Travaux dirigés : microscopie de Fourier, université Aix Marseille III Paul Cézanne, 4 heures, niveau M2
Cours magistral : Nanobioplasmonique, université Aix Marseille III Paul Cézanne, 2 heures, niveau M2
Cours magistral : Nanophotonics to improve single molecule fluorescence detection, université Aix Marseille III Paul Cézanne, 2 heures, niveau doctorat

2008
Encadrement de projet transverse : minispectromètre intégré USB, Ecole Centrale de Marseille, 60 heures, niveau M1
Cours magistral : Nanostructure - enhanced single molecule fluorescence detection, Nanolum workshop, Les Houches, 1,5 heure, niveau doctorat
Cours magistral : Nanophotonics to improve single molecule fluorescence detection, université Aix Marseille III Paul Cézanne, 2 heures, niveau doctorat

2007
Encadrement de projet transverse : microscopie de Fourier, Ecole Centrale de Marseille, 60 heures, niveau M1
Cours magistral : préparation optique de chats de Schrödinger, école prédoctorale des Houches : physique quantique, 2 heures, niveau doctorat

Diffusion de la culture scientifique

Fête de la Science : éditions 2008, 2009 et 2010

Responsable pour l’Institut Fresnel : préparation des supports de présentation, gestion de l’organisation, accueil de groupes de scolaires et de grand public sur le campus de St Jérôme et aux village des sciences de Marseille centre.

Exposition « une manip, un chercheur » au Palais de la Découverte en 2011

Exposition sur le thème de l’holographie montée par différents laboratoires de la région marseillaise.

Accueil de scolaires au laboratoire : collège x2, lycée x3, classes préparatoires x2

B2- Transfert technologique, relations industrielles et valorisation

Transfert technologique

La société Genewave, basée à Palaiseau, a été associée pleinement aux recherches menées dans le cadre de l'ANR PNANO Coexus sur l'exaltation de la fluorescence par des nano-ouvertures métalliques. Elle dispose donc de toutes les connaissances nécessaires à l'exploitation de ce phénomène pour des applications de type biopuces à ADN. Une démonstration de faisabilité a été réalisée en ce sens dans notre laboratoire au cours de l'année 2008.

Contrats de recherche

- Société Flamel (Vénissieux), septembre 2008 - décembre 2008
- Société Flamel (Vénissieux), avril 2009 - décembre 2009

Ces deux études portent sur l'application de la technique FCS à la caractérisation de nanoparticules de polyaminoacides. En particulier, nous avons caractérisé par FCS la cinétique d'échange des chaînes de polymères entre nanoparticules ainsi que la cinétique de capture de protéines par ces nanoparticules.

Dépôts de brevet sur la période 2007-2011

1. *Système de spectroscopie à guide d'onde pour l'analyse de particules dans un milieu*, Brevet CNRS FR2949560 (04/03/2011). J. Wenger, N. Sojic, H. Aouani, F. Deiss, P. Ferrand, H. Rigneault.
2. *Dispositif et procédé d'analyse exaltée d'un échantillon de particules*, Brevet CNRS FR2930031 (16/10/2009). J. Wenger, D. Gérard, H. Rigneault.
3. *Dispositif pour la détection exaltée de l'émission d'une particule cible*, Brevet CNRS FR2908888 (23/05/2008) H. Rigneault, P.-F. Lenne, J. Wenger, E. Popov, T. Ebbesen

B3- Animation de la recherche

Rapporteur dans des revues à comité de lecture

30 rapports effectués sur la période 2007-2011 : Nano Letters, Physical Review Letters, Small, Advanced Functional Materials, Optics Express, Optics Letters, Journal of the American Chemical Society, Journal of Physical Chemistry Letters, Chemical Physics Letters, Plasmonics, International Journal of Optics.

Expertise de projets

18 projets nationaux et internationaux expertisés sur la période 2007-2011.

Programmes nationaux : ANR PNANO 2007, ANR PCV 2007, CNRS PCB 2007, ANR PNANO 2008, ANR PCV 2008, ANR Blanc 2010, ANR JCJC 2010, ANR P2N 2011, ANR Blanc InterII 2011, Triangle de la Physique 2011

Programmes internationaux : Fundazione CRPR 2009 (Italie), NWO Vidi Scheme 2010 (Pays-Bas), ISF individual research grant 2011 (Israël) et ISF MOST 2011 (Israël)

Travaux d'expertise

Participation au groupe « Matériaux et composants pour l'optique » de l'Observatoire des micro et nanotechnologies OMNT (unité mixte de service CNRS-CEA 2920) sur toute la période 2007-2011.

Organisation de conférences

1. 12^{e} édition de la conférence Carl Zeiss sur la FCS, Cargèse, octobre 2009
2. Ecole d'été Plasmonics SSOP, Porquerolles, septembre 2009
3. Atelier thématique GT2 du GdR Ondes, Marseille, décembre 2006

Comité scientifique de conférences

1. Atelier franco-japonais en nanophotonique, Ise-Kanko, japon, novembre 2011
2. Colloque « Fabrication, caractérisation optique et application de nano-objets », 12^{e} journées de la matière condensée JMC12, Troyes, août 2010

Jurys de thèse

1. Heykel Aouani, Université Paul Cézanne Aix Marseille III, 2011
2. Oussama Mahboub, Université Strasbourg, 2011
3. Caijing Huang, Université de Bourgogne, 2010

Comité de sélection MCF

1. Université de Technologie de Troyes 2011
2. Université de Lyon 2012

Annexe C

Liste des Productions Scientifiques

PUBLICATIONS INTERNATIONALES AVEC COMITE DE LECTURE

Sélection de 5 publications :

1. F. Grosshans, G. Van Assche, J. Wenger, R. Tualle-Brouri, N.J. Cerf et P. Grangier, High-rate quantum cryptography using Gaussian-modulated coherent states, Nature 421, 238-241 (2003). Cité 327 fois.
2. J. Wenger, R. Tualle-Brouri et P. Grangier, Non-Gaussian statistics from individual pulses of squeezed light, Phys. Rev. Lett. 92, 153601 (2004). Cité 121 fois.
3. J. Wenger, F. Conchonaud, J. Dintinger, L. Wawrezinieck, T.W. Ebbesen, H. Rigneault, D. Marguet, et P.-F. Lenne, Diffusion analysis within single nanometric apertures reveals the ultrafine cell membrane organization, Biophys. J. 92, 913-919 (2007). Cité 58 fois.
4. H. Aouani, J. Wenger, D. Gérard, H. Rigneault, E. Devaux, T.W. Ebbesen, F. Mahdavi, T. Xu, S. Blair, Crucial Role of the Adhesion Layer on the Plasmonic Fluorescence Enhancement, ACS Nano 3, 2043-2048 (2009). Cité 19 fois.
5. H. Aouani, O. Mahboub, N. Bonod, E. Devaux, E. Popov, H. Rigneault, T.W. Ebbesen, J. Wenger, Bright unidirectional fluorescence emission of molecules in a nanoaperture with plasmonic corrugations, Nano Lett. 11, 637-644 (2011). Cité 9 fois.

Données bibliométriques (au 10/02/12, source ISI Web of Knowledge) :

Nombre d’articles = 42   Total de citations = 1211   Index h = 18

2012

1. J. Wenger, *Fluorescence Enhancement Factors on Optical Antennas: Enlarging the Experimental Values without Changing the Antenna Design*, Int. J. Optics **2012**, 828121 (2012).

2011

2. R. Hostein, H. Aouani, H. Rigneault, J. Wenger, *Deciphering fluorescence signals by quantifying separately the excitation intensity from the number of emitters*, Opt. Lett. **36**, 3317-3319 (2011).
3. H. Aouani, O. Mahboub, E. Devaux, H. Rigneault, T.W. Ebbesen, J. Wenger, *Plasmonic antennas for directional sorting of fluorescence emission*, Nano Lett. **11**, 2400-2406 (2011).
4. H. Aouani, O. Mahboub, E. Devaux, H. Rigneault, T. W. Ebbesen, J. Wenger, *Large molecular fluorescence enhancement by a nanoaperture with plasmonic corrugations*, Opt. Express **19**, 13056-13062 (2011).
5. C. Favard, J. Wenger, P.-F. Lenne, H. Rigneault, *FCS diffusion laws on two-phases lipid membranes : experimental and Monte-carlo simulations determination of domain mean size*, Biophys. J. **100**, 1242-1251 (2011).
6. H. Aouani, O. Mahboub, N. Bonod, E. Devaux, E. Popov, H. Rigneault, T.W. Ebbesen, J. Wenger, *Bright unidirectional fluorescence emission of molecules in a nanoaperture with plasmonic corrugations*, Nano Lett. **11**, 637-644 (2011).

2010

7. P. Schön, N. Bonod, E. Devaux, J. Wenger, H. Rigneault, T.W. Ebbesen, and S. Brasselet, *Enhanced second harmonic generation from individual metallic nanoapertures*, Opt. Lett. **35**, 4063-4065 (2010).
8. N. Djaker, R. Hostein, E. Devaux, T.W. Ebbesen, H. Rigneault, J. Wenger, *Surface Enhanced Raman Scattering on a Single Nanometric Aperture*, J. Phys. Chem. C **114**, 16250-16256 (2010).
9. H. Aouani, P. Schön, S. Brasselet, H. Rigneault, J. Wenger, *Two-photon fluorescence correlation spectroscopy with high count rates and low background using dielectric microspheres*, Biomed. Opt. Express **1**, 1075-1083 (2010).
10. H. Aouani, S. Itzhakov, D. Gachet, E. Devaux, T. W. Ebbesen, H. Rigneault, D. Oron, J. Wenger, *Colloidal Quantum Dots as Probes of Excitation Field Enhancement in Photonic Antennas*, ACS Nano **4**, 4571-4578 (2010)
11. J. Wenger, H. Rigneault, *Photonic Methods to Enhance Fluorescence Correlation Spectroscopy and Single Molecule Fluorescence Detection*, Int. J. Mol. Sci. **11**, 206-221 (2010)

2009

12. H. Aouani, F. Deiss, J. Wenger, P. Ferrand, N. Sojic, H. Rigneault, *Optical-fiber-microsphere for remote fluorescence correlation spectroscopy*, Opt. Express **17**, 18912-18919 (2009).
13. H. Aouani, J. Wenger, D. Gérard, H. Rigneault, E. Devaux, T.W. Ebbesen, F. Mahdavi, T. Xu, S. Blair, *Crucial Role of the Adhesion Layer on the Plasmonic Fluorescence Enhancement*, ACS Nano **3**, 2043-2048 (2009).
14. Gérard D., Devilez A., Aouani H., Stout B., Bonod N., Wenger J., Popov E., Rigneault H., *Efficient excitation and collection of single molecule fluorescence close to a dielectric microsphere*, J. Opt. Soc. Am. B **26**, 1473-1478 (2009).
15. Devilez A., Bonod N., Stout B., Gérard D., Wenger J., Rigneault H., Popov E., *Three-dimensional subwavelength confinement of light with dielectric microspheres*, Opt. Express **17**, 2089-2094 (2009).
16. J. Wenger, D. Gérard, H. Aouani, H. Rigneault, B. Lowder, S. Blair, E. Devaux, T. W. Ebbesen, *Nanoaperture-Enhanced Signal-to-Noise Ratio in Fluorescence Correlation Spectroscopy*, Anal. Chem. **81**, 834-839 (2009).
17. J. Wenger, D. Gerard, P.-F. Lenne, H. Rigneault, N. Bonod, E. Popov, D. Marguet, C. Nelep, T. W. Ebbesen, *Biophotonics applications of nanometric apertures*, Int. J. Materials and Product Technology **34**, 488-506 (2009)

2008

18. D. Gérard, J. Wenger, N. Bonod, E. Popov, H. Rigneault, J. Dintinger, T.W. Ebbesen, F. Mahdavi et S. Blair, *Nanoaperture-enhanced fluorescence: Towards higher detection rates with plasmonic metals*, Phys. Rev. B **77**, 045413 (2008).
19. N. Bonod, E. Popov, D. Gérard, J. Wenger, and H. Rigneault, *Field enhancement in a circular aperture surrounded by a single channel groove*, Opt. Express **16**, 2276-2287 (2008).
20. J. Wenger, D. Gérard, J. Dintinger, O. Mahboub, N. Bonod, E. Popov, T. W. Ebbesen, and H. Rigneault, *Emission and excitation contributions to enhanced single molecule fluorescence by gold nanometric apertures*, Opt. Express **16**, 3008-3020 (2008).
21. P.-F. Lenne, H. Rigneault, D. Marguet, J. Wenger, *Fluorescence fluctuations analysis in nanoapertures: physical concepts and biological applications*, HistoChem. Cell. Biol. **130**, 795-805 (2008).
22. Ferrand P., Wenger J., Devilez A., Pianta M., Stout B., Bonod N., Popov E., Rigneault H., *Direct imaging of photonic nanojets*, Opt. Express **16**, 6930-6940 (2008).
23. Wenger J., Gérard D., Aouani H., Rigneault H., *Disposable Microscope Objective Lenses for Fluorescence Correlation Spectroscopy Using Latex Microspheres*, Anal. Chem. **80**, 6800-6804 (2008).

24. Gérard D., Wenger J., Devilez A., Gachet D., Stout B., Bonod N., Popov E., Rigneault H., *Strong electromagnetic confinement near dielectric microspheres to enhance single-molecule fluorescence*, Opt. Express **16**, 15297-15303 (2008).

2007

25. E. Popov, M. Nevière, A. Sentenac, N. Bonod, A.-L. Fehrembach, J. Wenger, P.-F. Lenne, H. Rigneault, *Single-scattering theory of light diffraction by a circular subwavelength aperture in a finitely conducting screen*, J. Opt. Soc. Am. A **24**, 339-358 (2007).
26. Wenger J., Cluzel B., Dintinger J., Bonod N., Fehrembach A.-L., Popov E., Lenne P.-F., Ebbesen T.W., Rigneault H., *Radiative and Nonradiative Photokinetics Alteration Inside a Single Metallic Nanometric Aperture*, J. Phys. Chem. C **111**, 11469-11474 (2007).
27. J. Wenger, F. Conchonaud, J. Dintinger, L. Wawrezinieck, T.W. Ebbesen, H. Rigneault, D. Marguet, et P.-F. Lenne, *Diffusion analysis within single nanometric apertures reveals the ultrafine cell membrane organization*, Biophys. J. **92**, 913-919 (2007).

2006

28. E. Popov, M. Nevière, J. Wenger, P.F. Lenne, H. Rigneault, P. Chaumet, J. Dintinger, T.W. Ebbesen et N. Bonod, *Field enhancement in single subwavelength apertures*, J. Opt. Soc. Am. A **23**, 2342-2348 (2006).
29. J. Wenger, J. Dintinger, N. Bonod, E. Popov, P.F. Lenne, T.W. Ebbesen et H. Rigneault, *Raman scattering and fluorescence emission in a single nanoaperture: optimizing the local intensity enhancement*, Optics Comm. **267**, 224-228 (2006)
30. J. Wenger, H. Rigneault, J. Dintinger, D. Marguet et P.-F. Lenne, *Single fluorophore diffusion in a lipid membrane over a subwavelength aperture*, J. Biol. Phys. **32**, SN1-SN4 (2006).
31. J. Wenger, D. Gérard, P.-F. Lenne, H. Rigneault, J. Dintinger, T.W. Ebbesen, A. Boned, F. Conchonaud, D. Marguet, *Dual-color fluorescence cross-correlation spectroscopy in a single nanoaperture : towards rapid multicomponent screening at high concentrations*, Opt. Express **14**, 12206-12216 (2006).

2005

32. H. Rigneault, J. Capoulade, J. Dintinger, J. Wenger, N. Bonod, E. Popov, T.W. Ebbesen et P.F. Lenne, *Enhancement of single molecule fluorescence detection in subwavelength apertures*, Phys. Rev. Lett. **95**, 117401 (2005).
33. J. Wenger, P.F. Lenne, E. Popov, J. Dintinger, T.W. Ebbesen et H. Rigneault, *Single molecule fluorescence in rectangular nano-apertures*, Opt. Express **13**, 7035-7044 (2005).
34. J. Wenger, A. Ourjoumtsev, R. Tualle-Brouri et P. Grangier, *Time-resolved homodyne characterization of individual quadrature-entangled pulses*, Eur. Phys. J. D. **32**, 391-396 (2005).

2004

35. J. Wenger, R. Tualle-Brouri et P. Grangier, *Pulsed homodyne measurements of femtosecond squeezed pulses generated by single-pass parametric deamplification*, Opt. Lett. **29**, 1267 (2004).
36. J. Wenger, R. Tualle-Brouri et P. Grangier, *Non-Gaussian statistics from individual pulses of squeezed light*, Phys. Rev. Lett. **92**, 153601 (2004).
37. J. Wenger, J. Fiurasek, R. Tualle-Brouri, N.J. Cerf et P. Grangier, *Pulsed squeezed vacuum characterization with and without homodyning*, Phys. Rev. A **70** 053812 (2004)
38. R. Garcia Patron-Sanchez, J. Fiurasek, N.J. Cerf, J. Wenger, R. Tualle-Brouri et P. Grangier, *Proposal for a loophole-free Bell test using homodyne detection*, Phys. Rev. Lett. **93**, 130409 (2004).

2003

39. F. Grosshans, G. Van Assche, J. Wenger, R. Tualle-Brouri, N.J. Cerf et P. Grangier, *High-rate quantum cryptography using Gaussian-modulated coherent states*, Nature **421**, 238-241 (2003).

40. F. Grosshans, N.J. Cerf, J. Wenger, R. Tualle-Brouri et P. Grangier, *Virtual entanglement and reconciliations protocols for quantum cryptography with continuous variables*, Quant. Inf. and Comput. **3**, 535-552 (2003).
41. J. Wenger, M. Hafezi, F. Grosshans, R. Tualle-Brouri et P. Grangier, *Maximal violations for Bell inequalities using continuous variables measurements*, Phys. Rev. A **67**, 012105 (2003).

ACTES DE CONFERENCES AVEC COMITE DE LECTURE

2010

1. J. Wenger, H. Aouani, D. Gérard, S. Blair, T.W. Ebbesen and H. Rigneault, *Enhanced fluorescence from metal nanoapertures: physical characterizations and biophotonic applications,* Proc. of SPIE, Vol. 7577, pp.75770J (2010)
2. H. Aouani, N. Djaker, J. Wenger, and H. Rigneault, *High-efficiency single molecule fluorescence detection and correlation spectroscopy with dielectric microspheres,* Proc. of SPIE, Vol. 7571, pp.75710A (2010)

2009

3. A. Devilez, J. Wenger, B. Stout, N. Bonod, *Transverse and longitudinal confinement of photonic nanojets by compound dielectric microspheres,* Proc. of SPIE, Vol. 7393, pp.73930E-1 (2009)

CHAPITRES D'OUVRAGES COLLECTIFS

1. J. Wenger, *Aperture antennas: fundamentals and biophotonics applications*, à paraître dans Optical Antennas, édité par M. Agio et A. Alu, Cambridge University Press (Cambridge, 2012).
2. P. Ferrand, J. Wenger, H. Rigneault, *Fluorescence correlation spectroscopy*, à paraître dans Methods in Molecular Biology: Walker, J.M. (Ed.), Humana Press (Berlin, 2012).
3. S. Blair et J. Wenger, *Enhancing fluorescence with sub-wavelength metallic apertures*, dans *Topics on Surface Enhanced Fluorescence*, édité par C. Geddes, John Wiley & Sons (2010).
4. J. Wenger, A. Ourjoumtsev, J. Laurat, R. Tualle-Brouri et P. Grangier, *Experimental non-Gaussian manipulation of continuous variables* dans *Quantum information with continuous variables of atoms and light,* édité par N. Cerf, G. Leuchs et E. Polzik, Imperial College Press (London, 2007).

CONFERENCES INVITEES

Internationales

1. Japan-France Fontiers of Engineering symposium, Kyoto 2012
2. 5th International Conference on electromagnetic Near-field Characterization and Imaging ICONIC, Rouen 2011
3. Second Summer School on Plasmonics SSOPII, Porquerolles 2011
4. Plasmonics in biology and medicine VII, SPIE BIOS – Photonics West, San Francisco 2010
5. International Japanese – American – French workshop on NanoBioPhotonics, Marseille, 2009
6. 12th Carl Zeiss sponsored workshop on FCS and related methods, Cargèse, 2009
7. 1st French-Taïwan frontiers of science symposium, Taïwan, 2008
8. Nanolum workshop, Les Houches, 2008
9. International Workshop "Plasmonics in biology and in medicine", Paris, 2007
10. International Workshop : "Single Molecules and Nanophotonics", Marseille, 2007
11. 2nd ESF workshop on Continuous Variable Quantum Information Processing, Aix en Provence, 2003

Nationales

12. Premières journées GdR Plamonique Moléculaire et Spectroscopies Exaltées, Meudon 2011
13. Colloque Lasers et Optique Quantique Coloq'12, Marseille, 2011
14. Ecole thématique CNRS Nano-objets aux interfaces, Anglets, 2011
15. Journées scientifiques C'Nano PACA, Porquerolles 2010
16. Atelier du Forum de Microscopies à Sondes Locales, Hardelot, 2009
17. Ecole prédoctorale des Houches : physique quantique, Les Houches, 2007

Note : La liste complète et détaillée (titre, auteurs, dates…) des contributions à des conférences dont je suis co-auteur est disponible via le serveur HAL : http://hal.archives-ouvertes.fr/IF

BREVETS

1. *Système de spectroscopie à guide d'onde pour l'analyse de particules dans un milieu*, Brevet CNRS FR2949560 (04/03/2011). J. Wenger, N. Sojic, H. Aouani, F. Deiss, P. Ferrand, H. Rigneault.
2. *Dispositif et procédé d'analyse exaltée d'un échantillon de particules*, Brevet CNRS FR2930031 (16/10/2009). J. Wenger, D. Gérard, H. Rigneault.
3. *Dispositif pour la détection exaltée de l'émission d'une particule cible*, Brevet CNRS FR2908888 (23/05/2008) H. Rigneault, P.-F. Lenne, J. Wenger, E. Popov, T. Ebbesen
4. *High-rate quantum key distribution scheme relying on continuously phase- and amplitude-modulated coherent light pulses,* N.J. Cerf, R. Brouri, P. Grangier, F. Grosshans, G. Van Assche, J. Wenger. Brevet US 7,403,623 (22/07/2008).

ARTICLES DE VULGARISATION

1. Wenger J., Aouani H., Milutinovic M., Deiss F., Ferrand P., Sojic N., Rigneault H. *Sonde à fibre optique pour la spectroscopie de corrélation de fluorescence : l'analyse des dynamiques de fluorescence devient portable*, Spectra Analyse **275**, 43-47 (2010)
2. J. Wenger, *Détection exaltée de molécules fluorescentes avec des structures photoniques : application aux mesures dynamiques en solution* revue Perspectives de l'Ecole Supérieure d'Optique (2010)
3. J. Wenger et H. Rigneault, *Nanostructures photoniques pour la détection exaltée de la fluorescence de molécules individuelles*, Spectra Analyse **262**, 27-29 (2008).
4. Wenger J., Lenne P.-F., Popov E., Capoulade J., Rigneault H., Dintinger J., Ebbesen T.W., Bonod N., *Nanopuits métalliques pour exalter les contrastes en microscopie optique*, Photoniques **23**, 43-46 (2006)

Annexe D

Curriculum Vitae

Né le 06 avril 1978, Nationalité française, Marié, deux enfants

jerome.wenger@fresnel.fr http://jw-photonics-inside.over-blog.org/

1. PARCOURS PROFESSIONNEL RECHERCHE

Chargé de recherche CNRS : Micro et Nanostructures photoniques pour la détection exaltée de molécules

Institut Fresnel, Marseille, recruté CR2 en octobre 2005, promu CR1 en octobre 2009

Exploitation de structures métalliques et diélectriques pour exalter l'émission optique de molécules par fluorescence et diffusion Raman. Ces travaux concernent :

- La compréhension fondamentale de l'interaction lumière-matière au voisinage de nanoantennes optiques : antennes plasmoniques et microsphères diélectriques.
- Les applications biophotoniques : développement de nouvelles technologies de détection dynamique de biomolécules fluorescentes en solution ou dans des membranes cellulaires.

Domaines : nanophotonique, biophotonique, plasmonique, émission optique moléculaire

Post-Doctorat CNRS : Fluorescence de molécules uniques dans des puits nanométriques

Institut Fresnel, Groupe Mosaic, Marseille, octobre 2004 – septembre 2005

Mots-clés : nanotrous métalliques, microscopie confocale, corrélation de fluorescence

Thèse : Dispositifs impulsionnels pour la communication quantique à variables continues

Institut d'Optique, Groupe Optique Quantique, Orsay, mai 2001 – septembre 2004

Utilisation des propriétés quantiques d'impulsions lumineuses pour développer de nouveaux dispositifs de traitement de l'information quantique : cryptographie quantique à impulsions cohérentes et génération d'états quantiques non-gaussiens.

Domaines : optique quantique, optique non-linéaire, laser femtoseconde

FORMATION INITIALE

2001-2004	Doctorat de physique de l'Université Paris-XI (*Orsay*), sous la direction de Philippe Grangier. Mention Très Honorable.
1998-2001	Ingénieur de l'Ecole Supérieure d'Optique (*Orsay*).
	DEA « Optique et Photonique » de l'Université Paris-Sud. Mention Très Bien.

PRIX ET DISTINCTIONS

1. Prix Jeune Chercheur (Daniel Guinier) de la Société Française de Physique, Mention spéciale du Jury, édition 2004.
2. Prix La Recherche, Mention « Mobilités », édition 2004.
3. Prix d'installation pour chercheur de la ville de Marseille, édition 2005.
4. Lauréat financé ERC Starting Grant 2011
5. Prix Edouard Branly, édition 2011